2015

Experimental Investigation And Analysis Of High-Enthalpy Nitrogen Flow Over Graphite

Andrew Lutz
University of Vermont

EXPERIMENTAL INVESTIGATION AND ANALYSIS OF HIGH-ENTHALPY NITROGEN FLOW OVER GRAPHITE

A Dissertation Presented

by

Andrew J. Lutz

to

The Faculty of the Graduate College

of

The University of Vermont

In Partial Fullfillment of the Requirements
for the Degree of Doctor of Philosophy
Specializing in Mechanical Engineering

May, 2015

Defense Date: March 11, 2015
Dissertation Examination Committee:

Douglas G. Fletcher, Ph.D., Advisor
Britt Holmén, Ph.D., Chairperson
Yves Dubief, Ph.D.
Darren Hitt, Ph.D.
Cynthia J. Forehand, Ph.D., Dean of the Graduate College

Abstract

The high-enthalpy flow generated by hypersonic vehicles traveling within the Earth's atmosphere inherently delivers an elevated heat flux to the vehicle surface. In addition to conductive heating, the liberated energy generated by various exothermic chemical reactions occurring at the vehicle surface further augment the total heat load. Quantifying the rates at which these reactions take place is imperative and remains a significant challenge as developers attempt to design the next generation of thermal protection systems.

This study focused on nitrogen recombination and carbon nitridation, as these reactions are ubiquitous to the most aggressive atmospheric re-entry trajectories in which carbon-based ablative heat shields are conventionally employed. The 30-kW inductively coupled plasma torch located within the Plasma Diagnostics and Test Laboratory at the University of Vermont was used to produce high-enthalpy nitrogen plasma flow, which sufficiently simulated the various in-flight heat flux processes. A combination of optical-based techniques, including spontaneous emission spectroscopy and laser induced fluorescence were utilized to study the free jet and the interaction of the flow with samples constructed from POCO graphite.

Emission measurements within the free stream indicated that the nitrogen flow was in non-equilibrium due to the inverse predissociation of ground state nitrogen atoms into the $B^3\Pi_g$(v=13) vibrational level of molecular nitrogen. The degree of non-equilibrium was quantified by determining the overpopulation of ground state nitrogen with respect to equilibrium and its effects were considered throughout the analysis.

Results obtained through emission spectroscopy and laser induced fluorescence confirmed that the graphite material behaved as a catalytic surface that actively promoted nitrogen recombination. Additionally, the calculated carbon nitridation rate was several orders less efficient, although its effect on the sample surface erosion was evident in the sample mass loss measurements.

Subsequently, an independent set of heat flux measurements performed over materials of varying catalycities further supported the data obtained with optical diagnostics. Furthermore, the heat flux results yielded the surface accommodation factor of graphite for the nitrogen recombination rate and indicated that the surface was slightly less than fully-accommodating.

Acknowledgments

I would like to thank several individuals who have helped me along the way. First and foremost, thank you to my wife, Ronnell. Without her unwavering support and patience, this work would not have been possible. Thank you to all the wonderful friends who've come through Perkins 211 over the years and made this process more bearable, including Max, Walt, Jason, Corey, Luke, Juergen, Silas, Steve, Nick, Ian, Will, and all the others who may be reading this and thinking, "Where's my name?" A particular thank you to Floyd for all the help in the shop. A genuine thank you to my thesis committee: Dr. Britt Holmén, Dr. Yves Dubief and Dr. Darren Hitt, and my advisor, Dr. Douglas Fletcher. Thank you to all my loving friends and family. Lastly, a simple thank you to Patrick Ewing, for showing me how to dunk on TV.

Table of Contents

List of Tables

List of Figures

Abbreviations

ASR	Absolute Spectral Response
CCD	Charge-Coupled Device
DPLR	Data Parallel Line Relaxation
FWHM	Full Width Half Max
He-Ne	Helium-Neon
ICP	Inductively-Coupled Plasma
LeMANS	The Michigan Aerothermal Navier-Stokes Solver
LIF	Laser-Induced Fluorescence
LTE	Local Thermodynamic Equilibrium
MDFR	Microwave Discharge Flow Reactor
MUTATION	Multicomponent Transport, Thermodynamic and Chemistry Properties for Ionized Gases Software
Nd:YAG	Neodymium-doped Yttrium Aluminum Garnet
NEBOULA	Non-Equilibrium Boundary Layer Software
PDTL	Plasma Diagnostics and Test Laboratory
PICA	Phenolic Impregnated Carbon Ablator
S/N	Signal-to-Noise Ratio
TPS	Thermal Protection System
UVM	University of Vermont

Chapter 1

Introduction

1.1 Overview

Several government agencies, including NASA and the United States Air Force, have devoted significant research effort towards hypersonic, high-enthalpy flow since the advent of space travel, with particular attention on protecting hypersonic vehicles from elevated convective and radiative heat loads. Thermal protection systems (TPS) provide the necessary protective barrier between the external flow and the payload within the vehicle, although at a significant mass penalty. Atkinson illustrated the TPS mass percentage required for various atmospheric entry vehicles in terms of the stagnation pressure and peak heating conditions at the vehicle surface; the TPS material used in the Apollo missions accounted for 13.7% of the total vehicle mass, whereas the more aggressive Jovian entry required that more than 50% of the vehicle mass be dedicated to the TPS [16]. In 2012, NASA's Office of the Chief Technologist cited the need for "low mass TPS for higher entry speeds, and qualification over a wider range of conditions" and considered Entry, Descent and Landing and Thermal Management Systems among the agency's "Grand Challenges" [17], [18],

[19]. Clearly, researchers face a difficult task in developing highly-efficient, reliable materials while minimizing mass. To this end, TPS materials have progressively improved, owing to the extensive amount of experimental data extracted from in-flight and ground-based tests, in conjunction with numerical simulations. However, despite these improvements many fundamental questions regarding energy transport to the surface remain unanswered. This work investigates a set of nitrogen-based chemical reactions that are key to understanding hypersonic flight in Earth's atmosphere as well as the atmosphere of many other celestial bodies. Specifically, this investigation yields the reaction rates of carbon nitridation and nitrogen recombination on the surface of graphite at a particular thermodynamic condition.

1.1.1 High Temperature Gas Dynamics

The principal chemical species present in dry air at standard atmospheric conditions (T = 300-K, p = 1-atm) are molecular nitrogen and oxygen, with trace amounts of argon, carbon dioxide and other minor species including neon, helium and methane (N_2 : *78.1%*, O_2 : *20.9%*, *Ar : 0.9%*, CO_2 : *0.03%*) [20]. One often analyzes air as a mixture of nitrogen and oxygen exclusively with little loss in generality. Considering this reduced mixture, Figure 1.1 shows the equilibrium composition of air over a range of re-entry flight temperatures, as calculated by the MUTATION software package [7]. At low temperatures, the gas composition contains molecular nitrogen and oxygen exclusively. As the temperature increases, the molecular thermal velocity increases as well. At roughly 800-K, vibrational modes within the molecules become "excited," which provides them with an additional degree of freedom with which to store energy. It is at this point that the internal energy and the specific heat of the gas become functions of temperature and the gas is no longer considered calorically perfect. Near

2000-K, oxygen molecules begins to dissociate, introducing an equilibrium population of oxygen atoms into the gas. Oxygen fully-dissociates near 4000-K, and molecular nitrogen begins to dissociate at 4500-K, which allows for NO formation to occur over a short temperature interval before dissociating as well. Nitrogen molecule fully dissociates at 9000-K and ionization of the atomic particles appears at temperatures near 10,000-K, which subsequently introduces a population of free electrons into the gas.

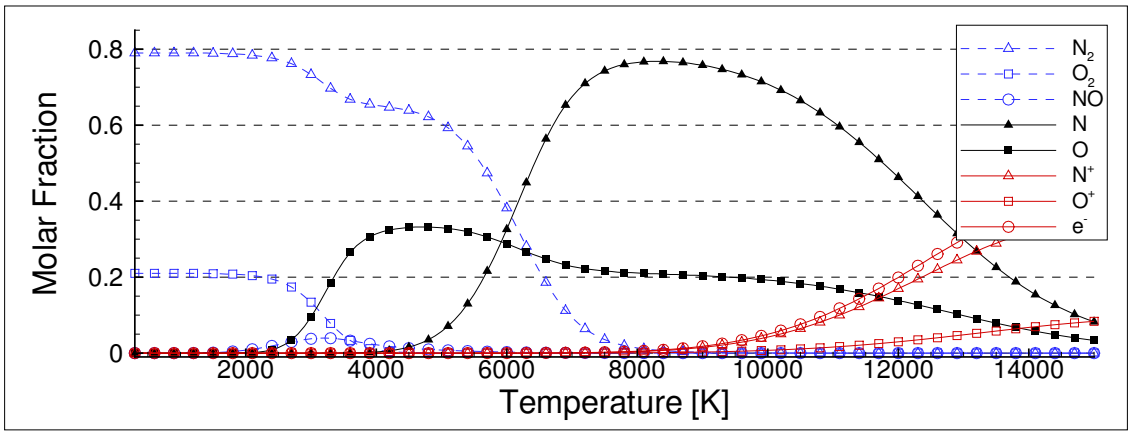

Figure 1.1: Molar fraction of 8-species air at 160-Torr [7].

Two independent intensive properties are required to fully describe the state of a gas in chemical equilibrium. Figure 1.1 corresponds to a pressure of 160-Torr, which matched the pressure condition utilized in all experimental phases of this investigation. The chemical processes that occur between two independent states (e.g. dissociation, recombination, ionization, etc.) proceed at finite rates, and the equilibrium assumption is not always valid in a system with multiple competing processes. The rates at which these processes occur provide the foundation for this investigation. Section 1.1.5 discusses this topic further.

1.1.2 Atmosphere Reentry Conditions

A hypersonic vehicle progressively passes through denser gases as it descends through the Earth's atmosphere. At the highest altitudes, the mean free path between the gas particles is of the same order or greater than the characteristic length scale of the vehicle. However, as the vehicle continues to descend, the ambient gas transitions from a low-density, rarified regime into a continuum field, where interactions between the air and the vehicle become important, causing the heat flux on the vehicle to rise. Allen and Eggers seminal paper from 1958 describes the ideal shapes of various classes of hypersonic vehicles where the objective is to minimize the total heat load. They indicate that for vehicles, such as space capsules, that are "... to be decelerated to relatively low speeds, ... convective heating is minimized by employing shapes with a high pressure drag [21]." A hypersonic vehicle with high pressure (or form) drag develops a detached bow shock at a fixed distance off its leading edge, which creates a region of subsonic flow in the post shock wake that propagates to the surface of the vehicle. Figure 1.2 provides an illustration of the shock wave on a blunt body and a slender body vehicle. Notice the standoff distance in the blunt body shape.

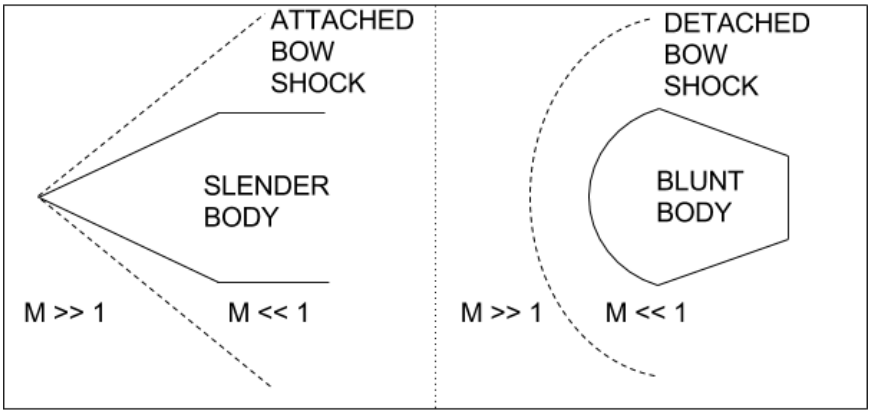

Figure 1.2: A comparison of the shock location for slender body and blunt body vehicles.

There are several methods with which to estimate the post shock thermodynamic conditions. The simplest approach is to assume that the air behaves as a calorically perfect gas, which denotes that the specific heats remain constant with respect to temperature throughout the system. Using this assumption, one calculates the post shock temperature from isentropic relations. Figure 1.3 shows the post-shock temperatures estimated using the calorically-perfect assumption for standard atmosphere conditions at an altitude of 52-km. These temperatures are plotted with respect to a range of realistic reentry speeds. In particular, the Apollo missions entered the Earth's atmosphere at $\approx$ 11-km-s^{-1}, which corresponds to an estimated post-shock temperature of 55,000-K under the chemically-perfect gas assumption [22].

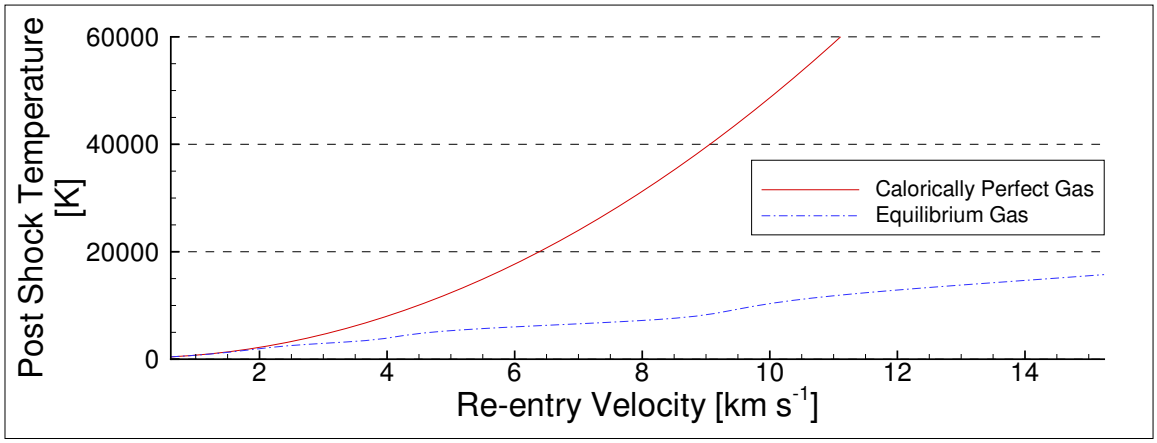

Figure 1.3: A comparison of the post-shock temperatures estimated for a chemically-perfect gas and an equilibrium gas at standard conditions at 52 km [8], [9].

In reality, the state of the gas changes rapidly across a shock, which invalidates the calorically-perfect gas assumption. This change in flow properties occurs nearly instantaneously, owing to the fact that a typical shock wave is very thin ($\approx 10^{-5}$-cm) [23]. As the gas passes through the shock wave, the collision frequency increases dramatically, which drives the molecular species into higher vibrational energy levels and eventually leads to significant dissociation and ionization, provided that the shock

is sufficiently strong. With respect to the calorically-perfect assumption, the post-shock enthalpy is more efficiently distributed within the gas. Wittliff and Curtis, along with the complementary works of Marrone provided an estimation of the post-shock temperatures by assuming chemical equilibrium in the post-shock region [9], [8]. The results from their work are plotted alongside the calorically-perfect assumption in Figure 1.3. In comparison, the equilibrium gas model predicts a more reasonable, albeit elevated, post shock temperature of $\approx$ 11,000-K for the re-entry velocities observed on Apollo.

1.1.3 Surface Catalycity and Heat Flux

In addition to the convection of high-enthalpy gas towards the vehicle surface, reactions occurring in the gas-phase and at the gas-surface interface can significantly increase the surface heat flux as well. Conventionally, one assumes that the surface is fully-accommodating, which indicates that the material absorbs the total energy released by all exothermic reactions at the surface. Fay and Riddell illustrate the impact of chemical reactions on the heat flux via Figure 1.4 [10].

Here, the heat transferred to the wall, expressed as a function of the Nusselt and Reynolds numbers, is plotted with respect to a recombination rate parameter (C_1), which the authors define as the frequency with which atomic species recombine in the gas phase. The recombination rate parameter is directly related to the Damköhler number, which is a dimensionless quantity conventionally used to compare the reaction rate timescale with the flow convection timescale. It is a useful quantity because it indicates whether a particular flow system is frozen ($Da \ll 1$), in equilibrium ($Da \gg 1$) or whether one must consider all rate-based processes discretely ($Da \approx 1$).

Briefly, frozen flow is a term used to describe flow systems wherein the reaction

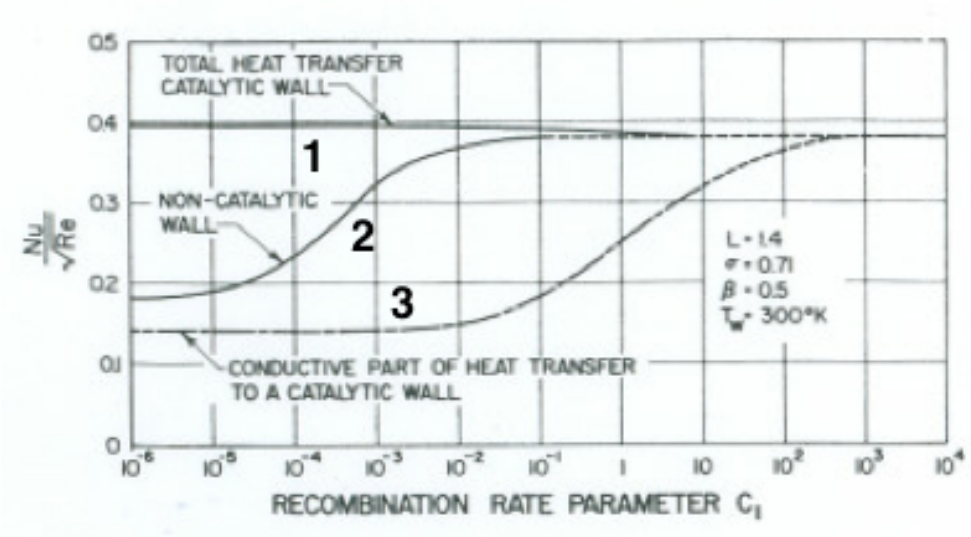

Figure 1.4: A comparison of the relative heat flux on materials of varying catalycities with respect to the gas-phase recombination rate parameter [10].

rates proceed several orders slower than convection flow rates. In this case, the gas-phase composition does not change unless it interacts with a third body. Hence, there is a large degree of chemical potential energy present in frozen flow systems that may be absorbed by catalytic materials that promote recombination at the surface. Conversely, flow fields with sufficiently large Damköhler numbers indicate equilibrium flow. Here, reaction rates proceed quickly enough to allow the system to adjust to an equilibrium composition at all locations within the flow. In Figure 1.4, frozen flow and equilibrium flow correspond to recombination rate parameters of 10^{-6} and values above 10^3, respectively.

Notice that Figure 1.4 contains three traces. Curve 1 represents the total heat transferred to a fully-catalytic wall. For this surface, the total heat transfer remains nearly constant with respect to the Damköhler number, which indicates that the potential energy contained within the flow is deposited onto the surface regardless of its chemical behavior. However, the fundamental process with which the heat is transferred to a fully-catalytic material does change with respect to the nature of the

flow field. This fact is highlighted by curve 3, which shows the heat transfer due to conduction only on a fully catalytic surface. Note that conduction dominates the heat transfer in an equilibrium flow field. However, as the system shifts towards lower Damköhler numbers, the portion of the total energy transferred to the surface due to conduction decreases. Eventually, the conduction heat transfer component levels off at frozen flow conditions. The gap between curve 1 and curve 3 shows that the exothermic chemical reactions occurring at the surface conserve the total heat flux.

In contrast, curve 2 shows that the total heat flux on a non-catalytic material is dependent upon the flow field. In equilibrium flow, the total heat flux is identical to the fully-catalytic material, owing to the fact that the energy is transferred to the surface through conduction exclusively. However, unlike the fully-catalytic surface, the total heat flux on the non-catalytic surface lowers as the Damköhler number decreases. The non-catalytic surface does not promote chemical reactions, thus it does not recover the energy deposited in equilibrium flow. Simply, Figure 1.4 illustrates the importance of chemical reactions occurring in the flow with respect to the heat flux experienced by a vehicle. It also reveals the importance of accurately quantifying the catalycity of a material.

1.1.4 Thermal Protection Systems

The analysis of high-enthalpy, chemically reacting flow is very complex due to the number of competing rate-based processes that occur, which include chemical reactions, diffusion and convection. The inherent complexities become slightly more solvable after making several simplifying assumptions. The first assumption is to disregard all minor chemical species and to consider air as a mixture of oxygen and nitrogen exclusively. However, this model is still too complex for initial consideration.

Aggressive re-entry trajectories may produce an 11-species gas mixture of oxygen and nitrogen, which are far too many variables to consider simultaneously (N_2, O_2, N, O, NO, N_2^+, O_2^+, N^+, O^+, NO^+, e^-). Additionally, chemical species released from the surface through an assortment of gas-surface interactions further increases chemical complexitiy present in the system. Therefore, it is best to reduce the problem by focusing separately on nitrogen and oxygen-based flows before attempting to analyze the full air mixture. This investigation focused exclusively on nitrogen flows with the intention of developing experimental methods and analytical techniques that could be applied to oxygen flows in the future.

TPS materials are conventionally identified as ablative or non-ablative. Ablative TPS are the preferred systems for the most aggressive atmospheric entry trajectories due to their ability to withstand extreme environments that are beyond the melting temperature of conventional non-ablative materials. Figure 1.5 shows a side-by-side comparison of the heat flux processes present in non-ablative and ablative materials.

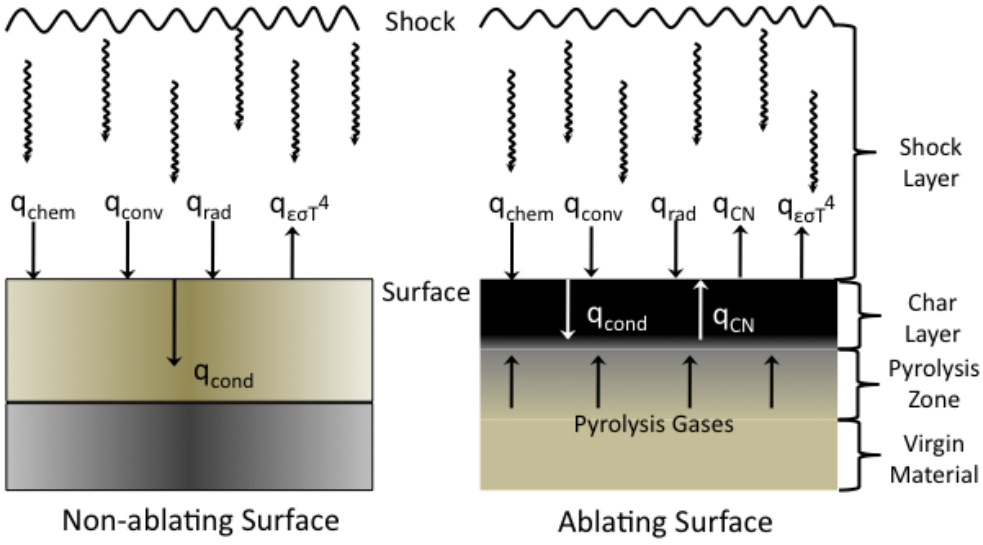

Figure 1.5: A comparison between the heat flux processes present in non-ablating and ablating thermal protection systems.

The heat flux delivered to the surface of a vehicle in post-shock flow is due to

the diffusion of chemically-reactive species to the surface, conduction transport of high-enthalpy gas, and radiation. Non-ablating surfaces will inherently conduct a significant portion of the oncoming heat flux and re-radiate the remaining portion, whereas ablative heat shields can withstand higher total heat fluxes because they employ an additional method with which to mitigate the energy. Typical ablative TPS employ a low-temperature phase change material impregnated within a dense carbon-based matrix structure. As the post-shock gases flow towards the vehicle, they rapidly react with the impregnated material, which convects outward from the surface. This convective efflux provides a substantial obstruction for the oncoming gases to penetrate. As the pyrolysis process permeates deeper into the surface, a char layer develops, composed of the carbon material. This investigation concentrates exclusively on the char layer by utilizing graphite samples, which is a common char layer simulator [24], [25], [11], [1].

1.1.5 Chemical Reactions

Accurately determining the ablation rates over the vehicle surface for a particular reentry is critical to the success of the mission. However, the inherent complexity of the system significantly complicates this task. On a fundamental level, the ablation rate at any discrete point on the surface is directly related to the rate at which surface-eroding reactions take place at that location. The reaction rate equation shown in Equation 1.1 applies to single and multiphase interactions. It takes into account the backwards and forwards reaction rate coefficients (k_f, k_b), which are often temperature dependent quantities, as well as the molar concentration of the reactants (X_j) raised to their respective stoichiometric coefficient (ν_j). The units for the reaction rate (r_i) vary between per volume or per area depending on whether the

reaction occurs as a gas-phase or gas-surface interaction, respectively.

$$r_i = k_{f,i} \prod_{j=1}^{NS} [X_j]^{\nu'_{j,i}} - k_{b,i} \prod_{j=1}^{NS} [X_j]^{\nu''_{j,i}} \tag{1.1}$$

In particular, there are four key reactions to consider for nitrogen flow over graphite: carbon nitridation, surface-catalyzed nitrogen recombination, gas-phase nitrogen recombination and nitrogen exchange with the cyano radical (CN). Each reaction is exothermic, which potentially increases the surface heat flux, as previously described in Section 1.1.3. Of the four reactions considered, there remains significant disagreement in the measured reaction rate coefficients for carbon nitridation and surface-catalyzed nitrogen recombination. Section 1.2 provides an extensive overview of the current set of data.

Carbon nitridation is a process whereby a nitrogen atom impinges on the surface, extracts a carbon atom from the solid phase, and combines to create CN. The chemical equation for this process appears in Equation 1.2. The liberated energy expressed in this equation stems from the heat of formation of the reactants and products. Appendix A provides a detailed overview on this analysis.

$$C(s) + N \rightarrow CN + 0.36\text{eV} \tag{1.2}$$

Additionally, there are two processes with which atomic nitrogen recombines in the boundary layer. The first process is surface-catalyzed recombination, which is a three-body reaction between two nitrogen atoms and the carbon surface. The reaction occurs when the two atomic species impinge on the surface simultaneously and combine to create molecular nitrogen, as shown in Equation 1.3. This liberated energy from nitrogen recombination is more than a full order of magnitude greater than carbon nitridation.

$$N + N + (s) \rightarrow N_2 + (s) + 9.8\text{eV} \tag{1.3}$$

Equations 1.2 and 1.3 are similar in that they both describe instantaneous gas-surface interactions. Some investigations choose to describe these processes more fully by assuming a series of intermediate steps involving adsorption, desorption and spallation [2], [26]. However, other studies choose to avoid these additional mechanisms by considering a single step process [27], [25], [28], [29].

Equation 1.4 is similar in form to Equation 1.3. The principal difference is that Equation 1.4 applies only to gas-phase recombination where M indicates an arbitrary third body. This study assumes a nitrogen molecule third body due to its prevalence throughout the flow field and the limited availability of experimental data for other third body species.

$$N + N + M \rightarrow N_2 + M + 9.8\text{eV} \tag{1.4}$$

The nitrogen exchange reaction between CN and atomic nitrogen is a relatively fast, gas-phase reaction. The cyano radical produced from the carbon-nitridation process is capable of diffusing upstream through the subsonic flow, where it can react with oncoming nitrogen atoms. This exothermic reaction is of the same order as nitrogen recombination.

$$CN + N \rightarrow N_2 + C + 2.0\text{eV} \tag{1.5}$$

In Scala and Gilbert's paper, they describe the various mass loss regimes over a range of thermodynamic conditions [11]. Figure 1.6 is from their paper and illustrates the mass loss regimes with respect to wall temperature and pressure at the boundary

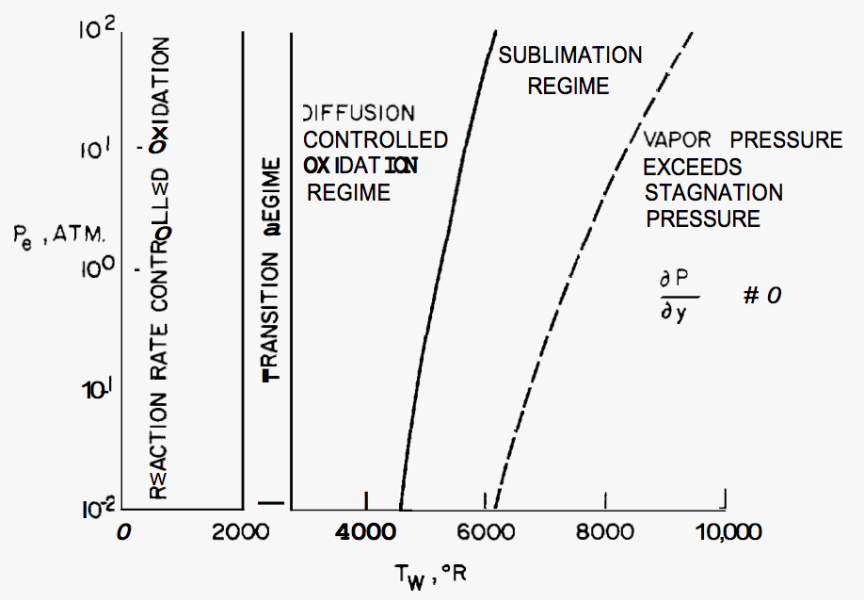

Figure 1.6: Mass transfer regimes for air over graphite [11].

layer edge. At low temperatures, the mass loss rate is independent of pressure and is due to the rate at which the gas can extract carbon from the surface. As the wall temperature increases, the reaction rate increases exponentially and the mass loss mechanism transitions into the diffusion controlled regime. In this region, the reaction rate is so quick that the limiting factor in the mass loss is the rate at which reactants can diffuse to the surface. At still higher temperatures, the lattice structure of the graphite begins to fail due to sublimation. The work performed in this investigation was below 1700-K (3060-^{o}R), and so sublimation byproducts were not considered.

1.2 Previous Investigations

There are two predominant ways to quantify gas-surface interactions. The most common is the reaction efficiency (γ), which indicates the probability that a particular chemical reaction will occur. Equation 1.6 defines the carbon nitridation reaction efficiency as the ratio of the departure flux of CN from the surface (Γ_{CN}) relative to

the arrival flux of nitrogen towards the surface (Γ_N).

$$\gamma_{CN} = \frac{\Gamma_{CN}}{\Gamma_N} \tag{1.6}$$

In reality, a particular chemical reaction occurs when the quantum mechanical and physical states of the reactants are sufficient to allow the reaction to occur. Therefore, comparing reaction rate efficiencies obtained from different facilities may be difficult unless the flow chemistry and thermodynamic conditions are identical. However, the reaction efficiency remains useful because it provides a general description of a complex flow system containing countless numbers of particles. Additionally, numerical models that simulate high-enthalpy flow systems customarily employ a reaction efficiency term in their gas-surface interaction algorithms. Therefore, the reaction efficiency is a sufficient metric, provided that one is able to accurately match the experimental and numerical conditions.

Another quantity that describes gas-surface interactions is the set of reaction rate coefficients (k_f, k_b), which factor directly into the reaction rate equation shown previously in Equation 1.1. This quantity is slightly more detailed than the reaction efficiency, since it requires specific knowledge of the collision rate of the reactants. For gas-surface interactions, Goulard relates the reaction efficiency and reaction rate coefficient for the carbon nitridation process through the expression shown in Equation 1.7 [30]. Here, the thermal speed of atomic nitrogen drives the collision rate with the surface.

$$k_f = \gamma \frac{\bar{\nu}_N}{4} \tag{1.7}$$

1.2.1 Analytical Model Development

A considerable amount of research concerning chemically reacting flows focuses exclusively on carbon-oxygen interactions owing to the high efficiency of the carbon oxidation process. References [31], [32], [33], [34] provide a small sample of the many studies. Metzger et al. provided a foundational relation between the mass loss rate of various graphite composites with respect to a range of thermodynamic flow conditions in air [35]. This model arose from a series of experiments in various arc-jet facilities, in which he exposed graphite samples to high-enthalpy air flow. Park later built upon this method and generated a set of expressions for the reaction efficiencies between carbon and oxygen [1]. Here, Park used a set of eleven experimental results to develop his efficiency models, which have since become foundational in the field. One advantage of Park's model is its simplicity. It assumes that the reactions occur instantaneously, with no intermediate adsorption, desorption or sublimation steps, and yields an exponential relation between the reaction rate efficiency and the surface temperature. Table 1.1 shows the three oxygen-graphite interactions described by Park.

In contrast, only Zhluktov and Abe have provided a temperature-dependent mathematical model for the nitrogen-carbon system, which they developed from several sets of experimental studies [2]. In particular, they provided a rigorous set of expressions for nitrogen adsorption onto a carbon surface, as well as the subsequent Eley-Rideal reaction, whereby gas-phase nitrogen atom extracts an adsorbed nitrogen atom from the surface and recombines into molecular nitrogen in a single step. However, they did not consider carbon nitridation, thus stopping short of providing an expression for gas-phase cyano radical production. Table 1.2 shows their expressions. Numerical models that predict surface erosion and heat flux often use the results provided

by Zhluktov and Abe [26], [36]. However they must implement results from carbon-nitridation studies, which vary between experiments by several orders of magnitude.

Table 1.1: Park Model Reaction Efficiencies for Oxygen [1]

Reaction	γ
$C_s + O_2 \rightarrow CO + O$	$\frac{1.43E-3+0.01\exp(-1450/T)}{1+2E-4\exp(13000/T)}$
$C_s + O \rightarrow CO$	$0.63\exp(\frac{-1160}{T})$
$C_s + O + O \rightarrow C_s + O_2$	$0.63\exp(\frac{-1160}{T})$

Table 1.2: Zhluktov and Abe Carbon-Nitrogen System Reaction Rates [2]

Model	Reaction	k_f	k_b
Z&A	$C_s + N \rightarrow CN_s$	$\frac{P_0}{\sqrt{2\pi m k_B T}}$	$\frac{k_B T}{h}\exp(\frac{-36.6E3}{T})$
Z&A	$CN_s + N \rightarrow C_s + N_2$	$\frac{\bar{\nu}_N}{4}\exp(\frac{-76.6E3}{T})$	JANAF data [6]

1.2.2 Experimental and Numerical Results

Zhluktov and Abe have provided the only known temperature-dependent expressions for the carbon-nitrogen system. However, several experimental and numerical investigations have yielded carbon-nitridation and nitrogen recombination reaction efficiencies at specific thermodynamic conditions. In many cases, the efficiencies measured at identical conditions in different facilities vary by several orders of magnitude, which puts numerical modelers in the unfavorable position of choosing between values [26], [36]. Oftentimes, they will elect the most conservative efficiencies, which inevitably

predicts higher surface recession rates and leads to significant over-sizing of the TPS material.

Chen and Milos use a constant temperature value ($\gamma_{CN} = 0.3$) determined experimentally by Park and Bogdanoff in a shock tube experiment [37], [27]. There is significant controversy surrounding this value, due to the fact that it of the same order as carbon oxidation and is independent of temperature. Comparisons between the measured mass loss and surface recession rates of graphite in nitrogen and oxygen repeatedly show that oxygen more efficiently erodes a carbon surface than nitrogen, as detailed further in Section 2.3.1. Despite the debate, the value derived by Park and Bogdanoff is one of the most prevalent expressions used to simulate the carbon nitridation reaction rate in modern numerical models owing to the ultra conservative predictions it yields.

In addition to Park and Bogdanoff, other experiments have investigated the interaction between graphite and high-enthalpy nitrogen flow. Gordeev et al. combined experimental heat flux analysis with numerical data to study the recombination of nitrogen on the surface of graphite [38]. In their investigation, they exposed various material samples to dissociated nitrogen at low pressures ($p = 0.1$ atm) within the VGU-2 plasma generator. For each material, they calculated the conductive heat flux transferred through the sample via direct measurement of the front and backside sample temperatures, or when active backside cooling of the sample was necessary, by measuring the temperature rise and the flow rate of the water coolant. They were able to estimate the reaction efficiency of any material by comparing the heat flux to a non-catalytic and fully-catalytic surface at the same wall temperature, which represented the lower and upper bounds possible at that condition, respectively. Ultimately, they estimated the catalycity of nitrogen recombination on graphite by comparing the heat flux and surface temperature to quartz and copper tests. The investigation yielded

a recombination efficiency and reaction rate over the surface of pyrographite (γ_{N_2} = 0.22, $k_{N_2} = 10^2$-m-s^{-1}) and pure carbon (γ_{N_2} = 0.07 - 0.11, $k_{N_2} = 28(10^2)$-m-s^{-1}).

This method of leveraging the heat flux data to determine the catalytic properties of various materials is straight-forward, but fails to provide a detailed description of the various exothermic processes occurring at the wall. Specifically, this investigation was incapable of resolving the competing nitrogen recombination and carbon-nitridation processes. Ultimately, the authors assumed a minimal carbon nitridation rate despite the change in sample mass. For completeness, the results provided by this experiment should not be attributed exclusively to nitrogen recombination, but rather, to all exothermic processes that occurred at the surface. This methodology serves as a very useful first step, however it fails in separating the individual mechanisms that define this complex system.

Additionally, David Driver and Matthew MacLean compared the surface recession of PICA exposed to nitrogen flow within the NASA Ames 60-MW arc heater facility to the numerical predictions from the DPLR software package [39]. Here, they restricted the chemical processes considered by the program to carbon nitridation and nitrogen recombination at the wall as well as the carbon nitridation exchange reaction with nitrogen in the gas phase. Briefly, they initially considered the results obtained by Park and Bogdanoff, which stated that the carbon nitridation reaction efficiency was of the same order as nitrogen recombination ($\gamma_{CN} = 0.3$) [27]. However, this provided them with an estimation of the recession rate far greater than what they observed experimentally. To address this discrepancy, they iteratively adjusted the nitrogen recombination and carbon nitridation rates until the recession and heating rates matched their experimentally determined values. They ultimately estimated the nitrogen recombination and carbon nitridation efficiencies to be $\gamma_{N_2} = 0.05$ and $\gamma_{CN} = 0.005$ respectively.

A set of papers published by Anna et al. studied the nitrogen recombination and carbon nitridation rate on the surface of graphite using numerical methods [40], [3]. These investigations used the Michigan Aerothermal Navier-Stokes (LeMANS) software package, coupled with the finite rate surface chemistry model developed by Marschall et al., to match the measured atomic nitrogen concentration along the stagnation point streamline within the Plasma Diagnostics and Test Laboratory (PDTL) at the University of Vermont (UVM) [26], [36], [13]. These studies demonstrated that gas-surface interactions caused the observed decrease in the atomic nitrogen population levels near the surface of the sample by showing that in the absence of chemical reactions, the nitrogen atom population increases towards the surface. Also, the studies focused on the individual impact of carbon nitridation and nitrogen recombination at the surface by varying the two efficiencies. In total, the campaign simulated five cases with varying gas-surface efficiencies, shown in Table 1.3.

Table 1.3: Simulation Test Cases from Anna et at. [3]

Case	Recombination Efficiency γ_{N_2}	Nitridation Efficiency γ_{CN}
Case 1	0	0
Case 2	0.07	0
Case 3	0.07	0.005
Case 4	0.07	0.3
Case 5	1	0

The values for the efficiencies in this investigation were taken from Gordeev et al., Park and Bogdanoff, and Driver and MacLean [38], [27], [39]. Cases 3 and 4 were the only two simulations that simultaneously tested nitridation and recombination, and they estimated the mass loss rates to be 3.7-mg-s^{-1} and 37-mg-s^{-1} respectively. In comparison, the experimentally measured mass loss rate was 0.33-mg-s^{-1}. Clearly, both cases over-predict the impact of carbon nitridation, indicating that the nitrida-

tion efficiency was $\gamma_{CN} < 0.005$.

Figure 1.7 shows the nitrogen atom density behavior approaching the surface for most of the cases studied by Anna [12]. Experimental data determined at the UVM PDTL appear as symbols. For a non-catalytic wall ($\gamma_{N2} = 0$), the nitrogen atom number density increases, which follows the bulk density behavior at the stagnation point. With subsequently higher reaction efficiencies, the nitrogen level decreases towards the wall. A fully-catalytic wall ($\gamma_{N2} = 1$) yields a zero population of nitrogen atom at the wall. Within the error of the experiment, the nitrogen recombination efficiency lay between $\gamma_{N2} = 0.07$ - 1.0.

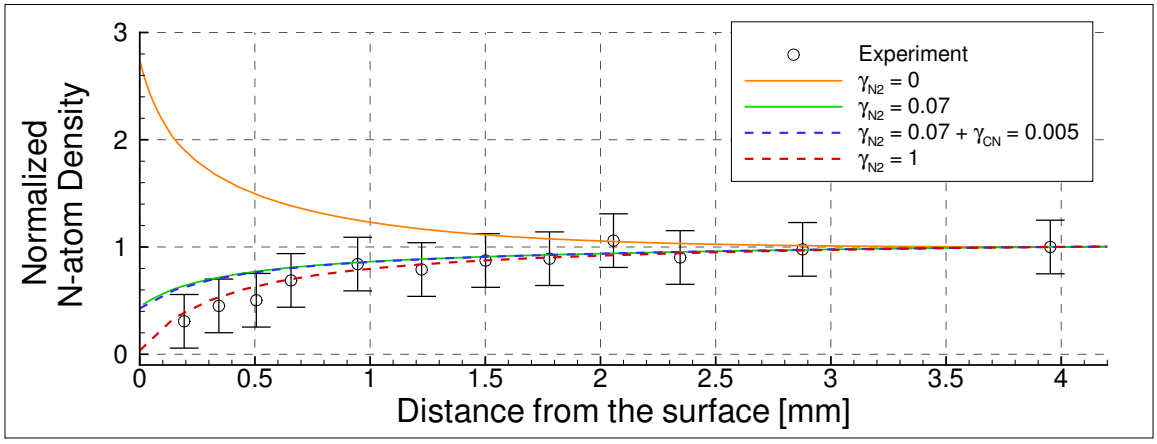

Figure 1.7: Nitrogen atom density approaching surfaces of varying catalycities predicted by LeMANS [12].

Zhang et al. studied carbon nitridation within a diffusion reactor and clamshell furnace, which increased the sample temperatures to the desired conditions [25]. They were motivated by the results of Park and Bogdanoff and developed a straight-forward method with which to determine the reaction efficiency. Their work spanned a significant temperature range, from 300-K to 1373-K, which yielded efficiencies from $\gamma_{CN} = 4(10^{-6})$ - $1.58(10^{-3})$. However, their method was incapable of extracting a recombination reaction efficiency.

Reference [13] provides a thorough description of several other experiments as well. The results from these experiments, in addition to the ones previously described are listed in Table 1.4. Notice the wide range of reported values. Additionally, the majority of investigations focused exclusively on one wall reaction, whereas the only investigations that yielded values for both reactions relied heavily upon numerical models with no experimental data to validate the results. In fact, all the investigations invoked numerical simulations to some degree and the authors oftentimes made simplifying assumptions concerning the nature of the flow, which were not experimentally verified. Clearly, there is a need for a detailed experimental investigation into the nitrogen recombination and carbon nitridation rates that relies upon proven methods and techniques.

Table 1.4: Reaction Efficiency of Carbon-Nitrogen System

Investigation	Temperature [K]	Recombination γ_{N_2}	Nitridation γ_{CN} * (10^3)
Gordeev et. al [38]			
(pyrographite)	2100	0.22	-
(carbon)	1680 - 1919	0.07 - 0.11	-
Goldstein [29]	1694 - 2365	-	0.41 - 1.70
	2031 - 2237	-	0.45 - 0.69
Park & Bogdanoff [27]	300 - 1100	-	300
Zinman [28]	1100	-	<0.1
Suzuki et. al [24]	1822 - 2184	-	2.5 - 3.2
Zhang et. al [25]	300 - 1373 K	-	0.004 - 1.58
Anna [12]	1598	0.07 - 1.0	<5
Driver & MacLean [39]	-	0.05	5

1.2.3 Initial Carbon Nitridation Investigation at UVM

This investigation builds upon a previous campaign carried out at the UVM PDTL in 2010, in which graphite samples were exposed to nitrogen plasmas [13]. Here, the carbon nitridation process was investigated from the perspective of a reaction

efficiency, introduced previously in Equation 1.6. Under the assumption that the observed sample mass loss is steady and isotropic across the exposed surface, and is due exclusively to carbon nitridation, one can then relate the particle flux of CN directly to the mass loss rate. The expression for the nitrogen atom arrival flux comes from the Maxwellian distribution function, which equates the distribution of particle velocities in a system to the a single temperature. Considering 1-D flow towards the surface for all possible velocities ultimately yields the nitrogen atom arrival flux. Equation 1.8 shows the final expression developed in the previous study.

$$\gamma_{CN} = \frac{\Delta m_C}{A \Delta t m_{a,C}} \left(\frac{n_{Nw}}{4} \sqrt{\frac{8 k_B T_w}{m_{a,N}}} \right)^{-1} \tag{1.8}$$

Note that Equation 1.8 is dependent upon quantities that are either tabulated, or measurable within the facility. The most readily obtainable values are the sample mass loss (Δm_C), surface area (A), exposure time (Δt), and the surface temperature (T_w). The majority of this investigation focused on determining the absolute nitrogen atom number density at the wall (n_{Nw}) and verifying local thermal equilibrium between the gas and surface. Ultimately, a two-photon laser-induced fluorescence (LIF) process described by Bamford et al. measured the absolute number density of nitrogen, which is described in detail in Section 4.3.2 [41].

The initial absolute nitrogen atom number density determined at the boundary layer edge was $n_{N,e} = 1.9(10^{16})$-cm^{-3}, which was a full order of magnitude below the expected equilibrium value of $n_{N,e} = 1.245(10^{17})$-cm^{-3}. Further analysis showed that this calculation was hindered by the measurement of the fluorescence lifetime within the inductively coupled plasma (ICP) torch, which factored prominently in the computation. To address this issue, the investigation calculated the lifetimes from the collisional quenching scaling developed by Copeland et al., which brought the

measured value to $n_N = 1.35(10^{17})$-cm^{-3} and within 8% of the expected value [42]. With this correction, the investigation ultimately yielded a near-wall nitrogen atom number density of $2.7(10^{16})$-cm^{-3} and a reaction efficiency of $\gamma_{CN} = 3.8(10^{-3})$, which agreed with other independent sources that studied this reaction [25], [24].

This campaign also investigated the assumption that the nitrogen atom translational temperature was in thermal equilibrium with the surface of the sample using the LIF technique. Briefly, the temperature was measured at several locations along the stagnation point streamline, which provided a 1-D profile of the temperature gradient. Figure 1.8 shows the results plotted from this portion of the experiment along with a trend line approximation. Notice that the temperature decreases across the boundary layer edge in the direction of the sample surface. A two-color pyrometer measured the surface temperature at 1320-K. Figure 1.8 does not conclusively prove that the nitrogen atom temperature drops to the surface temperature, however this downward trend was sufficient for the scope of the investigation.

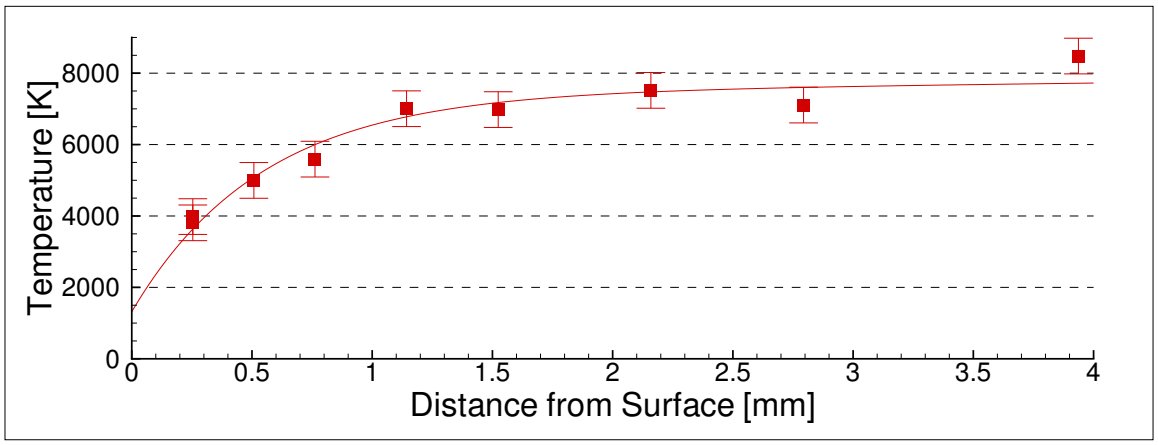

Figure 1.8: Nitrogen atom translational temperature along the stagnation point streamline [13].

Despite yielding a reasonable carbon nitridation rate, there were several drawbacks to this investigation. First, acquiring absolute number densities proved to be

a non-trivial task. The technique required performing simultaneous LIF measurements within the ICP chamber and a flow reactor setup, where the absolute nitrogen atom number density was known *a priori* through a chemical titration technique. The details of the chemical titration process are provided in Section 2.2.2. Moreover, experimental measurements of the beam waist and fluorescence lifetime measurements as well as a characterization of the detection optics efficiency at both measurement locations were necessary. Clearly, each item added more complexity and increased the uncertainty and opportunity for error, as evidenced by the impact of the fluorescence lifetime measurements.

Secondly, this technique did not consider any gas-surface interaction beyond carbon nitridation and this lack of completeness revealed a significant disparity amongst the measured data. From the LIF experiment, the nitrogen atom number density decreased strongly towards the wall. This behavior was attributed exclusively to carbon nitridation. However the low carbon nitridation efficiency determined through Equation 1.8 was far too weak to account for this behavior and the problem was left unsolved. Thus, a new approach to the problem was necessary to resolve these issues.

1.3 Discussion

This investigation focuses on nitrogen flow for several reasons. Clearly, there is a need for a detailed description of the various competing processes in the carbon-nitrogen system as there is significant disagreement among the published values. This is the first known experimentally-based study into both the carbon nitridation and nitrogen recombination rates on graphite. Using proven experimental techniques, this investigation aims to provide a detailed analysis of the nitrogen flow system within the UVM ICP facility as well as an initial determination of the carbon nitridation

and nitrogen recombination rates on graphite. The method employed within this investigation is compatible with many other high-enthalpy flow facilities, meaning the techniques employed within will translate to other laboratories for future comparison and validation.

Additionally, this investigation focuses on nitrogen in particular because with respect to oxygen, it does not react as aggressively with graphite. Graphite rapidly erodes when oxygen is present in the flow, which creates the need to continually monitor the location of the receding surface when extracting spatially-resolved data from the flow. Because the reactions between graphite and nitrogen are significantly slower, this campaign avoided many of these complications. Hence, it would have been considerably more difficult to develop these techniques with an initial study of oxygen on graphite due to the uncertainties of the receding surface.

Chapter 2

Plasma Diagnostics and Test Laboratory

2.1 Overview

The PDTL located at UVM is a suitable facility in which to test TPS material response in a high-enthalpy environment. It is capable of replicating many dominant flow phenomena experienced by a vehicle traveling at hypersonic speeds, which provides an efficient and cost-effective way to study gas-surface interactions over the surface of various materials. One key advantage of the ICP torch installed within the facility is its ability to operate continuously over long test durations without introducing any contaminants into the flow. In comparison, impulse facilities that employ shock tubes are limited by their testing times, which are typically on the order on milliseconds. Arc-jet facilities, which can have test durations of the same order as ICP torches, do not produce contaminant-free flow because they rely on arcing elements located upstream of the sample, which unavoidably introduces copper into the flow.

On the other hand, impulse and arc-jet facilities have advantages over ICP facil-

ities. Whereas impulse facilities are capable of replicating both the flow and energy structure present in-flight, ICP torches are only ideally suited to study flow chemistry and surface heat flux. Impulse facilities are capable of matching flight conditions by creating a shock wave that propagates through a long shock tube containing the test gas. Upon reaching the end wall of the tube, the shock reflects upstream. Hence, the test gas passes through the shock multiple times, which causes a rapid temperature and pressure increase before flowing through a converging-diverging nozzle and into the test chamber. Conventional blowdown wind tunnels are incapable of maintaining the sufficient upstream conditions required to produce all in-flight hypersonic flow conditions, which is why impulse facilities are highly-valued. Moreover, arc-jets are advantageous because they are well-suited to operate supersonically, and can thus more-accurately replicate the flow structure around a hypersonic vehicle than an ICP torch. Therefore, in conjunction with other high-enthalpy facilities, ICP torches are a useful tool that researchers use to study hypersonic flight.

2.2 Inductively Coupled Plasma Torch

The 30-kW ICP torch facility at in the PDTL was designed to test samples in high-enthalpy gas flows to simulate planetary entry and Earth atmosphere re-entry. It is currently configured to operate subsonically and to simulate post-shock conditions. Facility test conditions are related to flight trajectory and supersonic facility conditions through the similarity parameters controlling stagnation point heating, which allows for system validation [43]. Table 2.1 lists several performance specifications for the UVM ICP torch.

Table 2.1: UVM ICP Torch System Specifications [4]

Parameter	Rating
Inductive heater power	30-kW (max) @ 4-MHz
Enthalpy range	10 - 40-MJ-kg^{-1} (for air)
Mach range	0.3 - 1
Stagnation heat transfer rate	10 - 290-W-cm^{-2}
Static pressure	110 - 200-atm

The UVM ICP facility contains a number of subsystems, which includes the power supply, plasma chamber and gas injection system. An active water-cooling loop cycles through several locations to prevent key components from overheating. The sketch displayed in Figure 2.1 illustrates the locations of these subsystems within the laboratory.

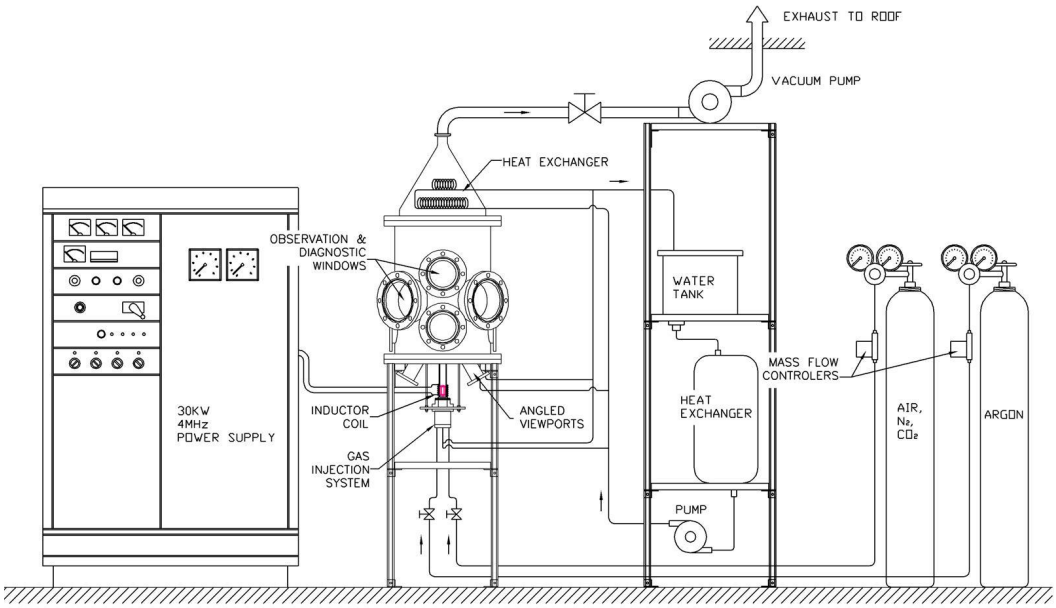

Figure 2.1: Schematic of subsystems within the UVM ICP facility. Included are the power supply, plasma chamber, gas injection system and water cooling system [4].

Operation starts with the gas injection system, which provides the desired test

gas to the plasma chamber through a set of dedicated MKS M100B Series mass flow controllers. A LabView program controls the gas flow remotely, regulates chamber pressure and monitors system performance. Additionally, gases flow through manual ball valves, which serve as an override, before entering the injector block assembly.

The injector block is based on a design by Playez and an illustration is provided in Figure 2.2a [43]. It is located at the base of the plasma chamber and is designed to provide laminar, annular gas flow through a quartz tube and into the chamber. The combination of water channels throughout the interior and the brass construction provides protection against overheating. High-temperature plasma is generated within the quartz tube and the annular flow prevents the tube from melting by continually introducing a fresh stream of low-temperature gas along the inner wall.

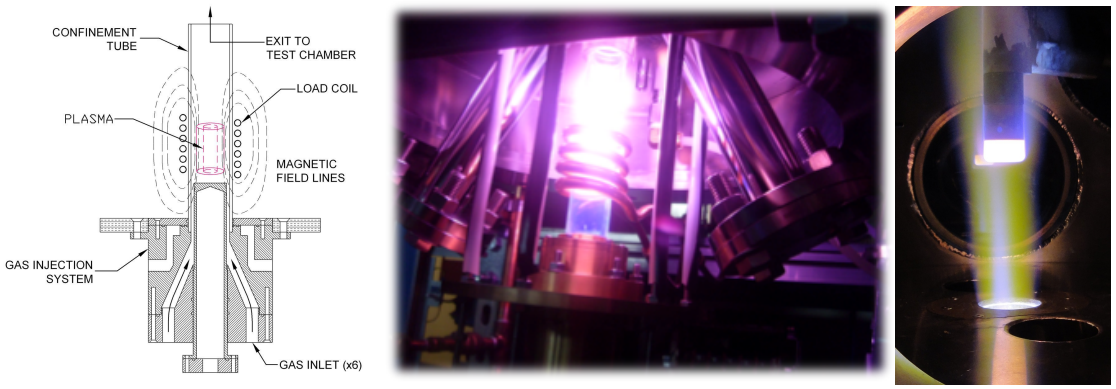

(a) Injector Block (b) Plasma Generation (c) Sample Test

Figure 2.2: A stable plasma ball within the interior of the quartz tube during operation. Inside the chamber, a graphite sample is exposed to plasma flow in the the stagnation point configuration.

An inductance coil is installed concentrically about the exterior of the quartz tube. The Lepel Model T-30-3-MC5-TLI RF power supply shown in Figure 2.1 provides radio-frequency AC power to the inductance coil, which creates a strong magnetic field within the tube. The field causes the flowing gas to increase in temperature and

ionize rapidly. When the system is coupled properly, a stable plasma ball is generated within the center of the tube, as shown in Figure 2.2b. The potential provided by the system requires the power supply and inductance coil to be cooled with de-ionized water during operation.

After passing through the quartz tube, the plasma enters the test chamber. The chamber is constructed from stainless steel to avoid contamination of oxidation byproducts and is capable of pumping down to high-altitude pressure levels with an attached vacuum pump, which doubles as the exhaust port. There are several viewports located around the perimeter and beneath the chamber, which provide observational and diagnostic access. The static pressure is monitored with an MKS 622A Series pressure gage and the combination of pressure and mass flow maintain laminar flow. Before exhausting to the exterior of the facility, the gases are sent through a water-fed heat exchanger, located beneath the chamber lid.

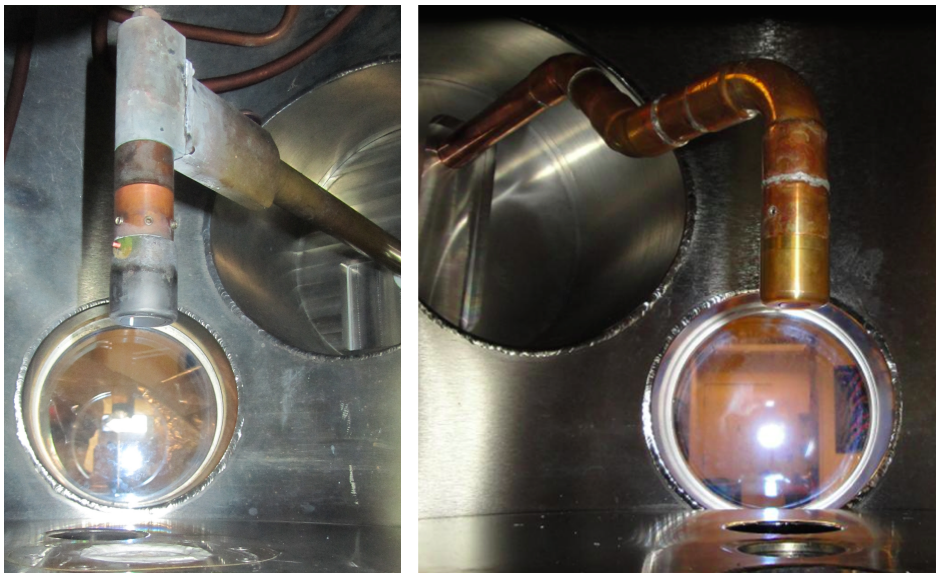

(a) Insertion Probe (b) Gooseneck Probe

Figure 2.3: Photographs of the insertion probe and gooseneck probes installed within the chamber.

Figure 2.3 shows the two probes installed within the chamber, which allow for separate test material exposures within the same run. The insertion probe linearly translates whereas the gooseneck probe rotates the sample into and out of the jet. The gooseneck probe contains an isolated thermocouple feedthrough line that allows access to backside temperature measurements of the sample. Oftentimes, the gooseneck probe is dedicated to measure the cold-wall heat flux with a copper slug calorimeter, as explained in Section 5.3, while the insertion probe is equipped with a sample constructed from a test material. During an exposure the heat flux probe or sample is inserted into the flow and is placed in the stagnation point configuration, as shown in Figure 2.2c. Note that in this configuration, the sample is held with the leading face perpendicular to the main flow axis.

2.2.1 Two-Color Pyrometer

The PDTL employs two Marathon Series two-color infrared pyrometers to measure the sample surface temperature during exposure to the flow. A pyrometer installed below the chamber base determines the front face surface temperature by viewing the sample through a dedicated viewport located at an off-axis angle from the flow propagation, as illustrated in Figure 2.4.

Each pyrometer determines the temperature of a solid body by calculating the ratio of measured emission over two overlapping IR bands (750 - 1100-nm; 950 - 1100-nm) and comparing this value to the Planck distribution, which is discussed further in Section 3.5. The advantage of the two-color method is that it does not require the operator to know the emissivity of the substance *a priori* and is particularly useful when detecting temperatures of substances with unknown emissivities.

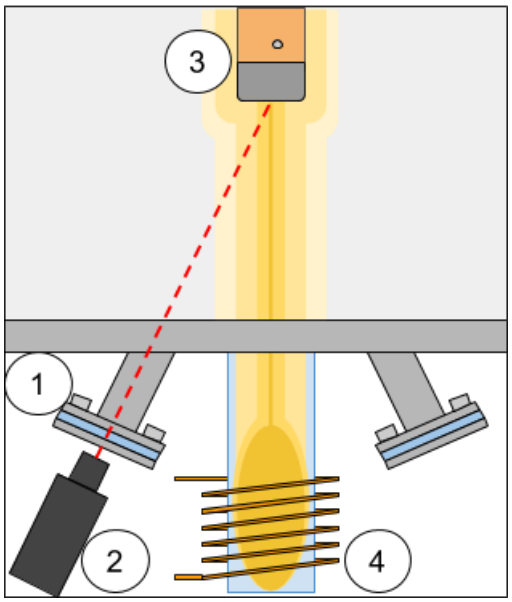

Figure 2.4: A schematic of the pyrometer location outside of the chamber. Also shown is the pyrometer viewport (1), pyrometer (2), sample and probe holder (3), and quartz tube, plasma ball and inductance coil (4).

2.2.2 Microwave Discharge Flow Reactor

The microwave discharge flow reactor (MDFR) is an independent gas flow system within the PDTL that helps establish species concentrations and translational temperatures within the ICP with the laser diagnostic techniques described in Chapter 4. Figure 2.5 shows a picture of the MDFR setup. Prior to entering the system, the N_2 and NO/He gas-mixture are each regulated and metered with an independent set of consecutive leak valves and MKS 1179A Series mass flow controllers. In the upper branch, molecular nitrogen passes through a microwave discharge powered by an OPTHOS Instruments MPG-4M model power generator, which causes partial dissociation and creates a population of atomic nitrogen upstream of the NO/He gas inlet port. Figure 2.5 does not show the microwave discharge explicitly and the upper branch denotes a partially dissociated nitrogen gas flow. Nitric oxide enters the sys-

tem downstream of the discharge, but above the PMT view location, as shown. The MDFR operates at room temperature and an operating pressure of 0.5-Torr, which is controlled by a vacuum pump installed at the exhaust port.

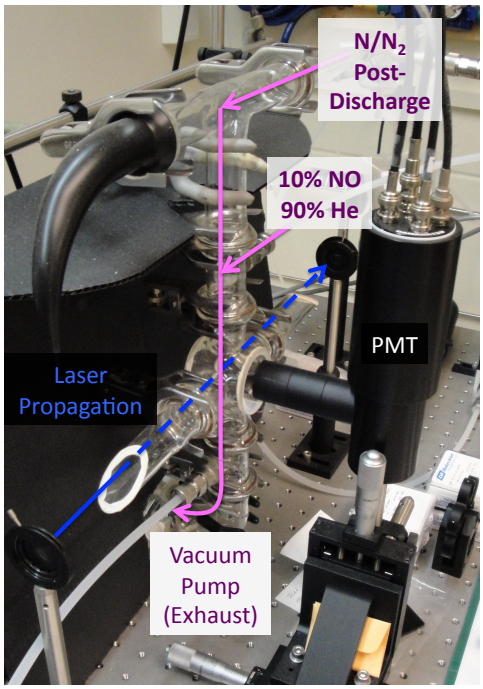

Figure 2.5: The MDFR helps yield absolute species concentrations and translational temperatures within the ICP flow through chemical titration.

A chemical titration process helps determine the atom concentration in the flow reactor by taking advantage of a very fast and well-characterized exchange reaction between atomic nitrogen and nitric oxide, expressed in Equation 2.1. Here, NO behaves as the titration gas and converts atomic nitrogen into molecular nitrogen.

$$N + NO \rightarrow N_2 + O \tag{2.1}$$

Thus, the composition of the gas within the MDFR at the PMT viewing location may contain as many as 5-species simultaneously (N, N_2, NO, O, and He). With rela-

tively low titration gas flow, only a portion of the atomic nitrogen species is consumed by the reaction in Equation 2.1. As the titration gas flow increases, the NO number density rises, which provides more chemical partners and allows more nitrogen atoms to undergo the reaction. The titration end point indicates the minimum titration gas flow necessary to consume all free nitrogen atoms. Experimentally, this value is determined by tracking the nitrogen atom population at progressively higher titration gas flows with the laser diagnostic techniques described in Chapter 4. Finally, knowing the NO flow rate at the titration end point, one can invoke the ideal gas law equation of state and determine the atomic nitrogen number density within the MDFR for any arbitrary NO flow rate. Oftentimes, no titration gas is added into the MDFR while probing nitrogen atom.

2.2.3 Duplication to In-Flight Conditions

Several papers dating back to the first stages of space flight have discussed the duplication of in-flight and ground-based testing through clever manipulation of the boundary layer equations [10], [30], [44], [45]. The methodology by which to transform these equations is accredited to several researchers, who progressively advanced the idea [46], [47], [48], [49], [50]. The motivation behind this transformation is to convert the boundary layer equations into a more generalized form whose solution is subsequently applied to any particular hypersonic flow system. The initial set of boundary layer equations describing axis-symmetric flow are expressed in Equation 2.2. Here, the x-direction and y-direction represent the local tangential and surface normal directions respectively.

$$\begin{aligned}
\tfrac{\partial(\rho u r)}{\partial x} + \tfrac{\partial(\rho v r)}{\partial y} &= 0 && (Continuity) \\
\rho u \tfrac{\partial u}{\partial x} + \rho v \tfrac{\partial u}{\partial y} &= -\tfrac{dp_e}{dx} + \tfrac{\partial}{\partial y}(\mu \tfrac{\partial u}{\partial y}) && (x - Momentum) \\
\tfrac{\partial p}{\partial y} &= 0 && (y - Momentum) \\
\rho u \tfrac{\partial h}{\partial x} + \rho v \tfrac{\partial h}{\partial y} &= \tfrac{\partial}{\partial y}(k \tfrac{\partial T}{\partial y}) + u \tfrac{dp_e}{dx} + \mu(\tfrac{\partial u}{\partial y})^2 && (Energy)
\end{aligned} \tag{2.2}$$

Clearly, these equations are system-specific because they depend upon particular flow conditions. Therefore, the transformation introduces the variables expressed in Equation 2.3, which remove the system dimensionality.

$$\begin{aligned}
\xi &= \textstyle\int_0^x \rho_e u_e \mu_e r^2 dx \\
\eta &= \tfrac{u_e r}{\sqrt{2\xi}} \textstyle\int_0^y \rho dy
\end{aligned} \tag{2.3}$$

Upon inserting Equations 2.3 into 2.2 and reducing, the transformation yields the set of equations shown in Equation 2.4 and 2.5. For clarity, Appendix B provides fully-detailed derivations of these resulting equations. Briefly, C represents the Chapman-Rubesin factor and f' and g are, respectively, the velocities and enthalpies normalized by their boundary layer edge values. The prime symbol represents the partial derivative with respect to η. Equation 2.5 expresses the heat transfer at the wall, as developed by Fay and Riddell [10].

$$\begin{aligned}
(Cf'')' + ff'' &= \tfrac{1}{2}[(f')^2 - g] && (x - Momentum) \\
\tfrac{\partial p}{\partial \eta} &= 0 && (y - Momentum) \\
(\tfrac{C}{Pr} g')' + fg' &= 0 && (Energy)
\end{aligned} \tag{2.4}$$

$$q_w = 0.763 Pr^{-0.6} (\rho_e \mu_e)^{0.4} (\rho_w \mu_w)^{0.1} \sqrt{\frac{du_e}{dx}} (h_e - h_w) \tag{2.5}$$

Notice that several flow properties drive the heat flux expression in Equation 2.5. Specifically, the boundary layer edge velocity gradient ($\frac{du_e}{dx}$), density (ρ), viscosity (μ),

and the total enthalpy difference across the boundary layer (h_e - h_w) represent the similarity parameters for ground-based simulation of heat flux experienced in-flight.

Figure 2.6 compares the flows experienced in-flight and within the ICP facility. Notice that the in-flight flow is hypersonic, which creates a detached bow shock off the leading edge of the vehicle. In comparison, the flow in the ICP facility is subsonic and therefore attempts to replicate the post-shock region of the flow exclusively. In both regimes, a boundary layer exists over the surface of the vehicle, which has been oversized here in order to clearly show the edge and wall locations.

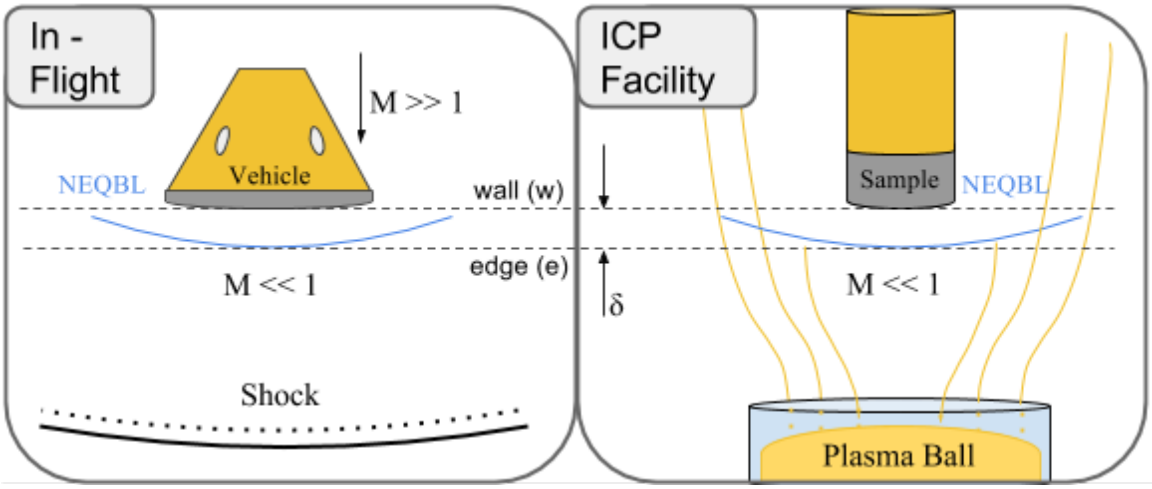

Figure 2.6: An illustration of the flow similarity parameters between in-flight and ICP facility tests.

2.3 Test Sample Geometry

This investigation employed samples fabricated from POCO DFP-2 graphite, which is a common char layer simulant material [29], [24], [51], [25]. Additionally, this study utilized quartz samples where appropriate to take advantage of the low-catalycity of the material, as explained further in Section 3.6.3. Every sample used had the

same external profile. Figure 2.7a illustrates the standard dimensions of the graphite samples. Namely, they were cylindrical in shape with a 25-mm diameter, 12.7-mm thick head and a 3.2-mm corner radius. Figure 2.7b shows a side-by-side photo of the quartz and graphite samples. Note that the discoloration on the quartz samples was on the interior surface and that the exterior surface was free of any deformities or blemishes.

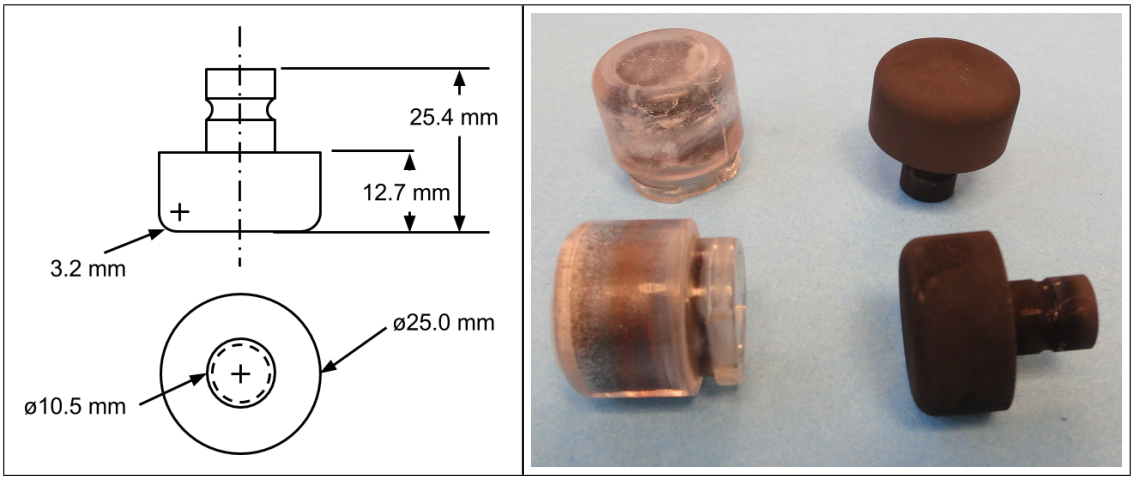

(a) Dimensions (b) Samples

Figure 2.7: A print indicating the major dimensions of the samples used in the investigation as well as a side-by-side photo of quartz and graphite samples.

2.3.1 Mass Loss Study

The sample mass loss rate is a key parameter when studying gas-surface reaction efficiencies because it serves as a preliminary indication of the rate with which carbon species enter the boundary layer. Specifically, an elevated mass loss rate indicates an increased total flux of carbon-based products entering the boundary layer, due to an assortment of gas-surface interactions. One can then isolate the efficiencies for a particular set of reactions by limiting the number of potential reaction pathways at the surface. Particularly, operating with high-purity nitrogen limits the number of

possible gas-surface interactions to the carbon-nitrogen system, which involves carbon nitridation and nitrogen recombination exclusively.

An initial step towards determining the desired reaction efficiencies involves fully-characterizing the nature of the mass loss of the graphite samples at a standard operating condition. Note that for this investigation, standard operating conditions were p = 160-Torr, $\dot{V}_{tot}$ = 40-SLPM, and P_{supply} = 14.14-kW. With that focus, the mass loss was measured from a collection of samples over a set of short duration exposures at these conditions. Table 2.2 shows three samples investigated during these trials. Each sample was rinsed in methanol prior to its first exposure and was handled with gloves thereafter to reduce contamination. All samples underwent a total exposure of 20-minutes separated in 5-minute increments, except where indicated.

Table 2.2: 5-Minute Exposure Mass Loss Trials

Sample #	Gas Flow [SLPM]	Exposure [mm:ss]	Temperature [K]	$m_{initial}$ [g]	$\dot{m}$ [mg/s]
2	Air - 11.1 : Ar - 30	5:00	1500	12.830	4.020
	Air - 10.5 : Ar - 30	5:00	1510	11.624	3.827
	Air - 10.7 : Ar - 30	5:00	1560	10.476	3.380
	Air - 10.4 : Ar - 30	5:00	1570	9.462	3.327
4	N_2 - 29.5 : Ar - 10.2	5:00	1530	12.948	0.3333
	N_2 - 30 : Ar - 10.2	5:00	-	12.848	0.2833
	N_2 - 29.1 : Ar - 10.3	5:30	1500	12.763	0.3212
	N_2 - 30 : Ar - 10	4:30	1510	12.657	0.3481
5	N_2 - 40	5:00	1550	12.943	0.3500
	N_2 - 10.2 : Ar - 30.3	5:00	1390	12.838	0.1933
	Ar - 39.8	5:00	<1270	12.531	0.0467

In an effort to observe the impact of the presence of oxygen in the flow, Sample 2 was tested in a mixture containing air and argon. The percentage of nitrogen to oxygen by volume in the air was 76.5% - 80.5% to 19.5% - 23.5% [52]. The facility requires a minimum operating flow rate and the argon served as a buffer gas to allow

lower test gas flow rates. As a noble gas, argon is assumed to be chemically inert and does not substantially affect the surface recession. Samples 4 and 5 were exposed to varying degrees of nitrogen and argon. Notice the difference in the mass losses in air mixtures and nitrogen mixtures. Specifically, Sample 2 experienced higher mass loss during the initial 10-minutes of exposure. Gradually, the mass loss rate leveled off to nearly a constant value ($\dot{m}$ = 3.3-mg-s^{-1}). In contrast, the mass loss rate from Sample 4 remained fairly constant throughout the 20-minute exposure, albeit at a significantly lower rate ($\dot{m}$ = 0.33-mg-s^{-1}). Thus, one recognizes that the mass loss rate increases appreciably when only a small percentage of oxygen is present.

The asymptotic approach towards a constant mass loss rate experienced by Sample 2 is due to the sample shape. During the initial ten minutes of exposure, the sample experienced elevated temperatures at the shoulder region caused by shear heating. This effect caused the sample to erode into a nearly-hemispherical profile, which then receded with a uniform mass loss occurring evenly over the exposed surface. Figure 2.8 shows a series of images extracted from a video recorded during the trials and clearly shows the recession behavior. Section 2.3.2 provides more analysis into the profile shape change and shows that the surface recession along the stagnation point streamline is constant despite the fact that the mass loss rate varies.

In contrast, Sample 4 did not exhibit varying recession rates throughout the trial. Instead, it remained constant over the course of the 20-minute exposure. This indicates that gas-surface interactions between carbon and nitrogen are far less efficient than those that occur between carbon and oxygen. As shown in Figure 2.8, Sample 4 did not deform to the same degree as Sample 2 over the same exposure time. Thus, it did not assume a hemispherical shape and the mass loss rate remained constant.

Sample 5 was tested under various nitrogen and argon mixtures to indicate if the surface recession rates were linearly related to nitrogen concentration. As expected,

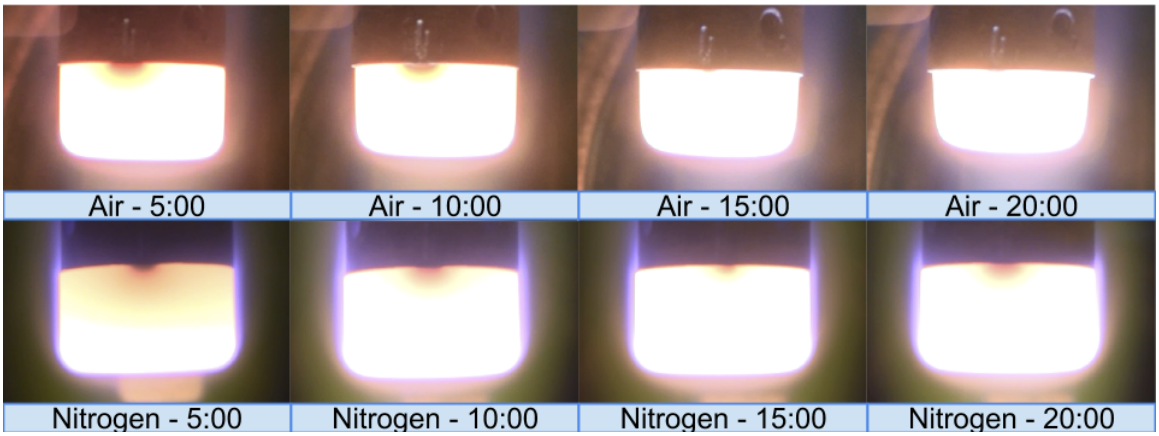

Figure 2.8: A series of images taken of Sample 2 and Sample 4 during the mass loss trials.

the mass loss rate decreased with a reduction in the nitrogen flow rate. In a pure argon plasma, Sample 5 saw minimal mass loss ($\dot{m} = 0.0467$-mg-s^{-1}), which confirmed the assumption that argon plays a relatively small role in extracting carbon from the surface. Additionally, the argon does not appear to increase the surface temperature too greatly, as the pure argon flow was incapable to producing a surface temperature within the operating range of the optical two-color pyrometer.

Table 2.3 shows the calculated mass loss for samples with longer exposure times. Samples 6 and 7 measured similar recession rates, but were slightly higher than the first exposure for Sample 5, which underwent the same nitrogen flow condition. This discrepancy is attributed to the difference in measured surface temperatures amongst the samples. Whereas Samples 6 and 7 reached a front face surface temperature of 1610-K, Sample 5 reached a temperature of 1550-K. It is believed that the reaction efficiency is dependent on temperature, and the reduced mass loss rate experienced by Sample 5 reflects a lower reaction efficiency.

Samples 8 - 11 were exposed to the same air-argon mixture as Sample 2 and the mass loss rate for these samples are in good-agreement. Again, there appears to be a

relative trend between the measured surface temperature and mass loss rate. Sample 12, which had a higher concentration of air, experienced the highest mass loss of all the samples tested, further demonstrating the efficiency of carbon oxidation. A full list of the samples tested throughout the course of this study is included in Appendix C.

Table 2.3: Mass Loss

Sample #	Gas Flow [SLPM]	Exposure [mm:ss]	Temperature [K]	$m_{initial}$ [g]	$\dot{m}$ [mg/s]
6	N_2 - 40	41:53	1610	12.891	0.5718
7	N_2 - 40	42:26	1610	12.970	0.6503
8	Air - 10 : Ar - 30	17:34	1490	12.919	3.617
9	Air - 10 : Ar - 30	33:22	1465	12.900	2.979
10	Air - 10 : Ar - 30	32:45	1400	12.645	2.867
11	Air - 9.7 : Ar - 30.1	32:03	1458	12.71	3.141
12	Air - 14.8 : Ar - 25.4	22:53	1480	12.72	4.390

2.3.2 Surface Recession Study

Additionally, the recession rate of each sample tested in the mass loss survey was calculated from the difference in the pre-test and post-test sample length measurements divided by the exposure time, which assumes that the recession rate is constant over the total exposure. As expected, the recession was significantly faster for samples exposed to air mixtures than for samples exposed to nitrogen. Table 2.4 shows a portion of the recession data obtained within this investigation. Length measurements from the base of the sample to the center point on the leading face were acquired with a set of calibrated verniers. Recall that in Section 2.3.1, the mass loss rate from Sample 2 was previously compared with Samples 4 and 5, which were exposed to nitrogen plasmas. The recession data for Sample 2 is shown below, however Samples 4 and 5

were omitted because they did not measurably recede over their exposure times.

Table 2.4: Surface Recession

Sample #	Gas Flow Rate [SLPM]	Exposure Time [mm:ss]	$L_{initial}$ [mm]	$\dot{L}$ [mm/min]
2	Air - 11.1 : Ar - 30	5:00	25.5	0.15
	Air - 10.5 : Ar - 30	5:00	24.75	0.10
	Air - 10.7 : Ar - 30	5:00	24.25	0.15
	Air - 10.4 : Ar - 30	5:00	23.5	0.15
6	N_2 - 40	41:43	25.5	0.018
7	N_2 - 40	42:26	25.5	0.012
8	Air - 10 : Ar - 30	17:34	25.5	0.128
9	Air - 10 : Ar - 30	33:22	25.5	0.112
10	Air - 10 : Ar - 30	32:45	25.5	0.115
11	Air - 9.7 : Ar - 30.1	32:03	25.5	0.117
12	Air - 14.8 : Ar - 25.4	22:53	25.5	0.175

The recession rate calculated for Sample 2 does not follow the same trend as the mass loss rate. That is, the recession remains linear over each 5-minute exposure and does not experience an initial elevated loss rate. The rate obtained from Sample 2 ($\dot{L} \approx 0.12$-mm-min^{-1}) was observed for longer exposures as well. Samples 8, 9, 10 and 11 had varying exposure durations and they individually produced a constant surface recession rate that agreed well with Sample 2. Sample 12 experienced a higher recession rate due to an increase in the air flowrate. Table 2.4 implies that although the mass loss rate from the sample changes over the course of the exposure, the recession at the center of the sample, corresponding to the stagnation point location, is constant. Samples 6 and 7 were exposed to nitrogen and were tested over the longest duration of all samples. The recession rate for these samples was an order of magnitude slower than those exposed to air.

A significant portion of the work in this investigation involves using optical diagnostic techniques that yield information about the flow at various locations with

respect to the sample surface. Surface recession complicates this because the surface location is time-dependent. However, Table 2.4 shows that the recession rates are linear over a given exposure. Therefore, if one knows the location of a particular measurement with respect to the sample surface before exposure, then the actual distance between the measurement location and the exposed surface is a function of the elapsed exposure time when the measurement is performed and the recession rate, which is determined post test. In nitrogen, the sample recession timescale is very low. However, in air the recession rate competes with the time required to perform optical measurements and this requires additional consideration. Although this investigation focuses exclusively on the carbon-nitrogen system, future tests will include investigating the carbon-oxygen and carbon-air systems. To provide a preliminary look into the nature of recession in air, a high-definition video system was used to record the sample during an air-argon exposure. Figure 2.9 shows the output from the surface tracking software program that was developed in the facility [53].

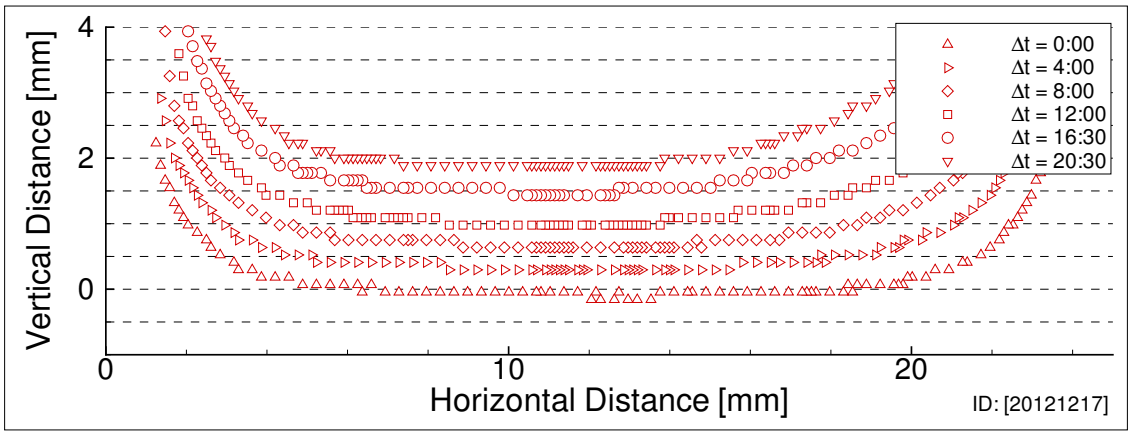

Figure 2.9: Surface recession of Sample 11 in an air-argon plasma mixture.

The surface profiles illustrated in Figure 2.9 were taken in 4 minute intervals except where indicated. Notice how they reveal the processes discussed in the mass

loss and surface recession trials. Specifically, the center point of the sample recedes linearly, while the shape of the sample deforms from a cylindrical to a hemispherical profile. The mass loss about the edges, brought on by shear heating, accounts for the initial spike in the mass loss rate, while the stagnation point recession remains linear.

Chapter 3

Emission Spectroscopy

3.1 Theory

Spontaneous emission spectroscopy is among the many techniques available to measure species concentrations and temperatures in a high-enthalpy gas flow environment, which take advantage of the quantized behavior of molecular and atomic species. Simply, emission spectroscopy is a passive technique that involves collecting electromagnetic radiation from an emitting sample with a spectrometer, where it is separated into its constituent wavelengths and processed. Figure 3.1 shows a common setup, which includes an emission source, focusing optics, spectrometer and data-acquisition system (DAQ). Here, a diffraction grating located within the device separates the light into discrete wavelengths, which are subsequently directed onto a CCD array and processed by the DAQ.

Alternatively, a monochromator is a spectroscopic device that ideally measures emission at discrete wavelengths rather than across a broad spectrum. However, due to quantum effects, diffraction and limitations on mechanical components, it measures a narrow, yet finite, bandwidth of intensities centered on the particular frequency. An

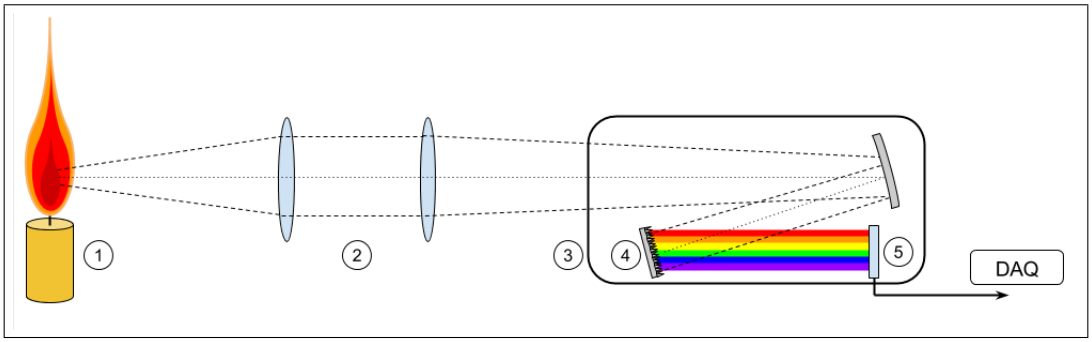

Figure 3.1: A general setup for an emission spectroscopy experiment. The principle requirements are a light source (1), focusing optics (2) and spectrometer (3), which contains a diffraction grating (4) and CCD array (5). The signal is ultimately passed to a data acquisition system.

apertured photon detector replaces the CCD array shown in Figure 3.1 and the turning angle of the diffraction grating controls the wavelength of light directed towards the detector. Although limited by the required scan time over a spectral range, monochromators have proven useful in detecting several molecular species relevant to ablation, including CO, NO, NO_2 and CO_2 [54], [55]. In particular, they are very well suited for detecting infrared emission, where conventional spectrometers are plagued by low S/N ratios brought upon by thermal noise. This issue is more-easily attenuated in monochromators by installing the photon detector in a liquid nitrogen-filled dewar, which maintains the detector at cryogenic temperatures.

Despite their utility in studying high-enthalpy flows, monochromators were not used in this investigation for two reasons. First, all but one of the molecular species studied in this campaign are homonuclear diatomic molecules, whose emission spectra are infrared forbidden. Briefly, transitions that emit in the infrared are less energetic than those that emit in the visible and UV range, and are generally rotational-vibrational transitions within a single electronic energy level. The nuclei within a homonuclear molecule are indistinguishable particles, which results in a symmetric rotation-vibrational transition function, which indicates a forbidden transition.

Therefore, this investigation considers ro-vibronic transitions of homonuclear diatomic molecules, which occur within the detection region of the spectrometer used in the facility.

Another reason why this investigation did not use monochromators is that the only heteronuclear molecule considered in this investigation, CN, has two strong electronic emission band heads located within the spectral range of the facility's spectrometer. Hence, the advantages afforded by the monochromator setup to probe the infrared region are not beneficial.

3.2 Relevant Emission Bands

Quantum mechanics has revealed that particles only exist in discretized energy states. Atoms and molecules both contain translational and electronic energy, which is associated with the translational motion of the particle and the distribution of the electrons surrounding the nucleus or nuclei. Moreover, molecules contain rotational and vibrational energy, which is due to the relative motion of the nuclei. Upon transitioning from a higher to lower energy state, a particle releases a photon with equivalent energy to the energy difference between the two states. Every molecule and atom has a unique emission spectrum, which is dictated by its internal structure and described by quantum mechanics. Additionally, the shape of a particular measured spectrum is temperature-dependent. That is, it becomes broader as the temperature increases. This behavior is due to the combination of Doppler broadening effects and a shift in the energy level populations. The relationship between Doppler broadening and temperature is considered further in Section 3.7.1. *A priori* knowledge of a molecule's spectrum allows one to study these species and to calculate discrete concentrations and temperatures. In this study, nitrogen and carbon species are the most pertinent.

A brief description of the relevant bands are included below.

- N_2 1st-Positive - This system describes the $B^3\Pi_g \rightarrow A^3\Sigma_u^+$ electronic transition of molecular nitrogen. Specifically, the band heads centered at 580.4-nm ($\Delta\nu$ = 4), 639.4-nm ($\Delta\nu$ = 3), 738.7-nm ($\Delta\nu$ = 2) and 857.4-nm ($\Delta\nu$ = 1) were observed in this investigation [14],[56].

- N_2 2nd-Positive - This system describes the $C^3\Pi_u \rightarrow B^3\Pi_g$ electronic transition of molecular nitrogen. This investigation focused on the 313.6-nm ($\Delta\nu$ = 1), 333.8-nm ($\Delta\nu$ = 0) and 353.6-nm ($\Delta\nu$ = -1) band heads [14],[56].

- CN Violet - This system represents the $B^2\Sigma^+ \rightarrow X^2\Sigma^+$ electronic transition of the CN molecule. The main band heads utilized in this investigation are located at 335.1-nm ($\Delta\nu$ = 2), 358.4-nm ($\Delta\nu$ = 1), 388.3-nm ($\Delta\nu$ = 0), 419.7-nm ($\Delta\nu$ = -1), 451.5-nm ($\Delta\nu$ = -2) [57].

- CN Red - This system represents the $A^2\Pi_i \rightarrow X^2\Sigma^+$ electronic transitions in the CN molecule. The principle vibrational band heads utilized in this study are located at 789-nm ($\Delta\nu$ = 2), 694-nm ($\Delta\nu$ = 3), 620-nm ($\Delta\nu$ = 4) and 570-nm ($\Delta\nu$ = 5) [58].

- C_2 Swan - This system represents the $A^3\Pi_g \rightarrow X^3\Pi_u$ electronic transition of the C_2 molecule. The principle electronic-vibrational band heads considered in this investigation lie at 470-nm ($\Delta\nu$ = 1) and 512-nm ($\Delta\nu$ = 0) [59].

- N_2^+ 1st-Negative - This system represents the $B^2\Sigma_u^+ \rightarrow X^2\Sigma_g^+$ electronic transition of the positive ion of molecular nitrogen. Particular band heads of interest in this investigation are at 329.9-nm ($\Delta\nu$ = 2), 356.3-nm ($\Delta\nu$ = 1), 388.4-nm ($\Delta\nu$ = 0), 423.6-nm ($\Delta\nu$ = -1) and 459.9-nm ($\Delta\nu$ = -2) [56].

- N-atom - Atomic nitrogen appears primarily in the infrared portion of the spectrum. The three main features observed in this investigation belong to a set of $2p^2 3s$ - $2p^2(^3P)3p$ transitions. Specifically, these are the ^4P - $^4D^0$, ^4P - $^4P^0$ and ^4P - $^4S^0$ transitions, centered at 869.2-nm, 821.2-nm, and 745.2-nm respectively [5].

- Si, Si^+, O^+ - These species appear exclusively over the quartz sample used in this investigation, which has a chemical formula of SiO_2. The observed Si and Si^+ lines occur at 390-nm from the 3p4s $^1P_1^0 \rightarrow$ $3p^2$ $^1S_0$ electronic transition and 420-nm from the $3s^2 8f$ $^2F_{7/2}^0 \rightarrow$ $3s^2 4d$ $^2D_{5/2}$ electronic transition. The observed O^+ lines appear at 337-nm and 339-nm, which are from the $2p^2(^3P)3d$ $^2P_{1/2} \rightarrow$ $2p^2(^3P)3p$ $^2S_{1/2}^0$ and $2p^2(^3P)3d$ $^2P_{3/2} \rightarrow$ $2p^2(^3P)3p$ $^2S_{1/2}^0$ electronic transitions.

- Na, K - These contaminants are occasionally observed in the free stream. The likely cause of these feature is insufficient cleaning of the quartz tube or inadvertent skin contact with the sample. Sodium and potassium lines appear at 589-nm and 768-nm respectively [60].

3.3 Spectrometer Calibration

This investigation used an Ocean Optics HR4000CG-UV-NIR spectrometer equipped with a 400-μm diameter, 2-m long fiber optic cable, which was subsequently calibrated in order to obtain measurements of absolute spectral radiance from the flow within the ICP torch. Table 3.1 lists several operating parameters of the spectrometer. Figure 3.2 provides a top view layout of the emission diagnostics setup relative to the ICP torch. Emission spectroscopy is a line-of-sight measurement. Thus, the device captures all emission located within the conical focal volume outlined in Figure 3.2.

Table 3.1: Ocean Optics HR4000CG-UV-NIR Specifications

Parameter	Rating
Wavelength Range	200 - 1100-nm
Cable Diameter	400-μm
Entrance Aperture	5-μm
Grating	300-lines-mm^{-1}
Internal Design	f/4 Czerny-Turner
Detector	3648-element linear-array CCD

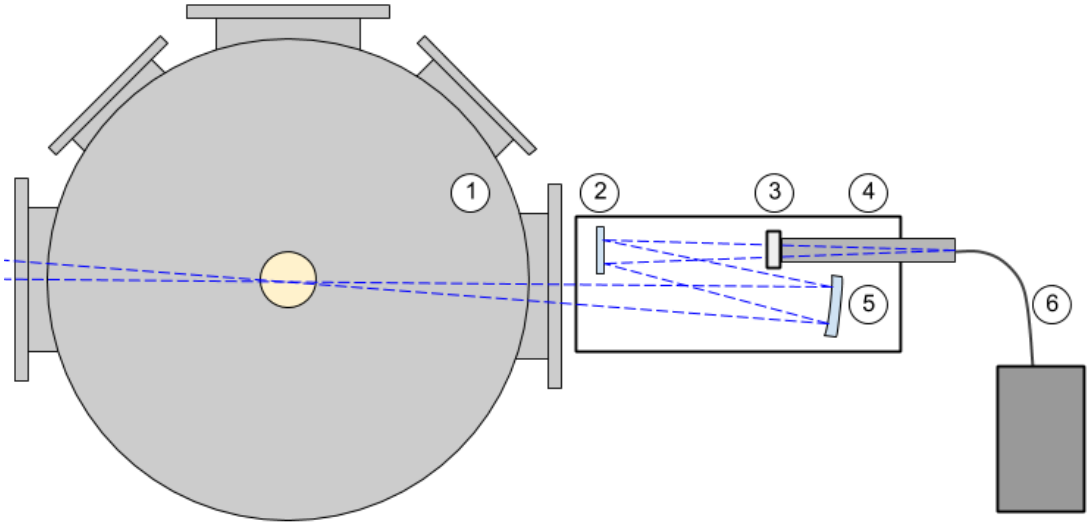

Figure 3.2: A top view of the emission spectrometer setup showing the location of the test chamber (1), 25-mm diameter flat mirror (2), aperture (3), lens tube (4), 50-mm diameter, 300-mm focal length concave mirror (5) and the fiber optic cable connection to the spectrometer (6).

The spectrometer collected emission through a series of reflections off a 50-mm diameter, 300-mm focal length concave mirror and a 25-mm diameter flat mirror. An adjustable aperture attached to the front of a 6.5-in long lens tube controlled the focal volume and the fiber optic cable connected the lens tube to the spectrometer as shown. The setup preserved 1:1 imaging by setting the object and focal distances to twice the focal length of the concave mirror (60 cm). All data in this investigation

were measured with a 3/16-in diameter aperture, which provided $\approx$ f/30 optics. Other aperture sizes were calibrated as well, but were not used in this investigation.

This setup proved advantageous because it captured a strong emission signal while simultaneously maintaining high spatial-resolution over a nearly-cylindrical focal volume across the plasma flow. Figure 3.3 shows a plot of the normalized radiance measured by the spectrometer with respect to the position of a light source along the principle focal axis. There is little deviation in the captured emission over a 50-mm range, which corresponds to the estimated diameter of the jet. These data support the assertion that the high optical f/# of the setup create a nearly-cylindrical focal volume along the plasma jet. Moreover, the focal volume divergence angle was $\approx 2^o$ and the sharp turning angles between the mirrors and the shape of the focal volume minimized the astigmatism between the vertical and horizontal focal planes.

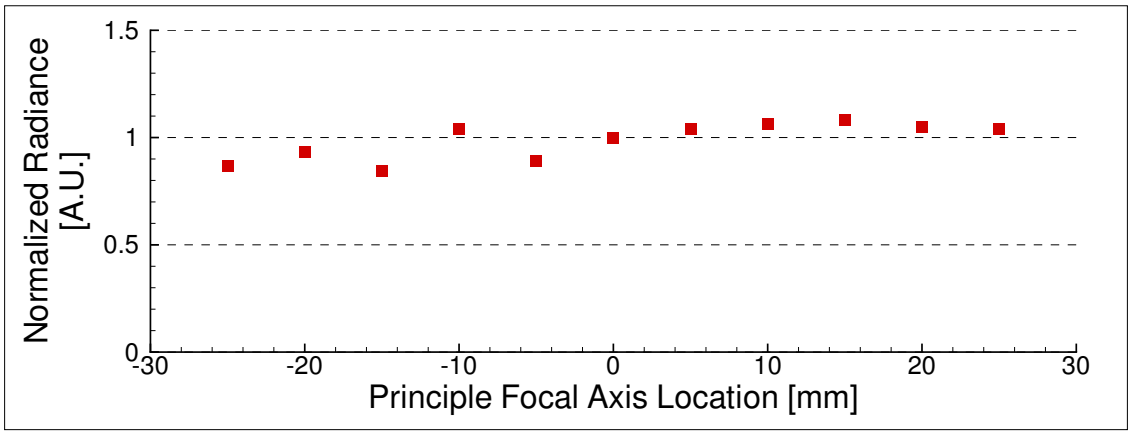

Figure 3.3: The normalized radiance measured from the the lamp positioned along the principle focal axis.

Initially, the uncalibrated setup yielded spectral emission in counts. Therefore, a calibration function was developed to convert these data into units of absolute spectral radiance using an Oriel Instruments Open Air Model 63966 tungsten filament light source. The spectral irradiance provided by this light source was determined

previously by the manufacturer using the NIST-traceable technique outlined in NBS Special Publication 250-20 [61].

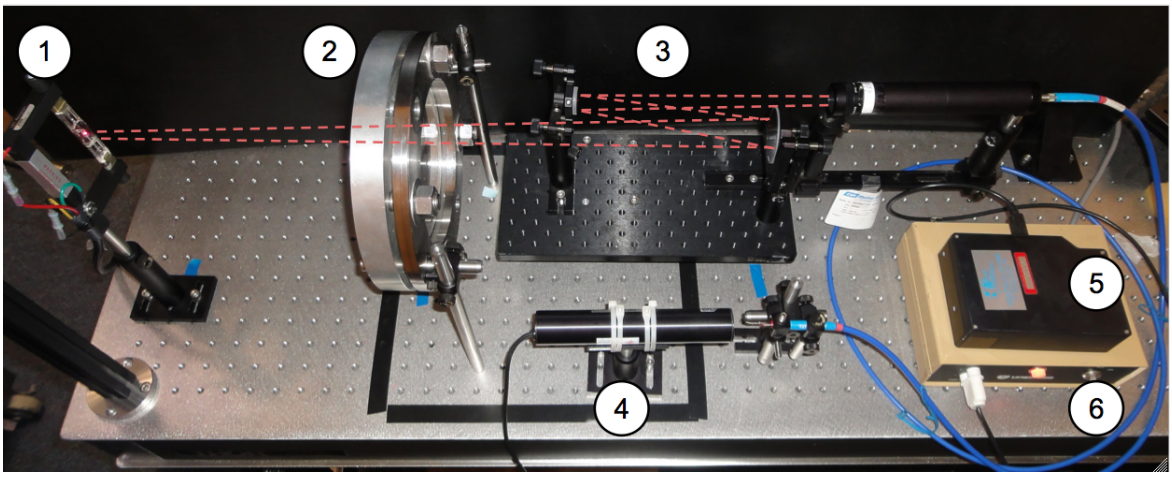

Figure 3.4: A photograph of the absolute intensity calibration setup. Labelled in this image are the calibrated light source (1), plasma chamber window (2), collection optics (3), He-Ne laser (4), spectrometer (5), He-Ne laser power source (6) and an estimated outline of the He-Ne light path (- - -).

Due to spatial difficulties and safety concerns, the spectrometer was not calibrated within the ICP chamber. Rather, a separate setup was constructed in the lab that preserved the relative spatial locations of the spectrometer to the center of the plasma jet, as shown in Figure 3.4. A He-Ne laser aided in the focal volume alignment procedure as illustrated. The output from the He-Ne was directed into the free end of the fiber optic cable and the opposite end was attached to the lens tube. Reflections within the cable caused the spatially-coherent light entering the cable to disperse upon exiting the opposite end. The location and shape of the focal volume was monitored by projecting the output onto an index card while the collection optics were adjusted appropriately until the beam was directed onto the light source.

Once aligned, the He-Ne laser was turned off and the free end of the cable was connected to the spectrometer. The calibration lamp was activated and allowed to warm up for 30 minutes. The lamp operating conditions were 6.5-A and 30-V, which

was provided by a dedicated Oriel Instruments 300-W Radiometric Power Supply Model 69931. Figure 3.5 shows the provided absolute spectral irradiance emitted by the light source at these operating conditions.

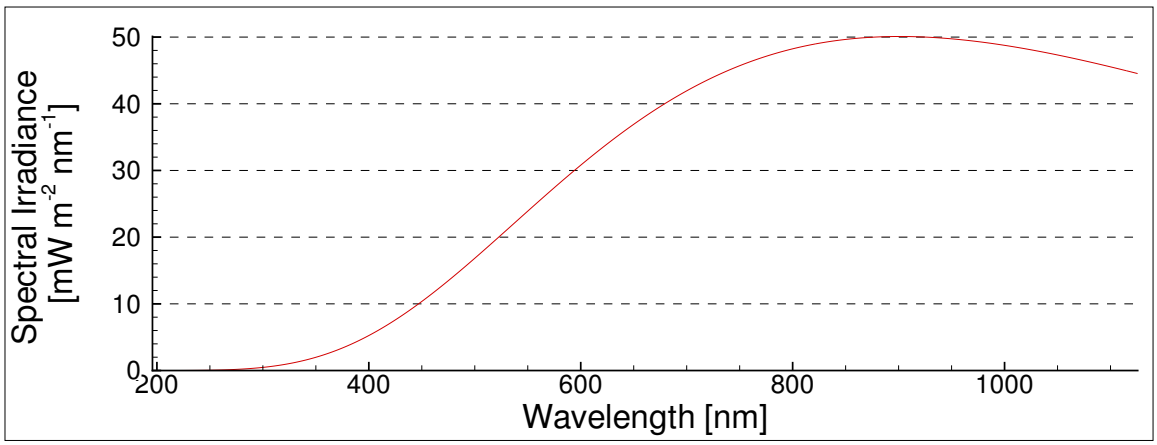

Figure 3.5: The spectral irradiance emitted by the calibration light source.

The spectrometer was independently calibrated at five aperture diameters (1/16-in, 3/32-in, 1/8-in, 3/16-in and 1/4-in) with the following procedure. First, the integration time in the spectrometer control software was adjusted until the peak of the acquired emission was just below the saturation limit. Next, a dark spectrum was acquired at this integration time by recording the emission while blocking the lens tube entrance. This dark spectrum represented background noise, which is attributable to electronic interference between the spectrometer and the data-acquisition system in addition to other effects. Finally, with the dark spectrum subtracted, the emission from the calibration lamp was recorded. The emission was subsequently divided through by the integration time, which yielded an intensity in units of counts-s^{-1}, as shown in Figure 3.6. This particular curve corresponds to the raw emission obtained with a 3/32-in diameter aperture and 80-ms integration time. Note that the extremes of the curve go to zero, indicating that the dark spectrum subtraction was applied properly.

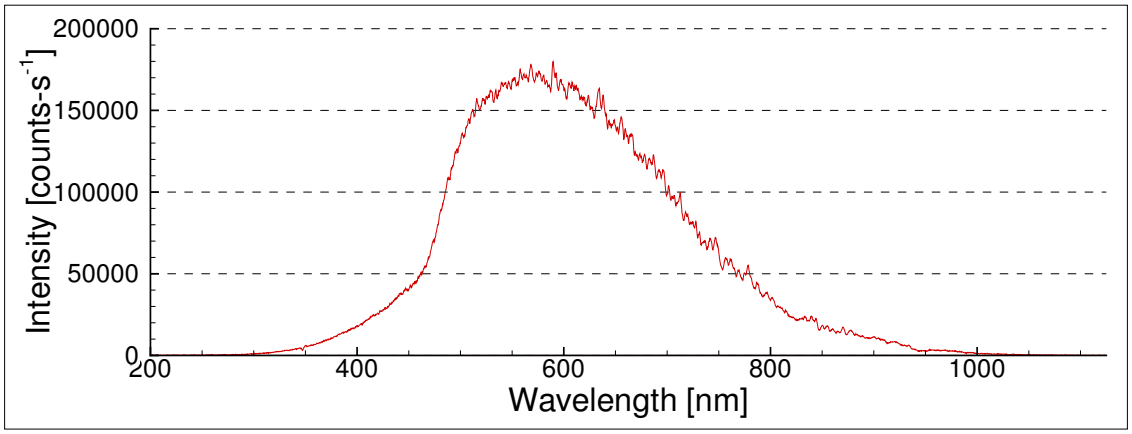

Figure 3.6: The background-subtracted raw emission signal obtained with the calibration light source and a 3/32-in diameter aperture. The emission is divided by the 80-ms integration time used to obtain the signal.

The absolute spectral response (ASR) is the desired calibration curve, which relates the absolute intensity provided by the calibrated light source to the spectrometer detectivity. The ASR was calculated using Equation 3.1, which is a function of the dark-subtracted raw emission ($I_{cal_{raw}}$), the corresponding integration time for the raw emission ($\tau_{cal_{raw}}$) and the absolute intensity provided by the light source (I_{abs}). To be clear, the data for the numerator and denominator in Equation 3.1 are plotted in Figure 3.5 and Figure 3.6 respectively.

$$ASR = \frac{I_{abs}}{I_{cal_{raw}}/\tau_{cal_{raw}}} \tag{3.1}$$

With the ASR determined for all aperture sizes, all subsequent measurements obtained in the ICP were converted into absolute spectral irradiance units with Equation 3.2. Note that the final irradiance measurement (I_{final}) is a function of the raw emission in counts ($I_{ICP_{raw}}$) and the integration time of the spectrum ($\tau_{ICP_{raw}}$) within the ICP.

$$I_{final} = (ASR)\left(\frac{I_{ICP_{raw}}}{\tau_{ICP_{raw}}}\right) \tag{3.2}$$

Figure 3.7 shows the ASR for the 3/32-in diameter aperture. With this curve, the setup is fully calibrated for this aperture size.

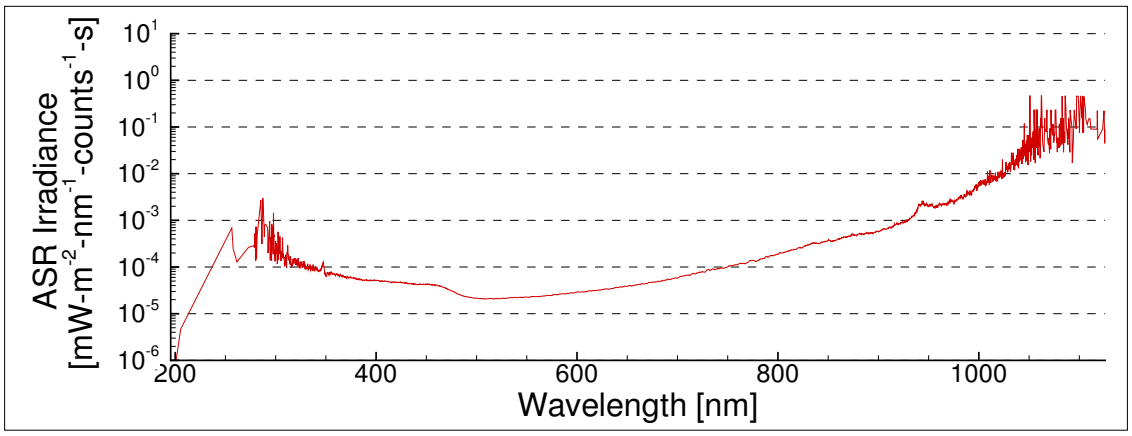

Figure 3.7: The adjusted spectral response curve for the 3/32-in diameter aperture setting.

The ASR is wavelength-dependent and it corrects for the detection efficiency of the spectrometer with respect to absolute intensity. It also illustrates the spectral range over which the spectrometer is reliable. In this case, the ASR varies significantly below 300-nm and above 900-nm. This behavior is due in part to the spectrometer detection efficiency and the shape of the spectral irradiance curve provided by the calibration lamp. Therefore, calibrated emission obtained outside of this range was not considered in this investigation.

Conventionally, emission data are presented in units of spectral radiance (mW-m^{-2}-nm^{-1}-sr^{-1}), which takes into account the solid angle of the optical detection system. The solid angle for this system was calculated with Equation 3.3, which depends on the cross-sectional area of the focal volume (Θ) at the measured distance from the object location (r) [53]. Spectral radiance units are obtained from dividing

the spectral irradiance by the solid angle of the detection system. Table 3.2 lists the solid angles measured at several aperture settings.

$$\Omega = \frac{\Theta}{r^2} \tag{3.3}$$

Table 3.2: Solid Angles

Aperture Diameter [in]	Solid Angle [sr]	f/#
1/16	$5.454(10^{-5})$	120
3/32	$2.182(10^{-4})$	60.0
1/8	$3.687(10^{-4})$	46
3/16	$8.727(10^{-4})$	30
1/4	$1.154(10^{-3})$	26

3.4 Emission Alignment Procedure

Aligning the emission spectrometer focal volume to the sample is a multi-step procedure that first involves assuring that the sample can be repeatedly inserted to the center of the free jet. Accordingly, a quartz sample was installed onto the insertion probe holder and inserted into the flow after the ICP was ignited and set to the standard test conditions. Once there, the sample location was adjusted until it was visually-aligned through two perpendicular observation ports with the center of the jet. The facility was then turned off and a hard stop was installed onto the insertion probe, which guaranteed that all subsequent insertions would return the sample to the same location. With the facility off, the He-Ne laser was used in the manner described in Section 3.3 to align the emission spectrometer focal volume to the desired location with respect to the sample using vertical and horizontal staging micrometers. Figure 3.8 shows an image taken from within the chamber of the He-Ne light grazing the

leading face of a graphite sample prior to a test. From this location, the vertical and horizontal micrometers adjusted the axial and radial location of the spectral volume respectively.

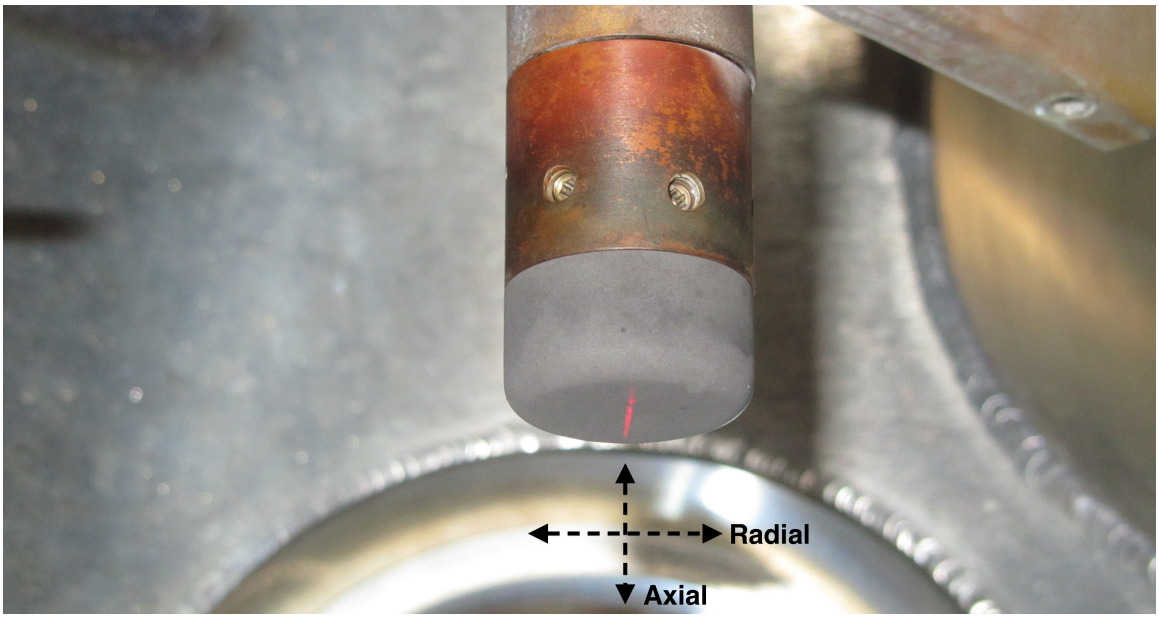

Figure 3.8: A photograph of a graphite sample installed onto the probe holder. The light provided by the He-Ne laser appears on the leading face.

3.5 Grey-body Emission Study

The Planck distribution describes the intensity of radiation emitted from a solid material, as shown in Equation 3.4 [62]. The emissivity (ϵ) is a material-specific quantity that depends on wavelength (λ) and temperature (T) and accounts for the efficiency with which an emitting surface radiates energy with respect to an idealized blackbody. This expression provides an alternative method with which to determine the sample surface temperature using the emission spectrometer. Ideally, the temperatures measured by this technique ought to match those determined by the two-color pyrometer.

$$B_\lambda(T) = \epsilon(\lambda, T)\frac{8\pi hc^2}{\lambda^5}\frac{1}{e^{\frac{hc}{\lambda k_B T}} - 1} \tag{3.4}$$

In this campaign, both of the facility's pyrometers were used to measure the sample surface temperature at separate locations during a nitrogen exposure. One pyrometer focused on the sample front face while the other focused on the sample side through an alternative observation port. Figure 3.9 shows the temperatures measured during this trial. Section (1) of the curve represents the front face temperature. Here, the pyrometer captured emission from a spot diameter of $\approx$ 8-mm on the surface. The initial drop-off in the figure is an artificial feature produced by the data acquisition system. However, the increasing temperature beginning at $t = 1300$-s indicates the transient temperature rise occurring as the sample warms. By $t = 1360$-s, the sample front face has reached a steady state temperature of $T = 1416$-K. The absence of data in Section (2) corresponds to the period of time required to change the DAQ system to the second pyrometer.

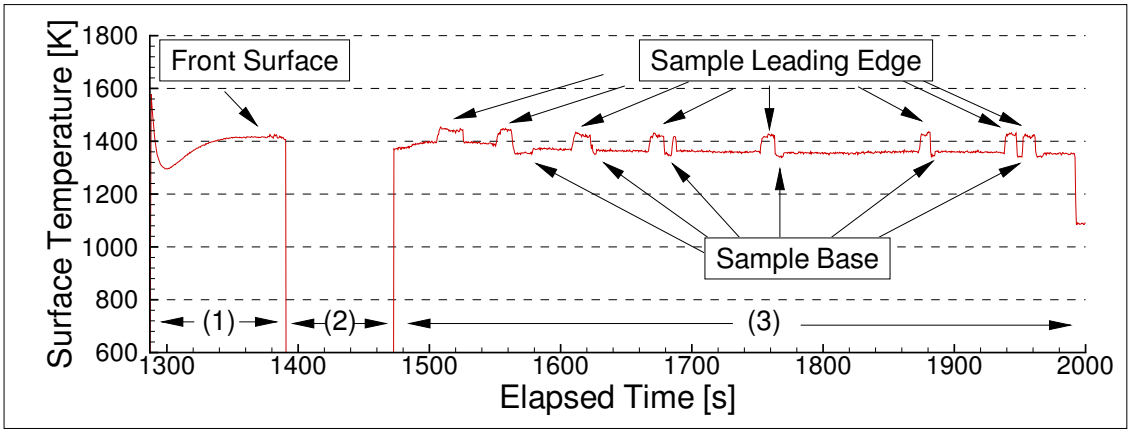

Figure 3.9: The graphite surface temperature for nitrogen exposure measured at various locations. Section (1) and (3) represent the front surface and side surface temperatures respectively.

Section (3) shows temperature measurements from the side of the sample. Here,

the focal area of the pyrometer rested approximately halfway up the sample, with a spot size of $\approx$ 2.3-mm in diameter. The pyrometer focus was temporarily adjusted towards the sample leading edge and base to capture the temperature at these locations as well. This technique was repeated several times throughout the exposure to verify thermal steady state and these locations are labelled appropriately on Figure 3.9. The leading edge and base temperatures deviated by nearly 1% during the trial. In particular, the leading edge dropped from 1440-K to 1423-K while the base temperatures dropped from 1354-K to 1339-K. This trend is due to the power supply, which tends to provide downward drifting supplied power during extended exposures. In general the drift is very slight, as observed in this case. However, later tests were closely monitored and the power supply was adjusted as necessary to maintain constant power levels. Notice that the temperature at the leading edge was higher than the front face steady state temperature. This behavior is due to shear heating, which originates from the favorable pressure gradient experienced by the flow as it passes around the corner radius.

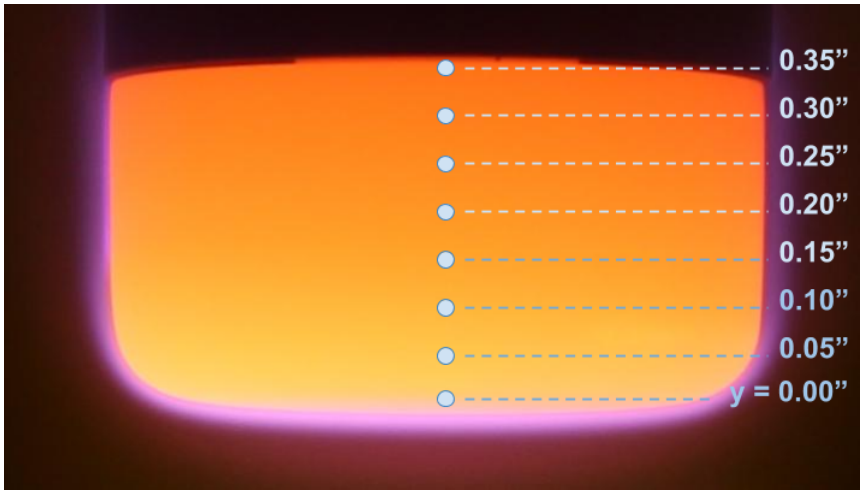

Figure 3.10: The approximate locations of the spectrometer focal area during the grey body experiment.

During the same trial, the spectrometer was directed towards several axial loca-

tions on the side of the sample, beginning with the leading edge (Δy = 0-in). The total thickness of the exposed portion of the sample head was 0.405-in, and a total of eight measurements in 0.05-in increments were performed with a 20-second integration time. The spectrometer focal diameter was $\approx$ 0.4-mm. Figure 3.10 shows the approximate focal area locations of the detection system. The data obtained were converted into units of absolute spectral radiance and fitted with a Planck distribution curve using a least squares routine with the temperature and emissivity as free variables. The emissivity was assumed constant with respect to wavelength, which is appropriate owing to the small spectral range of the fitted data. The full program used in this procedure is shown in Appendix G.

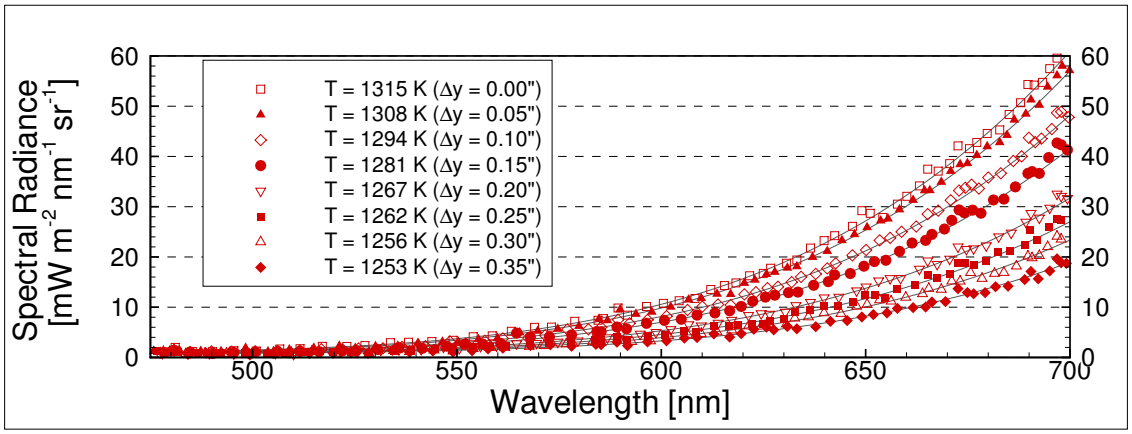

Figure 3.11: The spectral radiance measured at various axial locations on graphite along with the corresponding Planck distribution curves.

Figure 3.11 shows the Planck distribution curves obtained from the routine superimposed over the spectral radiance data captured by the spectrometer. Notice that the temperature steadily decreases from the leading edge towards the sample base (T_{edge} = 1315-K at Δy = 0-in; T_{base} = 1253-K at Δy = 0.35-in). Comparing these data with the values obtained from the pyrometers (T_{edge} = 1423 - 1440-K; T_{base} = 1339 - 1354-K) shows slight disagreement; namely the leading edge and base

temperatures were lower by 8% and 7% respectively.

Among the various possible explanations for the measured temperature disparity is the fundamental difference with which the temperatures were determined. The pyrometer calculates the surface temperature in two-color mode by measuring the emission from the overlapping IR bands at 950 - 1100-nm and 750 - 1100-nm and assuming a constant emissivity. In one-color mode, the pyrometer measures the emission from 750 - 1100-nm and applies a user-defined emissivity. In contrast, the Planck distribution curves were fitted to the emission captured at 475 - 700-nm. This range was selected because both the signal strength and spectrometer detectivity were high in this spectral region. If an unclassified absorber or emitter were present within the flow at the spectral range of either device, it may alter the measured emission and cause an artificial increase or decrease in the measured temperature.

It is believed that the pyrometer provided a more accurate temperature reading than the emission spectrometer. First, the temperatures measured by the pyrometer are consistent with the surface temperatures measured on similar materials with varying gas compositions [63], [64]. Moreover, an independent study performed in the facility showed that the temperature measured in one-color mode with an emissivity value of 0.82 reproduced the temperature measured in two-color mode. This value deviated $\approx 2\%$ from the value supplied by the manufacturer ($\epsilon = 0.803$). Other researchers using the same technique have reported lower surface temperatures via emission spectroscopy with respect to the pyrometer reading [51]. Therefore, it is more likely that the difference in measured temperatures is due to the spectrometer.

Another possible explanation is that the observation viewport may be absorbing some of the light. Although the material has a very high transmittance within the spectral range used in the data fitting algorithm, it is possible that some absorption occurs due to contamination that has accumulated on the window surface over the

life of the facility.

3.6 Gas Phase Flow Results

3.6.1 Flow Repeatability and Symmetry

It is important that the facility repeatedly create identical flow conditions between trials. One way to test the repeatability of the system is to measure emission from the same location within the flow during separate facility runs. If the system were to create repeatable flow conditions, the emission obtained at the chosen location would not significantly deviate between measurements. Figure 3.13 shows the spectral radiance measured from three separate trials at the jet centerline, 90-mm from the quartz tube outlet. Several vibrational band heads within the N_2 1^{st}-Positive (1+), 2^{nd}-Positive (2+) and N_2^+ 1^{st}-Negative (1-) systems are indicated. Clearly, the signals overlap throughout the spectral range, indicating repeatable thermal and chemical flow conditions in the free stream between tests. The curves corresponding to test IDs '20140625-168' and '20140626-129' were obtained with a 5-second exposure time. Test ID '20140326-080' was measured with a 20-second exposure, which significantly improved the signal-to-noise ratio (S/N).

Emission spectroscopy is a line-of-sight technique, thus it detects all emission occurring within the focal volume of an optically-thin gas. The Abel inversion is a mathematical transformation of spatial coordinates that converts emission obtained along plasma chords into a radial distribution of the spectral radiance, as described in Section 3.7. In this investigation, the Abel inversion technique was limited to axially-symmetric flow. To confirm this condition, the jet was analyzed by measuring the emission along 51 plasma chords at 1-mm increments within the jet free stream.

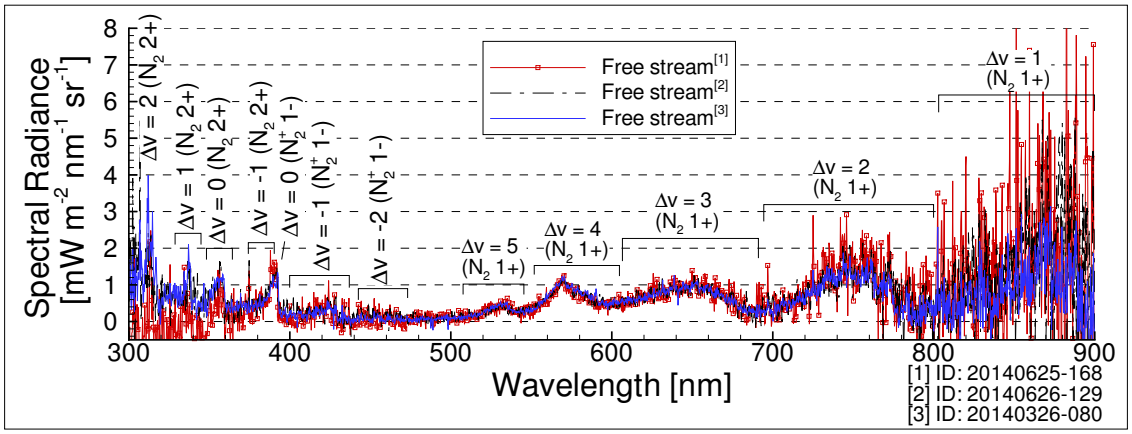

Figure 3.12: Spectra obtained from the centerline of the jet free stream during three separate trials.

This procedure was repeated on a second day for comparison.

Integrating each acquired spectrum over a known spectral feature yields the corresponding radiance along the plasma chord. Figure 3.13 shows the radiance from a portion of the $\Delta\nu = 4$ vibrational transition in the 1^{st}-Positive system. The limits of integration were 550 - 570-nm, which captured the main peak of the feature. The figure shows the two discrete data sets and their corresponding Gaussian fit, generated with a least-squares solver. The two curves are nearly identical, with strong correlation between the experimental data and the Gaussian fit, which supports the claim that the flow is axially-symmetric and repeatable. Note that the radiance goes to zero at the extremes, indicating that the radial scan extended to the jet edge.

The standard deviation between the measured data and analytical fit for Trial 1 and Trial 2 were 0.25-mW-m^{-2}-sr^{-1} and 0.20-mW-m^{-2}-sr^{-1} respectively, which is due to the combination of flow unsteadiness, noise within the spectrometer and data-acquisition, and the degree to which the flow is non-axisymmetric. One manner in which to calculate the error associated with the flow unsteadiness and system noise exclusively is by performing repeated measurements at a single location within the

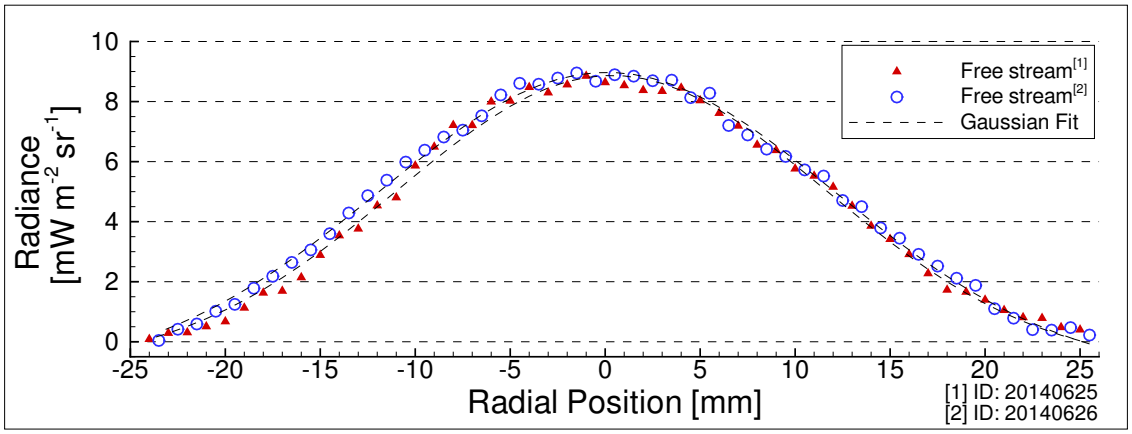

Figure 3.13: Radial distribution of the N_2 radiance across the plasma jet free stream.

flow and calculating the maximum residual between the measured data and the mean of the set. Using this method at the jet center location, the error associated with flow unsteadiness and system noise is $\pm$0.11-mW-m^{-2}-sr^{-1}.

3.6.2 Free Stream Conditions

The emission from Test ID '20140326-080' was examined further to investigate the degree to which the free stream flow was in local thermodynamic equilibrium (LTE) by comparing the experimental results with the Specair software package. Specair provides a predicted emission from plasmas at prescribed thermodynamic conditions using a numerical model for common molecular and atomic transitions [65]. Using the operating pressures for the trials (p = 160-Torr) and a free stream LTE temperature of 6000-K determined in previous experiments using LIF, Specair determined the predicted emission spectrum shown in Figure 3.14 [66], [64]. Here, the molar fractions for atomic and molecular nitrogen were set to the equilibrium composition values of $\chi_{N_2} = 0.59$, $\chi_N = 0.41$. The mole fraction of molecular nitrogen ion was lowered two orders of magnitude below its equilibrium value to $\chi_{N_2^+} = 6(10^{-7})$. This adjustment helped improve the quality of the numerical fit to the experiment and

was supported by the fact that careful analysis of each radial scan indicated that N_2^+ only appeared within 10-mm of the jet center. Specair does not consider a Gaussian intensity distribution, but an isotropic distribution across a fixed slab width, which yielded a higher predicted N_2^+ signal than what was observed experimentally. Clearly, N_2^+ is a minor species in the flow and this adjustment has little effect on the ensuing analysis.

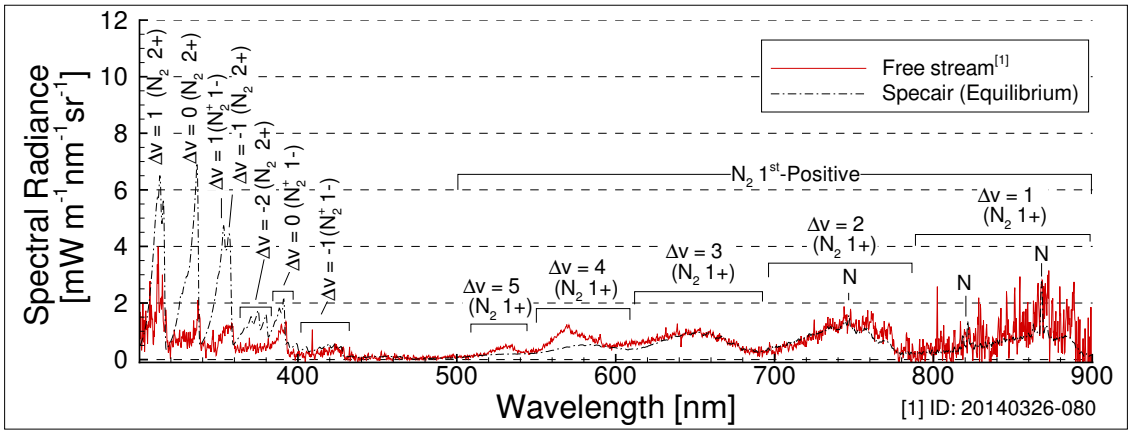

Figure 3.14: A comparison between the spontaneous emission measured along the centerline of the free stream and the model predicted by Specair.

Notice that Specair reasonably predicts the measured spectrum. The most noticeable deviations between the curves occur in the UV. Each vibronic band head in the N_2 2nd-Positive system predicted by Specair is higher than the experimental measurement, which is explained by the same reasoning provided for the discrepancy in the N_2^+ 1st-Negative system signal. The N_2 2nd-Positive requires a significant population of N_2 in the high-lying $C^3\Pi_u$ electronic state for detection, which only occurs within a small radius from the center of the jet where the local temperatures are greatest. Therefore, Specair over predicts the expected emission from this level.

The nitrogen atom lines predicted by Specair are not clearly evident in the experimental data. Again, the population of dissociated nitrogen atoms is likely limited

to a small portion of the total focal volume of the spectrometer and it is unclear if increased S/N would be capable of resolving these features. Note that the integration time for this spectrum was 20-s.

There is apparent disagreement between the measurement and prediction of the $\Delta v = 4$ and $\Delta v = 5$ vibronic transitions within the the N_2 1st-Positive system. Specifically, Specair does not capture the strong measured peaks in intensity near 530-nm and 570-nm, which correspond to the (13,8) and (13,9) vibrational transitions within N_2 1st-Positive, respectively. The divergence implies a non-Boltzmann population distribution amongst the vibrational modes within the N_2 $B^3\Pi_g$ state and significant overpopulation of the v'=13 vibrational level in particular. The overpopulation of a given energy level ($\rho_{e,v}$) expressed in Equation 3.5 is the ratio of the actual number density in the level ($n_{e,v}$) to the equilibrium number density ($n^{eq}_{e,v}$) for a particular thermodynamic condition.

$$\rho_{e,v} = \frac{n_{e,v}}{n^{eq}_{e,v}} \tag{3.5}$$

Figure 3.15 shows the molecular nitrogen energy level diagram. Recognize that the N_2 1st-Positive system describes electronic transitions between the B $^3\Pi_g$ and A $^3\Sigma^+_u$ energy levels. Additionally, the presumed overpopulation is potentially caused by an inverse predissociation event between two ground state nitrogen atoms (N $^4S_0$), which recombine into the N_2 $^5\Sigma^+_g$ electronic state. This extremely shallow state directly overlaps the N_2 $B^3\Pi_g(v = 13)$ vibrational level, which provides an efficient, steady supply of emitters to the 1st-Positive system. Owing to the low operating pressures, the spontaneous emission rate from this level is faster than the rate at which collisions can redistribute the particles into a Boltzmann distribution of vibrational levels.

Specair is capable of simulating spectra for prescribed overpopulation factors of the

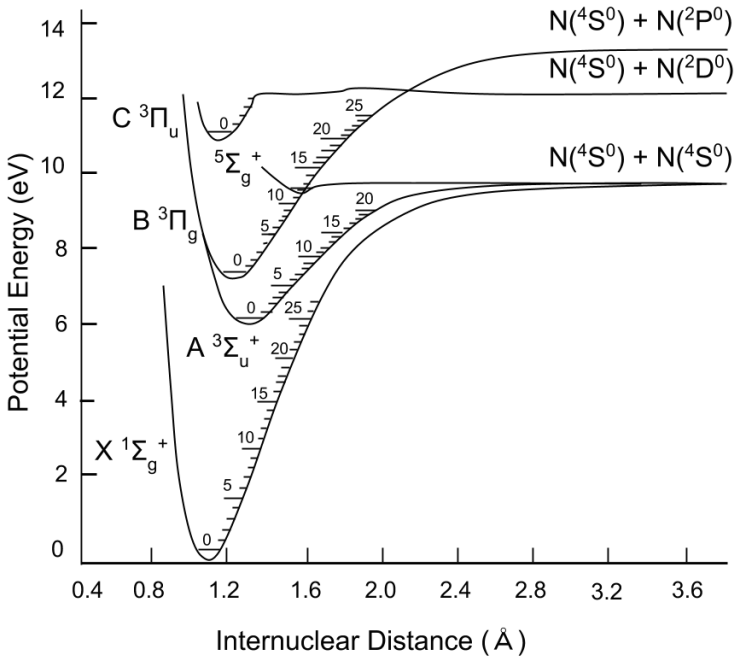

Figure 3.15: Molecular nitrogen energy level diagram.

N_2 $B^3\Pi_g$ vibrational levels. With this non-equilibrium model provided by Specair, an estimation of the overpopulation factors for the B-state vibrational levels were examined. Laux observed a stronger degree of non-equilibrium in an ICP facility operating at atmospheric pressure [14]. Using the scaling provided by Laux as an initial estimation, the overpopulation values were adjusted until the Specair prediction converged with the experimental data. The converged result is shown in Figure 3.16. Clearly, adjusting the overpopulation values appropriately yielded strong correspondence between Specair and experiment throughout the 1^{st}-Positive system, including the $\Delta v = 4$ and $\Delta v = 5$ vibrational bands.

The overpopulation values determined by this analysis are shown in Figure 3.17. Also plotted are the overpopulation values corresponding to the experiment conducted by Laux [14]. Clearly, the flow within the ICP facility in the PDTL is closer to equilibrium than the flow considered by Laux. In both instances, the maximum

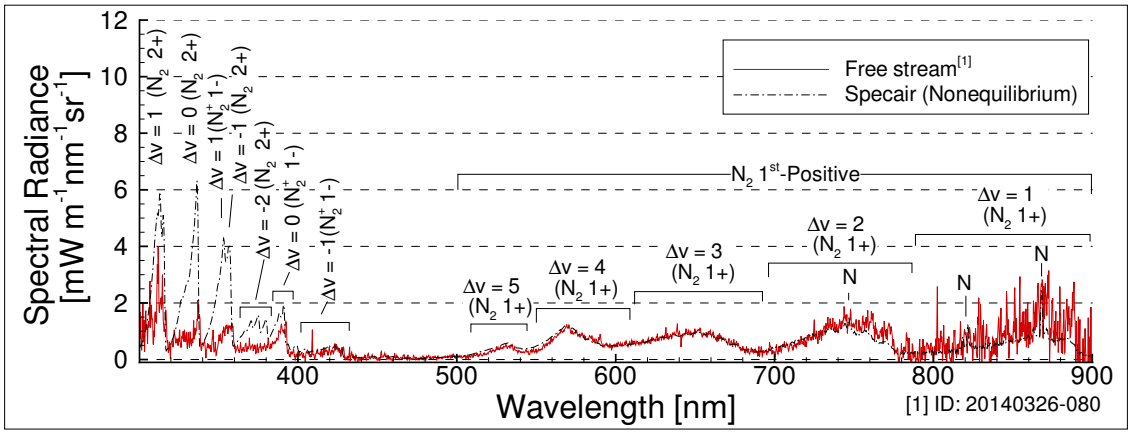

Figure 3.16: Emission from the centerline of the free jet and the spectrum computed by Specair with a non-equilibrium population distribution amongst N_2 B-state vibrational levels.

overpopulation occurred in the (v = 13) vibrational level, which supports the belief that inverse predissociation pathway dominates the observed behavior. The uncertainty on each overpopulation value was 30%, which was determined by considering the acceptable range over which the values would provide a reasonable match to the experimental data.

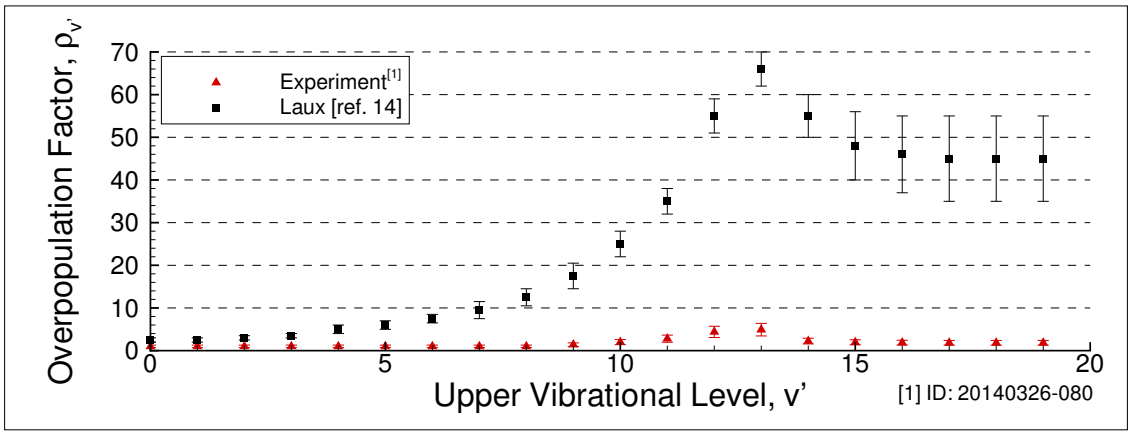

Figure 3.17: A comparison of the overpopulation values used by Specair to compute the spectrum in Figure 3.16 and those used by Laux [14].

In steady-state, the total number of N_2 molecules in the $B^3\Pi_g$(v=13) vibrational energy level remains fixed, which indicates that the rate of all processes depleting

the energy level population is balanced by the rate at which the energy level is populated. Among the depletion processes are predissociation, spontaneous emission, electron impact ionization and excitation, and vibrational-translational excitation to adjacent vibrational levels. Table 3.3 lists various depletion rates calculated by Laux from a collisional-radiative (CR) model for nitrogen at 1-atm and 4700-K [67]. Note that predissociation is the strongest contributor to the depletion rate with spontaneous emission and vibrational-translational excitation to adjacent vibrational modes two full orders lower. His model considered higher pressures than the operating conditions within this investigation. However, considering that predissociation is presumably not collision-driven and the free stream temperatures in this investigation were significantly higher than those considered in the CR model, it is assumed that the general relationship amongst the $B^3\Pi_g$(v=13) depletion mechanisms in this study is consistent with Laux's findings.

Figure 3.17 shows that vibrational-translational excitation plays an observable role in the overpopulation. Note that the vibrational levels directly above and below the v' = 13 level are overpopulated as well, indicating that a portion of the molecules entering the v' = 13 level shift to adjacent levels through this process. Electron impact excitation plays a minimal role owing to the limited amount of free electrons with the flow even at the hottest regions ($\chi_{e^-} = 6(10^{-5})$).

The steady state equation for the v' = 13 energy level is expressed in Equation 3.6 under the assumption that inverse predissociation and predissociation are the dominant populating and depleting processes within the energy level. Hence, spontaneous emission and vibrational-translational excitation are ignored. Note that this expression is valid for equilibrium and non-equilibrium systems.

Table 3.3: Depletion rates from the N_2 $B^3\Pi_g$(v=13) energy level

Term	Rate $[s^{-1}]$	Description
$k^{pred}_{v=13}$	$2.6(10^8)$	Predissociation
$\sum A_{v'=13,v''}$	$2.0(10^6)$	Spontaneous emission
$n_M(k^{13\rightarrow 14}_{VT} + k^{13\rightarrow 12}_{VT})$	$6(10^6)$	Vibrational-translational excitation
$n_e k^e_{B,v=13\rightarrow X}$	$3.7(10^4)$	Electron impact excitation to X-state
$n_e k^e_{B,v=13\rightarrow A}$	$3.7(10^5)$	Electron impact excitation to A-state
$n_e k^e_{B,v=13\rightarrow W}$	$3.7(10^6)$	Electron impact excitation to W-state
$n_e k^e_{B,v=13\rightarrow B'}$	$3.8(10^4)$	Electron impact excitation to B'-state
$n_e k^e_{B,v=13\rightarrow C}$	$6.0(10^1)$	Electron impact excitation to C-state

$$\frac{dn_{N_2,B,v=13}}{dt} = 0 \rightarrow \underbrace{n_{N_2,B,v=13}k^{pred}_{v=13}}_{\text{depletion}} \approx \underbrace{(n_N)^2 k^{inv.pred}_{v=13}}_{\text{addition}} \tag{3.6}$$

Dividing Equation 3.6 by the equivalent equilibrium rate equation yields the expression shown in Equation 3.7.

$$\frac{n_{N_2,B,v=13}}{n^{eq}_{N_2,B,v=13}} \approx \left(\frac{n_N}{n^{eq}_N}\right)^2 \tag{3.7}$$

This yields an estimation of the ground state nitrogen atom overpopulation value, as expressed in Equation 3.8.

$$\rho_{N_2,B,v=13} \approx \rho^2_N \tag{3.8}$$

For the experimental conditions considered, Figure 3.17 shows the overpopulation value of the $B^3\Pi_g$ (v=13) energy level is $\rho_{N_2,B,v=13} = 4.91\pm1.5$, yielding a ground state nitrogen atom overpopulation value of $\rho_N = 2.22\pm0.25$. At standard operating conditions, the equilibrium number density of atomic nitrogen is $1.03(10^{17})$-cm^{-3}. Thus, the total nitrogen atom number density measured in the free stream

is 2.29±0.65(10^{17})-cm^{-3}. Considering this population of atomic nitrogen, the molar composition of the flow becomes $\chi_N = 0.88$, $\chi_{N_2} = 0.12$, and $\chi_{N_2^+} = 10^{-6}$. Section 4.4 further investigates the nitrogen atom ground state population using a separate optical diagnostic technique and is discussed more in-depth there. Table 3.4 provides a summary of the various quantities determined from this analysis.

Table 3.4: Nitrogen in Free Stream

Species	ρ	n [cm^{-3}]
N ($^4S_0$)	2.22±0.25	2.29±0.65(10^{17})
N_2 (B,v=13)	4.91±1.5	-

3.6.3 Boundary Layer Conditions

Previous investigations have analyzed the changes in the free stream flow structure with a sample inserted into the center of the jet [13]. At the center of the jet, the temperature and species concentration gradients along the radial direction become more gradual when a sample is present. This flattens the Gaussian profile shown in Figure 3.13 and creates a more uniform flow towards the surface. To help visualize these effects, the LeMANS software package simulated the flow at the experimental conditions over quartz, which was modeled as a non-catalytic material [15]. Figure 3.18 shows the two-dimensional temperature field determined by the simulation. Note that the sample causes the flow to turn over the surface, which spreads the jet wider and creates a shallower radial temperature gradient at the jet center.

These effects are also observed experimentally from emission measurements obtained within the boundary layer over quartz and graphite. Moreover, these data show the evolution of chemical species in the boundary layer. Figure 3.19 shows a

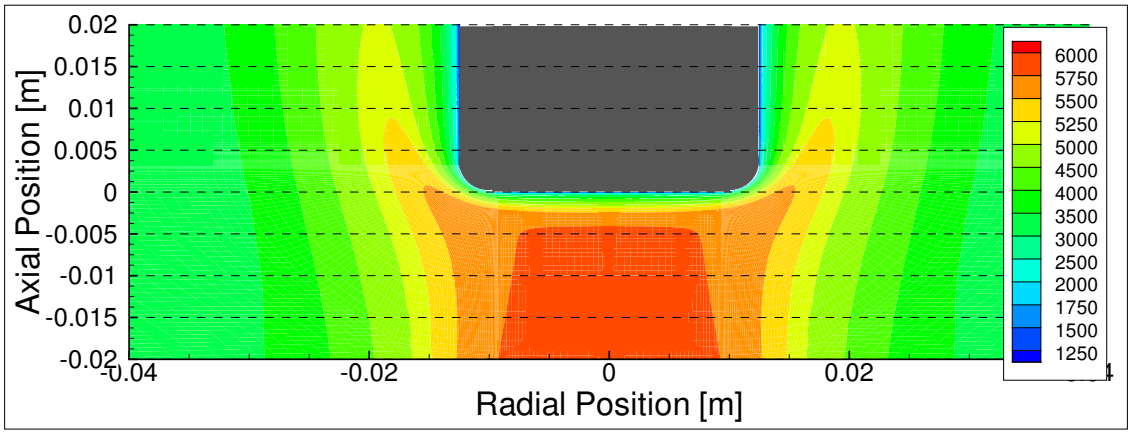

Figure 3.18: The temperature contour field over a non-catalytic material determined with the LeMANS software package [15].

high-resolution photo of graphite exposed to nitrogen. The approximate size of the emission focal volume at the centerline of the flow at two axial locations are indicated. For this discussion, these locations are subsequently referred to as the sample surface (y = 0-mm) and the boundary layer edge (y = 1.5-mm). The size of the boundary layer over graphite and quartz was determined previously and is discussed further in Section 4.4 [66], [64]. Additionally, note the violet glow around the perimeter of the sample, which is due to the strong CN violet system, generated via carbon nitridation at the surface.

Figure 3.20 shows spectra obtained from flow over quartz and within the free stream. In general, the two spectra are consistent. Within the N_2 2^{nd}-Positive and N_2^+ 1^{st}-Negative systems the spectral radiance is significantly higher at 337-nm and 391-nm at the boundary layer edge, which is due to a small population of silicon and oxygen in the flow created at the quartz surface (SiO_2). The impact of these species on the ensuing analysis is examined later. In the N_2 1^{st}-Positive system, there is strong overlap in the Δv = 4 and 5 transitions. In the Δv = 3, 2, and 1 transitions the spectrum at the boundary layer edge becomes progressively stronger.

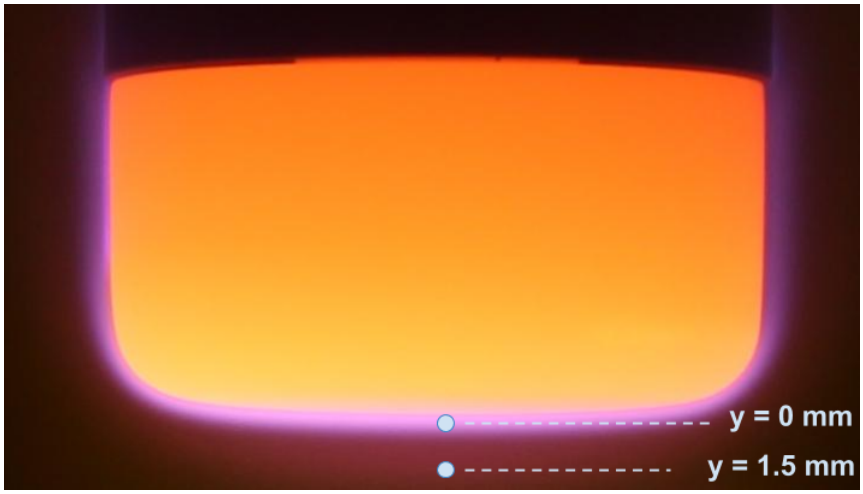

Figure 3.19: The boundary layer emission measurement locations with respect to the surface of graphite.

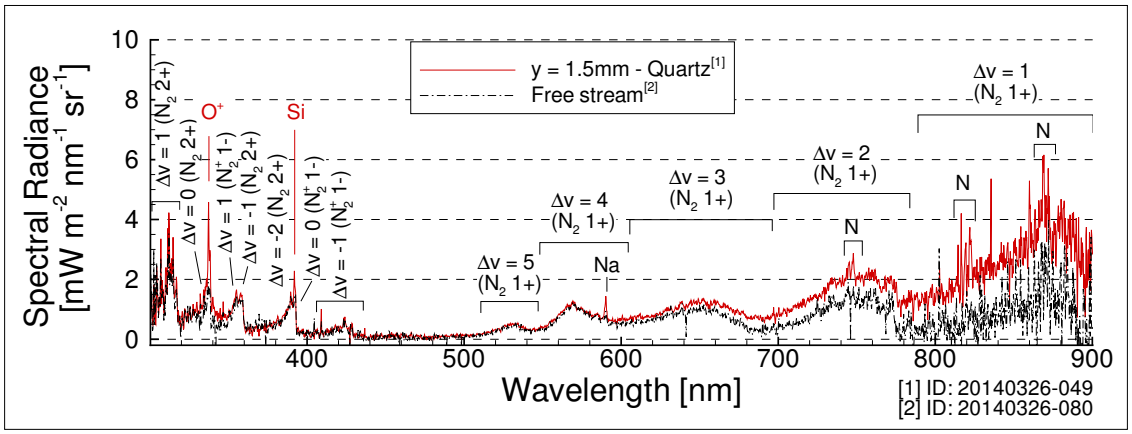

Figure 3.20: Spectra obtained from the centerline of the jet at the boundary layer edge over quartz and free stream.

This behavior indicates that the non-equilibrium conditions discussed previously are restricted to the centermost region of the jet. If non-equilibrium conditions existed throughout, then the intensity of the entire N_2 1^{st}-Positive system at the boundary layer edge would be greater. Therefore, one infers that the overpopulation of nitrogen atom determined in Section 3.6.2 in the free stream exists to the same degree at the boundary layer edge location. Several nitrogen atom lines become clearly visible with the sample present providing further indication that the flow structure has changed

with respect to the free stream. With the flattened temperature profile, there is a larger volume of emitters at elevated temperatures, including nitrogen atom.

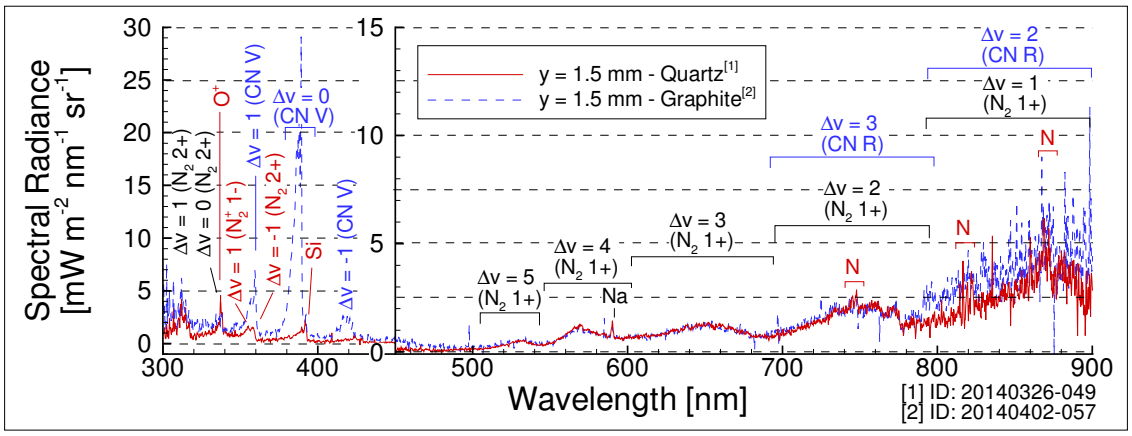

Figure 3.21: Emission at the boundary layer edge over quartz and graphite.

The spectra over graphite is inherently more complex due to the population of CN entering the boundary layer from the sample. The emission over quartz and graphite at the boundary layer edge is shown in Figure 3.21. Although the concentration of CN is several orders lower than N_2, the CN Violet system (CN V) dominates the ultraviolet. The few isolated N_2 2^{nd}-Positive and N_2^+ 1^{st}-Negative features are consistent over the two materials. Above 500-nm, there is notable overlap of the N_2 1^{st}-Positive system. The jagged features of the CN Red system (CN R) become increasingly more visible towards the infrared over graphite.

Note that the nitrogen atom signal is clearly distinguishable from the underlying N_2 1^{st}-Positive system over quartz, whereas over graphite the nitrogen atom signal is absent. This provides a preliminary glimpse into the flow behavior over the two materials. Although the conditions were identical between the two trials, a process unique to graphite is extracting nitrogen atom from the flow.

Emission measured at the surface and boundary layer edge locations over quartz is shown in Figure 3.22. The N_2 2^{nd}-Positive system is fairly consistent at the two

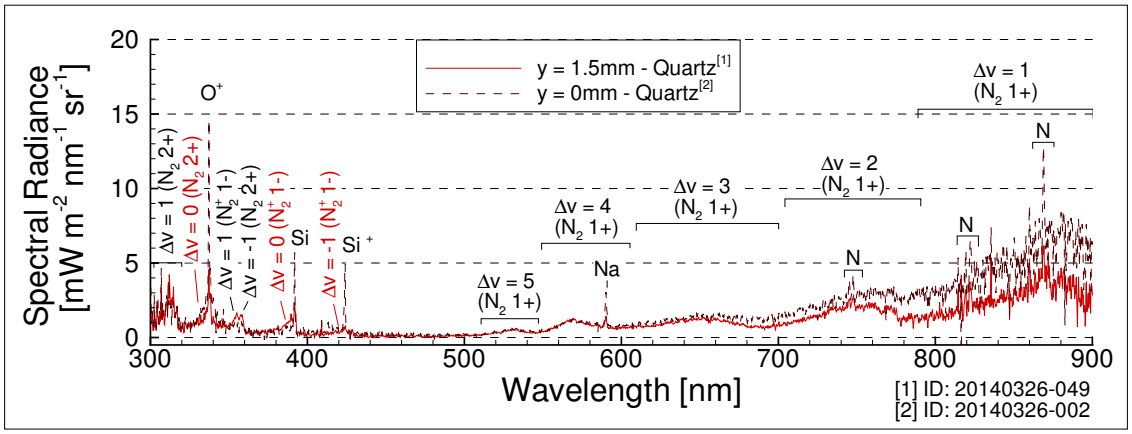

Figure 3.22: Emission spectra over quartz at the sample surface (y = 0-mm) and at the boundary layer edge (y = 1.5-mm).

locations. Moreover, the nitrogen atom signal detected at the boundary layer edge remains at the surface location as well, which further indicates that nitrogen atom is not actively extracted from the flow. The N_2 1st-Positive system intensity increases towards the sample, which is examined further in Section 3.7.2.

At lower wavelengths, lines corresponding to O^+, Si, and Si^+ appear prominently at the sample, which indicates that the flow causes the quartz (SiO_2) to break down and release a population of gas-phase chemical species into the boundary layer. These lines overlap the N_2 2nd-Positive $\Delta v = 0$ and N_2^+ 1st-Negative $\Delta v = 0, -1$ band heads. Referring back to Figure 3.20, it is evident that these species diffuse through the boundary layer due to their appearance at the boundary layer edge and absence from the free stream. Further evidence of the quartz material erosion is observed in the emission measurements below 300-nm. Although the spectrometer was not calibrated in this range, the raw intensity data clearly show additional Si lines at 252-nm, 288-nm and 298-nm, as shown in Figure 3.23. Note that each line is more intense at the sample than the boundary layer edge.

Two spectra from the boundary layer over graphite are shown in Figure 3.24. At

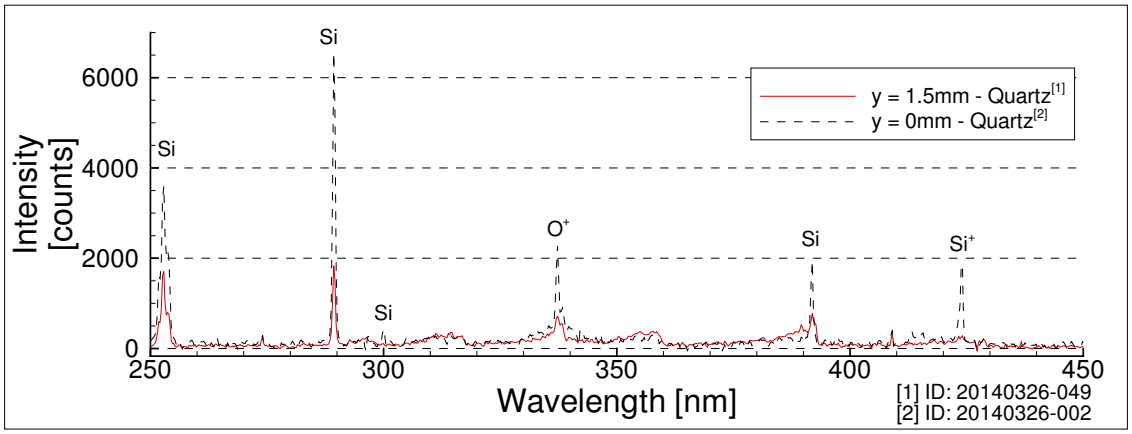

Figure 3.23: Uncalibrated emission spectra over quartz obtained directly off the surface ($y = 0$-mm) and at the boundary layer edge ($y = 1.5$-mm).

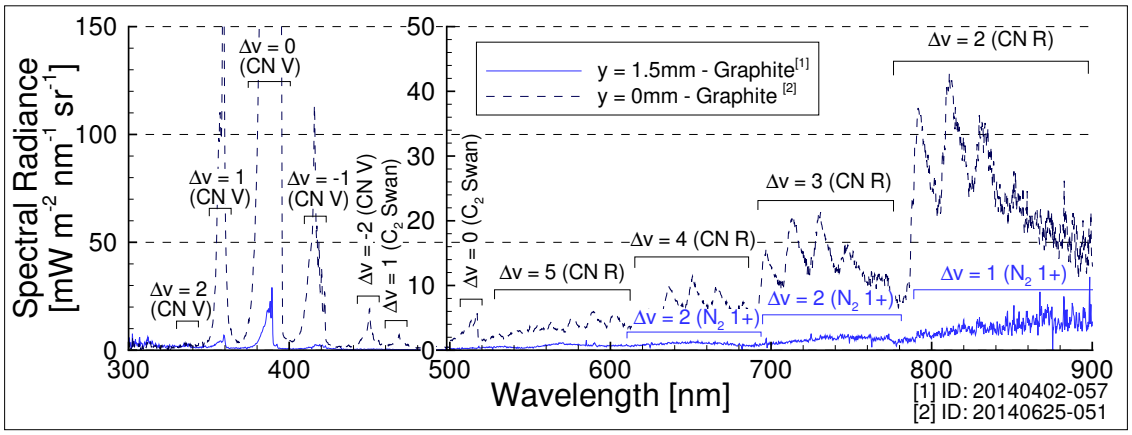

Figure 3.24: Emission spectrum over graphite at the sample surface ($y = 0$-mm) and at the boundary layer edge ($y = 1.5$-mm).

the sample surface the CN Violet and CN Red systems dominate the entire signal and it becomes difficult to determine the behavior of atomic and molecular nitrogen. Note the presence of the C_2 Swan system near 470-nm and 520-nm. The appearance of this species is likely due to spallation, which releases molecular carbon directly from the surface. Although C_2 may also be created through an exchange reaction with atomic carbon and CN, the raw emission signal obtained directly over graphite shows an absence of the strong carbon atom line at 248-nm, which is necessary for the reaction to proceed. Therefore, the presence of C_2 in the boundary layer is attributed to

spallation, which is believed to be a minor chemical process with respect to nitrogen recombination and carbon nitridation for the purpose of this investigation.

Supporting this assertion is that C_2 Swan was only observed directly against the sample surface. Subsequent measurements at y = 0.75-mm showed no C_2 signal, indicating very little upstream diffusion before being captured by the bulk flow. Secondly, the C_2 Swan feature at 516-nm is due to the (0,0) transition, with a spontaneous emission rate of $A_{0,0} = 7.19(10^6)$-s^{-1} and upper state energy of $9.19(10^3)$-eV. In comparison, the spontaneous emission rate of the main feature within the CN Violet Δv = -1 vibronic transition is more than half as slow ($A_{5,6} = 2.63(10^6)$-s^{-1}) while at a higher upper energy level (ϵ' = $37.0(10^3)$-eV). Despite this, the CN Violet feature is nearly 20 times stronger. Assuming that both features emit over the same focal volume, the CN feature is 50 times more prevalent within the flow than the lower lying C_2 feature, which is sufficient evidence for this investigation to consider spallation a minor process with respect to carbon nitridation and nitrogen recombination.

3.7 Abel Inversion

The Abel inversion is a mathematical transformation that converts line-of-sight emission measurements obtained along multiple chords within an axially-symmetric flow into a radial-distribution of emission. The axial-symmetry of the flow within the ICP chamber was addressed in Section 3.6.1. A top view illustration of the setup is shown in Figure 3.25. Here, the detector captures all emission along the principal focal axis. The measured radiance ($I(x)$) and the radially-distributed emission ($e(r)$) are labelled in the figure. Recall that Figure 3.13 showed the measured radiance for a feature within the N_2 2nd-Positive system. When the x-position is aligned with the center of the jet, the radiance is greatest because the jet core contains the highest

flow temperatures and the focal volume is maximum. Beyond the radius of the jet (R), the radiance is zero.

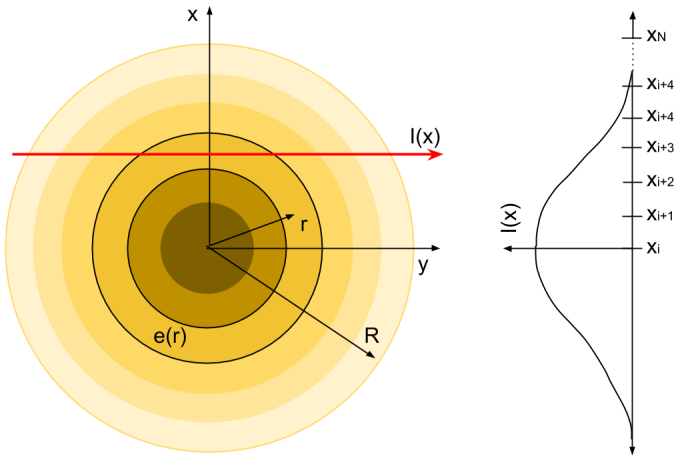

Figure 3.25: A top view of the axially-symmetric plasma. Emission measurements along plasma chords yield the total radiance within the focal volume ($I(x)$), which are converted to the radial distribution of emission ($e(r)$) via an Abel inversion.

The measured radiance and the radially-distributed emission are related via Equation 3.9.

$$I(x) = 2\int_r^R \frac{re(r)}{\sqrt{r^2 - x^2}}dr \tag{3.9}$$

In this experiment, the desired quantity is the radially-distributed emission and is determined by inverting Equation 3.9, which is termed the Abel inversion and is shown in Equation 3.10.

$$e(r) = -\frac{1}{\pi}\int_r^R \frac{dI/dx}{\sqrt{x^2 - r^2}}dx \tag{3.10}$$

A suitable curve fit of the measured radiance with respect to x is critical to properly evaluate Equation 3.10 since the radially-distributed emission is sensitive to the quality of the fit due to the derivative term in the integrand. There are several

suggested routines commonly employed. Gueron and Deutsch analyzed a cubic spline approach, which generates a large degree of control over the fit quality [68]. Kalal and Nugent expanded on the work of Tatekura by performing the Abel inversion via a fast Fourier transform [69], [70]. Playez used a rigorous, exponential series expansion that allowed him a high degree of control over very complex profiles [43].

This work used the polynomial expansion suggested by Laux owing to its simplicity and accuracy in fitting the experimental data [71]. Each profile was fitted with a polynomial of order 4 - 7 with a zero slope condition at the jet center to establish continuity. An advantage of the polynomial expansion is that Equation 3.10 reduced to the sum of a finite set of integrals, as shown in Equation 3.11.

$$e(r) = -\frac{1}{\pi}\int_r^R \frac{2a_n x}{\sqrt{x^2-r^2}}dx - \frac{1}{\pi}\int_r^R \frac{3a_{n+1}x^2}{\sqrt{x^2-r^2}}dx - \frac{1}{\pi}\int_r^R \frac{4a_{n+2}x^3}{\sqrt{x^2-r^2}}dx + ... \quad (3.11)$$

Each integral was calculated numerically with a MATLAB code that used the analytical expressions shown in Equation 3.12 [71]. A complete documentation of the Abel code is provided in Chapter H.

$$\begin{aligned} \int \tfrac{x^{2p}}{\sqrt{x^2-r^2}}dx &= \tfrac{(2p)!}{2^{2p}(p!)^2}[\sqrt{x^2-r^2}\sum_{k=1}^{p}\tfrac{k!(k-1)!}{(2k)!}r^{2(p-k)}(2x)^{2k-1} \\ &\quad + r^{2p}\ln(x-\sqrt{x^2-r^2})] \\ \int \tfrac{x^{2p+1}}{\sqrt{x^2-r^2}}dx &= \sqrt{x^2-r^2}\sum_{k=0}^{p}\tfrac{(2k)!(p!)^2}{(2p+1)!(k!)^2}(4r^2)^{p-k}x^{2k} \end{aligned} \quad (3.12)$$

Spontaneous emission is linearly related to the number density of species in the upper energy level ($n_{\epsilon'}$), the spontaneous emission rate ($A^{\epsilon'}_{\epsilon''}$), and the energy difference between the upper and lower states ($\epsilon' - \epsilon''$), as shown in Equation 3.13. The single and double primes represent values at the upper and lower energy level respectively. Additionally, the line shape function ($\Phi(\nu-\nu_0)$) describes the spectral broadening of a

given transition due to various mechanisms, such as instrumental, Doppler, collisional or natural broadening. Various broadening mechanisms are addressed in Section 3.7.1. One can determine the number density of emitters in the upper state at each radial location from the radially-distributed emission values determined through the Abel inversion using Equation 3.13.

$$e_i(\nu) = \frac{n_{\epsilon',i}}{4\pi} A^{\epsilon',i}_{\epsilon'',i}(\epsilon' - \epsilon'')\Phi(\nu - \nu_0) \tag{3.13}$$

Additionally, one can determine the radial temperature and species concentration profile from the radially-distributed emission if the flow is sufficiently near LTE. In this campaign, atomic nitrogen, molecular nitrogen, and molecular nitrogen ion features were all used to determine radial temperature profiles. Section 3.6.2 addressed the modest degree of non-LTE behavior present in the free stream and concluded that the overpopulation of nitrogen atom was $\rho_N = 2.22 \pm 0.25$. Moreover, Section 3.6.3 revealed that this value exists to the same degree at the boundary layer edge over quartz as well. The determination of the radial temperature profile utilizes the Boltzmann distribution, which expresses how particles within a system at LTE are partitioned amongst all possible energy levels at a given temperature. Although the observed flow exhibited non-LTE behavior, it is not precluded from a Boltzmann analysis because the deviation from LTE is moderate and well-characterized. Note that the succeeding analysis assumes that aside from the overpopulation of ground state nitrogen atom and the few vibrational levels within the N_2 B-state, which were all well-quantified in Section 3.6.2, each remaining energy level is assumed to be in Boltzmann equilibrium.

The Boltzmann distribution is shown in Equation 3.14. It states that the fraction of particles of species i in a given energy level ($\frac{n_{\epsilon,i}}{n_{tot,i}}$) is a function of the energy of the

level (ϵ), the temperature (T), the partition function (Q), and the degeneracy (g_ϵ), which accounts for the number of independent configurations that yield the energy in the level. Additionally, the partition function is a degeneracy-weighted sum of the distribution across all energy levels at a particular temperature.

$$\frac{n_{\epsilon,i}}{n_{tot,i}} = \frac{g_\epsilon e^{-\epsilon/k_B T}}{\sum_k g_k e^{-\epsilon_k/k_B T}} = \frac{g_\epsilon e^{-\epsilon/k_B T}}{Q_{tot}} \tag{3.14}$$

In atomic species, the energies are partitioned amongst discrete electronic energy levels. For molecules, nuclear motion creates partitioning across vibrational and rotational modes in addition to electronic energy levels. In any arbitrarily chosen level, the total energy (ϵ) is the sum of the state's vibrational ($G(v)$), rotational ($F(J)$) and electronic energy (T_e). This summation allows the denominator to separate into individual partition functions for vibrational, rotational, and electronic modes, as expressed in Equation 3.15.

$$\frac{n_{\epsilon,i}}{n_{tot,i}} = \frac{g_\epsilon e^{-\epsilon/k_B T}}{Q_{tot}} = \underbrace{\frac{g_\epsilon e^{-\epsilon/k_B T}}{Q_{el}}}_{\text{atoms}} = \underbrace{\frac{g_\epsilon e^{-\epsilon/k_B T}}{Q_{vib} Q_{rot} Q_{el}}}_{\text{molecules}} \tag{3.15}$$

For LTE flow, the number of emitters in any energy state (n_i) relates to the ground state ($n_{0,i}$) population, as shown in Equation 3.16.

$$n_{\epsilon',i} = \underbrace{n_{0,i} \frac{g_{\epsilon'}}{g_0} e^{-\epsilon'/k_B T}}_{\text{atoms}} = \underbrace{n_{0,i} \frac{g_{\epsilon'} e^{-\epsilon'/k_B T}}{g_0 e^{-G(0)/k_B T}}}_{\text{molecules}} \tag{3.16}$$

For atomic nitrogen, the ground state population is known from the overpopulation value determined in Section 3.6.2. However, for other species, the ground state population is not known *a priori* and remains to be determined. For these species, the number of particles in the ground state is shown in Equation 3.17. Notice that the

expression for molecules involves an exponential function, which is due to the nature of the discretization of vibrational quantum states. In atoms, there is no vibrational motion and the ground state has zero energy.

$$n_{0,i} = \underbrace{n_{tot,i}\frac{g_0}{Q_{el}}}_{\text{atoms}} = \underbrace{n_{tot,i}\frac{g_0 e^{-G(0)/k_B T}}{Q_{vib}Q_{rot}Q_{el}}}_{\text{molecules}} \tag{3.17}$$

Equation 3.17 explicitly includes the total number density of the particular species considered, which is provided by the ideal gas equation of state, as shown in Equation 3.18.

$$n_{tot,i} = \frac{p}{k_B T}\chi(T) \tag{3.18}$$

Combining Equations 3.16, 3.17 and 3.18 yields the final relation between the upper state number density to the equilibrium temperature, shown in Equation 3.19. Here, the upper state number density is determined experimentally with Equation 3.13. Thus, the temperature is the remaining unknown quantity, which is determined through an iterative computation using the MATLAB code shown in Appendix H.

$$n_{\epsilon',i} = \underbrace{\frac{p}{k_B T}\chi(T)\frac{g_{\epsilon'}e^{-\epsilon'/k_B T}}{Q_{el}(T)}}_{\text{atoms}} = \underbrace{\frac{p}{k_B T}\chi(T)\frac{g_{\epsilon'}e^{-\epsilon'/k_B T}}{Q_{vib}(T)Q_{rot}(T)Q_{el}(T)}}_{\text{molecules}} \tag{3.19}$$

Among the variables in Equation 3.19 is the molar fraction of the species, which was calculated for the non-LTE mixture in Section 3.6.2. In comparison, the composition of a five-species nitrogen mixture (N_2, N, N_2^+, $N+$ and $e-$) in LTE is shown in Figure 3.26. Considering the limited temperature range observed in this portion of the investigation (T = 4500 - 6000-K), there is very little change in the molecular nitrogen and atomic nitrogen curves. Further, the molar fraction of molecular

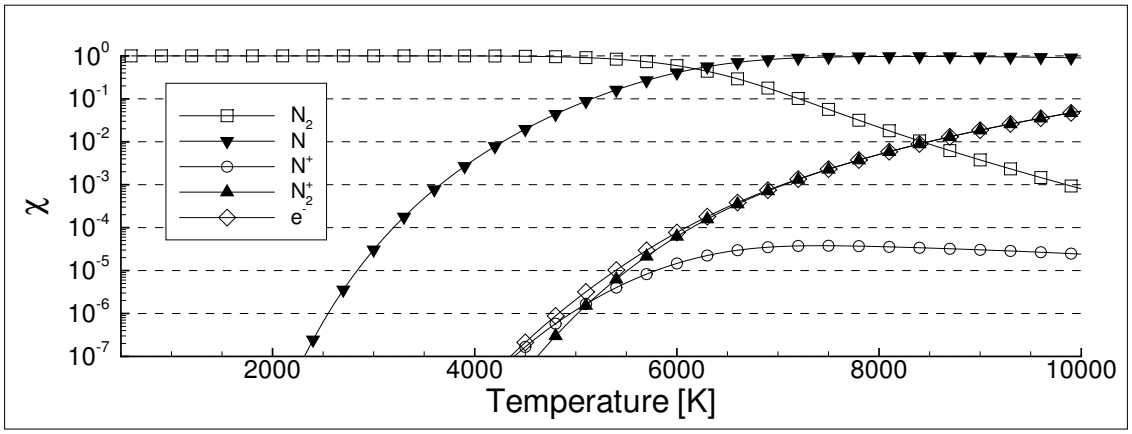

Figure 3.26: Equilibrium composition of 5-species nitrogen.

nitrogen ion does increase several orders over this range. Recognizing these behaviors, the molar fraction of atomic and molecular nitrogen were permanently set at the non-LTE values, while the molecular nitrogen ion molar fraction was fitted with a 10-order polynomial spline. The iterative convergence onto a single temperature is driven by the exponential terms in Equation 3.19 and setting a constant molar fraction for atomic and molecular nitrogen had no observable impact on the resulting temperature.

The partition functions are species and temperature dependent quantities fundamentally related to the quantum mechanical structure of the particle. The general form of the electronic partition function is shown in Equation 3.20. Generally, the electronic partition function can be truncated after a few terms because the electronic temperatures (θ_i) at each subsequent level quickly become much greater than any relevant temperature value considered in this investigation.

$$\begin{gathered} Q_{el} = g_0 + g_{\epsilon_1} e^{-\theta_{\epsilon_1}/T} + g_{\epsilon_2} e^{-\theta_{\epsilon_2}/T} + ... \\ \text{where: } \theta_{\epsilon_i} = \epsilon_i / k_B \end{gathered} \tag{3.20}$$

The solution to the Schrödinger equation for a harmonic oscillator potential yields

discretized energy levels separated by $h\nu$, where h is the Planck's constant and ν is the harmonic frequency of the system. Note that the degeneracy of each vibrational mode is unity. Recognizing the geometric series, the partition function can be considered continuous, as shown in Equation 3.21.

$$Q_{vib} = \sum_{i=0}^{\infty} e^{-i\theta_{vib}/T} = \frac{1}{1-e^{-\theta_{vib}/T}} \quad \text{where: } \theta_{vib} = h\nu/k_B \tag{3.21}$$

Solving the Schrödinger equation for a rigid-rotor potential yields the rotational partition function. The energy of a given level is shown in Equation 3.22, where the moment of inertia (I) is determined from the mass of the nuclei and the internuclear distance.

$$\epsilon_J = \frac{h^2}{8\pi^2 I} J(J+1) \tag{3.22}$$

The solution to the rotational partition function involves integrating over all J values. Adjacent rotational levels are separated by an order of 1-cm^{-1}, whereas vibrational levels are three orders higher, which justifies considering rotational lines to be nearly continuous. The rotational partition function is shown in Equation 3.23 for homonuclear ($\sigma = 2$) and heteronuclear ($\sigma = 1$) diatomic molecules.

$$Q_{rot} = \sum_{J=0}^{\infty} (2J+1) e^{-J(J+1)\theta_{rot}/T} = \int_0^{\infty} (2J+1) e^{-J(J+1)\theta_{rot}/T} dl = \frac{T}{\sigma\theta_{rot}} \quad \text{where: } \theta_{rot} = h^2/8\pi^2 I k_B \tag{3.23}$$

One calculates the total energy in any state with the Dunham series expansion shown in Equation 3.24, which is a function of experimentally-determined spectroscopic constants and the electronic, vibrational and rotational quantum numbers

Table 3.5: Partition Functions

Species	Q_{el}	Q_{rot}	Q_{vib}
N_2	$1 + O(e^{-100{,}000/T})$	$\frac{T}{(2)(2.9)}$	$\frac{1}{1-e^{-3390/T}}$
N_2^+	$2 + O(e^{-131{,}924/T})$	$\frac{T}{(2)(2.78)}$	$\frac{1}{1-e^{-3165/T}}$
N	$4 + O(e^{-28{,}000/T})$	-	-

[72]. The spectroscopic constants are fundamentally linked to the solution of the Schrödinger Equation for the rigid-rotor and spring-mass potentials, with additional considerations for anharmonicity effects.

$$\begin{gathered}
\epsilon_{e,v,J} = T_e + G(v) + F(J) \\
G(v) = \omega_e(v+\tfrac{1}{2}) - \omega_e x_e(v+\tfrac{1}{2})^2 + \omega_e y_e(v+\tfrac{1}{2})^3 + \omega_e z_e(v+\tfrac{1}{2})^4 + ... \\
F(J) = B_v J(J+1) - D_v J^2(J+1)^2 + H_v J^3(J+1)^3 ... \\
B_v = B_e - \alpha_e(v+\tfrac{1}{2}) + \gamma_e(v+\tfrac{1}{2})^2 + ... \\
D_v = D_e - \beta_e(v+\tfrac{1}{2}) + ...
\end{gathered} \tag{3.24}$$

3.7.1 Line Broadening Mechanisms

In an idealized system, radiated emission generated from a transition between two discrete energy levels would appear as Dirac lines. However, various broadening mechanisms are present in real systems, which cause the observed emission to spread over a spectral range. The line shape function ($\Phi(\nu - \nu_0)$), introduced in Equation 3.13 is a normalized, spectrally-dependent function that accounts for the various

broadening processes present within the system. Among the various mechanisms are Doppler broadening, instrumental broadening, natural broadening, and collisional broadening. Depending on the thermodynamic state of the system, each one may impact the total spectral width observed in a particular transition.

Doppler Broadening

Aside from the bulk convective velocity of the flow, particles are in constant thermal motion due to the thermodynamic state of the plasma. Owing to the large particle concentrations that exist even at the sub-atmospheric test pressure conditions ($n \approx 5(10^{18})$-cm^{-3}) it is not feasible to consider tracking the velocity of every individual particle within the system over time. Rather, the Maxwell velocity distribution function, shown in Equation 3.25 describes the distribution of all particle velocities within a gas at thermal equilibrium in a probabilistic manner [73].

$$f(v_1, v_2, v_3) = \left(\frac{m}{2\pi k_B T}\right)^{1/2} e^{-(\frac{m}{2k_B T})(v_1^2+v_2^2+v_3^2)} \tag{3.25}$$

Equation 3.25 is a normalized function and obeys the expressions shown in Equation 3.26. Specifically, integrating the product of the number of particles with a particular velocity over all possible velocities yields the total number of particles in the system.

$$\begin{aligned} 1 &= \int_{-\infty}^{\infty} f(v_1, v_2, v_3) dv \\ N &= \int_{-\infty}^{\infty} N f(v_1, v_2, v_3) dv \end{aligned} \tag{3.26}$$

The thermally-driven motion of the particles results in Doppler broadening. When a particle transitions from a higher to lower energy level, it emits a photon with the same energy as the difference between the two levels and is detected by the

spectrometer. Equivalently, the duality property of light allows one to consider the emitted photon as a traveling wave. The observed frequency of this wave changes depending on the relative velocity between the emitter and the observer, which may result in a blue or red shift of the emitted frequency, as expressed in Equation 3.27. Here, v_1 was arbitrarily chosen to represent velocity along the principle focal axis. Equation 3.27 states that particles traveling towards the observer emit light at a higher frequency than particles with no component of velocity along the observation axis (blue shift). Moreover, particles traveling away from the observer emit at longer wavelengths (red shift).

$$\nu = \nu_o(1 + \frac{v_1}{c}) \tag{3.27}$$

Ultimately, the full width half max (FWHM) of the Doppler broadened signal is desired. Thus, the Maxwell velocity distribution function, which describes the distribution of particle velocities at a given temperature, is transformed into frequency space, as shown in Equation 3.28.

$$f_\nu d\nu = f\frac{dv_1}{d\nu}d\nu = \sqrt{\frac{c^2 m}{2\pi\nu_o^2 k_B T}} e^{-(\frac{c^2 m}{2k_B T})\frac{(\nu-\nu_o)^2}{\nu_o^2}} d\nu \tag{3.28}$$

Note that the shape of the frequency distribution function is Gaussian, from which one can extract the FWHM directly, as shown in Equation 3.29 [74].

$$\Delta\nu_D = \nu_o\sqrt{\frac{8\ln(2)k_B T}{mc^2}} \tag{3.29}$$

Equation 3.30 shows the Doppler broadening in terms of wavelength. Recall that the Maxwell distribution function is driven by the temperature of the particles. Hence, the Doppler broadening is fundamentally related to the thermal motion of the particles

as well. As the temperature of the gas increases, the total internal energy and the velocity of the particles increase, which broadens the Doppler width (λ_D).

$$\Delta\lambda_D = \lambda_0\sqrt{\frac{8\ln(2)k_BT}{mc^2}} = 2.916(10^{-20})\lambda_0\sqrt{\frac{T}{m}} \tag{3.30}$$

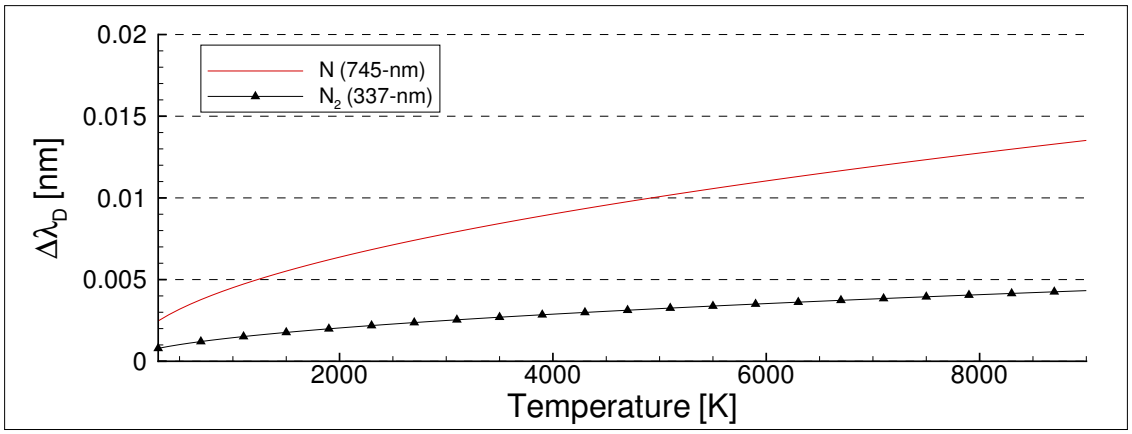

Figure 3.27: The Doppler FWHM for the atomic nitrogen transition at 745-nm and molecular nitrogen transition at 337-nm over relevant temperatures.

The Doppler width is plotted in Figure 3.27 for the nitrogen atom electronic transition at 745-nm and the N_2 ro-vibronic transition at 337-nm. The thermodynamic conditions and the species considered yield Doppler widths on the order of 10^{-3}-nm to 10^{-2}-nm.

Instrumental Broadening

Instrumental broadening is a commonly observed process caused by the interaction of the emitted light and the detector. It is fundamentally related to the spectrometer's entrance width, grating, and size of the CCD array. One can determine the degree of instrumental broadening with a monochromatic light source with a bandwidth smaller than the instrumental broadening width. In this campaign, a He-Ne laser provided a fixed output centered at 632.8-nm and a narrow bandwidth on the order

of 1.9(10^{-3})-nm. The laser bandwidth is primarily due to Doppler broadening within the gaseous lasing medium [75].

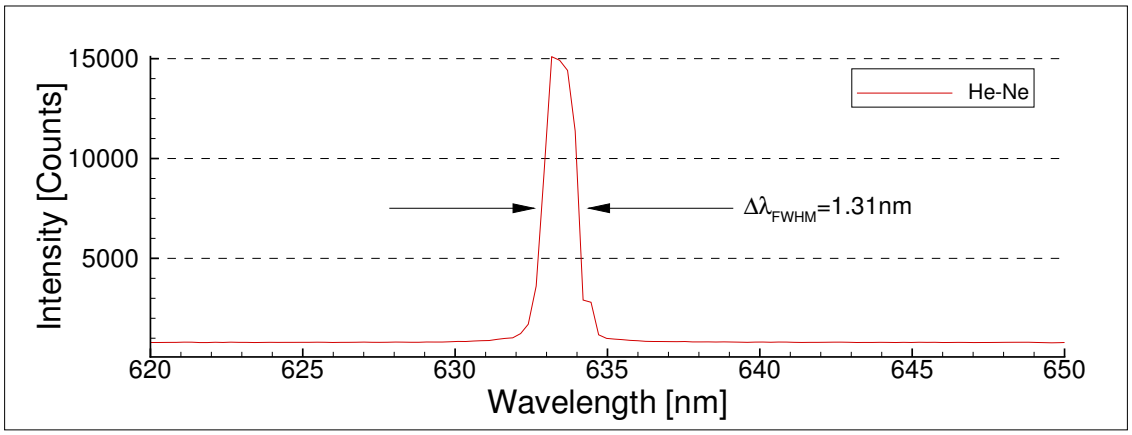

Figure 3.28: Emission from He-Ne laser centered at 632.8 nm. The spectral resolution of the emission spectrometer is 1.31-nm, measured from the FWHW.

The output of the He-Ne laser was directed into the spectrometer through the fiber optic cable. Figure 3.28 shows the emission obtained from this setup. The fundamental output from the laser is clearly visible at 632.8-nm. Additionally, the FWHM of this feature is 1.31-nm, which was determined from a Gaussian fit. Note that this is well above the bandwidth of the laser output and several orders higher than the Doppler broadening FWHM present at the flow conditions.

Natural Broadening

The Heisenberg uncertainty principle states that any pair of observable quantities whose operators do not commute cannot be known to arbitrarily-chosen uncertainties [76]. This directly impacts the nature of emission spectroscopy, which measures the emitted radiation between two energy levels at a fixed time. According to the energy-time uncertainty principle, the energy difference between the upper and lower state cannot be known with zero uncertainty for a measurement at a discrete time. This

uncertainty in the two states leads to a broadening of the spectral line, which is termed natural broadening. Natural broadening results in the profile shown in Equation 3.31 [71]. Using the nitrogen atom transition at 745-nm and the constants provided by Wiese, the natural broadening is $\Delta\lambda_{natural} = 8.42(10^{-5})$-nm [5]. Clearly, natural broadening plays a minor role with respect to Doppler and instrumental broadening.

$$\Delta\lambda_{natural} = \lambda_{ul}^2 \frac{1}{4\pi c} \left(\sum_{n<u} A_{un} + \sum_{m<l} A_{lm} \right) \tag{3.31}$$

Collisional broadening

Collisional broadening or pressure broadening is fundamentally related to natural broadening. When two particles collide during emission, it inherently shortens the characteristic timescale of the transition. Shortening the process time increases the uncertainty in the change of energy during the transition, causing a spectral distribution of intensities from the centerline wavelength. Collisional broadening mechanisms are less dominant in low pressure flows, where the particle collision rate is significantly reduced and is not considered in this investigation. Neglecting the collisional broadening processing is further supported by the reasoning discussed in Section 4.2.

3.7.2 Radial Profiles

The first step in determining the radial distribution of temperature and species concentrations using the technique outlined in Section 3.7 is to locate distinct spectral features that are close to the FWHM of the instrumental broadening ($\Delta\lambda_{instr.} =$ 1.31-nm) and are sufficiently spectrally isolated. Oftentimes it is difficult to find satisfactory molecular transitions because a given electronic transition can span a large spectral range due to the number of possible vibrational transitions, which individu-

ally contain many rotational transitions. In the N_2 1^{st}-Positive and CN Red system, a particular vibronic transition may span over 10-nm, making these features unfit for this technique. However, in the N_2 2^{nd}-Positive and N_2^+ 1^{st}-Negative, several usable features exist. The transitions considered in this investigation are shown in Table 3.6.

Table 3.6: Molecular Transitions for Abel Inversion

Species	(v',v")	λ_0 [nm]	$\Delta\lambda$ [nm]	$A^{T'v'}_{T''v''}\cdot\ 10^{-7}$ [s^{-1}]	ϵ'$\cdot 10^{18}$ [J]	ϵ"$\cdot 10^{18}$ [J]	g_u
N_2 2^{nd}-Positive	(0,0)	337.0	3.3	1.337	1.771	1.184	6
N_2^+ 1^{st}-Negative	(1,1)	388.2	4.2	0.4257	0.5768	0.06503	2
N_2^+ 1^{st}-Negative	(0,0)	391.1	4.3	1.214	0.5297	0.02184	2
N_2^+ 1^{st}-Negative	(2,3)	419.6	4.9	0.3690	0.6229	0.1495	2
N_2^+ 1^{st}-Negative	(1,2)	423.4	5.1	0.4522	0.5767	0.1076	2

The typical separation between adjacent ro-vibronic transitions in the N_2 2^{nd}-Positive and N_2^+ 1^{st}-Negative systems are on the order to 10^{-2}-nm, which are well below the resolution of the spectrometer. Thus, it is impractical to consider individual ro-vibronic transitions with the current instrumentation. Therefore, this investigation applies the Abel inversion technique described in Section 3.7 to the entire molecular vibronic systems listed in Table 3.6, which subsequently contain all rotational transitions. This approach is supported by considering Equation 3.13, which relates the total number of emitters in an upper energy level to the total measured emission. Recall that the line shape function accounts for all line broadening mechanisms present in the system. In addition to the dominant instrumental broadening, the various rotational transitions act as an additional process that spreads out measured emission about the central wavelength for a particular vibronic transition. Table 3.6 lists the spread from rotational transitions for each vibronic transition considered.

Using the rigorous expression provided by Gomes et al. in Equation 3.32, one can

separate the rotational transitions explicitly from the vibrational and electronic terms [77].

$$e_i(\nu) = \frac{n_{T'v'J'}}{4\pi} A^{T'v'J'}_{T''v''J''}(\epsilon' - \epsilon'')\Phi(\nu - \nu_0) \tag{3.32}$$

Here, the spontaneous emission rate is considered as the product between the vibronic transition rate and rotational transition rate, as shown in Equation 3.33.

$$A^{T'v'J'}_{T''v''J''} = A^{T'v'}_{T''v''} A^{J'}_{J''} \tag{3.33}$$

The first term on the right hand side is a function of the electronic and vibrational transitions only and the analytical expression for this term is shown in Equation 3.34. Among the quantities are the electronic transition strength $|R_e(\bar{r}_{v'v''})|$ and the Franck-Condon factor $q_{v'v''}$, which are provided by Laux and Playez for the transitions considered in this investigation [71], [43].

$$A^{T'v'}_{T''v''} = \frac{64\pi^4\nu^3}{3hc^3}|R_e(\bar{r}_{v'v''})|^2 q_{v'v''} \tag{3.34}$$

The second term in Equation 3.33 is the spontaneous emission rate for the rotational transition and its expression is shown in Equation 3.35. Here, the Hönl-London factor ($S^{J'}_{J''}$) is a normalized quantity representing the rotational line strength.

$$A^{J'}_{J''} = \frac{S^{J'}_{J''}}{(2J'+1)(2S+1)(2-\delta_{0,\Lambda'})} \tag{3.35}$$

The sum of the rotational line strengths for a given upper state is shown in Equation 3.36.

$$\sum_{J''} S_{J''}^{J'}(J'') = (2J'+1)(2S+1)(2-\delta_{0,\Lambda'}) \tag{3.36}$$

Therefore, the total emission over an entire vibronic transition is the summation off all allowable rotational transitions, which yields a spontaneous emission rate for rotation of unity ($A_{J''}^{J'} = 1$). Ultimately, Equation 3.32 reduces to Equation 3.37.

$$e_i(\nu) = \frac{n_{T'v'}}{4\pi} A_{T''v''}^{T'v'}(\epsilon' - \epsilon'')\Phi(\nu - \nu_0) \tag{3.37}$$

Radial Temperature Distribution

Provided that the entire vibronic transition is sufficiently well-isolated from other spectral features, the Abel inversion technique outlined in Section 3.7 can determine the radial temperature and species concentration distributions. Several free stream temperature distributions are shown in Figure 3.29, which were determined from the set of molecular nitrogen and nitrogen ion transitions listed in Table 3.6. Each trend yields a maximum temperature at the jet center, which decreases radially. The highest measured temperature is from the N_2 (0,0) feature at 337-nm, which produced a centerline temperature of 5939-K. At the 10-mm radial location the temperature drops to 5383-K. The lowest measured temperature corresponded to the N_2^+ (1,2) feature at 423-nm, which produced a centerline temperature of 5285-K, which subsequently decreased to 4899-K at 10-mm from the centerline.

Further examination of the temperature profiles and the figures listed in Table 3.6 shows that a slight correlation exists between the width of a particular spectral feature and the measured temperature. The highest measured temperature corresponds to the N_2 (0,0) transition, which has the narrowest width of all the features considered ($\Delta\lambda$ = 3.3-nm). Moreover, the three lowest temperature trends correspond to the

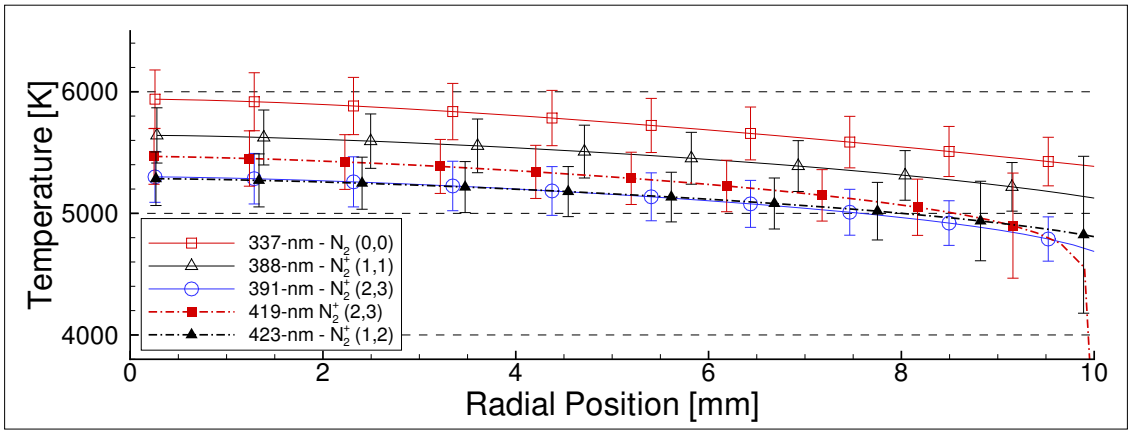

Figure 3.29: Radial temperature distribution in the free stream.

three broadest transitions ($\Delta\lambda$ = 4.3-nm, $\Delta\lambda$ = 4.9-nm, $\Delta\lambda$ = 5.1-nm). Ideally, if the transition were well isolated from other spectral features and the width were less than the instrumental broadening, then one would be able to capture the entire feature with high certainty. In this case, each of the transition widths were greater than the instrumental broadening, which increased the uncertainty of capturing the entire vibronic signal. Moreover, each transition considered was inherently a part of a larger vibrational band head and competing mechanisms became an issue when determining the appropriate spectral width over which to calculate the radiance. The combination of these factors ultimately yielded lower measured temperatures for the broader features considered.

Determining the radial temperature distribution at the boundary layer edge over quartz is complicated by the atomic and ionic species overlapping the N_2 (0,0), and N_2^+ (0,0) and (2,3) transitions. The presence of these features make it impossible to distinguish the competing processes. Fortunately, several nitrogen lines are visible at the boundary layer edge. Among these is the nitrogen atom triplet near 745-nm, which are sufficiently isolated, as shown in Table 3.7.

Figure 3.20 shows that the nitrogen lines clearly overlap the Δv = 2 band head

Table 3.7: Nitrogen Atom Transitions [5]

Species	λ_0 [nm]	$A^{\epsilon'}_{\epsilon''} \cdot 10^{-7}$ [s^{-1}]	ϵ'$\cdot 10^{18}$ [J]	ϵ"$\cdot 10^{18}$ [J]	g_u	Accuracy
N	742.4	0.52	1.922	1.654	4	25%
N	744.2	1.06	1.922	1.655	4	25%
N	746.8	1.61	1.922	1.656	4	25%

of the N_2 1^{st}-Positive system. Therefore, in order to obtain a temperature from the nitrogen atom feature, one must first decouple the two signals. As a first approximation, the signal attributable to the nitrogen atom emission was determined by subtracting out the rectangular area located below the base of the atomic feature, as illustrated in Figure 3.30. The remaining signal was attributed to nitrogen atom.

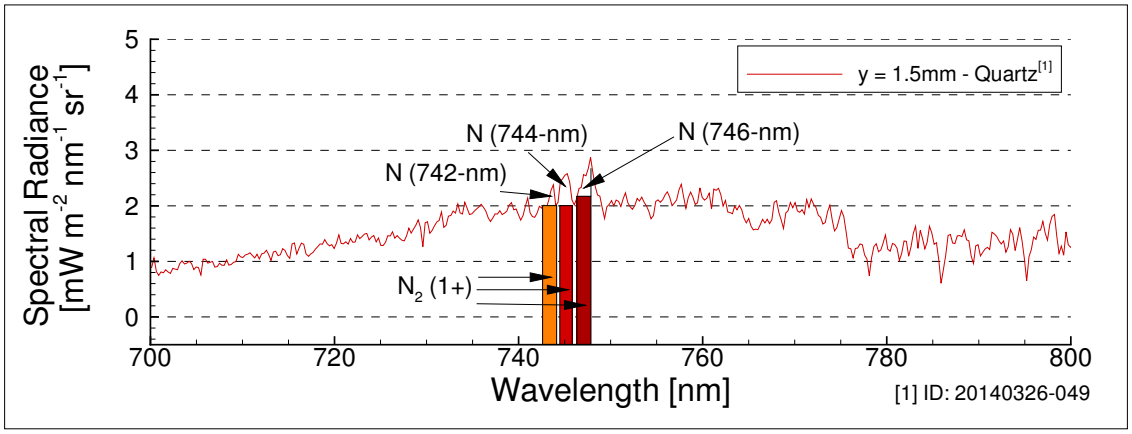

Figure 3.30: First order decoupling of nitrogen atom and N_2 1^{st}-Positive system.

Recognize from Table 3.7 that these features originate from the same upper level and do not allow for independent temperature measurements. The radial temperature determined from the collection of these three features are shown in Figure 3.31. Here, the centerline temperature of about 5000-K decreases radially. At 10-mm from the centerline, the temperature is $\approx$ 4800-K. With respect to the free stream conditions shown in Figure 3.29, the temperature decreases more gradually at the boundary

layer edge location, which confirms the more uniform flow conditions with the sample present.

In a prior study, Meyers measured the nitrogen atom temperature through the boundary layer over a water-cooled quartz sample using a two-photon absorption LIF approach [64]. At a distance of 1.5-mm from the surface, he obtained a temperature of 5250±250-K, which is 4.7% greater than the value determined by the Abel inversion.

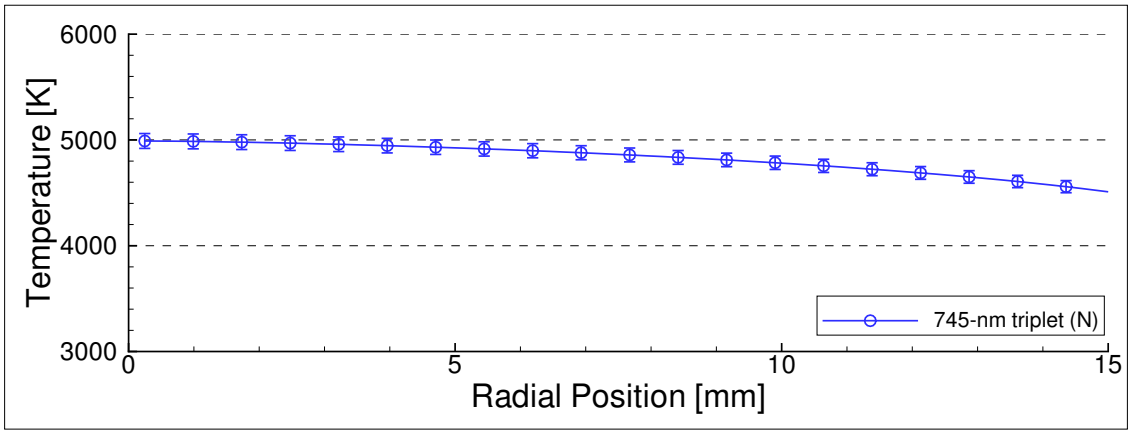

Figure 3.31: Radial temperature distribution at the boundary layer edge over quartz.

Radially-Distributed Emission

Assuming that graphite is highly-catalytic and actively promotes a larger degree of nitrogen recombination on the surface relative to quartz, one should expect to see more molecular nitrogen emission over graphite. Unfortunately, near wall values of the molecular nitrogen population on graphite are not directly available. Recall Figure 3.24, which compares the spectra obtained at the surface of graphite and the boundary layer edge. Notice that the N_2 1^{st}-Positive system competes with the strong CN Red system throughout much of the visible and near infrared portion of the spectrum. These two systems could not be separated from one another and this data set proved inadequate for the ensuing analysis. Therefore, a new set of radial

scans were performed at Δy = 1-mm and Δy = 2-mm over quartz and graphite. Additionally, the integration time was reduced from 20-seconds to 5-seconds, which allowed for more measurements with little sacrifice in the S/N.

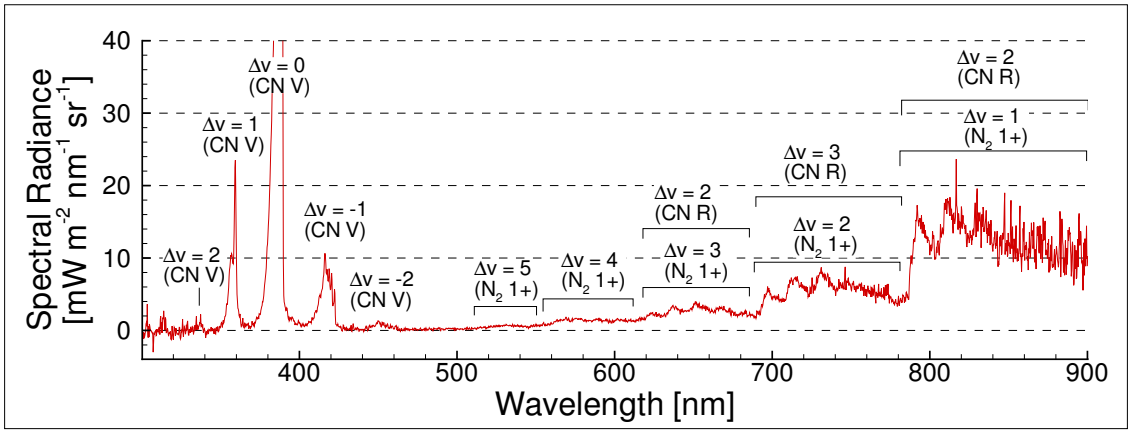

Figure 3.32: Emission spectra over graphite along the centerline, 1-mm from the surface.

Figure 3.32 shows the centerline scan acquired at Δy = 1-mm over graphite. Notice that the sharp features within the CN Red system are evident above 620-nm. However, these features quickly decrease in intensity and the Δv = 4 and Δv = 5 transitions within the 1st-Positive system are devoid of CN. Therefore, Δy = 1-mm represented the nearest location to the wall where the N_2 1st-Positive was distinguishable from the CN Red. Again, measurements were performed in 1-mm increments from the centerline to the edge of the jet. Additionally, the Abel inversion considered the total radiance emitted from the N_2 1st-Positive Δv = 5 transition. Recognize that the radially-distributed spectral radiance yielded by the Abel inversion technique is directly proportional to the number density of all upper state emitters at each radial location, as expressed in Equation 3.38.

$$n_{T'v'J'}(r) \propto e_i(r) \tag{3.38}$$

Figure 3.33 shows the radially-distributed spectral radiance acquired over graphite and quartz samples. In all locations, the intensity is greatest at the centerline location, and decreases towards the boundary layer edge. Note that the trend lines for $\Delta y =$ 2-mm are identical for the two materials, which indicates that the molecular nitrogen population is identical beyond the boundary layer edge location. Also, the highest total spectral radiance occurs at $\Delta y =$ 1-mm over graphite among the four trends, which indicates that the molecular nitrogen population increases faster over graphite with respect to quartz. Moreover, the elevated nitrogen molecule signal is restricted to the central region of the flow, which further supports the assertion that graphite behaves as a third-body, which actively promotes recombination. The exchange reaction introduced in Equation 1.5 may contribute to the increased molecular nitrogen population over graphite as well. However, owing to the absence of any carbon atom emission over graphite, the impact of this reaction is negligible. Beyond 10-mm from the centerline, all of the trends overlap, independent of the sample material.

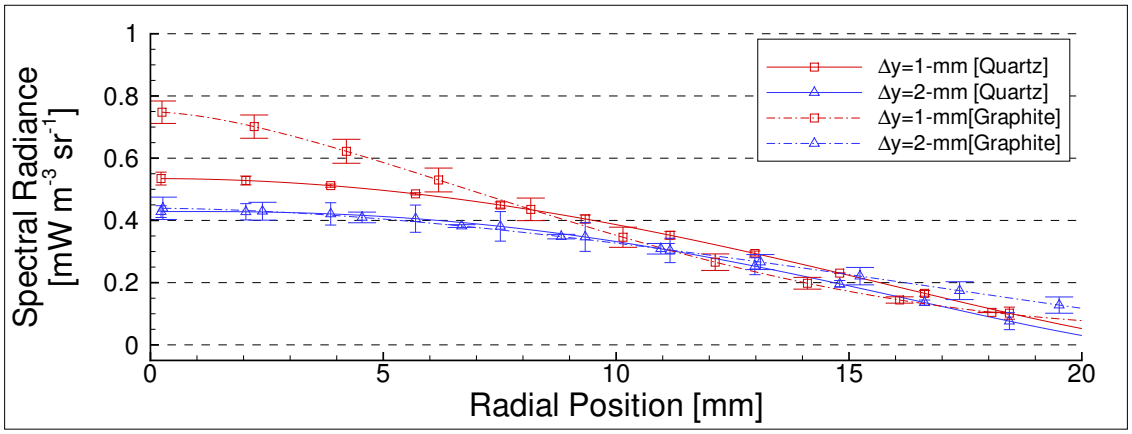

Figure 3.33: Radial emissivities determined from the Δv = 5 transition within the N_2 1^{st}-Positive system over graphite and quartz.

Chemical reactions within the flow are inherently linked to the collision rate amongst particles. Moreover, particle collisions are the fundamental processes that

equilibrate a flow. Due to the low operating pressure utilized in this study, the convection time scale describing flow through the boundary layer is significantly shorter than the interparticle collision rate timescale, which yields frozen flow. Therefore, over a non-catalytic surface, such as quartz, the chemical composition and energy level distribution throughout the boundary layer remains unchanged. Section 5.6 provides additional analysis into the frozen flow created by the standard operating condition by considering the recombination coefficient introduced by Fay and Riddell [10]. Measuring the nitrogen atom emission throughout the boundary layer over quartz provides an estimation of the density trend of the entire flow approaching the wall.

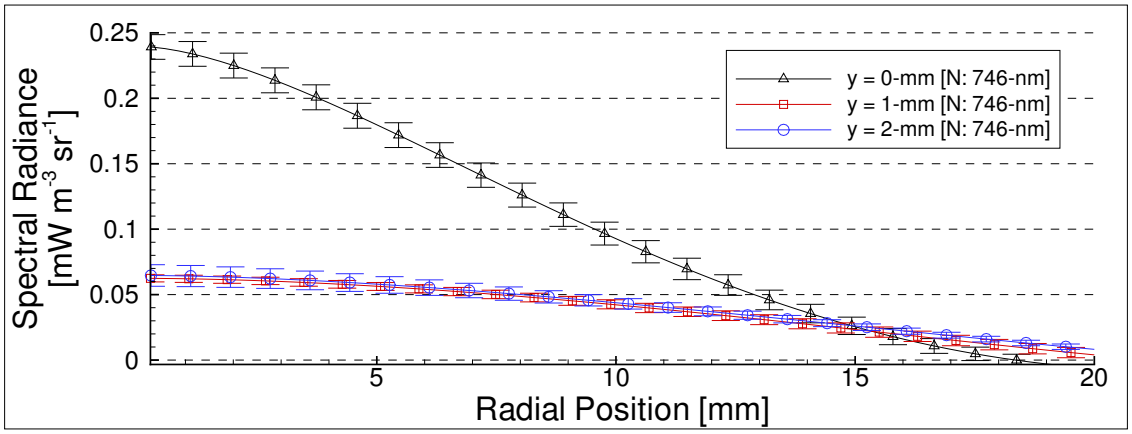

Figure 3.34: Radial-distribution of the nitrogen atom line at 746-nm over quartz at $\Delta y = 0$-mm, $\Delta y = 1$-mm, and $\Delta y = 2$-mm.

Figure 3.34 shows the radially-distributed spectral radiance from the atomic nitrogen line at 746-nm at $\Delta y = 0$-mm, $\Delta y = 1$-mm, and $\Delta y = 2$-mm over quartz. Recognize that the spectral radiance is a direct indication of the number of upper state emitters through Equation 3.38. At $\Delta y = 1$-mm, and $\Delta y = 2$-mm, the emission distribution is practically identical. However, directly off the surface ($\Delta y = 0$-mm) the radial distribution is significantly higher. Recall that the estimated temperature

of the free stream centerline was $T = 6000$-K, whereas the surface temperature was generally lower ($T_w = 1500$-K). Assuming a constant pressure boundary layer created by the subsonic flow, the ideal gas law predicts an increase in flow density proportional to the decrease in temperature. Note that Figure 3.34 shows the nitrogen atom population at the wall is ≈ 3.9 times greater than the level at the boundary layer edge. In comparison, the temperature scaling predicts a total number density increase of $\approx$ 1.6 times between the wall and boundary layer edge. Section 4.4 analyzes the validity of these values from an independent set of tests employing laser-induced fluorescence.

Uncertainty Analysis

Uncertainties for the temperature and radially-distributed spectral radiance values were determined from the average and standard deviation of all radiance measurements of a particular feature acquired at the same flow location. For each feature, a data set for the average measured radiance ($\bar{I}(x)$), and the corresponding radiance within one standard deviation ($\bar{I}(x)+\sigma_I$, $\bar{I}(x)$-σ_I) were created. Performing the Abel inversion technique on each set yielded the uncertainty in the radially-distributed emission. From here, the propagation of uncertainty shown in Equation 3.39 provided the uncertainty in the measured number density of the upper-state emitter, where the uncertainties on the energy levels ($\sigma_{\epsilon'}$, $\sigma_{\epsilon''}$) and emission rates ($\sigma_{\mathcal{A}}$) were provided by Wiese [5]. For molecular transitions, uncertainties were not provided and a value of 25% was estimated, which matched the provided uncertainty in the atomic transitions.

$$\sigma_{n_{T',v'}} = \sqrt{\sigma_e^2 \left(\frac{\partial n_{T',v'}}{\partial e}\right)^2 + \sigma_{\epsilon'}^2 \left(\frac{\partial n_{T',v'}}{\partial \epsilon'}\right)^2 + \sigma_{\epsilon''}^2 \left(\frac{\partial n_{T',v'}}{\partial \epsilon''}\right)^2 + \sigma_A^2 \left(\frac{\partial n_{T',v'}}{\partial A}\right)^2} \tag{3.39}$$

Recall that the temperature and upper state number density are related by Equation 3.19. Laux shows that one can relate the sensitivity in the upper state number density to the calculated temperature taking the logarithm of Equation 3.19 and differentiating, which produces the expression shown in Equation 3.40 [71].

$$\left|\frac{\Delta n_{\epsilon',i}}{n_{\epsilon',i}}\right| = \left|\frac{\Delta \chi_i}{\chi_i}\right| + \left|\frac{\Delta T}{T}\right| + \left|\frac{\Delta Q_{tot}}{Q_{tot}}\right| + \frac{\epsilon'}{k_B T}\left|\frac{\Delta T}{T}\right| \tag{3.40}$$

Section 3.6.2 and 3.7 addressed the flow composition over a temperature range applicable to this experiment and yielded that the atomic and molecular nitrogen molar fractions could be assumed constant ($\chi_N = 0.88$, $\chi_{N_2} = 0.12$). Recognize that this is particularly true at the locations considered in this experiment, which were either in the free stream or sufficiently removed from the surface of the sample. Moreover, Figure 3.26 indicates that the molecular nitrogen ion fraction does not deviate greatly over the conditions ultimately determined within the flow ($T = 5200$ - 6000-K).

Similarly, Table 3.5 introduced the partition functions for the three species considered. Notice that the electronic partition function for each species all vary by less than 0.5% up to 6000-K. Hence, the electronic partition functions can be set to $Q_{el,N_2} = 1$, $Q_{el,N_2^+} = 1$, and $Q_{el,N} = 4$. Additionally, the rotational and vibrational partition function vary about 10% over the temperatures yielded in this campaign and were subsequently regarded as constants. With these assumptions, Equation 3.40 reduces to the expression shown in Equation 3.41.

$$\frac{\Delta T}{T} = \frac{1}{1 + \frac{\epsilon'}{k_B T}}\left|\frac{\Delta n_{\epsilon',i}}{n_{\epsilon',i}}\right| \tag{3.41}$$

Using the nitrogen atom line at 746-nm at 6000-K, the sensitivity between the measured upper state number density and temperature is shown in Equation 3.42.

Here, an uncertainty in the upper state number density measurement of 50% would yield a 2% uncertainty in temperature (within 120-K). Clearly, this technique is capable of providing highly-resolved temperature data even when significant error in the acquired signal exists.

$$\frac{\Delta T}{T} \approx 0.04 \left| \frac{\Delta n_{\epsilon',i}}{n_{\epsilon',i}} \right| \tag{3.42}$$

Chapter 4

Laser Diagnostics

4.1 Overview

Researchers have used laser-based diagnostic techniques to study flow phenomena since shortly after the development of the first ruby laser in 1960 [78]. Whereas emission spectroscopy is a passive technique that relies upon the naturally occurring spontaneous emission within the plasma, laser-based studies have the advantage of probing the flow in a minimally invasive manner, which yields spatially-resolved data without using mathematical transformations, such as an Abel inversion. Another significant drawback of emission spectroscopy is that there is no spontaneous emission from the ground state, which results in no direct measurement of this state. Subsequent analysis assumes that captured emission occurs from an equilibrium distribution of energy levels. Laser-based techniques avoid this assumption because the typical target energy level is the ground state of the probed species. Moreover, laser-based techniques are capable of studying lower temperature flows where there may be little or no spontaneous emission.

The laser diagnostic instrumentation in the PDTL is configured to perform two-

photon absorption LIF measurements within the ICP chamber and MDFR. Figure 4.1 shows a diagram of the laboratory setup. The system includes an injection seeded, Powerlite 8000 Nd:YAG pump laser, which provides a 10-Hz pulsed, 532-nm output to an ND6000 dye laser. A Stanford Research DG645 delay generator controls the injection seeder, pump laser's flash lamps, q-switch timing, and DAQ system. Consecutive Inrad Autotrackers frequency triple the dye laser output to the desired wavelength. For nitrogen atom detection, the dye laser uses DCM dye. Frequency tripling the dye laser output provides tunable UV radiation over a wavelength range of 205 - 220-nm. This campaign utilized an LIF scheme employing 211-nm light, as indicated in the diagram. Downstream of the Autotrackers, a beam divider separates the UV output in two directions, with 90% of the power directed toward the test chamber and 10% toward the MDFR.

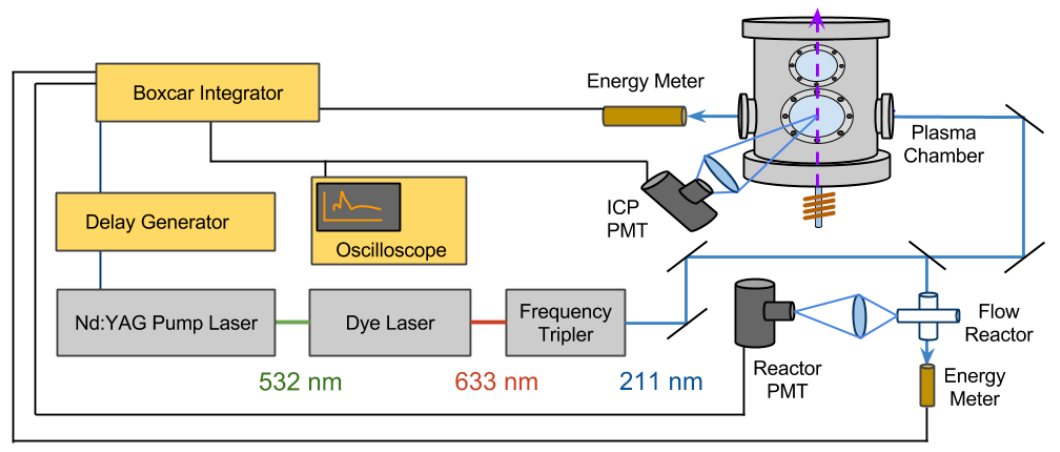

Figure 4.1: Laser and instrumentation configuration for measuring two-photon absorption LIF in the UVM ICP Facility.

Two separate, gated R636 photomultiplier tubes (PMTs) equipped with narrow bandpass filters detect the LIF signal within the ICP and MDFR (λ_0 = 870-nm, $\Delta\lambda$ = 10-nm). A tilting stage sets an appropriate PMT view angle at the ICP location to

avoid sample obstruction of the signal. The two Molectron energy meters (MN: J3-09-030) indicated in the diagram measure the beam energy after passing through the ICP and MDFR. Ultimately, a Stanford Research SR250 and SR280 Gated Integrator and Boxcar Averager system integrates and records all LIF signals. Typical laser pulse energies at each wavelength are summarized in Table 4.1.

Table 4.1: Laser System Specifications

Parameter	Rating
Nd:YAG pulse energy	740 mJ @ 532 nm
Dye fundamental output	100 mJ @ 633 nm
Tripled output	3-4 mJ @ 211 nm
Temporal pulse width	7 ns

4.2 Laser Induced Fluorescence

The following campaign aimed to determine the transformation of the nitrogen atom population and translational temperature along the stagnation point streamline towards a graphite sample using a two photon absorption LIF technique. The LIF target species was atomic nitrogen because its arrival flux to the surface presumably controlled the carbon nitridation and nitrogen recombination rates at the surface. Figure 4.2 depicts the excitation strategy used in this campaign to perform these measurements.

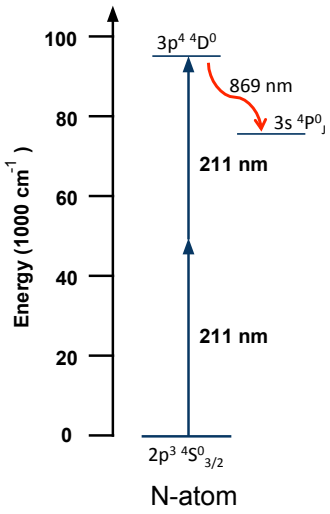

Figure 4.2: Nitrogen atom two-photon absorption LIF scheme used in the investigation.

During the LIF process, a small percentage of ground-state nitrogen atoms undergo a 3p $^4D^0_{7/2} \leftarrow 2p^3\ ^4S^0_{3/2}$ electronic transition via simultaneous absorption of two photons at 211-nm. Subsequently, at a discrete time later, these atoms begin to undergo a 3p $^4D^0_{7/2} \rightarrow$ 3s $^4P^0_J$ relaxation transition, which releases photons at 869-nm. Here, the PMT located at the measurement location captures this emission and the Gated Integrator System system ensures that the total emission corresponding to each laser pulse is determined.

Due to unavoidable line broadening mechanisms present within the flow and the laser system, obtaining data experimentally involved measuring the fluorescence signal within the ICP and MDFR simultaneously while scanning the dye laser output over a 0.05-nm wavelength range centered at 211-nm with a scan rate of 0.0005-nm-s^{-1}. This procedure required a total scan time is 100-s. Steady state conditions were assumed over the entirety of the scan, which is supported by the emission data introduced in Section 3.6.1.

Figure 4.3 shows a typical data set for an individual scan performed simultaneously in the ICP and MDFR. The normalized LIF signal represents the total captured emission divided by the laser pulse energy squared. Clearly, this value depends on the dye laser output wavelength. The normalization scaling is discussed further in Section 4.3.2. Overlaid on each raw signal is a Gaussian distribution curve determined with a least-squares solver. Note that frequency tripling the dye laser output is equivalent to reducing the wavelength by one-third. Hence, the peak intensity at $\approx$ 632.945-nm corresponds to 210.982-nm light downstream of the frequency tripler.

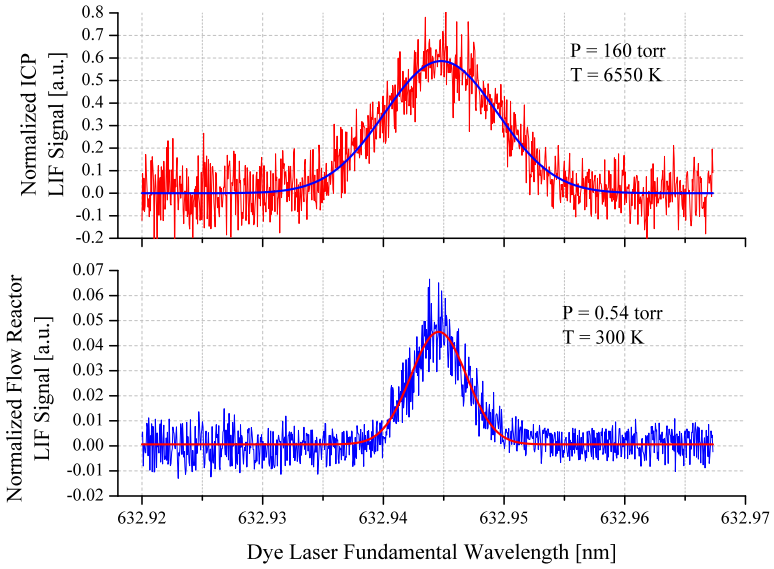

Figure 4.3: Nitrogen atom LIF signals acquired from nitrogen flow within the ICP and MDFR. A Gaussian line shape fit is shown over each data set.

Figure 4.3 also illustrates the typical relationship observed between the ICP and MDFR signals. Note that the LIF signal is broader in the ICP than in the MDFR, which is due to Doppler broadening and is an indication of higher temperature within the chamber. Recall that Section 3.7.1 discussed various line broadening mechanisms. Specifically, Doppler broadening increases at higher translational velocities, indicating

higher internal energy and temperature. In addition, Doppler broadening was several orders weaker than the resolution of the emission spectrometer, and hence was not considered. Here, instrumental broadening in the detector is not a factor due to the fundamental difference between the PMT and spectrometer detection process. Figure 4.4 shows the degree of Doppler broadening present in the emission feature in the LIF scheme. Notice that it is on the order of 10^{-3} - 10^{-2}-nm for the temperature range considered. Specifically, the MDFR operates at room temperature (T = 300-K), which corresponds to an expected Doppler width of 0.003-nm. In contrast, Figure 4.3 indicates that the FWHM of the MDFR signal was 0.005-nm, which is greater than the expected degree of Doppler broadening. Clearly there is at least one other competing broadening mechanism present in the system.

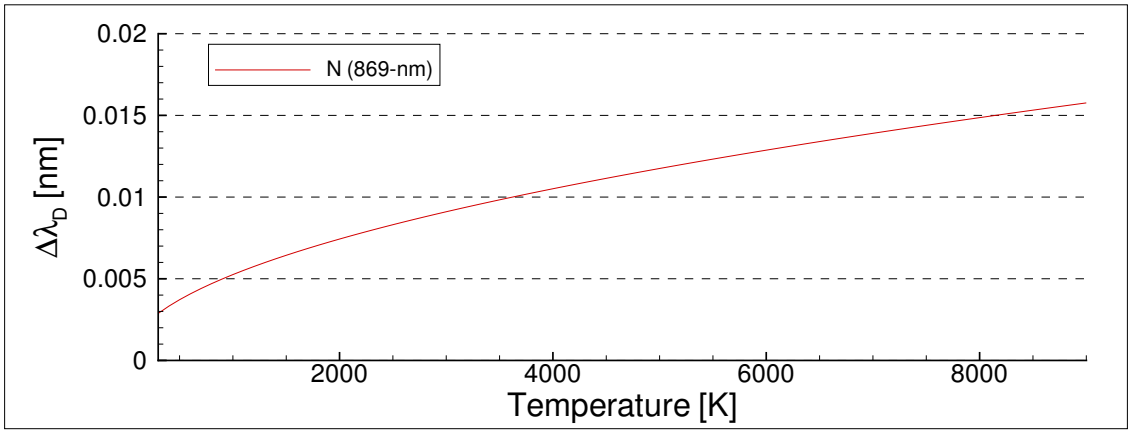

Figure 4.4: The Doppler broadening of the 869-nm emission feature of atomic nitrogen employed by the LIF scheme.

One competing mechanism is the laser line width, which results from natural broadening within the laser medium and limitations on the internal components of the laser. On a fundamental level, lasers create a population inversion within the lasing medium amongst various energy levels. Gain builds up within the oscillator cavity via stimulated emission until it discharges in a single pulse over a finite duration. The

pulse event occurs over a discrete time and the uncertainty on the energy level spacing within the lasing medium increases in accordance with the Heisenberg uncertainty principle, which results in a broadened output [76].

Also, the diffraction grating within the dye laser impacts the laser line width [75]. The fundamental output provided by the pump laser provides the necessary energy to create the population inversion required to lase the DCM dye. Within the DCM dye are long strands of molecules that emit a nearly continuous band of radiation across a wide spectral range (615-nm - 660-nm). Ideally, the diffraction grating is capable of separating monochromatic light from the broadband source. In reality, quantum mechanical considerations of the interaction of light and matter restrict this ideal behavior. Instead, the grating creates a Gaussian beam with a finite spectral width surrounding a central wavelength.

Another possible contributor to the observed LIF signal is collisional broadening. Whereas Doppler broadening and the laser line width yield Gaussian profiles, collisional broadening creates a Lorentzian profile [74]. A combination of the two curves is a Voigt profile. Collisional broadening is not believed to play a significant role in the broadening of the signal in the ICP or MDFR due to the low pressure conditions and reduced particle collision rate. To verify this assertion, Meyers individually fitted the signals obtained within the ICP and MDFR with a Voigt profile using a least-squares solver. Upon performing the fit, the goodness-of-fit did not significantly improve from the Gaussian fit curve, indicating that collisional broadening was not a meaningful contributor to the observed profile [79].

4.3 Experimental Procedure and Data Reduction

Prior to each test the laser beam and sample were aligned with the center of the plasma jet using the jig shown in Figure 4.5. The alignment jig was designed to sit concentrically within the quartz tube and indicated the center of the jet with the vertical post as shown. Once installed, the sample location was adjusted until the front face was centered over the jig and positioned at the same height as the end of the post. A hard stop installed onto the insertion probe ensured that the sample could be reinserted to the same location of the flow repeatedly. With the sample retracted, the laser light was directed into the ICP chamber and was spatially adjusted until a portion of the light scattered off the end of the vertical post. Next, the ICP PMT was aligned to the scattered light by removing the filter and observing the captured scattered light signal on a Lecroy 9360 oscilloscope. The PMT horizontal and vertical locations were adjusted until the scattered light signal was maximized. Finally, the jig was removed, and with the sample re-inserted into the test location, the pyrometer was directed towards the front face of the sample through an optical viewport located below the chamber base. After completing the alignment procedure, the sample was retracted before system startup. Once the system reached standard test conditions, the sample was inserted into the flow to the hard stop location and visual observation verified that the sample was in the center of the jet.

Figure 4.6 shows a diagram illustrating the plasma flow, laser propagation and LIF detection axes. Notice that the laser beam passes perpendicular to the main flow axis. Additionally, the observation axis for the detection system is orthogonal to the laser propagation and flow axes, and is tilted such that the sample does not interfere with the focal volume. In order to more accurately determine the location of the sample front face, the sample was slightly lowered ($<$ 1-mm) until the energy meter

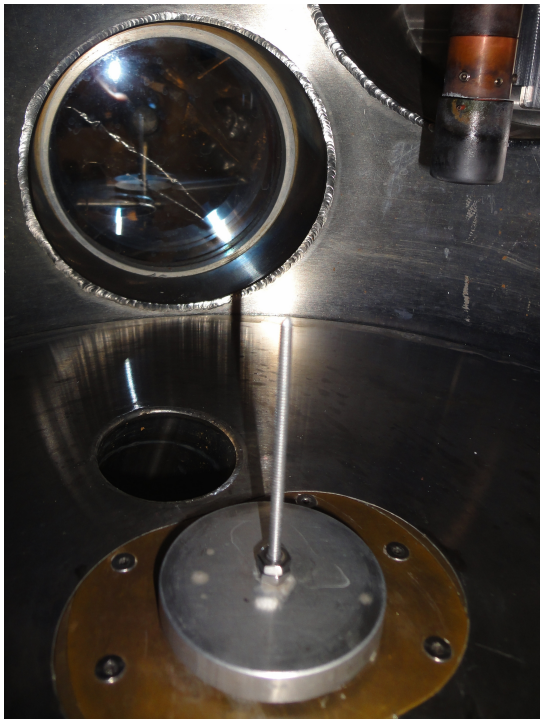

Figure 4.5: The optical instrumentation alignment jig installed in the quartz tube.

reading decreased by a factor of 2, which indicated that it was partially blocking the beam. An initial scan performed at this location corresponded to the origin shown in Figure 4.6. Subsequent scans were performed along the stagnation point streamline by translating the laser, ICP PMT and energy meter along the y-axis shown. Prior to each scan, the running exposure time of the sample was recorded, which ultimately helped account for the degree of surface recession at that time.

After performing all the desired scans, the sample was removed from the flow and the total exposure time was recorded. Once the sample was removed from the chamber, the final length was determined with a set of vernier calipers, and the recession rate was calculated assuming constant recession, as supported in Section 2.3.2. The location of each particular scan was then adjusted according to the exposure time at which the scan was performed and the measured recession rate, as shown in Equation

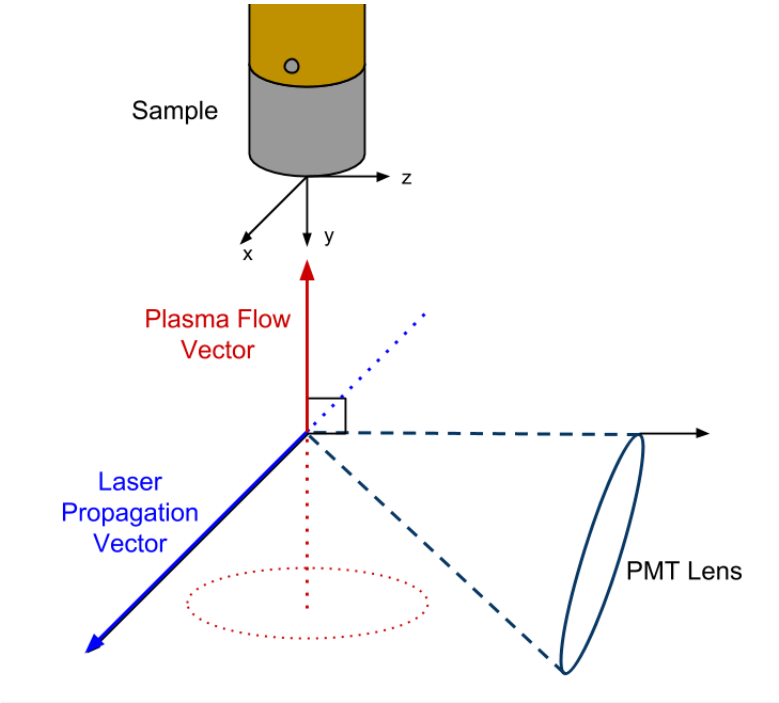

Figure 4.6: The LIF boundary layer scan configuration.

4.1. Here, the adjusted location (Δy), the initial and final lengths (L_i, L_f), the total exposure time (Δt_{total}) and the scan exposure time (Δt_{scan}) are all included.

$$\Delta y = \underbrace{\frac{L_i - L_f}{\Delta t_{total}}}_{constant\,rate} \Delta t_{scan} \tag{4.1}$$

4.3.1 Translational Temperature

Commonly, local translational temperatures are extracted from LIF measurements by determining the Doppler width of the signal [87]. The Doppler width in terms of wavenumbers is shown in Equation 4.2 and provides a direct link between the captured LIF signal and the local translational temperature of target species within the flow.

$$\Delta\hat{\nu}_D = \hat{\nu}_o\sqrt{\frac{8ln(2)k_BT}{mc^2}} \tag{4.2}$$

However, as explained in Section 4.2, the LIF signal width is due to the combination of Doppler broadening present at the measurement location and the laser line width. This relation is expressed in Equation 4.3 below for both the ICP and MDFR. Note that in this equation, the square of the measured LIF signal width ($\Delta\hat{\nu}_T^2$) is the sum of the squares of the laser line width ($\Delta\hat{\nu}_L^2$) and Doppler broadening width ($\Delta\hat{\nu}_D^2$). Additionally, the laser line width is independent of the system in which it is measured.

$$\begin{aligned}\Delta\hat{\nu}_{T,ICP}^2 &= 2\Delta\hat{\nu}_L^2 + \Delta\hat{\nu}_{D,ICP}^2 \\ \Delta\hat{\nu}_{T,MDFR}^2 &= 2\Delta\hat{\nu}_L^2 + \Delta\hat{\nu}_{D,MDFR}^2\end{aligned} \tag{4.3}$$

To obtain a temperature in the ICP, one must deconvolve the laser line width contribution from the total signal width before applying Equation 4.2. The MDFR is a suitable system with which to determine the laser line width because it operates at room temperature and thus the Doppler width component of the LIF signal is known *a priori*. Combining the two expressions in Equation 4.3 with Equation 4.2 yields the final expression between the measured signal width to the ICP temperature, as shown in Equation 4.4.

$$T_{Trans,icp} = \frac{m_Nc^2}{8ln(2)k_Bn_A\hat{\nu}^2}[\Delta\hat{\nu}_{T,icp}^2 - (\Delta\hat{\nu}_{T,fr}^2 - \Delta\hat{\nu}_{D,fr}^2)] \tag{4.4}$$

Section 4.4 shows that over graphite, the temperature profile along the stagnation point streamline decreased towards the sample. Using the expression suggested by Meyers, shown in Equation 4.5, a least-squares solver program was written to best fit the data trend using the four constants (A_i) as free parameters [64]. Note that

the surface temperature measured by the pyrometer provided a boundary condition, which anchored the expression at the wall location ($y = 0$). Assuming ideal gas behavior throughout the boundary layer, this temperature fit ultimately provided an estimation of the total number density trend towards the wall, as discussed in Section 4.3.3.

$$T(y) = T_{surf} + A_1(1 - e^{-\frac{y}{A_2}}) + A_3(1 - e^{-\frac{y}{A_4}}) \tag{4.5}$$

4.3.2 Nitrogen Atom Number Density

In addition to the translational temperature, the ICP and MDFR LIF signals provided information about the ground state nitrogen atom number density in both systems. Bamford et al. studied oxygen atom as the target species in a similar LIF experiment to the scheme shown in Figure 4.2. There, they used UV light at 225.7-nm and developed a method in which they could determine the ground state number density of the probed species directly [41]. Equation 4.6 shows the final expression they developed, which is a function of the beam waist (ω_0), photon energy ($h\nu$), calibration constant for the detection system (D), effective two-photon absorption cross-section of the probed species ($\hat{\sigma}^{(2)}$), temporal integral of the pulse shape function ($F^2(t)$), the quantum yield ($\frac{A}{A+Q}$), and the total emission of the LIF signal normalized by the laser pulse energy squared ($\frac{S}{E^2}$).

$$n_N = \frac{(2\pi\omega_0 h\nu)^2}{D\hat{\sigma}^{(2)} \int_{-\infty}^{\infty} F^2(t)dt} \frac{A+Q}{A} \int \frac{S}{E^2} d\lambda \tag{4.6}$$

During the graphite boundary layer survey, the LIF signal was obtained at various locations along the stagnation point. In Equation 4.6, the normalized spectral integral was the only term that varied significantly at each location. That is, the beam waist,

detection efficiency, cross-section, pulse integral and quantum yield were assumed to remain constant at each scan location. Therefore, the ground state nitrogen atom number density inherently scales with the normalized spectral integral, as shown in Equation 4.7.

$$n_N \propto \int \frac{S}{E^2} d\lambda \tag{4.7}$$

Although Equation 4.7 does not yield absolute number densities for nitrogen atom, it indicates the relative amount of ground state nitrogen present with respect to a measurement at another location. Over graphite, the fluorescence signal ($\int S/E^2 d\lambda$) decreased towards the sample surface indicating that at least one process was removing nitrogen atom from the flow. Dividing each measured fluorescence signal by the signal measured at the boundary layer edge created a set of normalized fluorescence signals with a maximum value of unity at the boundary layer edge. Equation 4.8 shows that this normalized fluorescence signal is equivalent to the ratio of the absolute number density at a particular location (n_i) with respect to the boundary layer edge (n_e).

$$\frac{n_{N,i}}{n_{N,e}} = \frac{\left[\frac{(2\pi\omega_0 h\nu)^2}{D\hat{\sigma}^{(2)}\int_{-\infty}^{\infty} F^2(t)dt}\frac{A+Q}{A}\int \frac{S}{E^2}d\lambda\right]_i}{\left[\frac{(2\pi\omega_0 h\nu)^2}{D\hat{\sigma}^{(2)}\int_{-\infty}^{\infty} F^2(t)dt}\frac{A+Q}{A}\int \frac{S}{E^2}d\lambda\right]_e} = \frac{(\int S/E^2 d\lambda)_i}{(\int S/E^2 d\lambda)_e} \tag{4.8}$$

Section 4.3.3 uses the normalized fluorescence signal trend in order to determine the reaction rate at the wall. Similar to the temperature trend shown in Equation 4.5, the fluorescence signal distribution was fitted with a trend line, as shown in Equation 4.9 using a least squares solver routine. In the temperature trend line, the pyrometer provided an independent measurement of the surface temperature with which to anchor the leading term. Here, there was no independent measurement of

the normalized fluorescence at the wall and as a first approximation, a suitable value based on the trending data was chosen. The appropriateness of the value ultimately chosen is addressed in Section 4.4.

$$\frac{n_N(y)}{n_{N,e}} = \frac{n_{surf}}{n_{N,e}} + B_1(1 - e^{-\frac{y}{B_2}}) + B_3(1 - e^{-\frac{y}{B_4}}) \tag{4.9}$$

4.3.3 Reaction Rates

Consider the conservation of mass at the sample surface, as expressed by Goulard, in Equation 4.10 [30]. Here, the expression for the total mass flux of nitrogen atoms towards the wall ($j_{N,w}$) illustrates a balance between the mass diffusion and all potential gas-surface reactions. Note the linear relationship between the reaction rate (k_w) and the concentration gradient ($\frac{\partial c_N}{\partial y}$). Over a non-catalytic surface, there is no surface erosion nor surface reactions, which creates a zero concentration gradient at the surface. The results obtained through Abel inversion of spontaneous emission in Chapter 3 as well as the heat flux measurements discussed in Chapter 5 indicate that graphite is a catalytic material that actively promotes nitrogen recombination. Moreover, carbon nitridation is assumed to control the observed mass loss discussed in Section 2.3.1. Both processes remove atomic nitrogen from the boundary layer. Therefore, the total reaction rate over graphite is non-zero, which leads to a measurable concentration gradient approaching the wall.

$$j_{N,w} \rightarrow \underbrace{k_w \rho_w c_{N,w}}_{reactions} = \underbrace{D_N \rho_w \left(\frac{\partial c_N}{\partial y}\right)_w}_{diffusion} \tag{4.10}$$

Goulard considered the mass flux in his formulation. In this experiment, the LIF procedure yields the relative nitrogen atom number density and it is advantageous to

consider the particle flux instead. The equivalent expression in terms of the particle flux ($\Gamma_{N,w}$) is shown in Equation 4.11. Note that the mole fraction gradient ($\frac{\partial \chi_N}{\partial y}$), created by gas-surface reactions, drives the diffusion of atomic nitrogen towards the wall.

$$\Gamma_{N,w} \rightarrow k_w n_w \chi_{N,w} = D_{N,w} n_w \left(\frac{\partial \chi_N}{\partial y} \right)_w \tag{4.11}$$

Solving for the reaction rate gives Equation 4.12.

$$k_w = D_{N,w} \frac{1}{\chi_{N,w}} \left(\frac{\partial \chi_{N,w}}{\partial y} \right)_w \tag{4.12}$$

The reaction rate depends explicitly on the diffusion coefficient of atomic nitrogen (D_N). Pallix and Copeland developed an empirical expression for the diffusion of nitrogen as a function of pressure and temperature, which is utilized here [80]. Their expression is shown in Equation 4.13 and is a function of the flow pressure and temperature, with $D_0 = 0.365$-cm^2-s^{-1}, $p_0 = 760$-Torr and $T_0 = 298$-K.

$$D_N = D_0 \left(\frac{p_0}{p} \right) \left(\frac{T}{T_0} \right)^{1.64} \tag{4.13}$$

In addition to the diffusion constant, the wall reaction depends on the nitrogen atom molar fraction and molar fraction gradient at the wall. Assuming ideal gas behavior, the molar fraction of a given species is the ratio of its partial pressure to the total pressure in the flow, as shown in Equation 4.14.

$$\chi_N = \frac{n_N}{n_{total}} = \frac{p_N/(k_B T)}{p_{total}/(k_B T)} = \frac{p_N}{p_{total}} \tag{4.14}$$

Recall that the specific LIF technique employed in this campaign does not yield the absolute nitrogen atom number density. Without this information, the molar

fraction cannot be determined directly. Therefore, the normalized mole fraction ($\hat{\chi}_N$) is defined, as shown in Equation 4.15. The advantage of $\hat{\chi}_N$ will become apparent in the subsequent analysis, which was first introduced by Meyers [64]. Notice that $\hat{\chi}_N$ at any location within the boundary layer is the local nitrogen mole fraction (χ_N) normalized by the nitrogen mole fraction at the boundary layer edge ($\chi_{N,e}$).

$$\hat{\chi}_N(y) = \frac{\chi_N(y)}{\chi_{N,e}} \tag{4.15}$$

Substituting the nitrogen atom and total number densities into the definition of $\hat{\chi}_N$ gives Equation 4.16. Here, the advantage of introducing $\hat{\chi}_N$ becomes clearer. Note the ratio between the nitrogen atom number density in the boundary layer with respect to the boundary layer edge location ($n_N/n_{N,e}$), which is identical to the normalized fluorescence trend determined from the LIF measurements.

$$\hat{\chi}_N(y) = \frac{n_N(y)/n_{total}(y)}{n_{N,e}/n_{total,e}} = \frac{n_N(y)/n_{N,e}}{n_{total}(y)/n_{total,e}} \tag{4.16}$$

Next, the normalized total number density expressed in the denominator of Equation 4.16 must be considered in order to determine $\hat{\chi}_N$. Assuming ideal gas behavior, this quantity is explicitly related to the temperature change throughout the boundary layer, which is determined with LIF measurements. Ultimately, the normalized total number density can be written as the ratio of the boundary layer edge and local temperature, as shown in Equation 4.17. Note that this formulation assumes constant pressure within the boundary layer. Pitot probe measurements carried out in the facility have indicated that the total pressure is $\approx 1\%$ greater than the static pressure, which supports this technique.

$$\frac{n_{total}(y)}{n_{total,e}} = \frac{p(y)/(k_B T(y)}{p_e/(k_B T_e)} = \frac{T_e}{T(y)} \tag{4.17}$$

Finally, in order to determine the total reaction rate at the wall, Equation 4.12 must be re-expressed in terms of $\hat{\chi}_N$. First, recognize that Equation 4.15 rearranges to Equation 4.18.

$$\chi_N(y) = \chi_{N,e}\hat{\chi}_N(y) \tag{4.18}$$

The molar fraction of nitrogen atom at the boundary layer edge remains constant. Hence, the derivative with respect to y is shown in Equation 4.19.

$$\frac{\partial \chi_N(y)}{\partial y} = \chi_{N,e}\frac{\partial \hat{\chi}_N(y)}{\partial y} \tag{4.19}$$

Combining Equation 4.12 with Equation 4.18 and Equation 4.19 replaces the nitrogen atom molar fraction with $\hat{\chi}_N$, as shown in Equation 4.20. Customary units for the reaction rate are m-s^{-1}, which fundamentally relates to the dimensions of the gas-surface interface.

$$k_w = D_{N,w}\frac{1}{\hat{\chi}_{N,w}}\left(\frac{\partial \hat{\chi}_N}{\partial y}\right)_w \tag{4.20}$$

4.4 Results and Discussion

Figure 4.7 shows the measured temperature over the surface of graphite along with the temperature trend line, which appears to track the temperature measurements well. Error bars indicating ±500-K are included for each discrete measurement, which were determined from the standard deviation of multiple repeated temperature measurements performed at the same location within the free stream. Notice that the

temperature fit decreases from 6000-K to the surface temperature of 1600-K determined by the pyrometer, which provides an initial indication that the flow achieves thermal equilibrium with the surface.

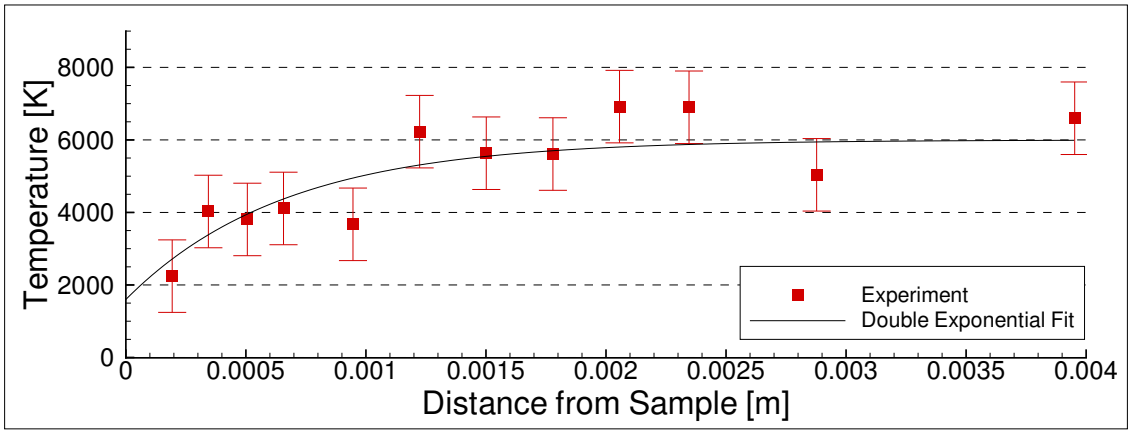

Figure 4.7: Measured temperature along the stagnation point stream line and the trend line fit from Equation 4.5.

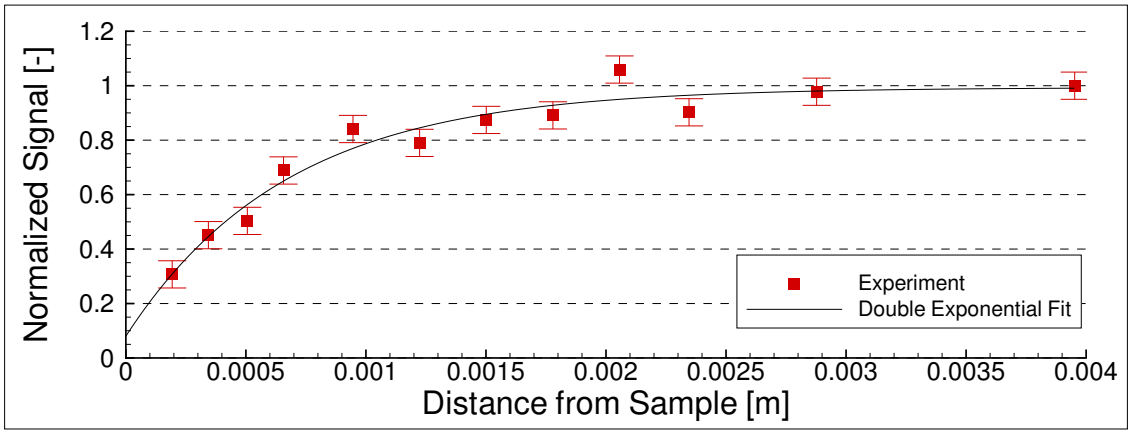

Figure 4.8: Normalized nitrogen atom number density measurements along the stagnation streamline with trend line fit from Equation 4.9.

Figure 4.8 shows the normalized fluorescence signal and the trend line fit of the discrete data. Again, this represents the relative nitrogen atom number density throughout the boundary layer. Away from the sample, the normalized signal is unity, which drops to a value of 0.08 at the sample surface. Additionally, the trend line appears

to track the measured data well.

The normalized total number density trend is shown in Figure 4.9. The discrete data points and trend line shown were determined directly from Equation 4.17 using the discrete temperature and temperature trend line shown in Figure 4.7 respectively. Here, the uncertainty reflects the propagation of error due to the temperature measurement uncertainty. Beyond the boundary layer edge, the uncertainty is relatively low, which is a reflection of the fact that the temperature remains steady in the free stream. At locations progressively nearer to the wall, the uncertainty increases as the temperature drops because the bulk number scaling is inversely proportional to the decreasing local temperature. Note how the normalized bulk number density increases by ≈ 3.6 times the boundary layer edge value. Recall the nitrogen atom trends over quartz, shown previously in Figure 3.34. Notice that over quartz, the nitrogen atom trend increases by nearly the same amount (≈ 3.9) across the boundary layer, which further demonstrates the non-catalytic behavior of the quartz as well as supports the assertion that the bulk number density in the boundary layer can be described by the ideal gas law for constant pressure flow.

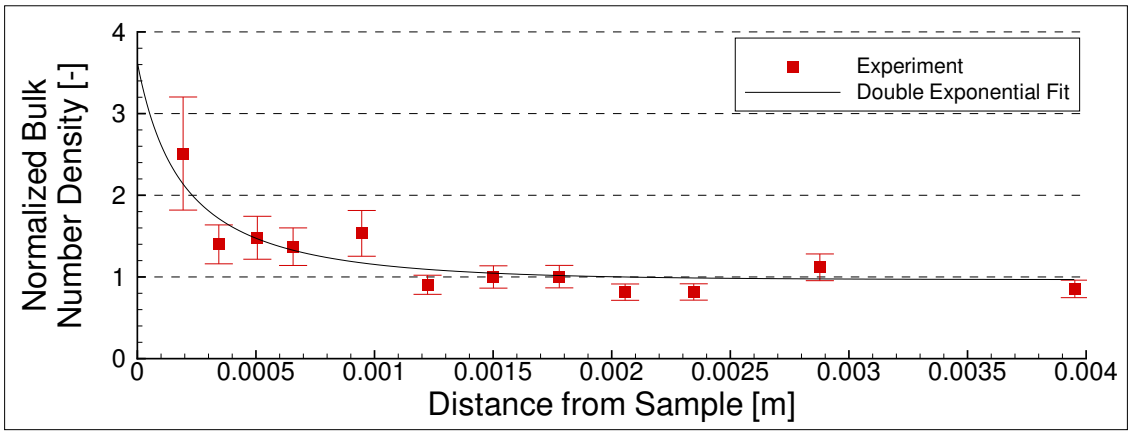

Figure 4.9: The normalized total number density profile determined from the temperature fit and Equation 4.17.

Ultimately, Figure 4.10 shows the ($\hat{\chi}_N$) distribution along the stagnation point stream line. In addition to the discrete data points and the trend line determined from the double exponential fits, a third trace is shown representing a linear fit of the three $\hat{\chi}_N$ values closest to the wall. Meyers suggested a linear fit of the near wall data points to determine the quantities ultimately used in Equation 4.20 [64]. Clearly, the two trend lines yield comparable values of $\hat{\chi}_N$ and $\frac{\partial \hat{\chi}_N}{\partial y}$ at the wall, which additionally supports the near wall normalized fluorescence value used in Equation 4.9.

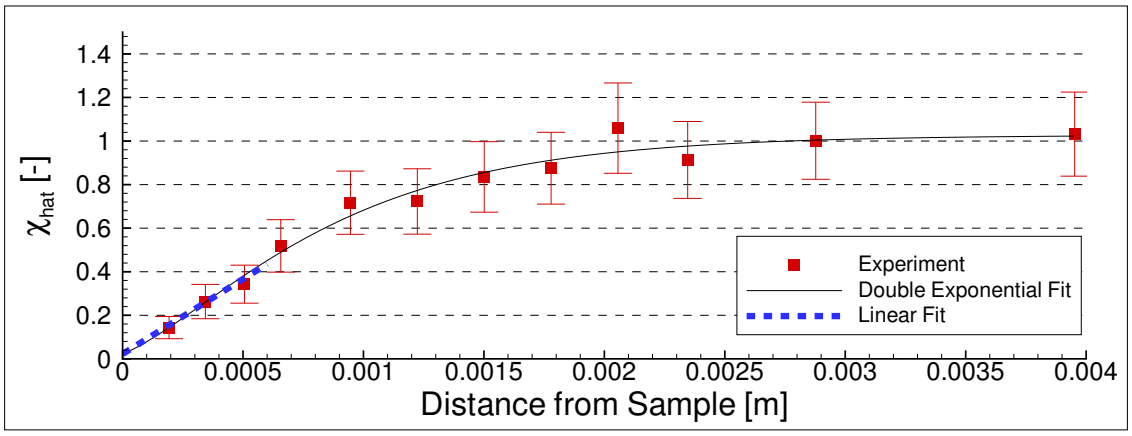

Figure 4.10: The $\hat{\chi}_N$ distribution along the stagnation point streamline determined from Equation 4.16.

The behavior of the curve in Figure 4.10 clearly indicates that nitrogen atom is removed from the boundary layer over graphite. Recognize that if no reactions were occurring, the curve would remain at unity along the stagnation point streamline. Consider again Figures 4.8 and 4.9. Clearly, the total number density is increasing as the flow approaches the wall. This is in agreement with stagnation point flow, where the convective velocity drops to zero and causes an increase in density. Conversely, the nitrogen atom trend decreases as it approaches the wall. If nitrogen atom were not removed from the boundary layer, then this trend would follow the total number density behavior.

Knowing the value of $\hat{\chi}_N(y)$ and $\chi_{N,e}$, one can immediately determine the value of $\chi_N(y)$ anywhere along the stagnation point streamline from Equation 4.18. Implementing the results from Section 3.6.2, the atom nitrogen molar fraction at the boundary layer edge is $\chi_{N,e} = 0.88$. Furthermore, Equation 4.21 estimates the nitrogen atom number density at any location along the stagnation point streamline once $\chi_N(y)$ is known.

$$\chi_N(y) = \frac{n_N(y)}{n_{total(y)}} \rightarrow n_N(y) = \chi_N(y)\frac{p}{k_B T} \tag{4.21}$$

In a previous LIF experiment performed by the author, the absolute number density of nitrogen atom was determined at y = 0.25-mm with the expression shown in Equation 4.6 [13]. This experiment was performed at a slightly higher free stream temperature (T = 7000-K) and a slightly lower pressure condition (p = 110-Torr). Ultimately, the campaign yielded an absolute number density of nitrogen of n_N(0.25-mm) = 2.7(10^{16})-cm^{-3}. At this location, the trend line in Figure 4.10 yields a value of $\hat{\chi}_N$(0.25-mm) = 0.188, which corresponds to a local nitrogen mole fraction of χ_N(0.25-mm) = 0.165. Employing Equation 4.21, the nitrogen atom number density at this location becomes n_N(0.25-mm) = 8.53(10^{16})-cm^{-3}, which is significantly higher than the direct measurement. However, this result is justified considering that the standard operating conditions used in this campaign maintained higher pressures and lower temperatures, which both tend to increase the total population of flow species. As an initial approximation, one can adjust the flow conditions in Equation 4.21. Using the flow conditions from the previous experiment, the nitrogen atom number density in this campaign becomes n_N(0.25-mm) = 4.25(10^{16})-cm^{-3}, which is 57% above the direct measurement.

Finally, the reaction rates at the wall are calculated using Equation 4.20, where

$\hat{\chi}_{N,w}$ and $(\frac{\partial \hat{\chi}_N}{\partial y})_w$ are determined from Figure 4.10. Additionally, the static pressure and wall temperature are used in Equation 4.13 to determine the diffusion coefficient $D_{N,w}$, which yields a total reaction rate of $k_{w,total} = 59.8 \pm 14.9$-m-s^{-1}. The Hertz-Knudsen equation, introduced in Chapter 1, is restated below and relates the total reaction rate at the wall to the reaction efficiency (γ_{total}) and thermal velocity of nitrogen ($\bar{\nu}_N$). From here, the reaction efficiency becomes $\gamma_{total} = 0.153 \pm 0.039$.

$$k_{w,total} = \gamma_{total} \frac{\bar{\nu}_N}{4} = \frac{\gamma_{total}}{4} \sqrt{\frac{8 k_B T}{\pi m_{a,N}}}$$

Recognize that the reaction rate and reaction efficiency determined here represent all processes extracting nitrogen atom from the boundary layer. Up until this point, there has been no delineation between the nitrogen recombination and carbon nitridation exclusively, which together control the observed nitrogen atom behavior. Now, the respective reaction rates and reaction efficiencies for carbon nitridation and carbon recombination must be determined. Equation 4.22 shows that the reaction rate describing all potential gas-surface interactions is the summation of the rates of each individual reaction.

$$k_{w,total} = \sum_{i}^{N} k_{w,i} = \underbrace{k_{w,CN}}_{nitridation} + \underbrace{k_{w,N_2}}_{recombination} \tag{4.22}$$

Fundamentally, the reaction efficiency of the carbon nitridation process is the ratio of the departure flux of the cyano radical from the surface with respect to the arrival flux of nitrogen atoms to the surface, as introduced in Chapter 1 and re-expressed here.

$$\gamma_{N,CN} = \frac{\Gamma_{CN}}{\Gamma_N}$$

Section 3.6.3 addressed the limited degree of carbon spallation occurring at the surface, and determined that it was more than a full order slower than carbon nitridation. Hence, neglecting spallation and attributing the total sample mass loss to carbon nitridation exclusively, Equation 4.23 estimates the departure flux of cyano radicals from the surface. This expression depends on the total sample mass loss (Δm_{sample}), surface area of the sample leading face (A), exposure time (Δt), and the atomic mass of carbon ($m_{a,C}$).

$$\Gamma_{CN} = \frac{\Delta m_{sample}}{A\, m_{a,C}\, \Delta t} \tag{4.23}$$

Additionally the nitrogen atom arrival flux comes from the Maxwellian distribution function, introduced in Equation 3.25, and restated here. Again, it relates the distribution of particle velocities to a discrete temperature.

$$f(C_1, C_2, C_3) = \left(\frac{m}{2\pi k_B T}\right)^{3/2} e^{-(\frac{m}{2k_B T})(C_1^2+C_2^2+C_3^2)}$$

The advective velocity at the stagnation point is zero. Therefore, diffusion controls the atomic nitrogen arrival flux at the wall. Assuming thermal equilibrium between the atomic nitrogen population adjacent to the wall and the surface of the sample, one calculates the nitrogen atom arrival flux to the surface by integrating the Maxwellian distribution function, as shown in Equation 4.24. Here, the x_3 spatial dimension was arbitrarily chosen as the axial flow direction towards the surface. Thus, all nitrogen atoms directly adjacent to the wall with a positive velocity in this direction (C_3) will contact the surface.

$$\Gamma_N = n_N \left(\frac{m}{2\pi k_B T}\right)^{3/2} \int_{-\infty}^{\infty}\int_{-\infty}^{\infty}\int_{0}^{\infty} e^{-(\frac{m}{2k_B T})(C_1^2+C_2^2+C_3^2)} dC_1 dC_2 dC_3 \tag{4.24}$$

Upon integrating Equation 4.24, the arrival flux of nitrogen atoms to the wall reduces to Equation 4.25. Here, the nitrogen atom arrival flux depends on the local nitrogen atom number density (n_N) and temperature (T).

$$\Gamma_N = \frac{n_N}{4}\sqrt{\frac{8k_BT}{\pi m_{a,N}}} \tag{4.25}$$

Inserting Equation 4.25 and Equation 4.23 into the reaction efficiency equation yields the relation introduced in Equation 1.8 and re-expressed here.

$$\gamma_{CN} = \frac{\Delta m_C}{A\, m_{a,C}\, \Delta t}\left(\frac{n_{N,w}}{4}\sqrt{\frac{8k_BT_w}{\pi m_{a,N}}}\right)^{-1}$$

The mass loss, sample surface area, exposure time, and wall temperature are known directly from measurement whereas the nitrogen atom number density at the wall is determined from Equation 4.21 with y = 0-mm. Here, the nitrogen atom number density becomes $n_{N,w} = 1.87(10^{16})$-cm^{-3}. Moreover, the carbon nitridation efficiency becomes $\gamma_{w,CN} = 0.00645\pm0.002$. This value compares favorably with published data, including the previous investigation performed by the author ($\gamma_{CN} = 0.0038$), as well as the work of Driver and MacLean ($\gamma_{CN} = 0.005$), and Zhang et al. ($\gamma_{CN} = 0.002$ - 0.0098) [25].

Using the Hertz-Knudsen relation once again yields a carbon nitridation reaction rate of $k_{w,CN} = 2.51\pm0.44$-m-s^{-1}. Subsequently, the nitrogen recombination rate and reaction efficiencies determined by rearranging Equation 4.22 are $k_{w,N_2} = 57.25\pm14.9$-m-s^{-1} and $\gamma_{w,N_2} = 0.147\pm0.039$. Note that the recombination efficiency is higher than the value estimated by Driver and MacLean (γ_{w,N_2} 0.05), but in good agreement with Gordeev (γ_{w,N_2} 0.22) and Anna (γ_{w,N_2} 0.07 - 1.0).

Table 4.2 provides a summary of the determined reaction rates and reaction efficiencies. Note that the carbon nitridation rate and efficiency are both well below the

Table 4.2: Reaction Rates and Efficiencies

Reaction	k [m-s^{-1}]	γ
Total	59.8±14.9	0.153±0.039
Carbon Nitridation	2.51±0.44	0.00645±0.002
Nitrogen Recombination	57.25±14.9	0.147±0.039

nitrogen recombination rate and efficiency. These data support the observed behavior within the flow. Namely, the nitrogen atom number density clearly decreased significantly throughout the boundary layer. Conversely, the mass loss rate, which was attributed to carbon nitridation exclusively, was too low to account for the observed nitrogen atom behavior. Section 5.6 introduces the reaction efficiency threshold commonly employed to separate non-catalytic and catalytic materials ($\gamma = 10^{-2}$). Table 4.2 indicates that the carbon nitridation efficiency was below this threshold. The nitrogen atom number density and bulk number density did not follow the same trend, which implies that a more dominant chemical reaction was depleting nitrogen atom from the boundary layer and the nitrogen recombination efficiency shown in Table 4.2 is clearly strong enough to cause the observed trend.

Chapter 5

Surface Heat Flux

5.1 Overview

Heat flux measurements provide an effective means to study gas-surface interactions owing to their repeatability and simplicity. However, they are limited in their ability to study gas-surface interactions since multiple combinations of chemical reactions may yield the same measured heat flux. Section 1.1.3 introduced the concept that a catalytic surface will experience a higher heat flux than a non-catalytic surface within flows of low Damköhler number. This augmented heat flux is due to the absorption of liberated energy generated by recombination reactions occurring at the wall. This chapter describes a set of heat flux experiments conducted at standard operating conditions over materials of varying catalycities, including graphite, copper and silicon carbide. The resulting analysis supports the assertion that graphite behaves as a highly-catalytic material, which efficiently promotes nitrogen recombination. The results also allow for an estimation of the energy accommodation of the surface.

5.2 Theory

Heat flux measurements in high-enthalpy flow stem from energy conservation. Specifically, the decrease in energy within the gas flow across the boundary layer is balanced by the energy transmitted to the material. Figure 5.1 illustrates the various potential energy transfer mechanisms inherent in hypersonic flight. The processes considered within this investigation are convective transport (q_{conv}), atomic recombination (q_{recom}), conduction through the surface (q_{cond}), and re-radiation from the surface (q_{rerad}). The principle source of radiation (q_{rad}) in-flight comes from the shock wave itself. Because the facility does not recreate this shock during operation, it is not considered. Owing to the test conditions and limited mass loss rate, convective blockage (q_{block}) is subsequently ignored. Additionally, vaporization (q_{vap}) and sublimation (q_{sub}) processes are negligible at the testing conditions as discussed in Section 1.1.5.

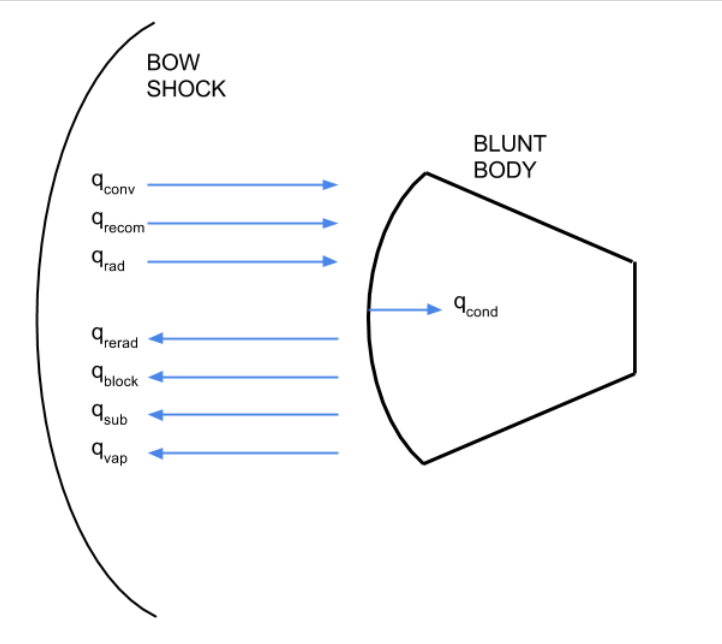

Figure 5.1: Various possible heat flux processes occurring in hypersonic flight.

There are several techniques with which to measure the surface heat flux for a particular material. This campaign measured the cold wall heat flux on copper and the hot wall heat flux on graphite and silicon carbide. Figure 5.2 shows a schematic of the two probes used in this experiment. In each, only the front face of the test material, which rested flush with the corresponding sleeve, was directly exposed to the flow.

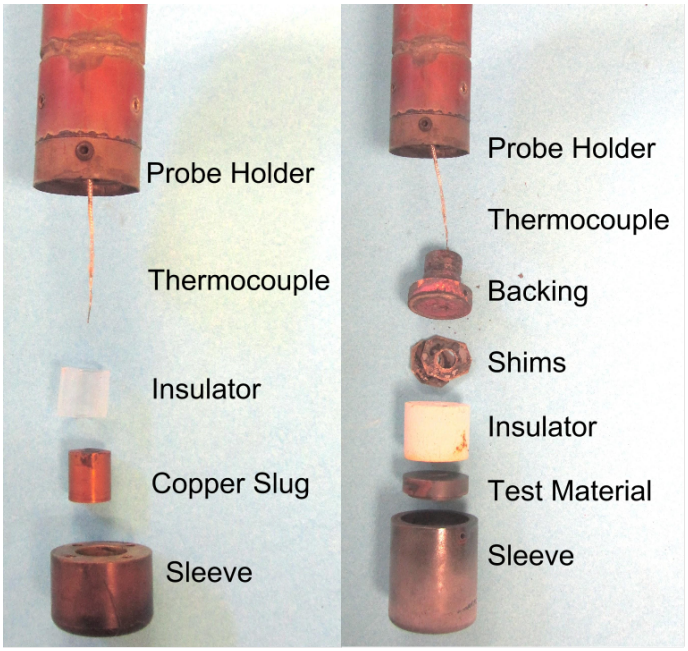

(a) Cold Wall Probe (b) Hot Wall Probe

Figure 5.2: A comparison of the cold wall and hot wall heat flux probe assemblies.

The cold-wall heat flux probe shown in Figure 5.2a is capable of withstanding short exposure times. It contains a k-type thermocouple, which attaches to the backside of the copper slug, where it subsequently measures the backside surface temperature. A teflon collar placed around the curved surface of the slug provides thermal insulation between the slug and brass sleeve.

In contrast, the hot-wall heat flux probe shown in Figure 5.2b can withstand longer exposure times, which allows the test material to achieve and maintain ther-

mal steady-state. Similar to the cold-wall heat flux probe, a k-type thermal couple attaches to the backside of the test material and measures the surface temperature. The thermocouple line feeds through the backing, shims and the insulator piece, which is constructed from type RSLE-57 ZIRCAR. The entire stack ultimately rests inside a SiC sleeve. The metal shims installed between the backing and insulator ensure that the test material rests securely at the base of the sleeve with the front face flush with the leading edge. They also ensure that the test piece cannot retract upwards into the sleeve.

5.3 Cold-Wall Heat Flux

The cold-wall heat flux over the copper slug was the first test performed in this campaign. Copper is commonly considered a fully-catalytic material ($\gamma_{Cu} = 1$), although recent LIF experiments conducted by Meyers et al. in the UVM PDTL have yielded a lower, finite value ($\gamma_{Cu} = 0.0173$), which was ultimately employed by this investigation [64]. Section 5.5 addresses the appropriateness of this choice with a comparison to the fully-catalytic material behavior.

The cold-wall heat flux test involved inserting the probe into the center of the nitrogen flow at standard operating conditions. Meanwhile, the thermocouple recorded the backside temperature response at a 2-Hz sampling rate. The melting temperature of the teflon insulator limited the allowable exposure time for the probe. Therefore, the slug only remained within the flow for a few seconds. If the copper slug were truly isolated from the rest of the assembly, no heat loss would occur after removal from the flow. In reality, the backside temperature gradually decreased after removal, indicating a slight heat loss. Therefore, all cold-wall heat flux tests continued to measure the backside temperature for a period of time after removal in order to determine the

heat loss rate during post processing. Assuming 1-D heat flow through the slug and a constant material catalycity with respect to temperature, Equation 5.1 shows the energy balance at the sample. The heat flux rate is a function of the density (ρ_{Cu} = 8.96-g-cm^{-3}) and specific heat (c_{Cu} = 0.386-J-g^{-1}-K^{-1}) of copper, as well as the length (L_{slug} = 1.3-cm) of the slug.

$$\dot{q} = \rho_{Cu} c_{Cu} L_{slug} \left(\frac{dT}{dt}|_{rise} - \frac{dT}{dt}|_{loss} \right) \tag{5.1}$$

Figure 5.3 shows the backside temperature measured during a cold-wall heat flux experiment. The curve illustrates the principle behavior observed during each test. In particular, it shows the initial sharp rise in temperature corresponding to sample insertion and the gradual decay in temperature after sample removal. Highlighted on the curve are the temperature slopes for the rise and loss terms appearing in Equation 5.1.

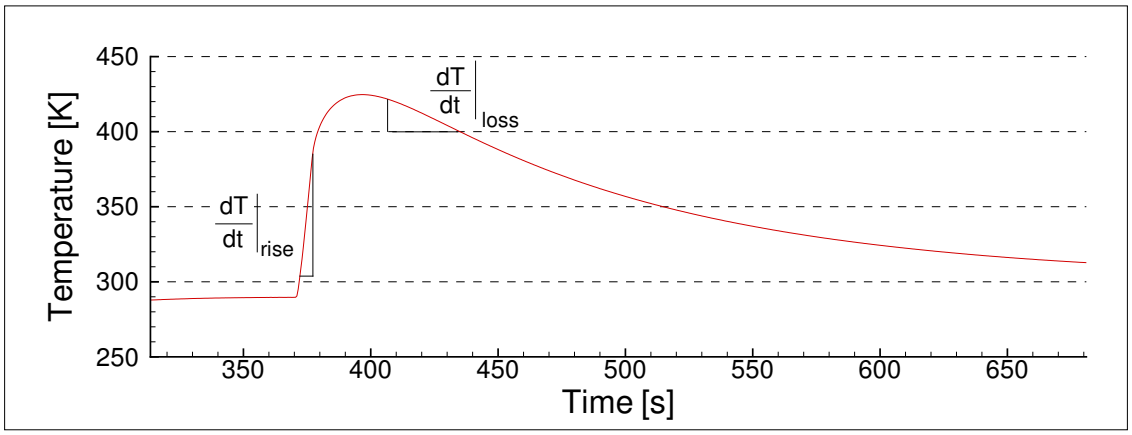

Figure 5.3: The backside temperature of the copper slug measured during a cold-wall heat flux test.

Table 5.1: Cold Wall Heat Flux Data

Test #	Gas	Power [kW]	Gas Flow Rate [SLPM]	Pressure [Torr]	Height [mm]	Heat Flux [W/cm^2]
1a	N_2	14.14	40	160	90	62.93
1b	N_2	14.14	40	160	90	58.94
2a	N_2	14.14	40	160	90	61.51
2b	N_2	14.14	40	160	90	59.83
3	N_2	14.14	40	160	90	61.60
				Average Copper Heat Flux:		**60.96**

Several cold-wall heat flux measurements performed over the span of several days verified the repeatability of the experiment. Table 5.1 shows the results from five tests. Tests 1a and 1b correspond to the heat flux measured during the same run spaced 43 minutes apart, while Tests 2a and 2b are from the same run on a separate day, spaced 23 minutes apart. Test 3 is a measurement from a third day. Note that in each instance where multiple measurements were performed during the same trial, the initial cold wall heat flux measurement was slightly higher, which may reflect a subtle change in the flow conditions over time. The measured values differed by 6.3%, indicating that the heating condition remained relatively constant and repeatable between runs. Moreover, these data further validate the steady flow assumption over the time scale of a particular heat flux test as introduced in Chapter 3.

5.4 Hot-Wall Heat Flux

The second portion of the heat flux campaign involved measuring the energy balance over the leading edge of graphite and silicon carbide samples at standard operating conditions using the hot-wall heat flux probe shown in Figure 5.2b. Once at thermal steady state, the heat flux delivered by the gas is balanced by conduction through the material and re-radiation from the surface, as expressed in Equation 5.2. Terms

appearing on the left side of the equation correspond to gas-phase heat transfer processes and on the right side, heat transfer within the material. The equation clearly illustrates that highly-catalytic materials experience an augmented heat flux not experienced by low-catalytic materials due to the number of exothermic chemical reactions occurring at the wall. Direct measurement of the conduction and re-radiative heat fluxes allow one to calculate the total heat flux through a particular material. Subsequently, one can then determine the catalycity of any material by comparing it to materials with well-characterized catalycities. Here, the catalycity of graphite was determined from the known silicon carbide and copper catalycities.

$$\underbrace{\dot{q}_{convection} + \dot{q}_{reactions}}_{gas\,phase} = \underbrace{\dot{q}_{conduction} + \dot{q}_{re-radiation}}_{material\,response} \tag{5.2}$$

Fourier's Law of thermal conduction relates the heat transfer through a solid body to the temperature gradient ($\frac{dT}{dx}$) and the thermal conductivity (k) of the material, as shown in Equation 5.3. Each sample originally measured 0.635-cm in thickness, which was remeasured after each test in case any erosion occurred. The thermal conductivity for graphite and silicon carbide was 0.5-W-cm^{-1}-K^{-1}, according to the documentation provided by the manufacturer [82]. The front and backside temperatures were measured with the pyrometer and k-type thermal couple, respectively.

$$\dot{q}_{conduction} = -k\frac{dT}{dx} \tag{5.3}$$

Conversely, the Stefan-Boltzmann Law, shown in Equation 5.4, relates the radiative heat flux to the surface temperature. This expression depends on the emissivity of the material (ϵ), the Stefan-Boltzmann constant (σ) and the temperature (T). The graphite material manufacturer provided an emissivity value of $\epsilon_{graphite} = 0.83$, which

was independently verified using the pyrometer using 1-color and 2-color mode as explained in Section 3.5 [82]. Moreover, information about the emissivity of silicon carbide varied between $\epsilon_{SiC} = 0.75$ - 0.9, and was set to $\epsilon_{SiC} = 0.8$ throughout this investigation [83].

$$\dot{q}_{radiation} = \epsilon \sigma T^4 \tag{5.4}$$

Table 5.2 shows the results obtained from all samples tested in this portion of the campaign. Notice that the front face temperature of the graphite is significantly lower than the silicon carbide, which leads to a lower radiative heat flux. However, due to higher conductivity, the total heat flux through graphite is larger than silicon carbide.

Table 5.2: Hot Wall Heat Flux Data

Test [#]	Sample	Height [mm]	T_{front} [K]	T_{back} [K]	$\dot{q}_{cond}$ [W/cm^2]	$\dot{q}_{rad}$ [W/cm^2]	$\dot{q}_{tot}$ [W/cm^2]
1	Graphite	90	1455	1405	37.98	20.98	58.96
2	Graphite	90	1490	1440	37.13	23.00	60.13
3	Graphite	90	1495	1463	35.96	23.51	59.46
4	Graphite	90	1509	1475	38.20	24.40	62.60
						Average Graphite Heat Flux:	**60.28**
Test [#]	Sample	Height [mm]	T_{front} [K]	T_{back} [K]	$\dot{q}_{cond}$ [W/cm^2]	$\dot{q}_{rad}$ [W/cm^2]	$\dot{q}_{tot}$ [W/cm^2]
5	SiC	90	1539	1513	20.47	26.40	46.87
						Average Silicon Carbide Heat Flux:	**46.87**

5.5 Heat Flux Scaling and Energy Conservation

Recall the energy conservation expression in Equation 5.2. Using a suitable analytical expression, one can determine the energy lost in the gas phase across the boundary layer. Fay and Riddell provided a closed-form solution to the stagnation point heating

on a hypersonic vehicle in dissociated gases [10]. Building off their solution, White developed a simplified expression, as shown in Equation 5.5 [84].

$$\dot{q} = 0.763 Pr^{-0.6} (\rho_e \mu_e)^{0.4} (\rho_w \mu_w)^{0.1} \sqrt{\frac{du_e}{dx}} (h_e - h_w) \tag{5.5}$$

Among the controlling parameters on the heat flux are the Prandtl number (Pr), density (ρ), viscosity (μ), velocity gradient ($\frac{du}{dx}$), and enthalpy difference across the boundary layer (h_e - h_w), where subscripts e and w represent values located at the boundary layer edge and wall locations respectively. Although Equation 5.5 yields the absolute heat flux for a particular set of flow conditions, it is advantageous to consider the ratio of measured heat fluxes between any two materials tested. The advantage of this approach is that each experiment was conducted at standard operating conditions with a consistent sample shape. This subsequently allows for all parameters corresponding to the boundary layer edge in Equation 5.5 to cancel. Ultimately, the predicted heat flux ratio between any two materials reduces to the expression shown in Equation 5.6.

$$\frac{\dot{q}_i}{\dot{q}_j} = \frac{[(\rho_w \mu_w)^{0.1} (h_e - h_w)]_i}{[(\rho_w \mu_w)^{0.1} (h_e - h_w)]_j} \tag{5.6}$$

The Non-Equilibrium BOUndary LAyer (NEBOULA) software package is a numerical tool capable of simulating high-enthalpy flow along the stagnation point streamline. It utilizes the similarity equations introduced in Section 2.2.3 to calculate the flow properties for a variety of gas compositions. Note that Equation 5.5 is driven by the total enthalpy difference across the boundary layer. The total enthalpy is equal to the sum of the formation enthalpy, which relates to the chemical composition of the flow, and the sensible enthalpy, which depends on the thermal state of the flow. NEBOULA considers both the chemical and thermal state of the plasma

while determining flow properties and the density, viscosity, and enthalpy values determined by NEBOULA inherently account for the effects of a chemically-reacting gas. Using an LTE condition at the boundary layer edge, NEBOULA calculated the desired quantities expressed in Equation 5.6 using a five-species nitrogen gas model (N_2, N, N^+, N_2^+, e^-). The wall temperature in each simulation was set to the value obtained by the pyrometer for each material. Due to a lack of front-side temperature data during the cold-wall heat flux test, the model utilized the steady-state temperature determined by Meyers et al. on a water-cooled copper sample (T_{copper} = 650-K) [64].

In addition to the thermodynamic state of the flow, NEBOULA also required a catalycity for each material. The catalycities of silicon carbide ($\gamma_{N_2,SiC} = 0.00587$) and copper ($\gamma_{N_2,Cu} = 0.0173$) used in this investigation came from a set of published data by Meyers et al. [64]. These values were determined experimentally using the LIF technique and analysis method explained in detail in Chapter 4. Moreover, the graphite catalycity value determined in Section 4.4 was used ($\gamma_{N_2,gr} = 0.147$).

The values determined by NEBOULA are shown in Table 5.3. Notice that the wall enthalpy over copper is a full order lower than graphite and silicon carbide. This is due to the fact that the copper was water-cooled, unlike the other two materials, which drove the surface temperature down. A larger enthalpy difference across the boundary layer indicates an increase in energy transmitted to the material.

Table 5.3: Heat Flux Data Comparison

Material	$\rho \cdot 10^2$ [kg/m^3]	$\mu \cdot 10^5$ [kg/(m-s)]	h_e [MJ/kg]	h_w [MJ/kg]
Copper	10.6	3.09	16.6	0.696
Graphite	4.89	5.42	16.6	2.04
Silicon Carbide	4.24	5.64	16.6	5.20

Table 5.4 compares the measured heat flux ratios and those predicted by the scal-

ing shown in Equation 5.6. In each case, the error was below 2%, indicating a strong agreement between the analytical approach and the experimental results. Moreover, the heat loss rate within the gas across the boundary layer, which is indicated by the enthalpy change, correlates directly to the magnitude of the heat flux through the material. Note that the highest measured heat flux occurred during the copper cold-wall heat flux test. This aligns with the scaling provided by White, which is due to the large enthalpy difference across the boundary layer for water-cooled copper. The measured graphite heat flux was just over 25% higher than silicon carbide, and only slightly lower than copper, indicating that the catalytic values yielded by Meyers et al. and Lutz are justified, and that graphite is a highly-catalytic material.

Using the same approach with copper treated as a fully-catalytic material ($\gamma_{N_2,Cu} = 1$), the scaling between copper to graphite and copper to silicon carbide become $\frac{\dot{q}_{Cu}}{\dot{q}_{gr}} = 1.15$ and $\frac{\dot{q}_{Cu}}{\dot{q}_{SiC}} = 1.45$ respectively, which are greatly inconsistent with the measured values and further supports the values obtained by Meyers, which assert that copper is less than fully-catalytic.

Table 5.4: Heat Flux Data Comparison

Ratio	Experiment	NEBOULA	% Error
$\frac{\dot{q}_{Cu}}{\dot{q}_{gr}}$	1.011	1.020	0.97
$\frac{\dot{q}_{Cu}}{\dot{q}_{SiC}}$	1.300	1.317	0.29
$\frac{\dot{q}_{gr}}{\dot{q}_{SiC}}$	1.286	1.290	1.3

5.6 Surface Accommodation Factor

Fay and Riddell developed their analytical expression for stagnation point heating by considering fully-catalytic and non-catalytic materials exclusively. Goulard advanced their work by introducing a normalized correction term (ϕ) to analyze partially catalytic materials [30]. His expression is shown in Equation 5.7.

$$\dot{q} = 0.664\sqrt{(\frac{du_e}{dx}\mu_e\rho_e)}Pr^{-2/3}(h_e - h_w)\left[1 + (Le^{2/3}\phi - 1)\frac{c_{A,e}h_{R,A}}{h_e}\right] \tag{5.7}$$

In addition to addressing chemical reactions on surfaces with finite catalycity, this equation is particularly useful in estimating the surface accommodation factor (β), which is defined as the ratio between the total amount of chemical energy absorbed by the surface with respect to the total energy released by chemical reactions occurring at the surface. Many numerical models assume a fully-accommodating wall, which indicates that the surface absorbs all released chemical energy ($\beta = 1$). This is a conservative approach owing to the fact that the actual heat flux may be significantly lower than the value predicted by these programs. Determining the surface accommodation factor through experiment involves independently measuring the correction factor and isolating the heat flux on the surface due to chemical reactions.

In addition to the parameters included in White's scaling (Equation 5.5), Equation 5.7 depends on the Lewis number (Le), and the product of the atomic concentration at the boundary layer edge ($c_{A,e}$) and its formation enthalpy ($h_{R,A}$). The Lewis number is the ratio between the mass diffusivity and thermal diffusivity, whereas the product $c_{A,e}h_{R,A}$ is the total potential chemical energy stored in the atomic species at the boundary layer edge. For nitrogen flows, atomic nitrogen is the only atomic species considered. Thus, this product reduces to $c_{N,e}h_{R,N}$, which indicates the maximum possible amount of additional heating transmitted to the surface due to nitro-

gen recombination. Taking into account the overpopulation of nitrogen atom at the boundary layer edge, as determined in Section 3.6.2, the nitrogen atom mass fraction at the boundary layer edge is $c_{N,e} = 0.786$.

In his analysis, Goulard explicitly relates the correction term to the reaction rate at the wall (k_{w,N_2}) via Equation 5.8 [30]. Therefore, in order to determine the expected value of the total heat flux on graphite via Equation 5.7, one must know the rate at which nitrogen recombination reactions take place at the surface. Using the results obtained from the LIF measurements outlined in Section 4.4, the reaction rate for nitrogen recombination was determined to be $\mathrm{k}_{w,N_2} = 57.25 \pm 14.9$-m-s^{-1}. Moreover, notice that the term $0.664\sqrt{(\frac{du_e}{dx}\mu_e\rho_e)}Pr^{-2/3}$ appears in both Equation 5.7 and Equation 5.8, and depends on the velocity gradient at the boundary layer edge, whose value is not easily determined through experiment. The present analysis leverages the SiC heat flux to determine this entire term, which is labelled by the constant coefficient A_1 for simplicity as shown.

$$\phi = \frac{1}{1 + \frac{(0.664\sqrt{(\frac{du_e}{dx}\mu_e\rho_e)}Pr^{-2/3})Le^{2/3}}{\rho_w k_{w,N_2}}} = \frac{1}{1 + \frac{A_1 Le^{2/3}}{\rho_w k_{w,N_2}}} \tag{5.8}$$

An investigation by Fletcher and Thoemel demonstrated that a suitable catalycity cutoff value separating non-catalytic materials from partially-catalytic materials is $\gamma = 10^{-2}$, which indicates that silicon carbide is an acceptable material with which to study non-catalytic behavior ($\gamma_{N_2,SiC} = 0.00587$) [85]. Thus, the heat flux measured on silicon carbide is due to conduction exclusively and Equation 5.7 reduces to the expression shown in Equation 5.9. Using the measured heat flux and the total enthalpy change across the boundary layer calculated by NEBOULA, the entire leading multiplication factor becomes $A_1 = 4.11(10^{-6})$-kg-cm^{-2}-s^{-1}. Recognize that the advantage of leveraging the SiC heat flux data allowed for the multiplication factor to

be determined without calculating several boundary layer edge flow properties.

$$\dot{q} = 0.664\sqrt{(\frac{du_e}{dx}\mu_e\rho_e)}Pr^{-2/3}(h_e - h_w) = A_1(h_e - h_w) \tag{5.9}$$

Regardless, provided that one could determine the density and viscosity at the boundary layer edge using a suitable numerical model, one could then estimate the velocity gradient at the boundary layer edge ($\frac{\partial u_e}{\partial x}$) from Equation 5.10. Using an LTE assumption at the boundary layer edge, the edge velocity gradient becomes $\frac{\partial u_e}{\partial x} =$ 1480-s^{-1}.

$$\frac{\partial u_e}{\partial x} = \left(\frac{A_1}{0.664Pr^{-2/3}}\right)^2 \frac{1}{\mu_e\rho_e} \tag{5.10}$$

In comparison, White provided a velocity gradient scaling for stagnation flow over the end of a cylinder, as shown in Equation 5.11 [84]. Here, d and V represent the sample diameter and the velocity of the flow respectively. With a sample diameter of $d = 0.0254$-m, the velocity was adjusted until the velocity gradient predicted by White's scaling matched the value determined from Equation 5.10. At a velocity of 25-m-s^{-1}, White's scaling yielded a velocity gradient of $\frac{\partial u_e}{\partial x} = 1556$-s^{-1}, which is 4.8% from the target value.

$$\frac{\partial u_e}{\partial x} = 1.58\frac{d}{V} \tag{5.11}$$

Moreover, the correction factor becomes $\phi = 0.98$ via Equation 5.8, where Le = 1.38, as determined by NEBOULA. Note that the correction factor is close to unity, which supports the assertion that graphite is highly-catalytic. Ultimately, the heat flux predicted by Equation 5.7 becomes $\dot{q}_{tot} = 66.57$-W-cm^{-2}, which is $\approx 10\%$ higher than the average measured heat flux on graphite of $\dot{q}_{meas} = 60.28$-W-cm^{-2}.

Figure 1.4 shows that for the flow conditions considered by Fay and Riddell, the total heat flux on the non-catalytic surface was roughly 20% higher than the conduction portion of the total heat flux on the fully-catalytic surface when the flow is frozen. This is due to the fact that a portion of the total heat flux absorbed by the non-catalytic surface is from atoms directly depositing energy onto the surface via conduction. Conversely, a fully-catalytic material only absorbs conduction from molecules because any atoms reaching a catalytic surface instantly recombine. Figure 5.4 illustrates the difference in the flow chemistry over a non-catalytic and fully-catalytic surface. In both cases, atomic and molecular species exist within the boundary layer. However, the fully-catalytic material instantaneously causes any atomic species to recombine at the surface, and only molecular species are present near the wall. In contrast, both atomic and molecular species exist directly off the surface of the non-catalytic material.

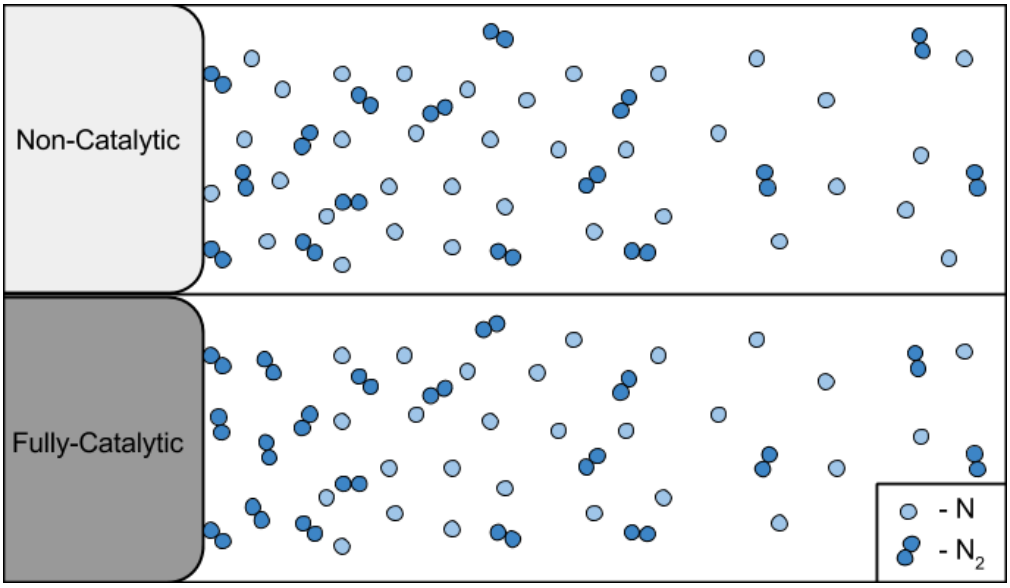

Figure 5.4: An illustration of the flow chemistry over a fully-catalytic and non-catalytic material.

In their analysis, Fay and Riddell considered a gas mixture with an atomic mass

fraction of $c_{A,e} = 0.55$ at the boundary layer edge, which is slightly lower than the atomic nitrogen mass fraction determined in the facility ($c_{N,e} = 0.79$). Note that for the standard operating conditions, the recombination rate parameter for the flow is $C_1 = 6.88(10^{-6})$, which, by inspection of Figure 1.4, is clearly in the frozen flow region. The higher atomic concentration in the experiment would potentially create a greater difference between the total heat flux on the non-catalytic surface and the conduction on the fully-catalytic surface since there are fewer molecules in the flow. However, Fay and Riddell did not consider other atomic concentrations in their analysis and it is unclear to what degree the higher atomic concentration impacts this difference. Therefore, as a first approximation, the measured silicon carbide heat flux was adjusted by 20% in order to determine the conduction portion of the total heat flux on a fully-catalytic material. This yielded a conduction value of $\dot{q}_{cond,\gamma=1} = 37.5\text{-W-cm}^{-2}$.

Subtracting the conduction from the total heat flux on a catalytic wall yields the heat flux due to chemical reactions. Equation 5.12 illustrates how to calculate the surface energy accommodation using the measured heat flux on graphite, and the predicted heat flux for the flow conditions using Equation 5.7.

$$\beta = \frac{\dot{q}_{chem,absorbed}}{\dot{q}_{chem,released}} = \frac{\dot{q}_{meas} - \dot{q}_{cond}}{\dot{q}_{tot} - \dot{q}_{cond}} \tag{5.12}$$

Specifically, the conduction portion was subtracted from the measured and predicted heat flux values and compared, which yielded a value of $\beta = 0.78$. This value, determined through experimental means, is slightly below the fully-accommodating surface assumption $\beta = 1$ and shows that the majority of the liberated energy released during exothermal chemical reactions is ultimately absorbed by the surface.

Chapter 6

Conclusion

6.1 Overview

The results obtained within this study have significantly enhanced the understanding of the nitrogen flow produced within the facility at standard operating conditions, as well as the interaction of the nitrogen flow with graphite samples. The initial mass loss trials clearly showed that introducing even a small amount of oxygen into the flow considerably increased the surface erosion rate. With oxygen present, the mass loss rate was initially very high during the first few minutes of exposure, which was due to shear heating occurring on the corner of the sample. However, once the sample reached a hemispherical shape, the mass loss rate plateaued to a constant value. In comparison, the nitrogen flow produced a much lower recession rate and the sample never eroded to a hemispherical shape over the testing times considered. Hence, the mass loss rate was constant throughout all exposures. Regardless of the mass loss rate behavior, the surface recession was linear in the center of the sample, which corresponded to the stagnation point streamline location. Therefore, for all exposures, the measurement location with respect to the sample could be adjusted

post test by considering the running exposure time at the moment the measurement was taken.

The emission spectroscopy campaign revealed much useful information about the nitrogen flow. First, the grey body experiment provided sufficient agreement with the surface temperature measurements captured by the two-color pyrometer, which yielded a temperature distribution along the side of the sample. In the free stream, the emission spectrometer showed that the flow conditions were repeatable and the jet was axis-symmetric. Over quartz samples, the nitrogen atom emission was apparent throughout the boundary layer, which supported the assertion that the material was non-catalytic. In comparison, the nitrogen atom signal was very low at the boundary layer edge over graphite, and disappeared quickly within the boundary layer. Additionally, the strongest CN features appeared nearest to the surface, which verified that carbon nitridation actively occurred at that location. Although the C_2 Swan system was visible directly off the sample surface, the feature was very weak, and it was determined that the population of C_2 was sufficiently lower than the CN population, and was subsequently ignored. Analysis of the raw emission below 300-nm revealed that there was no observable atomic carbon line at 248-nm.

In the free stream, non-equilibrium was observed in the N_2 2^{nd}-Positive system, which was due to inverse predissociation of ground state nitrogen atoms. Ultimately, the degree of non-equilibrium was quantified by calculating the overpopulation of atomic nitrogen. Aside from this behavior, the remainder of the flow was shown to be in chemical equilibrium by comparing the measured emission with the predicted emission generated by Specair.

Using an Abel inversion, the radial temperature profile within the free stream was determined from several isolated vibronic transitions of N_2 and N_2^+. These trends indicated that the centerline of the free stream was near 5400 - 6000-K and decreased

steadily in the radial direction. In a similar way, the boundary layer edge radial temperature was determined using the nitrogen atom lines at 742-nm, 744-nm, and 746-nm. Here, the three lines predicted the same temperature distribution out to a radius of 15-mm. The centerline temperature of 5000-K agreed well with LIF measurements performed by Meyers over quartz [64].

The final set of information provided by the emission spectroscopy test was the radially distributed emission of N_2 over graphite and quartz and atomic nitrogen over quartz. With respect to the quartz sample, the molecular nitrogen emission increased more rapidly over graphite. Due to the fact that the molecular nitrogen population scaled with the emission, this result supported the contention that graphite increased the molecular nitrogen population through catalytic recombination of atomic nitrogen at the surface. Additionally, the atomic nitrogen population increased dramatically over quartz, which was a direct indication of the non-catalytic behavior of the substance and the increase in density towards the wall driven by the decreasing translational temperature.

Using Goulard's expression relating the diffusion of reactants to the surface to the reaction rate at the surface, the total chemical reaction rate was determined experimentally with LIF. The advantage of the approach utilized in this study was that it avoided the difficulties involved with measuring the absolute number density of the reactants approaching the surface. Instead, the study used the relative atomic nitrogen number density and the measured temperature trend along with the atomic nitrogen molar fraction scaled by its value at the boundary layer edge. Ultimately, this yielded both the reaction rate of carbon nitridation and nitrogen recombination on graphite. To the author's knowledge, this represents the first estimation of these two rates determined exclusively through experimental means for a single trial.

Lastly, the heat flux investigation further supported the data yielded by emission

spectroscopy and LIF. The total heat flux over graphite, silicon carbide and copper was determined experimentally. Moreover, the experimental data was substantiated by using NEBOULA to verify that the energy loss rate within the gas phase across the boundary layer over a particular material was consistent with the measured heat flux through the material at the experimental conditions. Using the correction term introduced by Goulard, the surface accommodation factor was estimated as well, which was slightly below the value describing a fully-accommodating surface.

6.2 Future Work

The methods utilized in this investigation can be applied to future studies on other chemical systems as well. Here, the nitrogen-carbon system was considered because many of the techniques required long test times, and the minimal impact generated by the low surface recession rate could be accounted for in the post processing. However, future studies in the oxygen-carbon system may require slight modifications due to the fact the impact of oxygen on the sample erosion rate. One potential solution is to run a lean mixture of pure oxygen with argon as the buffer gas, which would reduce the recession rate in proportion to the the oxygen mass fraction employed. Of course, this would inherently reduce the oxygen population within the flow and generate a weaker signal. Thus, a suitable flow rate that maintains a sufficient oxygen population while minimizing the erosion rate will need to be determined. Appendix F shows preliminary data from a two photon absorption LIF investigation performed in an air-argon mixture over graphite. Here, the sample surface location was determined by adjusting the optical diagnostic staging until the beam energy dropped by one-half. Repeated scans were performed at this location while the sample receded away from the focal volume. Reducing the total scan time would have a significant impact

here since the sample location at the beginning of the scan is appreciably different than the location at the end of the scan. Perhaps using a smaller total scan width or increasing the stepping rate would be sufficient.

Spontaneous emission measurements are not as time intensive as the LIF measurements and provide more potential in the oxygen-carbon system. A reasonable integration time to use may be 3 - 5-s. Thus, one can acquire centerline scans throughout the boundary layer much quicker than with LIF. Moreover, one can choose to adjust the stepping rate while obtaining spectra for an Abel inversion. In this investigation, all of the spectral features studied dropped off significantly beyond 15-mm from the center of the jet. If limiting the sample exposure time is an issue, then it may be beneficial to employ a finer radial step near the center of the jet and a progressively coarser interval step further away.

The non-equilibrium caused by inverse predissociation could be analyzed by introducing varying degrees of oxygen into the test gas. With oxygen present, the ground state nitrogen atoms may prefer to recombine into NO rather than undergo inverse predissociation. In this experiment, the oxygen flow rate would be progressively increased, while monitoring for a decrease in the non-equilibrium behavior in the N_2 1^{st}-Positive system. At a particular flow rate, the N_2 1^{st}-Positive signal should not change, indicating that the entire atomic nitrogen population had been converted into NO. Hence, the mass flow rate of oxygen here would balance the atomic nitrogen flow rate and would allow for a direct estimate of the nitrogen atom number density.

Sodium lines appeared in several spectra, including the free stream, which indicates that it likely entered the flow from the surface of the quartz tube, which is a consumable component within the facility that occasionally is replaced. Improper sterilization or handling may have transmitted sodium onto the surface directly via inadvertent skin contact. Appendix D shows the integrated emission signal from mul-

tiple plasma chords at two locations relative to quartz. Recognizing that sodium does not participate in any chemical reactions, a future investigation may consider analyzing these sodium trends in order to estimate the radial flow temperature throughout the boundary layer over quartz.

Using the spectrometer, one could analyze the spontaneous emission within the plasma ball, which would provide valuable information about the region of highest energy within the system. Appendix E provides preliminary spectra obtained along the centerline of the quartz tube during operation. Moreover, spectra obtained through Specair is used, which gives an initial estimation of the plasma ball temperature. Using an Abel inversion technique, one could potentially calculate the temperature distribution within the quartz tube. With these data, the facility performance could be maximized to ensure axis-symmetric flow at the plasma creation site as well.

The detection range of the spectrometer was restricted to above 300-nm due to the single available calibration light source used in this study. There are many spectral features below 300-nm of interest that are potentially very useful. Procuring a deuterium light source that emits intense radiation above 200-nm would allow one to calibrate the spectrometer throughout this portion of the spectrum. Among the candidate species of interest are carbon atom (248-nm), silicon (255-nm and 290-nm) and the several lines within the N_2 2^{nd}-Positive system (310-nm, 311-nm, 313-nm, 315-nm). In particular, these molecular nitrogen vibronic lines are sufficiently isolated from the CN Violet features that dominate the near wall locations and may potentially reveal the behavior of the higher energy states of molecular nitrogen towards the surface.

Lastly, there are an assortment of laser diagnostic tests one could employ to study the evolution of other species through the boundary layer beyond atomic nitrogen. Owing to the state of the laser, this investigation was not able to study N_2, CN or

C. Rather, emission spectroscopy and the heat flux measurements were leveraged to support the atomic nitrogen LIF findings. Regardless, utilizing laser diagnostics to probe the flow for these species is a desirable test, since, unlike emission spectroscopy, it actively determines the local temperature and species number densities present within the flow. Further improvements on the laser system would include installing a dual grating into the dye laser, which would significantly decrease the laser line width and provide higher spectral resolution and lower measurement uncertainty.

Appendix A

Calculation of Heat of Formation

The heat of formation equation, as noted by Anderson, is shown in Equation A.1 [22]. Here, the change in enthalpy of the system at a constant temperature ($\Delta H_f^{T_s}$) is related to the difference in the individual sums of the heat of formation of all products and the heat of formation of the reactants. In Equation A.1, i and N represent the index and total number of species in the chemical reaction, respectively. The term ν represents the stoichiometric coefficients and assumes a negative value for the reactants and a positive value for the products in the system. Values from the JANAF Thermochemical tables were used at standard temperatures to determine the heat of formation for each chemical reaction [6]. The values utilized in this study are listed in Table A.1.

$$\Delta H_f^{T_s} = \sum_{i=1}^{N} \nu_i H_{f,i}^{T_s} \tag{A.1}$$

Table A.1: Heat of Formation [6]

Species	$H_f^{T_s}$ [kJ mol^{-1}]
N	472.683
N_2	0
CN	435.136
C	716.670
C_s	0

Appendix B

Non-dimensionalized Boundary Layer Equations

Under the combined set of assumptions that the boundary layer thickness is sufficiently smaller than the characteristic length of the vehicle and that the Reynolds number is sufficiently high, the boundary layer equations become those expressed in Equation 2.2, which are repeated below [22].

$$\begin{aligned}
\frac{\partial(\rho u r)}{\partial x} + \frac{\partial(\rho v r)}{\partial y} &= 0 && (Continuity) \\
\rho u \frac{\partial u}{\partial x} + \rho v \frac{\partial u}{\partial y} &= -\frac{dp_e}{dx} + \frac{\partial}{\partial y}(\mu \frac{\partial u}{\partial y}) && (x - Momentum) \\
\frac{\partial p}{\partial y} &= 0 && (y - Momentum) \\
\rho u \frac{\partial h}{\partial x} + \rho v \frac{\partial h}{\partial y} &= \frac{\partial}{\partial y}(k \frac{\partial T}{\partial y}) + u \frac{dp_e}{dx} + \mu(\frac{\partial u}{\partial y})^2 && (Energy)
\end{aligned}$$

The following set of non-dimensionalized lengths, which were introduced previously, are restated again.

$$\begin{aligned}
\xi &= \int_0^x \rho_e u_e \mu_e r(x)^2 dx \\
\eta &= \frac{u_e r(x)}{\sqrt{2\xi}} \int_0^y \rho dy
\end{aligned}$$

Here, the variable r represents the radial distance from the axis of rotation of the vehicle profile. It is a function of the variable x, which is directed along the local surface tangent. Assuming a spherical shape, Equation B.1 expresses the relationship between these two variables. Notice that the equation simplifies under the small angle assumption.

$$r(x) = x\frac{sin(\theta)}{\theta} \approx x\frac{\theta}{\theta} = x \tag{B.1}$$

The partial derivatives with respect to x and y convert to ξ and η with Equations B.2

$$\begin{aligned}
\frac{\partial}{\partial x} &= \frac{\partial}{\partial \xi}\frac{\partial \xi}{\partial x} + \frac{\partial}{\partial \eta}\frac{\partial \eta}{\partial x} \\
\frac{\partial}{\partial y} &= \frac{\partial}{\partial \xi}\frac{\partial \xi}{\partial y} + \frac{\partial}{\partial \eta}\frac{\partial \eta}{\partial y} \\
where: & \\
\frac{\partial \eta}{\partial x} &= \rho_e u_e \mu_e x^2 \\
\frac{\partial \eta}{\partial y} &= 0 \\
\frac{\partial \eta}{\partial y} &= \frac{u_e x}{\sqrt{2\xi}}\rho
\end{aligned} \tag{B.2}$$

An explicit term for $\frac{\partial \eta}{\partial x}$ is not required in this transformation and will remain in this form. Additionally, introducing the stream function and invoking the small angle approximation gives Equation B.3.

$$\begin{aligned}
\frac{d\psi}{dy} &= \rho u x \\
\frac{d\psi}{dx} &= -\rho v x
\end{aligned} \tag{B.3}$$

Equation B.4 shows the x-momentum equation in terms the non-dimensionalized length units before simplifying.

$$\begin{aligned}\frac{u_e x\rho}{\sqrt{2\xi}}\frac{1}{x}\frac{\partial\psi}{\partial\eta}(\rho_e u_e \mu_e x^2\frac{\partial u}{\partial\xi}+\frac{\partial\eta}{\partial x}\frac{\partial u}{\partial\eta})-\frac{u_e x\rho}{\sqrt{2\xi}}\frac{1}{x}\frac{\partial u}{\partial\eta}(\rho_e u_e\mu_e x^2\frac{\partial\psi}{\partial\xi}+\frac{\partial\eta}{\partial x}\frac{\partial\psi}{\partial\eta}) \\ =-(\rho_e u_e\mu_e x^2\frac{\partial\rho}{\partial\xi}+\frac{\partial\eta}{\partial x}\frac{\partial p}{\partial\eta})+\frac{u_e x\rho}{\sqrt{2\xi}}\frac{\partial}{\partial\eta}(\mu\frac{u_e x\rho}{\sqrt{2\xi}}\frac{\partial u}{\partial\eta})\end{aligned} \tag{B.4}$$

The second term on the right hand side of the equation is equal to zero due to no pressure gradient in the y-direction, which is expressed in the y-momentum equation. Similarly, the second and fourth terms on the left hand side of the equation are equivalent and cancel out. Simplifying gives Equation B.5.

$$\rho_e u_e\mu_e\frac{\partial\psi}{\partial\eta}\frac{\partial u}{\partial\xi}-\rho_e u_e\mu_e\frac{\partial u}{\partial\eta}\frac{\partial\psi}{\partial\xi}=-\sqrt{2\xi}\frac{\rho_e\mu_e}{\rho}\frac{\partial\rho}{\partial\xi}+\frac{\partial}{\partial\eta}(\frac{u_e\rho\mu}{\sqrt{2\xi}}\frac{\partial u}{\partial\eta}) \tag{B.5}$$

Clearly, the dependence on the velocity gradient within the gradient must be converted into a non-dimensional form. To this end, the variable f' is defined as the velocity normalized by the boundary layer edge velocity. The definition of f' is shown in Equation B.6. Here, the prime represents the partial derivative with respect to η.

$$f'\equiv\frac{\partial f}{\partial\eta}=\frac{u}{u_e} \tag{B.6}$$

Thus, taking the partial derivative of u with respect to ξ and η develops the following set of equations. Notice that the velocity at the boundary layer edge is only dependent ξ and not η.

$$\begin{aligned}\frac{\partial u}{\partial\xi} &= f'\frac{du_e}{d\xi}+u_e\frac{\partial f'}{\partial\xi} \\ \frac{\partial u}{\partial\eta} &= u_e f''\end{aligned} \tag{B.7}$$

The definitions for the stream function in Equation B.3 and the partial derivative

with respect to y gives Equation B.8, which relates the stream function and the normalized velocity function.

$$\frac{u_e \rho x}{\sqrt{2\xi}} \frac{\partial \psi}{\partial \eta} = \rho u x = \rho f' u_e \tag{B.8}$$

Upon simplifying,

$$\frac{\partial \psi}{\partial \eta} = \sqrt{2\xi} f' \tag{B.9}$$

After integrating Equation B.9 and differentiating with respect to ξ, Equation B.10 is obtained.

$$\frac{\partial \psi}{\partial \xi} = \sqrt{2\xi} \frac{\partial f}{\partial \xi} + \frac{1}{\sqrt{2\xi}} f \tag{B.10}$$

Lastly, recall from fundamental fluid mechanics that Euler's Equations represent the Navier-Stokes Equations for inviscid flow. That is, they more accurately describe flow at increasing Reynolds numbers. Thus, Euler's Equations provide a suitable method to describe the inviscid flow external of the boundary layer. Equation B.11 shows the x-momentum Euler Equation in two dimensions for steady flow [86].

$$\rho_e u_e \frac{\partial u_e}{\partial x} + \rho_e v_e \frac{\partial u_e}{\partial y} = -\frac{\partial p_e}{\partial x} \tag{B.11}$$

Clearly, the second term is zero; the boundary layer edge velocity in the x-direction is independent of y. This converts Equation B.11 into the ordinary differential equation, shown in Equation B.12 which has been simplified in terms of dp_e.

$$dp_e = -\rho_e u_e du_e \tag{B.12}$$

Equations B.7, B.9, B.10 and B.12 are now plugged into Equation B.5 and simplified, yielding the x-momentum equation in transformed coordinates, shown in Equation B.13

$$(Cf'')' + ff'' = \frac{2\xi}{u_e}\frac{du_e}{d\xi}[(f')^2 - \frac{\rho_e}{\rho}] + 2\xi(f'\frac{\partial f'}{\partial \xi} - \frac{\partial f}{\partial \xi}f'') \tag{B.13}$$

The Chapman-Rubesin factor appears in Equation B.13. It relates the density and viscosity with respect to the boundary layer edge conditions and is expressed in Equation B.14 below.

$$C = \frac{\rho\mu}{\rho_e\mu_e} \tag{B.14}$$

Equation B.13 represents the general non-dimensional form of the x-momentum, which can be simplified further under certain conditions. First, a self-similar form of the equations is desired. Thus, it is argued that the velocity profile at any ξ-location remains constant. In doing so, the final two terms in Equation B.13 are neglected since $\frac{\partial f'}{\partial \xi}$=0 and $\frac{\partial f}{\partial \xi}$=0.

Additionally, for flow along the stagnation point streamline, the velocity is low enough to assume that it is incompressible. Thus, one can relate the boundary layer edge velocity at any x-location with respect to the stagnation point streamline velocity gradient located at the boundary layer edge. This is expressed in Equation B.15.

$$u_e = (\frac{du_e}{dx})_s x. \tag{B.15}$$

Next, revert back to our definition for ξ, shown in Equation 2.3. Here, the expression for the boundary layer edge velocity, Equation B.15, is inserted as shown in Equation B.16. Also shown in Equation B.16 is the explicit form of ξ after integration.

$$\begin{aligned} \xi &= \int_0^x \rho_e \mu_e (\tfrac{du_e}{dx})_s x^3 dx \\ \xi &= \rho_e \mu_e (\tfrac{du_e}{dx})_s \tfrac{x^4}{4} \end{aligned} \tag{B.16}$$

Recognize that one can now solve explicitly for the derivative of u_e with respect to ξ via the Chain Rule, as shown in Equation B.17

$$\frac{du_e}{d\xi} = \frac{du_e/dx}{d\xi/dx} = \frac{1}{\rho_e \mu_e x^3} \tag{B.17}$$

Upon multiplying by the coefficient that appears before the third term in Equation B.13, one obtains the results shown in Equation B.18.

$$\frac{2\xi}{u_e}\frac{du_e}{d\xi} = \frac{2\rho_e \mu_e (\frac{du_e}{dx})_s x^4}{4(\frac{du_e}{dx})_s x}\frac{1}{\rho_e \mu_e x^3} = \frac{1}{2} \tag{B.18}$$

Inserting this result into Equation B.13 provides the x-momentum equation for stagnation point flow over an axis-symmetric body, as shown in Equation B.19. This equation is equivalent to the equation presented in Section 2.2.3.

$$(Cf'')' + ff'' = \frac{1}{2}[(f')^2 - g] \tag{B.19}$$

Appendix C

Full Test Sample Information

Table C.1: Complete Mass Loss Data

Sample [#]	Gas Flow Rate [SLPM]	Exposure Time [mm:ss]	Temperature [^{o}C]	$m_{initial}$ [g]	$\dot{m} \cdot 10^4$ [g/s]
1	N2 - 40.5	5:00	1281	12.829	2.200
	N2 - 40.6	5:00	1275	12.763	2.333
	N2 - 40.5	5:00	1330	12.693	2.600
	N2 - 40.6	5:00	1290	12.615	2.800
2	Air - 11.1 : Ar - 30	5:00	1230	12.830	40.20
	Air - 10.5 : Ar - 30	5:00	1240	11.624	38.27
	Air - 10.7 : Ar - 30	5:00	1290	10.476	33.80
	Air - 10.4 : Ar - 30	5:00	1300	9.462	33.27
3	N_2 - 30 : Ar - 10	5:00	1230	12.826	5.100
	N_2 - 30 : Ar - 10	5:00	1240	12.673	4.733
	N_2 - 29.2 : Ar - 10.3	5:00	1230	12.531	4.533

Continued on next page

Table C.1 – continued from previous page

Sample [#]	Gas Flow Rate [SLPM]	Exposure Time [mm:ss]	Temperature [^{o}C]	$m_{initial}$ [g]	$\dot{m} \cdot 10^4$ [g/s]
	N_2 - 29.5 : Ar - 10.2	5:00	1230	12.395	4.033
4	N_2 - 29.5 : Ar - 10.2	5:00	1260	12.948	3.333
	N_2 - 30 : Ar - 10.2	5:00	-	12.848	2.833
	N_2 - 29.1 : Ar - 10.3	5:30	1225	12.763	3.212
	N_2 - 30 : Ar - 10	4:30	1240	12.657	3.481
5	N_2 - 40	5:00	1280	12.943	3.500
	N_2 - 10.2 : Ar - 30.3	5:00	1120	12.838	1.933
	Ar - 39.8	5:00	<1000	12.531	0.467
6	N_2 - 40	41:53	1330	12.891	5.718
7	N_2 - 39.5	42:26	1340	11.429	6.052
8	Air - 10 : Ar - 30	17:34	1215	12.919	36.17
9	Air - 10 : Ar - 30	5:03	1230	12.900	-
	Air - 10 : Ar - 30	28:19	1180	-	29.79
10	Air - 10 : Ar - 30	32:45	1130	12.645	28.67
11	Air - 9.7 : Ar - 30.1	32:03	1185	12.710	31.41
12	Air - 14.8 : Ar - 25.4	22:53	1205	12.720	43.90
13	N_2 - 40	12:35	1280	12.930	2.146
	N_2 - 40	18:10	1265	12.768	1.247
	N_2 - 40	4:15	-	12.632	-
	N_2 - 40	30:55	1245	-	1.290
14	N_2 - 40	32:47	1250	12.855	1.37

Continued on next page

Table C.1 – continued from previous page

Sample [#]	Gas Flow Rate [SLPM]	Exposure Time [mm:ss]	Temperature [^{o}C]	$m_{initial}$ [g]	$\dot{m} \cdot 10^4$ [g/s]
	N_2 - 40	00:55	-	12.564	8.545
15	N_2 - 39.7	21:25	1080	12.900	0.872
	N_2 - 39.7	13:05	1095	12.788	0.586
	N_2 - 39.9	16:30	1070	12.742	1.030
16	N_2 - 40	10:50	1190	12.563	1.523
	N_2 - 40	21:55	1150	12.464	1.810
17	N_2 - 40	8:00	1260	12.520	2.167
18	N_2 - 40	28:11	1165	12.564	1.833
	N_2 - 39.3	11:46	1145	12.254	1.997
19	N_2 - 40	18:37	1250	12.507	1.325
20	N_2 - 40	32:00	1190	12.616	2.094

Table C.2: Complete Surface Recession Data

Sample [#]	Gas Flow Rate [SLPM]	Exposure Time [mm:ss]	$L_{initial}$ [mm]	$\dot{L}$ [mm/min]
1	N2 - 40	20:00	25.5	-
2	Air - 11.1 : Ar - 30	5:00	25.5	0.15
	Air - 10.5 : Ar - 30	5:00	24.75	0.10
	Air - 10.7 : Ar - 30	5:00	24.25	0.15
	Air - 10.4 : Ar - 30	5:00	23.5	0.15

Continued on next page

Table C.2 – continued from previous page

Sample [#]	Gas Flow Rate [SLPM]	Exposure Time [mm:ss]	$L_{initial}$ [mm]	$\dot{L}$ [mm/min]
3	N2 - 30 : Ar - 10	20:00	25.5	-
4	N2 - 30 : Ar - 10	20:00	25.5	-
5	N2 : Ar	15:00	25.5	-
6	N_2 - 40	41:43	25.5	0.018
7	N_2 - 40	42:26	25.5	0.012
8	Air - 10 : Ar - 30	17:34	25.5	0.128
9	Air - 10 : Ar - 30	33:22	25.5	0.112
10	Air - 10 : Ar - 30	32:45	25.5	0.115
11	Air - 9.7 : Ar - 30.1	32:03	25.5	0.117
12	Air - 14.8 : Ar - 25.4	22:53	25.5	0.175
13	N_2 - 40	1:05:55	25.5	0.0038
14	N_2 - 40	33:42	25.5	0.0045
15	N_2 - 40	51:00	25.5	0.0023
16	N_2 - 40	32:45	23.6	0.0031
17	N_2 - 40	8:00	24.7	0.056
18	N_2 - 40 N_2 - 39.3	51:00 51:00	24.75 24.6	0.0053 0.0043
19	N_2 - 40	18:37	24.7	0.0027
20	N_2 - 40	32:00	24.8	0.0063

Appendix D

Sodium Emission

Sodium lines commonly appear in the emission spectra and are an indication of surface contamination caused by skin contact. One way in which sodium may enter the flow is by improper sanitization and improper handling of key components within the facility. Interestingly, these sodium lines occasionally appear in the free stream, which indicates that the contamination is within the quartz tube and not on the sample. Assuming that sodium is capable of diffusing to the center of the jet, it may potentially behave as a useful tracer particle within the flow. Recognize that sodium is assumed inert with respect to the other flow species and is not expected to participate in any chemical reactions.

In a recent set of emission scans performed over quartz, the sodium line at 589-nm was observed in the free stream and throughout the boundary layer. Figure D.1 shows the radiance captured along plasma chords at $y = 1.5$-mm and $y = 0$-mm from the sample surface. Interestingly, the radiance appears to steadily increase at $y = 1.5$-mm, before dropping severely at a radial position of $x = 18$-mm. Comparatively, the trend at $y = 0$-mm appears to generally stay constant before decreasing at $x = 14$-mm. Figure 3.18 introduced the predicted contour field generated with the Le-

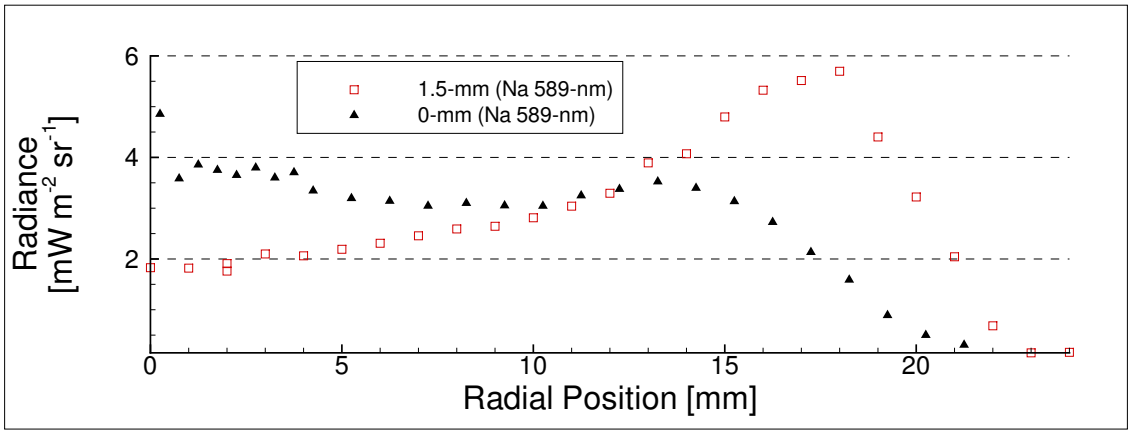

Figure D.1: The captured radiance from the Na line observed at 589-nm at $y = 0$-mm and $y = 1.5$-mm over quartz.

MANS software package over a non-catalytic material. Notice the radial temperature distribution directly off the surface and at the boundary layer edge. At the surface, the temperature is steady, with a slight increase near the corner radius. Moreover, at the boundary layer edge, the flow has more space to turn and the higher temperature regions are located beyond the radius of the sample. It is unclear whether the sodium lines follow this behavior since converting emission captured along plasma chords into radial distributions is inherently difficult to envision. However, Abel inverting these lines with a suitable fit ought to yield the radially distributed emission and possibly the temperature distribution anywhere within the boundary layer.

Appendix E

Plasma Ball Emission

Spontaneous emission from within the quartz tube during full nitrogen flow was captured with the spectrometer. In this experiment, the emission spectrometer assembly was installed upside down to the vertical stage in order to view the quartz tube. The setup was adjusted for 1:1 imaging of the center of the quartz tube with a 3/16" aperture setting. Figure E.1 shows the spectral radiance measured at this location. The ASR shown previously in Figure 3.7 was utilized to convert the raw emission to absolute quantities. Note that the true ASR for this setup is likely different due to the shape of the quartz tube, the material used and the setup itself. Therefore, these data should only be considered a first approximation.

Note the several prominent nitrogen atom lines in Figure E.1. Among the most intense are the lines near 745-nm, 820-nm, and 870-nm, which were observed over quartz as well. Additional lines appear at 650-nm, 665-nm, 675-nm and 790-nm.

Figure E.1 shows the strongest spectral features observed in this investigation. The integration time for these data was 10-ms, whereas the typical integration times utilized throughout Chapter 3 was 1-sec to 20-sec. Figure E.2 shows the spectral radiance of weaker features emitted from within the quartz tube, which are primarily

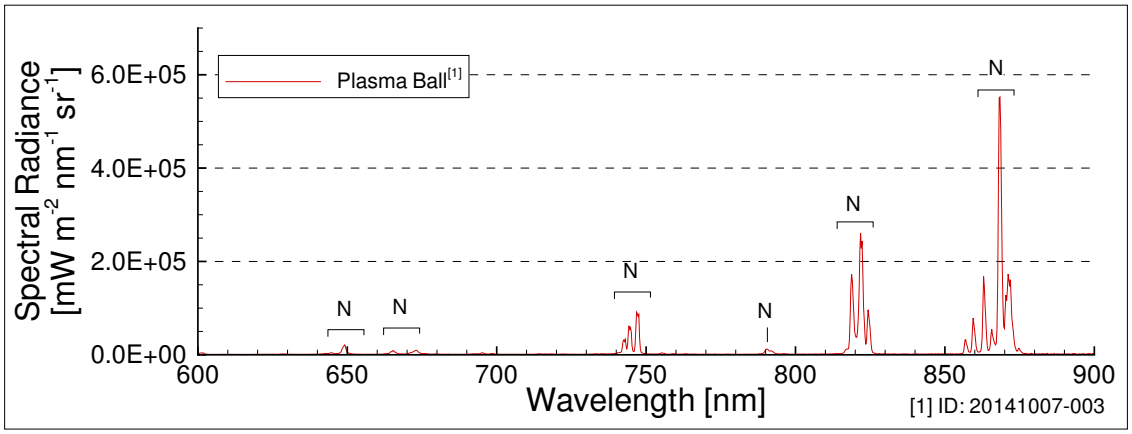

Figure E.1: Major spontaneous emission features from within the quartz tube during full nitrogen flow.

nitrogen atom and nitrogen ion (N^+) lines. Classification of each line was beyond the scope of this investigation. However, it is clear that no broadband features exist, indicating an absence of molecular species.

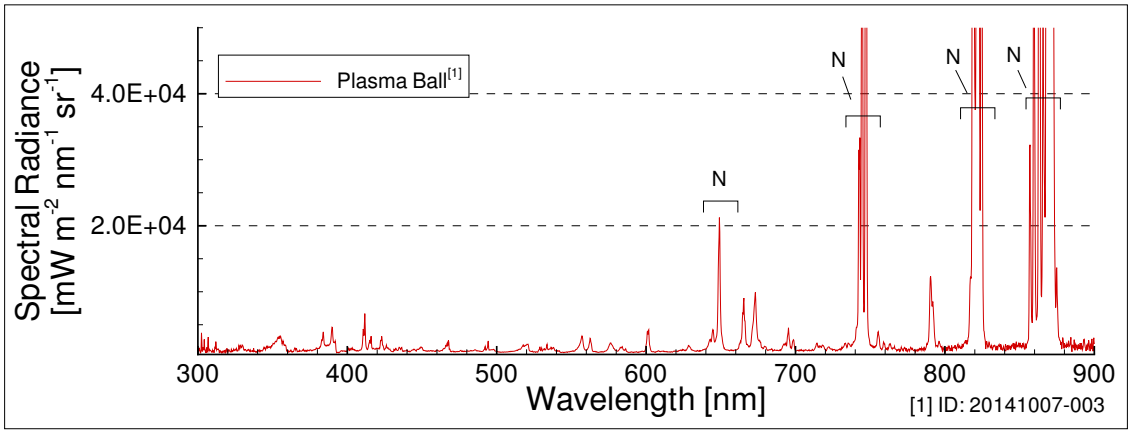

Figure E.2: Minor features emission features from within the quartz tube during full nitrogen flow.

During this investigation, the total emission changed significantly. Although the ratio of the peaks remained constant, the intensity of a given peak alternated between a constant minimum and maximum, which was attributed to the alternating magnetic field within quartz tube. The frequency of the alternating current provided by the

power supply was 4-MHz. The corresponding Nyquist Frequency is thus 8-MHz. This would require measurements be taken every $2.5(10^{-7})$-s in order to truly validate that the behavior is from the supplied power. However, this is well below the minimum sampling rate of the device $\tau_{min} = 3(10^{-3})$-s.

Using the measured spontaneous emission, a lower bound of the plasma ball temperature can be made using Specair. Assuming a pure mixture of nitrogen atom at the known static pressure ($p = 160$-Torr), the translational and electronic temperatures were increased until the spectrum determined by Specair was greater than the measured emission. The slab width was initially set to 36-cm, which corresponded to the inner diameter of the quartz tube. Using these values, the minimum temperature was determined to be 8500-K. Recognize that this represents an overly-conservative estimation considering that a near wall temperature of that value would cause the quartz to instantly melt. Using images acquired from within the facility, an estimation of the plasma ball width in the most intense region was determined to be 22-cm. Using this value for the slab width, the minimum temperature was determined to be 8700-K. Again, this is overly conservative, considering that the temperature within the quartz tube is likely not uniform over the entire slab width. Regardless, the minimum temperature determined with this technique lends some useful insight into the plasma ball conditions.

Appendix F

Preliminary Oxygen LIF Data

Using a similar two photon absorption laser induced fluorescence technique as the one described in Chapter 4, the atomic oxygen relative number density and translational temperature were determined in an air-argon mixture. Here, the volumetric flow rates for each gas was $\dot{V}_{air}$ = 10-SLPM and $\dot{V}_{argon}$ = 30-SLPM. Even with the small degree of oxygen present in the flow, the sample recession rate was significant. Thus, instead of repositioning the optical stages controlling the beam path, PMT and energy meter locations, the focal volume remained in the same location and repeated measurements were taken as the sample receded. Each scan lasted 100-s, which corresponded to a recession of 0.17-mm during every scan and the sample location at the midway point of each scan was considered the average location.

The normalized fluorescence signal is shown in Figure F.1. Similar to the nitrogen atom behavior, the oxygen signal decreased towards the sample surface. This particular data set did not provide many useful scans near the sample surface. This was not an issue with nitrogen flow, since the recession rate is so low, repeated scans at the same location were possible. With the technique used for this test, repeated measurements were not possible and only one near-wall data point was recorded. In-

stalling a dual grating within the dye laser may reduce the possibility of acquiring poor data in the future.

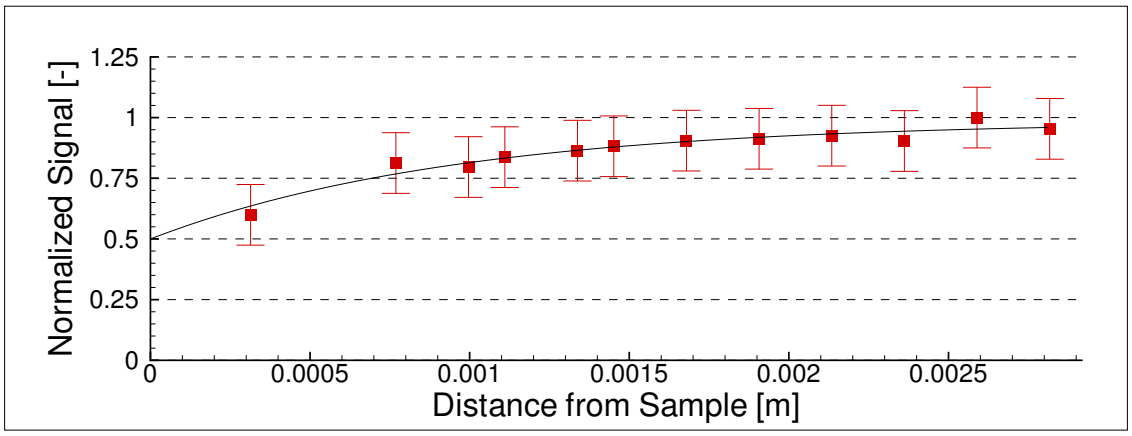

Figure F.1: Relative number density of atomic nitrogen over graphite.

Figure F.2 shows the oxygen atom translational temperature trend towards the sample. Again, the temperature at the boundary layer edge was $T \approx 6000$-K. Moreover, the temperature appeared to decrease towards the wall. In this test, the measured surface temperature of the wall was $T = 1460$-K. Again, an investigation dedicated to the oxygen-carbon system using this technique may reveal more key information about carbon oxidation and oxygen recombination on the surface.

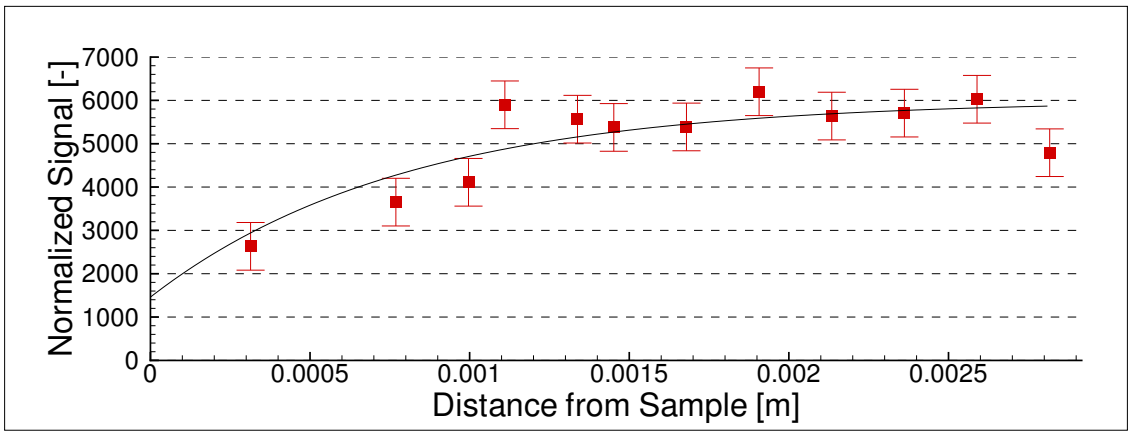

Figure F.2: Temperature distribution of atomic nitrogen over graphite.

Appendix G

Emission Reduction Program

```
%%%%%%%%%%%%%%%%%%%%%%%%%%%%%%%%%%%%%%%%%%%%%%%%%%%%%%%%%%%%%%%%%%%%%%%%%%%%
% Abel Inversion Program
% Andrew Lutz 10/10/2014
%%%%%%%%%%%%%%%%%%%%%%%%%%%%%%%%%%%%%%%%%%%%%%%%%%%%%%%%%%%%%%%%%%%%%%%%%%%%

%This program does the following:
%1. Reads in a .txt file: 1 - positions, 2 - intensity
%2. Fits the I vs x data with polynomial of users choosing
%3. Calculates dI/dx
%4. Using the identity provided by Laux (A.3/A.4), determines e
%5. Using Laux's approach, determines T_LTE

%User inputs the file names and directory location

clear %clears variables from memory
clc %clears command window
clf %clears figures


%-----------User Variables-------------%
%----Data-----%
file_name = '20140625-FS';%YYYYMMDD
wavelength = 744;%nm
%N2(2+): 310,311,313,315,337
%N2(1+): 656,660,668,773
%N2+(1-): 388.1,391
%N: 744,746,824,822
%CN(V): 359,388
%Si: 390
%Na: 588

order = 4;%2-7
qty = 1;%0-pt qty; 1-int qty
num_points = 100;
FWHM = 1.3076;%nm
p = 21331;%Pa (BL edge)
%p = 21598;%Pa (at sample)

%------------Constants----------%
k_B = 1.38E-23;%J/K
T = 1000:1:8000;%K

%%%%%%%%%%%%%%%%%%%%%%%%%%%%%%%%%%%%
%N2 2nd Positive
%%%%%%%%%%%%%%%%%%%%%%%%%%%%%%%%%%%%
if wavelength == 310
    species = 0;%0-N2, 1-N-atom, 2-Si-atom, 3-N2+, 4-CN
    A_ul = 3.063E6;%1/s
    E_l = 1.3012E-18;%J
    E_u = 1.94207E-18;%J
    g_u = 6;
elseif wavelength == 311
    species = 0;%0-N2, 1-N-atom, 2-Si-atom, 3-N2+, 4-CN
    A_ul = 6.149E6;%1/s
    E_l = 1.2685E-18;%J
    E_u = 1.90592E-18;%J
    g_u = 6;
```

```
elseif wavelength == 313
    species = 0;%0-N2, 1-N-atom, 2-Si-atom, 3-N2+, 4-CN
    A_ul = 10.65E6;%1/s
    E_l = 1.2352E-18;%J
    E_u = 1.86865E-18;%J
    g_u = 6;
elseif wavelength == 315
    species = 0;%0-N2, 1-N-atom, 2-Si-atom, 3-N2+, 4-CN
    A_ul = 1.266E7;%1/s
    E_l = 1.2014E-18;%J
    E_u = 1.83025E-18;%J
    g_u = 6;
elseif wavelength == 337
    species = 0;%0-N2, 1-N-atom, 2-Si-atom, 3-N2+, 4-CN
    A_ul = 1.337E7;%1/s
    E_l = 1.184E-18;%J
    E_u = 1.7705E-18;%J
    g_u = 6;


%%%%%%%%%%%%%%%%%%%%%%%%%%%%%%%%%%%%
%CN Violet
%%%%%%%%%%%%%%%%%%%%%%%%%%%%%%%%%%%%
elseif wavelength == 359
    species = 4;%0-N2, 1-N-atom, 2-Si-atom, 3-N2+, 4-CN
    A_ul = 1.59E6;%1/s
    E_l = 0;%J
    E_u = 5.124E-19;%J
    g_u = 4;
elseif wavelength == 388
    species = 4;%0-N2, 1-N-atom, 2-Si-atom, 3-N2+, 4-CN
    A_ul = 1.53E7;%1/s
    E_l = 4.0569E-20;%J
    E_u = 5.12422E-19;%J
    g_u = 4;


%%%%%%%%%%%%%%%%%%%%%%%%%%%%%%%%%%%%
%N2+ 1st Negative
%%%%%%%%%%%%%%%%%%%%%%%%%%%%%%%%%%%%
elseif wavelength == 388.1
    species = 3;%0-N2, 1-N-atom, 2-Si-atom, 3-N2+, 4-CN
    A_ul = 4.257E6;%1/s
    E_l = 6.5034E-20;%J
    E_u = 5.7677E-19;%J
    g_u = 2;
elseif wavelength == 391
    species = 3;%0-N2, 1-N-atom, 2-Si-atom, 3-N2+, 4-CN
    A_ul = 1.214E7;%1/s
    E_l = 2.18388E-20;%J
    E_u = 5.29656E-19;%J
    g_u = 2;
elseif wavelength == 419
    species = 3;%0-N2, 1-N-atom, 2-Si-atom, 3-N2+, 4-CN
    A_ul = 3.69E6;%1/s
    E_l = 1.4948E-19;%J
    E_u = 6.2286E-19;%J
```

```
    g_u = 2;
elseif wavelength == 423
    species = 3;%0-N2, 1-N-atom, 2-Si-atom, 3-N2+, 4-CN
    A_ul = 4.522E6;%1/s
    E_l = 1.07583E-19;%J
    E_u = 5.767E-19;%J
    g_u = 2;


%%%%%%%%%%%%%%%%%%%%%%%%%%%%%%%%%%%%%
%Si Atom
%%%%%%%%%%%%%%%%%%%%%%%%%%%%%%%%%%%%%
elseif wavelength == 390
    species = 2;%0-N2, 1-N-atom, 2-Si-atom, 3-N2+, 4-CN
    A_ul = 3.99E7;%1/s
    E_l = 3.0578E-19;%J
    E_u = 8.1422E-19;%J
    g_u = 1;

%%%%%%%%%%%%%%%%%%%%%%%%%%%%%%%%%%%%%
%Na Atom
%%%%%%%%%%%%%%%%%%%%%%%%%%%%%%%%%%%%%
elseif wavelength == 588
    species = 5;%0-N2, 1-N-atom, 2-Si-atom, 3-N2+, 4-CN, 5-Na
    A_ul = 2.46E8;%1/s
    E_l = 0;%J
    E_u = 3.3713E-19;%J
    g_u = 1;


%%%%%%%%%%%%%%%%%%%%%%%%%%%%%%%%%%%%%
%N2 1st Positive
%%%%%%%%%%%%%%%%%%%%%%%%%%%%%%%%%%%%%
elseif wavelength == 656
    species = 0;%0-N2, 1-N-atom, 2-Si-atom, 3-N2+, 4-CN
    A_ul = 3.115E4;%1/s
    E_l = 1.3124E-18;%J
    E_u = 1.585E-18;%J - Determined from Dunham expansion;
    g_u = 6;
elseif wavelength == 660
    species = 0;%0-N2, 1-N-atom, 2-Si-atom, 3-N2+, 4-CN
    A_ul = 6.889E4;%1/s
    E_l = 1.09528E-18;%J
    E_u = 1.39585E-18;%J - Determined from Dunham expansion;
    g_u = 6;
elseif wavelength == 668
    species = 0;%0-N2, 1-N-atom, 2-Si-atom, 3-N2+, 4-CN
    A_ul = 5.02E4;%1/s
    E_l = 1.068E-18;%J
    E_u = 1.3649E-18;%J - Determined from Dunham expansion;
    g_u = 6;
elseif wavelength == 773
    species = 0;%0-N2, 1-N-atom, 2-Si-atom, 3-N2+, 4-CN
    A_ul = 3.676E4;
    E_l = 0;%J
    E_u = 2.5689017E-19;%J
    g_u = 6;
```

```
%%%%%%%%%%%%%%%%%%%%%%%%%%%%%%%%%%%%%%%%
%N atom
%%%%%%%%%%%%%%%%%%%%%%%%%%%%%%%%%%%%%%%%
elseif wavelength == 742
    species = 1;%0-N2, 1-N-atom, 2-Si-atom, 3-N2+, 4-CN
    A_ul = 5.2E6;%1/s
    E_l = 1.6543E-18;%J
    E_u = 1.9218E-18;%J
    g_u = 4;
elseif wavelength == 744
    species = 1;%0-N2, 1-N-atom, 2-Si-atom, 3-N2+, 4-CN
    A_ul = 1.06E7;%1/s
    E_l = 1.655E-18;%J
    E_u = 1.9218E-18;%J
    g_u = 4;
elseif wavelength == 746
    species = 1;%0-N2, 1-N-atom, 2-Si-atom, 3-N2+, 4-CN
    A_ul = 1.61E7;%1/s
    E_l = 1.6559E-18;%J
    E_u = 1.9218E-18;%J
    g_u = 4;
elseif wavelength == 822
    species = 1;%0-N2, 1-N-atom, 2-Si-atom, 3-N2+, 4-CN
    A_ul = 2.02E7;%1/s
    E_l = 1.65497E-18;%J
    E_u = 1.89646E-18;%J
    g_u = 2;
elseif wavelength == 824
    species = 1;%0-N2, 1-N-atom, 2-Si-atom, 3-N2+, 4-CN
    A_ul = 1.02E7;%1/s
    E_l = 1.6559E-18;%J
    E_u = 1.89682E-18;%J
    g_u = 4;

end

if species == 1 || species == 2 || species == 5
    RHS = p/k_B*F_LTE_ATOM(E_u,species,T);
elseif species == 0 || species == 3 || species == 4
    RHS = p/k_B*F_LTE_MOL(E_u,species,T);
end

%Reads in file and associates position and intensity info
fileID = fopen(['/Users/andrewlutz/Documents/00 - Research/00 - '...
    'Lab Data/00 - Emission/Abel Data/',file_name,'.txt']);
data = textscan(fileID, '%10.2f %f');
positions = data{1};%mm
intensity = data{2};%mW/m^2-sr if integrated; mW/m^2-nm-sr if point

fclose(fileID);

resolved = zeros(101,1);
dx = (max(abs(positions)))/100;%mm
for j = 1:1:length(resolved)
```

```
    resolved(j) = (j-1)*dx;
end
R = round(resolved(end));

%Fits the I vs. x data with polynomial
Abel_Guess = [1,0,0,0,0,0,0,0,0,0,0];

if order == 2
    [a] = lsqcurvefit(@FAbel_order2, Abel_Guess, positions, intensity,...
        [],[],optimset('MaxFunEvals', 1e5,'MaxIter',1e5,'TolX',1E-6,...
        'TolFun',1E-6));
    I = FAbel_order2(a, resolved);

elseif order == 3
    [a] = lsqcurvefit(@FAbel_order3, Abel_Guess, positions, intensity,...
        [],[],optimset('MaxFunEvals', 1e5,'MaxIter',1e5,'TolX',1E-6,...
        'TolFun',1E-6));
    I = FAbel_order3(a, resolved);

elseif order == 4
    [a] = lsqcurvefit(@FAbel_order4, Abel_Guess, positions, intensity,...
        [],[],optimset('MaxFunEvals', 1e5,'MaxIter',1e5,'TolX',1E-6,...
        'TolFun',1E-6));
    I = FAbel_order4(a, resolved);

elseif order == 5
    [a] = lsqcurvefit(@FAbel_order5, Abel_Guess, positions, intensity,...
        [],[],optimset('MaxFunEvals', 1e5,'MaxIter',1e5,'TolX',1E-6,...
        'TolFun',1E-6));
    I = FAbel_order5(a, resolved);

elseif order == 6
    [a] = lsqcurvefit(@FAbel_order6, Abel_Guess, positions, intensity,...
        [],[],optimset('MaxFunEvals', 1e5,'MaxIter',1e5,'TolX',1E-6,...
        'TolFun',1E-6));
    I = FAbel_order6(a, resolved);

elseif order == 7
    [a] = lsqcurvefit(@FAbel_order7, Abel_Guess, positions, intensity,...
        [],[],optimset('MaxFunEvals', 1e5,'MaxIter',1e5,'TolX',1E-6,...
        'TolFun',1E-6));
    I = FAbel_order7(a, resolved);

elseif order == 11
    [a] = lsqcurvefit(@FAbel_order11, Abel_Guess, positions, intensity,...
        [],[],optimset('MaxFunEvals', 1e5,'MaxIter',1e5,'TolX',1E-6,...
        'TolFun',1E-6));
    I = FAbel_order11(a, resolved);

end

%Determines dI/dx from fit
dI_dx = zeros(101,1);
for j = 1:1:length(resolved)
    %dI_dx = 0 at y = 0, so start at 2nd order term in I (mW/m^2-mm-sr)
    dI_dx(j) = 2*a(2) * resolved(j) ...
```

```
        + 3*a(3)*resolved(j).^2 + 4*a(4)*resolved(j).^3 ...
        + 5*a(5)*resolved(j).^4 + 6*a(6)*resolved(j).^5 ...
        + 7*a(7)*resolved(j).^6 + 8*a(8)*resolved(j).^7 ...
        + 9*a(9)*resolved(j).^8 + 10*a(10)*resolved(j).^9 ...
        + 10*a(10)*resolved(j).^9;

end

emiss = zeros(num_points,1);
n_u = zeros(num_points,1);
T_LTE = zeros(num_points,1);
r = zeros(num_points,1);
term_1 = zeros(num_points,1);
term_2 = zeros(num_points,1);
term_3 = zeros(num_points,1);
term_4 = zeros(num_points,1);
term_5 = zeros(num_points,1);
term_6 = zeros(num_points,1);
term_7 = zeros(num_points,1);
Integrand = zeros(length(resolved),num_points);
LHS = zeros(num_points,1);

for i = 1:1:num_points
    %Using Laux's identity, calculates the integral
    r(i) = (resolved(end-1)/num_points)*i;

    %no x^0 term.
    %t_1 = 2 * a(2) * S( x / sqrt(x^2-r^2)) dx
    term_1(i) = 2*a(2)*sqrt(R^2-r(i).^2);

    %t_2 = 3 * a(3) * S( x^2 / sqrt(x^2-r^2)) dx
    term_2(i) = 3*a(3)*1/2*(R*sqrt(R^2-r(i).^2)+r(i).^2*log(R+sqrt...
        (R^2-r(i).^2))-r(i).^2*log(r(i)));

    %t_3 = 4 * a(4) * S( x^3 / sqrt(x^2-r^2)) dx
    term_3(i) = 4*a(4)*sqrt(R^2-r(i).^2)*(2/3*r(i).^2+1/3*R^2);

    %t_4 = 5 * a(5) * S( x^4 / sqrt(x^2-r^2)) dx
    term_4(i) = 5*a(5)*3/8*(sqrt(R^2-r(i).^2)*(r(i).^2*R+2/3*R^3)...
        +r(i).^4*log(R+sqrt(R^2-r(i).^2))-r(i).^4*log(r(i)));

    %t_5 = 6 * a(6) * S( x^5 / sqrt(x^2-r^2)) dx
    term_5(i) = 6*a(6)*sqrt(R^2-r(i).^2)*(8/15*r(i).^4+4/15*...
        r(i).^2*R^2+1/5*R^4);

    %t_6 = 7 * a(7) * S( x^6 / sqrt(x^2-r^2)) dx
    term_6(i) = 7*a(7)*5/16*(sqrt(R^2-r(i).^2)*(r(i).^4*R+2/3*...
        r(i).^2*R^3+8/15*R^5) ...
        +r(i).^6*log(R+sqrt(R^2-r(i).^2))-r(i).^6*log(r(i)));

    %t_7 = 8 * a(8) * S( x^7 / sqrt(x^2-r^2)) dx
    term_7(i) = 8*a(8)*sqrt(R^2-r(i).^2)*(16/35*r(i).^6+...
        8/35*r(i).^4*R^2+6/35*r(i).^2*R^4+R^6/7);

    %Gives the emissivity coefficient
    %mW/m^2-mm-sr = W/m^3-sr (if intensities are integrated quantities.)
```

```
    %mW/m^2-mm-nm-sr = W/m^3-nm-sr (if intensities are at a point.)

    emiss(i) = -1/pi*(term_1(i)+term_2(i)+term_3(i)+term_4(i)+term_5(i)+...
        term_6(i)+term_7(i));

    if qty == 0
        emiss(i) = FWHM*emiss(i);
        %if you have point qts, you need to mult by the FWHM of slit fn.
    end

    n_u(i) = 4*pi*emiss(i)/(A_ul*(E_u-E_l));
    LHS(i) = n_u(i)/g_u;

    for j = 1:1:length(T)
        if LHS(i) < RHS(j)
            T_LTE(i) = T(j);
            break
        end
    end
end



plot(positions,intensity,'x',resolved,I,resolved,dI_dx)
grid on
xlabel('Positions [mm]')
ylabel('Spectral Radiance [mW/m^2-sr]')

figure
plot(r,emiss,'x')
grid on
xlabel('Positions [mm]')
ylabel('Local Emission [W/m^3-sr]')

figure
plot(r,LHS,'x')
grid on
xlabel('Positions [mm]')
ylabel('n_u / g_u [1/m^3]')

figure
plot(T,RHS)
grid on
xlabel('Temperature [K]')
ylabel('RHS [1/m^3]')
axis([min(T), max(T), min(RHS), max(RHS)])

figure
plot(r,T_LTE,'x')
grid on
xlabel('Radial Position [mm]')
ylabel('Temperature [K]')

%%%%%%%%%%%%%%%%%%%%%%%%%%%%%%%%%%%%%%%%%%%%%%%%%%%%%%%%%%%%
%
%Uncertainty Analysis
```

```
%
%%%%%%%%%%%%%%%%%%%%%%%%%%%%%%%%%%%%%%%%%%%%%%%%%%%%%%%%


Sig_D = (intensity-mean(intensity))*...
    transpose(intensity-mean(intensity))/(length(intensity)^2);

for i = 1:1:length(Sig_D)
    for j = 1:1:length(Sig_D)
        if j ~= i
            Sig_D(i,j) = 0;
        end
    end
end

P = zeros(length(intensity),order);
L_A = zeros(length(positions),order);

for i = 1:1:length(intensity)
    for j = 1:1:order
        P(i,j) = positions(i)^j/sqrt(Sig_D(i,i));
    end
end

L_f = inv(transpose(P)*P)*transpose(P);%check this step.
Sig_Rf = L_f*Sig_D*transpose(L_f);



for i = 1:1:length(positions)

    %t_1 = 1 * S( 1 / sqrt(x^2-r^2)) dx
    L_A(i,1) = 0;
    %L_A(i,1) = log(R+sqrt(R^2-positions(i).^2))-log(positions(i));

    %t_1 = 2 * S( x / sqrt(x^2-r^2)) dx
    L_A(i,2) = 2*sqrt(R^2-positions(i).^2);

    %t_2 = 3 * S( x^2 / sqrt(x^2-r^2)) dx
    L_A(i,3) = 3*1/2*(R*sqrt(R^2-positions(i).^2)+positions(i).^2*...
        log(R+sqrt(R^2-positions(i).^2))-positions(i).^2*...
        log(positions(i)));

    %t_3 = 4 * S( x^3 / sqrt(x^2-r^2)) dx
    L_A(i,4) = 4*sqrt(R^2-positions(i).^2)*...
        (2/3*positions(i).^2+1/3*R^2);

    %t_4 = 5 * S( x^4 / sqrt(x^2-r^2)) dx
    L_A(i,5) = 5*3/8*(sqrt(R^2-positions(i).^2)*...
        (positions(i).^2*R+2/3*R^3)+positions(i).^4*log(R+...
        sqrt(R^2-positions(i).^2))-positions(i).^4*log(positions(i)));

    %t_5 = 6 * S( x^5 / sqrt(x^2-r^2)) dx
    L_A(i,6) = 6*sqrt(R^2-positions(i).^2)*(8/15*positions(i).^4+...
        4/15*positions(i).^2*R^2+1/5*R^4);
```

```
    %t_6 = 7 * S( x^6 / sqrt(x^2-r^2)) dx
    L_A(i,7) = 7*5/16*(sqrt(R^2-positions(i).^2)*(positions(i).^4*...
        R+2/3*positions(i).^2*R^3+8/15*R^5)+positions(i).^6*...
        log(R+sqrt(R^2-positions(i).^2))-positions(i).^6*...
        log(positions(i)));

    %t_7 = 8 * S( x^7 / sqrt(x^2-r^2)) dx
    L_A(i,8) = 8*sqrt(R^2-positions(i).^2)*(16/35*positions(i).^6+...
        8/35*positions(i).^4*R^2+6/35*positions(i).^2*R^4+R^6/7);

end

L_A = 1/pi*L_A;
Sig_Ra = L_A(:,1:order)*Sig_Rf*transpose(L_A(:,1:order));

std_dev = zeros(length(positions),1);
for i = 1:1:length(positions)
    std_dev(i) = sqrt(Sig_Ra(i,i));
end
```

Appendix H

Abel Inversion Program

```
%%%%%%%%%%%%%%%%%%%%%%%%%%%%%%%%%%%%%%%%%%%%%%%%%%%%%%%%%%%%%%%%%%%%%%%%%%%%
% Abel Inversion Program
% Andrew Lutz 10/10/2014
%%%%%%%%%%%%%%%%%%%%%%%%%%%%%%%%%%%%%%%%%%%%%%%%%%%%%%%%%%%%%%%%%%%%%%%%%%%%

%This program does the following:
%1. Reads in a .txt file: 1 - positions, 2 - intensity
%2. Fits the I vs x data with polynomial of users choosing
%3. Calculates dI/dx
%4. Using the identity provided by Laux (A.3/A.4), determines e
%5. Using Laux's approach, determines T_LTE

%User inputs the file names and directory location

clear %clears variables from memory
clc %clears command window
clf %clears figures


%-----------User Variables-------------%
%----Data-----%
file_name = '20140625-FS';%YYYYMMDD
wavelength = 744;%nm
%N2(2+): 310,311,313,315,337
%N2(1+): 656,660,668,773
%N2+(1-): 388.1,391
%N: 744,746,824,822
%CN(V): 359,388
%Si: 390
%Na: 588

order = 4;%2-7
qty = 1;%0-pt qty; 1-int qty
num_points = 100;
FWHM = 1.3076;%nm
p = 21331;%Pa (BL edge)
%p = 21598;%Pa (at sample)

%------------Constants----------%
k_B = 1.38E-23;%J/K
T = 1000:1:8000;%K

%%%%%%%%%%%%%%%%%%%%%%%%%%%%%%%%%%%%
%N2 2nd Positive
%%%%%%%%%%%%%%%%%%%%%%%%%%%%%%%%%%%%
if wavelength == 310
    species = 0;%0-N2, 1-N-atom, 2-Si-atom, 3-N2+, 4-CN
    A_ul = 3.063E6;%1/s
    E_l = 1.3012E-18;%J
    E_u = 1.94207E-18;%J
    g_u = 6;
elseif wavelength == 311
    species = 0;%0-N2, 1-N-atom, 2-Si-atom, 3-N2+, 4-CN
    A_ul = 6.149E6;%1/s
    E_l = 1.2685E-18;%J
    E_u = 1.90592E-18;%J
    g_u = 6;
```

```
elseif wavelength == 313
    species = 0;%0-N2, 1-N-atom, 2-Si-atom, 3-N2+, 4-CN
    A_ul = 10.65E6;%1/s
    E_l = 1.2352E-18;%J
    E_u = 1.86865E-18;%J
    g_u = 6;
elseif wavelength == 315
    species = 0;%0-N2, 1-N-atom, 2-Si-atom, 3-N2+, 4-CN
    A_ul = 1.266E7;%1/s
    E_l = 1.2014E-18;%J
    E_u = 1.83025E-18;%J
    g_u = 6;
elseif wavelength == 337
    species = 0;%0-N2, 1-N-atom, 2-Si-atom, 3-N2+, 4-CN
    A_ul = 1.337E7;%1/s
    E_l = 1.184E-18;%J
    E_u = 1.7705E-18;%J
    g_u = 6;


%%%%%%%%%%%%%%%%%%%%%%%%%%%%%%%%%%%%
%CN Violet
%%%%%%%%%%%%%%%%%%%%%%%%%%%%%%%%%%%%
elseif wavelength == 359
    species = 4;%0-N2, 1-N-atom, 2-Si-atom, 3-N2+, 4-CN
    A_ul = 1.59E6;%1/s
    E_l = 0;%J
    E_u = 5.124E-19;%J
    g_u = 4;
elseif wavelength == 388
    species = 4;%0-N2, 1-N-atom, 2-Si-atom, 3-N2+, 4-CN
    A_ul = 1.53E7;%1/s
    E_l = 4.0569E-20;%J
    E_u = 5.12422E-19;%J
    g_u = 4;


%%%%%%%%%%%%%%%%%%%%%%%%%%%%%%%%%%%%
%N2+ 1st Negative
%%%%%%%%%%%%%%%%%%%%%%%%%%%%%%%%%%%%
elseif wavelength == 388.1
    species = 3;%0-N2, 1-N-atom, 2-Si-atom, 3-N2+, 4-CN
    A_ul = 4.257E6;%1/s
    E_l = 6.5034E-20;%J
    E_u = 5.7677E-19;%J
    g_u = 2;
elseif wavelength == 391
    species = 3;%0-N2, 1-N-atom, 2-Si-atom, 3-N2+, 4-CN
    A_ul = 1.214E7;%1/s
    E_l = 2.18388E-20;%J
    E_u = 5.29656E-19;%J
    g_u = 2;
elseif wavelength == 419
    species = 3;%0-N2, 1-N-atom, 2-Si-atom, 3-N2+, 4-CN
    A_ul = 3.69E6;%1/s
    E_l = 1.4948E-19;%J
    E_u = 6.2286E-19;%J
```

```
    g_u = 2;
elseif wavelength == 423
    species = 3;%0-N2, 1-N-atom, 2-Si-atom, 3-N2+, 4-CN
    A_ul = 4.522E6;%1/s
    E_l = 1.07583E-19;%J
    E_u = 5.767E-19;%J
    g_u = 2;


%%%%%%%%%%%%%%%%%%%%%%%%%%%%%%%%%%%%%
%Si Atom
%%%%%%%%%%%%%%%%%%%%%%%%%%%%%%%%%%%%%
elseif wavelength == 390
    species = 2;%0-N2, 1-N-atom, 2-Si-atom, 3-N2+, 4-CN
    A_ul = 3.99E7;%1/s
    E_l = 3.0578E-19;%J
    E_u = 8.1422E-19;%J
    g_u = 1;

%%%%%%%%%%%%%%%%%%%%%%%%%%%%%%%%%%%%%
%Na Atom
%%%%%%%%%%%%%%%%%%%%%%%%%%%%%%%%%%%%%
elseif wavelength == 588
    species = 5;%0-N2, 1-N-atom, 2-Si-atom, 3-N2+, 4-CN, 5-Na
    A_ul = 2.46E8;%1/s
    E_l = 0;%J
    E_u = 3.3713E-19;%J
    g_u = 1;


%%%%%%%%%%%%%%%%%%%%%%%%%%%%%%%%%%%%%
%N2 1st Positive
%%%%%%%%%%%%%%%%%%%%%%%%%%%%%%%%%%%%%
elseif wavelength == 656
    species = 0;%0-N2, 1-N-atom, 2-Si-atom, 3-N2+, 4-CN
    A_ul = 3.115E4;%1/s
    E_l = 1.3124E-18;%J
    E_u = 1.585E-18;%J - Determined from Dunham expansion;
    g_u = 6;
elseif wavelength == 660
    species = 0;%0-N2, 1-N-atom, 2-Si-atom, 3-N2+, 4-CN
    A_ul = 6.889E4;%1/s
    E_l = 1.09528E-18;%J
    E_u = 1.39585E-18;%J - Determined from Dunham expansion;
    g_u = 6;
elseif wavelength == 668
    species = 0;%0-N2, 1-N-atom, 2-Si-atom, 3-N2+, 4-CN
    A_ul = 5.02E4;%1/s
    E_l = 1.068E-18;%J
    E_u = 1.3649E-18;%J - Determined from Dunham expansion;
    g_u = 6;
elseif wavelength == 773
    species = 0;%0-N2, 1-N-atom, 2-Si-atom, 3-N2+, 4-CN
    A_ul = 3.676E4;
    E_l = 0;%J
    E_u = 2.5689017E-19;%J
    g_u = 6;
```

```
%%%%%%%%%%%%%%%%%%%%%%%%%%%%%%%%%%%%%%%%
%N atom
%%%%%%%%%%%%%%%%%%%%%%%%%%%%%%%%%%%%%%%%
elseif wavelength == 742
    species = 1;%0-N2, 1-N-atom, 2-Si-atom, 3-N2+, 4-CN
    A_ul = 5.2E6;%1/s
    E_l = 1.6543E-18;%J
    E_u = 1.9218E-18;%J
    g_u = 4;
elseif wavelength == 744
    species = 1;%0-N2, 1-N-atom, 2-Si-atom, 3-N2+, 4-CN
    A_ul = 1.06E7;%1/s
    E_l = 1.655E-18;%J
    E_u = 1.9218E-18;%J
    g_u = 4;
elseif wavelength == 746
    species = 1;%0-N2, 1-N-atom, 2-Si-atom, 3-N2+, 4-CN
    A_ul = 1.61E7;%1/s
    E_l = 1.6559E-18;%J
    E_u = 1.9218E-18;%J
    g_u = 4;
elseif wavelength == 822
    species = 1;%0-N2, 1-N-atom, 2-Si-atom, 3-N2+, 4-CN
    A_ul = 2.02E7;%1/s
    E_l = 1.65497E-18;%J
    E_u = 1.89646E-18;%J
    g_u = 2;
elseif wavelength == 824
    species = 1;%0-N2, 1-N-atom, 2-Si-atom, 3-N2+, 4-CN
    A_ul = 1.02E7;%1/s
    E_l = 1.6559E-18;%J
    E_u = 1.89682E-18;%J
    g_u = 4;

end

if species == 1 || species == 2 || species == 5
    RHS = p/k_B*F_LTE_ATOM(E_u,species,T);
elseif species == 0 || species == 3 || species == 4
    RHS = p/k_B*F_LTE_MOL(E_u,species,T);
end

%Reads in file and associates position and intensity info
fileID = fopen(['/Users/andrewlutz/Documents/00 - Research/00 - '...
    'Lab Data/00 - Emission/Abel Data/',file_name,'.txt']);
data = textscan(fileID, '%10.2f %f');
positions = data{1};%mm
intensity = data{2};%mW/m^2-sr if integrated; mW/m^2-nm-sr if point

fclose(fileID);

resolved = zeros(101,1);
dx = (max(abs(positions)))/100;%mm
for j = 1:1:length(resolved)
```

```
    resolved(j) = (j-1)*dx;
end
R = round(resolved(end));

%Fits the I vs. x data with polynomial
Abel_Guess = [1,0,0,0,0,0,0,0,0,0,0];

if order == 2
    [a] = lsqcurvefit(@FAbel_order2, Abel_Guess, positions, intensity,...
        [],[],optimset('MaxFunEvals', 1e5,'MaxIter',1e5,'TolX',1E-6,...
        'TolFun',1E-6));
    I = FAbel_order2(a, resolved);

elseif order == 3
    [a] = lsqcurvefit(@FAbel_order3, Abel_Guess, positions, intensity,...
        [],[],optimset('MaxFunEvals', 1e5,'MaxIter',1e5,'TolX',1E-6,...
        'TolFun',1E-6));
    I = FAbel_order3(a, resolved);

elseif order == 4
    [a] = lsqcurvefit(@FAbel_order4, Abel_Guess, positions, intensity,...
        [],[],optimset('MaxFunEvals', 1e5,'MaxIter',1e5,'TolX',1E-6,...
        'TolFun',1E-6));
    I = FAbel_order4(a, resolved);

elseif order == 5
    [a] = lsqcurvefit(@FAbel_order5, Abel_Guess, positions, intensity,...
        [],[],optimset('MaxFunEvals', 1e5,'MaxIter',1e5,'TolX',1E-6,...
        'TolFun',1E-6));
    I = FAbel_order5(a, resolved);

elseif order == 6
    [a] = lsqcurvefit(@FAbel_order6, Abel_Guess, positions, intensity,...
        [],[],optimset('MaxFunEvals', 1e5,'MaxIter',1e5,'TolX',1E-6,...
        'TolFun',1E-6));
    I = FAbel_order6(a, resolved);

elseif order == 7
    [a] = lsqcurvefit(@FAbel_order7, Abel_Guess, positions, intensity,...
        [],[],optimset('MaxFunEvals', 1e5,'MaxIter',1e5,'TolX',1E-6,...
        'TolFun',1E-6));
    I = FAbel_order7(a, resolved);

elseif order == 11
    [a] = lsqcurvefit(@FAbel_order11, Abel_Guess, positions, intensity,...
        [],[],optimset('MaxFunEvals', 1e5,'MaxIter',1e5,'TolX',1E-6,...
        'TolFun',1E-6));
    I = FAbel_order11(a, resolved);

end

%Determines dI/dx from fit
dI_dx = zeros(101,1);
for j = 1:1:length(resolved)
    %dI_dx = 0 at y = 0, so start at 2nd order term in I (mW/m^2-mm-sr)
    dI_dx(j) = 2*a(2) * resolved(j) ...
```

```
        + 3*a(3)*resolved(j).^2 + 4*a(4)*resolved(j).^3 ...
        + 5*a(5)*resolved(j).^4 + 6*a(6)*resolved(j).^5 ...
        + 7*a(7)*resolved(j).^6 + 8*a(8)*resolved(j).^7 ...
        + 9*a(9)*resolved(j).^8 + 10*a(10)*resolved(j).^9 ...
        + 10*a(10)*resolved(j).^9;

end

emiss = zeros(num_points,1);
n_u = zeros(num_points,1);
T_LTE = zeros(num_points,1);
r = zeros(num_points,1);
term_1 = zeros(num_points,1);
term_2 = zeros(num_points,1);
term_3 = zeros(num_points,1);
term_4 = zeros(num_points,1);
term_5 = zeros(num_points,1);
term_6 = zeros(num_points,1);
term_7 = zeros(num_points,1);
Integrand = zeros(length(resolved),num_points);
LHS = zeros(num_points,1);

for i = 1:1:num_points
    %Using Laux's identity, calculates the integral
    r(i) = (resolved(end-1)/num_points)*i;

    %no x^0 term.
    %t_1 = 2 * a(2) * S( x / sqrt(x^2-r^2)) dx
    term_1(i) = 2*a(2)*sqrt(R^2-r(i).^2);

    %t_2 = 3 * a(3) * S( x^2 / sqrt(x^2-r^2)) dx
    term_2(i) = 3*a(3)*1/2*(R*sqrt(R^2-r(i).^2)+r(i).^2*log(R+sqrt...
        (R^2-r(i).^2))-r(i).^2*log(r(i)));

    %t_3 = 4 * a(4) * S( x^3 / sqrt(x^2-r^2)) dx
    term_3(i) = 4*a(4)*sqrt(R^2-r(i).^2)*(2/3*r(i).^2+1/3*R^2);

    %t_4 = 5 * a(5) * S( x^4 / sqrt(x^2-r^2)) dx
    term_4(i) = 5*a(5)*3/8*(sqrt(R^2-r(i).^2)*(r(i).^2*R+2/3*R^3)...
        +r(i).^4*log(R+sqrt(R^2-r(i).^2))-r(i).^4*log(r(i)));

    %t_5 = 6 * a(6) * S( x^5 / sqrt(x^2-r^2)) dx
    term_5(i) = 6*a(6)*sqrt(R^2-r(i).^2)*(8/15*r(i).^4+4/15*...
        r(i).^2*R^2+1/5*R^4);

    %t_6 = 7 * a(7) * S( x^6 / sqrt(x^2-r^2)) dx
    term_6(i) = 7*a(7)*5/16*(sqrt(R^2-r(i).^2)*(r(i).^4*R+2/3*...
        r(i).^2*R^3+8/15*R^5) ...
        +r(i).^6*log(R+sqrt(R^2-r(i).^2))-r(i).^6*log(r(i)));

    %t_7 = 8 * a(8) * S( x^7 / sqrt(x^2-r^2)) dx
    term_7(i) = 8*a(8)*sqrt(R^2-r(i).^2)*(16/35*r(i).^6+...
        8/35*r(i).^4*R^2+6/35*r(i).^2*R^4+R^6/7);

    %Gives the emissivity coefficient
    %mW/m^2-mm-sr = W/m^3-sr (if intensities are integrated quantities.)
```

```
    %mW/m^2-mm-nm-sr = W/m^3-nm-sr (if intensities are at a point.)

    emiss(i) = -1/pi*(term_1(i)+term_2(i)+term_3(i)+term_4(i)+term_5(i)+...
        term_6(i)+term_7(i));

    if qty == 0
        emiss(i) = FWHM*emiss(i);
        %if you have point qts, you need to mult by the FWHM of slit fn.
    end

    n_u(i) = 4*pi*emiss(i)/(A_ul*(E_u-E_l));
    LHS(i) = n_u(i)/g_u;

    for j = 1:1:length(T)
        if LHS(i) < RHS(j)
            T_LTE(i) = T(j);
            break
        end
    end
end



plot(positions,intensity,'x',resolved,I,resolved,dI_dx)
grid on
xlabel('Positions [mm]')
ylabel('Spectral Radiance [mW/m^2-sr]')

figure
plot(r,emiss,'x')
grid on
xlabel('Positions [mm]')
ylabel('Local Emission [W/m^3-sr]')

figure
plot(r,LHS,'x')
grid on
xlabel('Positions [mm]')
ylabel('n_u / g_u [1/m^3]')

figure
plot(T,RHS)
grid on
xlabel('Temperature [K]')
ylabel('RHS [1/m^3]')
axis([min(T), max(T), min(RHS), max(RHS)])

figure
plot(r,T_LTE,'x')
grid on
xlabel('Radial Position [mm]')
ylabel('Temperature [K]')

%%%%%%%%%%%%%%%%%%%%%%%%%%%%%%%%%%%%%%%%%%%%%%%%%%%%%%%%%%%%
%
%Uncertainty Analysis
```

```
%
%%%%%%%%%%%%%%%%%%%%%%%%%%%%%%%%%%%%%%%%%%%%%%%%%%%%%%%%


Sig_D = (intensity-mean(intensity))*...
    transpose(intensity-mean(intensity))/(length(intensity)^2);

for i = 1:1:length(Sig_D)
    for j = 1:1:length(Sig_D)
        if j ~= i
            Sig_D(i,j) = 0;
        end
    end
end

P = zeros(length(intensity),order);
L_A = zeros(length(positions),order);

for i = 1:1:length(intensity)
    for j = 1:1:order
        P(i,j) = positions(i)^j/sqrt(Sig_D(i,i));
    end
end

L_f = inv(transpose(P)*P)*transpose(P);%check this step.
Sig_Rf = L_f*Sig_D*transpose(L_f);



for i = 1:1:length(positions)

    %t_1 = 1 * S( 1 / sqrt(x^2-r^2)) dx
    L_A(i,1) = 0;
    %L_A(i,1) = log(R+sqrt(R^2-positions(i).^2))-log(positions(i));

    %t_1 = 2 * S( x / sqrt(x^2-r^2)) dx
    L_A(i,2) = 2*sqrt(R^2-positions(i).^2);

    %t_2 = 3 * S( x^2 / sqrt(x^2-r^2)) dx
    L_A(i,3) = 3*1/2*(R*sqrt(R^2-positions(i).^2)+positions(i).^2*...
        log(R+sqrt(R^2-positions(i).^2))-positions(i).^2*...
        log(positions(i)));

    %t_3 = 4 * S( x^3 / sqrt(x^2-r^2)) dx
    L_A(i,4) = 4*sqrt(R^2-positions(i).^2)*...
        (2/3*positions(i).^2+1/3*R^2);

    %t_4 = 5 * S( x^4 / sqrt(x^2-r^2)) dx
    L_A(i,5) = 5*3/8*(sqrt(R^2-positions(i).^2)*...
        (positions(i).^2*R+2/3*R^3)+positions(i).^4*log(R+...
        sqrt(R^2-positions(i).^2))-positions(i).^4*log(positions(i)));

    %t_5 = 6 * S( x^5 / sqrt(x^2-r^2)) dx
    L_A(i,6) = 6*sqrt(R^2-positions(i).^2)*(8/15*positions(i).^4+...
        4/15*positions(i).^2*R^2+1/5*R^4);
```

```
    %t_6 = 7 * S( x^6 / sqrt(x^2-r^2)) dx
    L_A(i,7) = 7*5/16*(sqrt(R^2-positions(i).^2)*(positions(i).^4*...
        R+2/3*positions(i).^2*R^3+8/15*R^5)+positions(i).^6*...
        log(R+sqrt(R^2-positions(i).^2))-positions(i).^6*...
        log(positions(i)));

    %t_7 = 8 * S( x^7 / sqrt(x^2-r^2)) dx
    L_A(i,8) = 8*sqrt(R^2-positions(i).^2)*(16/35*positions(i).^6+...
        8/35*positions(i).^4*R^2+6/35*positions(i).^2*R^4+R^6/7);

end

L_A = 1/pi*L_A;
Sig_Ra = L_A(:,1:order)*Sig_Rf*transpose(L_A(:,1:order));

std_dev = zeros(length(positions),1);
for i = 1:1:length(positions)
    std_dev(i) = sqrt(Sig_Ra(i,i));
end
```

```
function Fun = F_LTE_ATOM(E_u,species,T)

k_B = 1.38E-23;%J/K

if species == 1 %N-atom

    if T < 8000
        A = -5.169793145297368885 95E-01;
        B =  2.429661097157827416 57E-03;
        C = -4.624887398456396381 40E-06;
        D =  4.725595057496285807 93E-09;
        E = -2.893883438579718842 73E-12;
        F =  1.118944256795258702 96E-15;
        G = -2.786850758040323070 84E-19;
        H =  4.442420010659971552 34E-23;
        I = -4.361706792673145246 49E-27;
        J =  2.395166987468947470 13E-31;
        K = -5.618157614537459065 67E-36;
    else

        A = 1;
        B = 0;
        C = 0;
        D = 0;
        E = 0;
        F = 0;
        G = 0;
        H = 0;
        I = 0;
        J = 0;
        K = 0;

    end

    Fun =
(A+B*T+C*T.^2+D*T.^3+E*T.^4+F*T.^5+G*T.^6+H*T.^7+I*T.^8+J*T.^9+K*T.^10)
...
        ./(4*T).*exp(-E_u./(T*k_B));

elseif species == 2 %Si atom

    A = 1E0;
    Fun = A./T.*exp(-E_u./(T*k_B))./(1+3.*exp(-110./T)+5*exp(-
318.82./T));

elseif species == 5 %Na atom

    A = 1E-10;
    Fun = A./T.*exp(-E_u./(T*k_B));

end
end
```

```
function Fun = F_LTE_MOL(E_u,species,T)

k_B = 1.38E-23;%J/K

if species == 0

    %%%%%%%%%%%%%%%%%%%%%%%%%%%%%%%%%%%
    % N2
    %%%%%%%%%%%%%%%%%%%%%%%%%%%%%%%%%%%

    if T > 8000
        A =  1.3152678171515368443 8E+00;
        B = -1.5211064353968101192 6E-03;
        C =  2.9770609970067298036 3E-06;
        D = -3.1267336497262155647 1E-09;
        E =  1.9646656696398060933 2E-12;
        F = -7.7723586166292296905 1E-16;
        G =  1.9735509844472234925 5E-19;
        H = -3.1944845508874853249 0E-23;
        I =  3.1714280488814208317 7E-27;
        J = -1.7538597442313691589 2E-31;
        K =  4.1279425058199261684 4E-36;

    else
        A =  1.4115352162748325781 6E+02;
        B = -7.6846936785258265767 4E-02;
        C =  1.6765198285977602691 7E-05;
        D = -1.8312641960113727611 1E-09;
        E =  1.0011288203320151534 8E-13;
        F = -2.1906797141276940378 7E-18;
        G = 0;
        H = 0;
        I = 0;
        J = 0;
        K = 0;
    end

    Theta_r = 2.9;%K
    Theta_v = 3390;%K

    Fun = (A+B*T+C*T.^2+D*T.^3+E*T.^4+F*T.^5+G*T.^6+H*T.^7+I*...
        T.^8+J*T.^9+K*T.^10)./((T/(2*Theta_r)).*(1./...
        (1-exp(-Theta_v./T)))./T.*exp(-E_u./(T*k_B));


elseif species == 3

    %%%%%%%%%%%%%%%%%%%%%%%%%%%%%%%%%%%
    % N2+
    %%%%%%%%%%%%%%%%%%%%%%%%%%%%%%%%%%%

    if T > 6000

        A =  2.8369806070715891666 0E-01;
        B = -5.5283398990691725791 2E-04;
        C =  4.6386168535724773626 6E-07;
```

```
        D = -2.2236420398468853842E-10;
        E =  6.7778185290556815369OE-14;
        F = -1.3774737048752013795 3E-17;
        G =  1.8954824272901243371 8E-21;
        H = -1.7473679495660885066 9E-25;
        I =  1.0339766187186296667 2E-29;
        J = -3.5467329960444769426 7E-34;
        K =  5.3548324799360618153 9E-39;
    elseif T < 4000
        A = 10E-9;
        B = 0;
        C = 0;
        D = 0;
        E = 0;
        F = 0;
        G = 0;
        H = 0;
        I = 0;
        J = 0;
        K = 0;
    else
        A = -2.5556530972929970141 3E-02;
        B =  6.3455093611094131418 3E-05;
        C = -7.0565336215113597172 0E-08;
        D =  4.6277150782985855091 2E-11;
        E = -1.9816405818382915260 9E-14;
        F =  5.7879066005782552347 8E-18;
        G = -1.1672857061364763620 1E-21;
        H =  1.6041491442052637895 7E-25;
        I = -1.4364241317829209639 2E-29;
        J =  7.5585902912912639899 5E-34;
        K = -1.7716673510571841403 2E-38;
    end

    Theta_r = 2.78;%K
    Theta_v = 3165;%K
    %Q_el = 2 + O(exp(-131924/T))

    Fun = (A+B*T+C*T.^2+D*T.^3+E*T.^4+F*T.^5+G*T.^6+H*T.^7+I*T.^8+...
        J*T.^9+K*T.^10)./(2*(T/(2*Theta_r)).*(1./(1-exp(-
Theta_v./T))))...
        ./T.*exp(-E_u./(T*k_B));

elseif species == 4

    %%%%%%%%%%%%%%%%%%%%%%%%%%%%%%%%%%%%
    % CN
    %%%%%%%%%%%%%%%%%%%%%%%%%%%%%%%%%%%%

    A = 0.000224;%from LIF measurement at the wall
    Theta_r = 2.73;%K
    Theta_v = 2968;%K
    %Q_el = 2 + 4*exp(-13305/T) + 2*exp(-37060/T) + O(exp(-78412/T))

    Fun = A./((2+4.*exp(-13305./T)+2*exp(-37060./T)).*(T/Theta_r).*...
        (1./(1-exp(-Theta_v./T))))...
        ./T.*exp(-E_u./(T*k_B));
```

```
    %Fun = A./((2+4.*exp(-13305./T)+2*exp(-
37060./T)).*(T/Theta_r).*(1./(1-exp(-Theta_v./T))))...
    %    ./T.*exp(-E_u./(T*k_B));

end

end
```

Appendix I

Data Reduction Program

```
%%%%%%%%%%%%%%%%%%%%%%%%%%%%%%%%%%%%%%%%%%%%%%%%%%%%%%%%%%%%%%%%%%%%%%%%%%%%
Temperature Curve Fit Program
% Andrew Lutz [6 - 7 - 2013]
%%%%%%%%%%%%%%%%%%%%%%%%%%%%%%%%%%%%%%%%%%%%%%%%%%%%%%%%%%%%%%%%%%%%%%%%%%%%

%Objective:
%- Plot all data points included in data file
%- Fit the temperature and integrated area with trend lines starting from
%       first usable data point (near wall points may be untrustworthy)
%- Calculate chi_hat from density trend line
%- Calculate chi_hat from discrete density data
%- Calculate 'k' from diffusion and chi_hat data
%- Calculate gamma from 'k' value and thermal speed

%Plots:
%- Temp data/fit; Int. area data/fit; n_bulk data/fit; chi_X
%- All temp data; All int. area data
%- Chi_hat (trend_fit); Chi_hat (discrete_fit)

%To Do:
%- Set a rule (perhaps based on laser thknss) for first usable data point


clear
clc
clf
global SurfTemp SurfDens

UserInputs

%------------Universal Constants----------%
Ru = 8.31446; %J/(mole*K) Universal gas constant
kB = 1.381E-23;%J/K Boltzmann Constant
Na = 6.02E23;%part/mole Avogadro's Constant
M_C = 12.01E-03;%kg/mole
m_C = M_C/Na;%kg/particle
M_Ar = 39.95E-03;%kg/mole
m_Ar = M_Ar/Na;%kg/particle
if species == 0 %O-atom
    M_X = 16E-03;%kg/mole, O-atom
    m_X = M_X/Na;%kg/particle
    M_X2 = 28E-03;%kg/mole
    m_X2 = M_X2/Na;%kg/mole
    M_CX = 28E-03;%kg/mole
    m_CX = M_CX/Na;%kg/particle
    Do = 0.0000365;%m^2/s
else            %N- atom
    M_X = 14E-03;%kg/mole, N-atom
    m_X = M_X/Na;%kg/particle
    M_X2 = 28E-03;%kg/mole
    m_X2 = M_X2/Na;%kg/particle
    M_CX = 26E-03;%kg/mole
    m_CX = M_CX/Na;%kg/particle
    Do = 0.0000364;%m^2/s
end

%------------Set Quantities---------%
Area = pi*(Diameter)^2/4;%m^2
res = 1E-05;%m - Resolution of x-axis for plotting fit-functions
BLDens = 1; %unitless - set to '1' because normalized
```

```
FR_total = FR_X+FR_Ar;%total flow rate SLPM
chi_X_BL = (FR_X/FR_total)*chi_X_BL;%adjusted chi_X value for Ar
chi_Ar_BL = (FR_Ar/FR_total);%molar fraction of Argon.
D = Do*(760/p)*(SurfTemp/298)^1.64;%m^2/s
thermspeed_X = sqrt((8*Ru*SurfTemp)/(pi*M_X)); %thermal speed m/s


%Read in Data
data = textread(['/Users/andrewlutz/Documents/00 - Research/00 - '...
    'Lab Data/ReducedData/',datafile],'',-1,'delimiter',...
        '\t','headerlines',header);
    %\t - tab delimited; 'headerlines',1 - skip 1 line;

Distance = 1E-03*data(:,1);%m
Temperature = data(:,2);%K
Density = data(:,3);%AU
HighRes_Distance = 0:res:Distance(end);%m

%-----------Double Exponential Temperature Fit---------------%
%A + B = C where C = TempBL - SurfTemp
TempCoeffGuess = 0.5*(BLTemp - SurfTemp);
Initial_TempFit_Guess = [TempCoeffGuess, 1, TempCoeffGuess, 1];
[Temp_Coeffs] = lsqcurvefit(@FDoubleExpTemp, Initial_TempFit_Guess, ...
    Distance(ini_fit_loc:end), Temperature(ini_fit_loc:end));
%K vs. m
Temp_Function_trend = FDoubleExpTemp(Temp_Coeffs, HighRes_Distance);


%------------Double Exponential Integrated Area Fit -------------%
%Downward Trending Data
if Density(1) < Density(end)
    %A + B = C where C = DensBL - SurfDens
    DensCoeffGuess = 0.5*(BLDens - SurfDens);
    Initial_DensFit_Guess = [DensCoeffGuess,.001,DensCoeffGuess,.001];
    [Dens_Coeffs] = lsqcurvefit(@FDownwardDensFit, ...
        Initial_DensFit_Guess,Distance(ini_fit_loc:end), ...
        Density(ini_fit_loc:end));
    Dens_Function_trend = FDownwardDensFit(Dens_Coeffs, ...
        HighRes_Distance);%AU vs. m

    %------For Plotting-----%
    y_min = 0;
    y_max = max(Density)+0.1;

%Upward Trending Data
else
    Initial_DensFit_Guess = [Density(ini_fit_loc), .001];
    [Dens_Coeffs] = lsqcurvefit(@FUpwardDensFit, Initial_DensFit_Guess, ...
        Distance(ini_fit_loc:end), Density(ini_fit_loc:end));
    %AU vs. m
    Dens_Function_trend = FUpwardDensFit(Dens_Coeffs, HighRes_Distance);

    %------For Plotting-----%
    y_min = 0;
    y_max = max(Density)+0.1;

end

%-----------Chi-hat & Gamma Determined from Trendline Fit of Density------%
```

```
norm_fit_loc = round(Distance(norm_loc)/Distance(end)*...
    length(Temp_Function_trend));
n_Bulk_Norm_trend = Temp_Function_trend(norm_fit_loc)./...
    Temp_Function_trend;
chi_hat_trend = Dens_Function_trend./n_Bulk_Norm_trend;
koverD_trend = (1/chi_hat_trend(1))*(chi_hat_trend(2)-...
    chi_hat_trend(1))/res;%m^-1
gamma_trend = koverD_trend*D/(thermspeed_X/4);



%-----------Chi-hat & Gamma Determined from Discrete Points Directly------%
%Temp at each meas. location
Temp_Function_discrete = FDoubleExpTemp(Temp_Coeffs, Distance);
n_Bulk_Norm_discrete = Temp_Function_discrete(norm_loc)./...
    Temp_Function_discrete;
%n_Bulk_Norm_discrete = Temperature(end)./Temperature;
chi_hat_discrete = Density./n_Bulk_Norm_discrete;

Initial_ChiHatFit_Guess = [0.4, 1];
[ChiHatFit_Coeffs] = lsqcurvefit(@FChiHatFit, Initial_ChiHatFit_Guess, ...
    Distance(ini_fit_loc:ini_fit_loc+num_pts), ...
    chi_hat_discrete(ini_fit_loc:ini_fit_loc+num_pts));
chi_hat_FitFunc = FChiHatFit(ChiHatFit_Coeffs, HighRes_Distance);

koverD_discrete = (1/chi_hat_FitFunc(1))*(chi_hat_FitFunc(2)-...
    chi_hat_FitFunc(1))/res;%m^-1
gamma_discrete = koverD_discrete*D/(thermspeed_X/4);

output = zeros(length(HighRes_Distance),11);
output(:,1) = transpose(HighRes_Distance);
output(:,2) = transpose(Temp_Function_trend);
output(:,3) = transpose(Dens_Function_trend);
output(:,4) = transpose(n_Bulk_Norm_trend);
output(:,5) = transpose(chi_hat_trend);

output(1:12,6) = Distance;
output(1:12,7) = Temperature;
output(1:12,8) = Density;
output(1:12,9) = Temperature(end)./Temperature;
output(1:12,10) = chi_hat_discrete;
output(:,11) = transpose(chi_hat_FitFunc);




%-------------Double Exponential Fit Plots----------------------------%

subplot(2,2,1);
plot(HighRes_Distance, Temp_Function_trend, Distance(1:ini_fit_loc),...
    Temperature(1:ini_fit_loc), 'o','LineWidth', 2)
hold on
plot(Distance(ini_fit_loc:end), Temperature(ini_fit_loc:end),'ok',...
    'markerfacecolor', 'red')
grid on
axis([Distance(1)-0.0005 Distance(end)+0.0005 0 max(Temperature)+500])
xlabel('Distance [m]')
ylabel('Temperature [K]')
```

```
text(mean(HighRes_Distance), max(Temp_Function_trend)/2, ...
    {datafile,['T_{wall} = ',num2str(Temp_Function_trend(1)),'K'], ...
    ['T_{edge} = ',num2str(BLTemp)]}, 'BackgroundColor', 'White')
title('Double Exponential Fit')
hold on

%Plot Numberdensity vs. Distance with fit function and discrete data
subplot(2,2,2);
plot(HighRes_Distance, Dens_Function_trend, Distance(1:ini_fit_loc),...
    Density(1:ini_fit_loc), 'o','LineWidth', 2)
hold on
plot(Distance(ini_fit_loc:end), Density(ini_fit_loc:end),'ok',...
    'markerfacecolor', 'red')
grid on
axis([Distance(1)-0.0005 Distance(end)+0.0005 y_min y_max])
xlabel('Distance [m]')
ylabel('Norm. Int. Area [AU]')
text(mean(HighRes_Distance), (y_min+y_max)/2, ...
    ['nwall = ',num2str(Dens_Function_trend(1))], 'BackgroundColor',...
    'White')

%Plot Bulk_Number_Density vs. Distance
subplot(2,2,3)
plot(HighRes_Distance, n_Bulk_Norm_trend, Distance(1:ini_fit_loc),...
    Temperature(end)./Temperature(1:ini_fit_loc), 'o','LineWidth', 2)
hold on
plot(Distance(ini_fit_loc:end), Temperature(end)./...
    Temperature(ini_fit_loc:end),'ok', 'markerfacecolor', 'red')
grid on
axis([Distance(1)-0.0005 Distance(end)+0.0005 0 ...
    max(n_Bulk_Norm_trend)+0.5])
xlabel('Distance [m]')
ylabel('Bulk Num. Density')

%Discrete chi-hat, full trend line and linear trendline

%Plot Chi_X vs. Distance
subplot(2,2,4)
plot(HighRes_Distance, chi_hat_trend, ...
    HighRes_Distance(1:Distance(ini_fit_loc+num_pts)/res), ...
    chi_hat_FitFunc(1:Distance(ini_fit_loc+num_pts)/res),'LineWidth', 2)
hold on
plot(Distance(ini_fit_loc:end), chi_hat_discrete(ini_fit_loc:end),...
    'ok', 'markerfacecolor', 'red')
grid on
axis([Distance(1)-0.0005 Distance(end)+0.0005 0 1.1])
xlabel('Distance [m]')
ylabel('$$\hat{\chi}$$', 'Interpreter', 'Latex')
text(mean(HighRes_Distance), 0.5*(max(chi_hat_discrete)+...
    min(chi_hat_discrete)), ...
    {['\gamma_{REF} = ',num2str(gamma_ref)] ...
     ['\gamma_{TrendLineFit} = ',num2str(gamma_trend)] ...
     ['\gamma_{DiscretePtFit} = ',num2str(gamma_discrete)] ...
     ['Number of Pts = ',num2str(num_pts+1)]}, 'BackgroundColor', 'White')
```

```
%%%%%%%%%%%%%%%%%%%%%%%%%%%%%%%%%%%%%%%%%%%%%%%%%%%%%%%%%%%%%%%%%%%%%%%%%%%%
% User Inputs Initialization
% Andrew Lutz [6 - 7 - 2013]
%%%%%%%%%%%%%%%%%%%%%%%%%%%%%%%%%%%%%%%%%%%%%%%%%%%%%%%%%%%%%%%%%%%%%%%%%%%%

%This program develops a least-squares curve fit for the temperature
%profile and number density towards the wall.
%Instructions:
% - Create tab-delim data file with y-dist (mm), Temp (K) and
normalized-to-BLedge density columns
% - Save as 'yyyymmdd.txt'
% - Place in '/Users/andrewlutz/Documents/Research/LabData/ReducedData
% - Change User Inputs
% - 'X' refers to probed species
% - Set quantities can be updated periodically as more data become
% available.


Test_Date = 20120829;
%20101105 - N2 w/ Graphite
%20120402 - N2 w/ Copper
%20120404 - N2 w/ Cold Quartz
%20120503 - N2 w/ SiC
%20120829 - N2 w/ Graphite
%20121217 - Air/Ar w/ Graphite
%20121218 - Air/Ar w/ Graphite

%Air-Argon tests show different O-atom evolution.  BLMoleFractions is
not
%developed to handle these situations.


if Test_Date == 20101105;
%-------------------------------------------------------------%
%User Inputs - Need to change when changing data sets
p = 100; %Torr
species = 1; % 0 - O, 1 - N;
SurfTemp = 1318; %K - from pyrometer
BLTemp = 7500; %K - estimate from data (adjustable)
SurfDens = 0.5; %unitless - estimate from trend (adjustable)
Diameter = .0125;%m
Exp_time = 63*60+20;%s
FR_X = 38;%SLPM
FR_Ar = 0;%SLPM
datafile = '20101105.txt';
header = 1; %number of headerlines
chi_X_BL = 0.9;%MUTATION LTE at BL_edge condition w/o Argon
mass_loss = (7.831-6.570)*1E-03;%kg - total mass loss
ini_fit_loc = 1;%position in data file where temp fit starts from
num_pts = 3;%additional number of points to fit linear curve
norm_loc = 8;%location of int. area normalization
gamma_ref = 0.0038;%from abs. measurement (11/05/2010), for comparison
%-------------------------------------------------------------%

elseif Test_Date == 20120402;
%-------------------------------------------------------------%
%User Inputs - Need to change when changing data sets
```

```
p = 160; %Torr
species = 1; % 0 - O, 1 - N;
SurfTemp = 650; %K - from pyrometer
BLTemp = 6000; %K - estimate from data (adjustable)
SurfDens = 17.5; %unitless - estimate from trend (adjustable)
Diameter = .025;%m
Exp_time = 0;%s
FR_X = 40;%SLPM
FR_Ar = 0;%SLPM
datafile = '20120402.txt';
header = 1; %number of headerlines
chi_X_BL = 0.9;%MUTATION LTE at BL_edge condition w/o Argon
mass_loss = 0*1E-03;%kg - total mass loss
ini_fit_loc = 4;%position in data file where temp fit starts from
num_pts = 4;%additional number of points to fit linear curve
norm_loc = 14;%location of int. area normalization
gamma_ref = 0.0173;%Jason's paper
%-----------------------------------------------------------%

elseif Test_Date == 20120404;
%-----------------------------------------------------------%
%User Inputs - Need to change when changing data sets
p = 160; %Torr
species = 1; % 0 - O, 1 - N;
SurfTemp = 800; %K - from pyrometer
BLTemp = 6000; %K - estimate from data (adjustable)
SurfDens = 16.3; %unitless - estimate from trend (adjustable)
Diameter = .025;%m
Exp_time = 0;%s
FR_X = 40;%SLPM
FR_Ar = 0;%SLPM
datafile = '20120404.txt';
header = 1; %number of headerlines
chi_X_BL = 0.9;%MUTATION LTE at BL_edge condition w/o Argon
mass_loss = 0*1E-03;%kg - total mass loss
ini_fit_loc = 4;%position in data file where temp fit starts from
num_pts = 5;%additional number of points to fit linear curve
norm_loc = 15;%location of int. area normalization
gamma_ref = 0.00587;%Jason's paper
%-----------------------------------------------------------%



elseif Test_Date == 20120503;
%-----------------------------------------------------------%
%User Inputs - Need to change when changing data sets
p = 160; %Torr
species = 1; % 0 - O, 1 - N;
SurfTemp = 1500; %K - from pyrometer
BLTemp = 7000; %K - estimate from data (adjustable)
SurfDens = 2.6; %unitless - estimate from trend (adjustable)
Diameter = .025;%m
Exp_time = 0;%s
FR_X = 40;%SLPM
FR_Ar = 0;%SLPM
datafile = '20120503.txt';
header = 1; %number of headerlines
```

```
chi_X_BL = 0.9;%MUTATION LTE at BL_edge condition w/o Argon
mass_loss = 0*1E-03;%kg - total mass loss
ini_fit_loc = 3;%position in data file where temp fit starts from
num_pts = 5;%additional number of points to fit linear curve
norm_loc = 16;%location of int. area normalization
gamma_ref = 0.000755;%Jason's paper
%-----------------------------------------------------------------%

elseif Test_Date == 20120829;
%-----------------------------------------------------------------%
%User Inputs - Need to change when changing data sets
p = 160; %Torr
species = 1; % 0 - O, 1 - N;
SurfTemp = 1600; %K - from pyrometer
BLTemp = 6000; %K - estimate from data (adjustable)
SurfDens = 0.08; %unitless - estimate from trend (adjustable)
Diameter = .025;%m
Exp_time = 42*60+26;%s
FR_X = 39.5;%SLPM
FR_Ar = 0;%SLPM
datafile = '20120829.txt';
header = 1; %number of headerlines
chi_X_BL = 0.9;%MUTATION LTE at BL_edge condition w/o Argon
mass_loss = (12.97-11.429)*1E-03;%kg - total mass loss
ini_fit_loc = 1;%position in data file where temp fit starts from
num_pts = 2;%additional number of points to fit linear curve
norm_loc = 9;%location of int. area normalization
gamma_ref = 0.0038;%from abs. measurement (11/05/2010), for comparison
%-----------------------------------------------------------------%

elseif Test_Date == 20121217;
%For Oxygen:
%1. Need to update diffusion constants
%-----------------------------------------------------------------%
%User Inputs - Need to change when changing data sets
p = 160; %Torr
species = 0; % 0 - O, 1 - N;
SurfTemp = 1460; %K - from pyrometer
BLTemp = 6000; %K - estimate from data (adjustable)
SurfDens = 0.5; %unitless - estimate from trend (adjustable)
Diameter = .025;%m
Exp_time = 32*60+3;%s
FR_X = 9.7;%SLPM
FR_Ar = 30.1;%SLPM
datafile = '20121217.txt';
header = 1; %number of headerlines
%chi_X_BL = 0.99;%MUTATION LTE at BL_edge condition w/o Argon
%Because BLMoleFractions can't handle Nitrogen reactions, add N
component
%to Argon and assume it's inert with oxygen.  Therefore, O-atom is 0.99
%(from MUTATION at BL conditions) times the 0.21 percentage in air.
chi_X_BL = 0.99*.21;%Assume N is Ar for now, so Oxygen only makes up
.21 of air
mass_loss = (12.71-6.67)*1E-03;%kg - total mass loss
ini_fit_loc = 1;%position in data file where temp fit starts from
norm_loc = 11;%location of int. area normalization
gamma_ref = 0;
%-----------------------------------------------------------------%
```

```
elseif Test_Date == 20121218;
%-------------------------------------------------------------%
%User Inputs - Need to change when changing data sets
p = 160; %Torr
species = 0; % 0 - O, 1 - N;
SurfTemp = 1478; %K - from pyrometer
BLTemp = 5500; %K - estimate from data (adjustable)
SurfDens = 0.5; %unitless - estimate from trend (adjustable)
Diameter = .025;%m
Exp_time = 22*60+53;%s
FR_X = 14.8;%SLPM
FR_Ar = 25.4;%SLPM
datafile = '20121218.txt';
header = 1; %number of headerlines
%chi_X_BL = 0.99;%MUTATION LTE at BL_edge condition w/o Argon
%Because BLMoleFractions can't handle Nitrogen reactions, add N
component
%to Argon and assume it's inert with oxygen.  Therefore, O-atom is 0.99
%(from MUTATION at BL conditions) times the 0.21 percentage in air.
%chi_X_BL = 0.99;%MUTATION LTE at BL_edge condition w/o Argon
chi_X_BL = 0.99*.21;%Assume N is Ar for now, so Oxygen only makes up
.21 of air
mass_loss = (12.720-6.693)*1E-03;%kg - total mass loss
ini_fit_loc = 1;%position in data file where temp fit starts from
norm_loc = 8;%location of int. area normalization
gamma_ref = 0;
%-------------------------------------------------------------%

else
    fprintf('Dataset not found.  Test_Date = yyyymmdd')
end
```

References

[1] Park, C. Effects of atomic oxygen on graphite ablation. (1976).

[2] Zhluktov, S. V. & Abe, T. Viscous shock-layer simulation of airflow past ablating blunt body with carbon surface. (1999).

[3] Anna, A., Alkandry, H. & Boyd, I. *Computational Modeling of Gas-Surface Interactions for High-Enthalpy Reacting Flows* (American Institute of Aeronautics and Astronautics, 2013). URL `http://dx.doi.org/10.2514/6.2013-187`.

[4] Owens, W., Uhl, J., Dougherty, M., Lutz, A. & Fletcher, D. G. Development of a 30 kw inductively coupled plasma torch facility for aerospace material testing. (10th AIAA/ASME Joint Thermophysics and Heat Transfer Conference, Chicago, Illinois, 2010).

[5] Wiese, W. L., Smith, M. W. & Glennon, B. M. tomic transition probabilities. volume 1. hydrogen through neon. Tech. Rep., US Government Printing Office, Washington, D.C. (1966).

[6] Chase, M. W. Thermochemical tables, 4th edition. Tech. Rep., NIST-JANAF, Washington, D.C. (1998).

[7] Magin, T. E. *A Model for Inductive Plasma Wind Tunnels.* Ph.D. thesis, Université Libre de Bruxelles (2004).

[8] Marrone, P. V. Normal shock waves in air: Equilibrium composition and flow parameters for velocities from 26,000 to 50,000 ft/sec. CAL Report AG-1729-A-2, Cornell Aeronautical Laboratory (1962).

[9] Wittliff, C. E. & Curtis, J. T. Normal shock wave parameters in equilibrium air. Tech. Rep. CAL-111, Cornell Aeronautical Laboratory (1961).

[10] Fay, J. & Riddell, F. Theory of stagnation point heat transfer in dissociated air. (1958).

[11] Scala, S. M. & Gilbert, L. M. The sublimation of graphite at hypersonic speeds. (1965).

[12] Anna, A. *Numerical Modeling of Surface Chemistry Processes for Hypersonic Entry Environments.* Ph.D. thesis, University of Michigan (2013).

[13] Lutz, A. *Investigation of CN Production from Carbon Materials in Nitrogen Plasmas.* Master's thesis, University of Vermont (2011).

[14] Laux, C. Radiation and nonequilibrium collisional-radiative models. (von Karman Institute for Fluid Dynamics Lecture Series, Rhode St Genese, Belgium, 2002).

[15] Anna, A. Personal communication with author (2014).

[16] Atkinson, D. Exploring saturn with shallow probes. Lecture (2013).

[17] Adler, M. *et al.* Entry, descent and landing roadmap - technology area 09. URL `http://www.nasa.gov/pdf/501326main_TA09-ID_rev5_NRC_wTASR.pdf`.

[18] Hill, C., Scott A. Kostyk, Motil, B., Notardonato, W., Rickman, S. & Swanson, T. hermal management systems roadmap - technology area 14. URL `http://www.nasa.gov/pdf/501320main_TA14-ID_rev6a-NRC-wTASR.pdf`.

[19] URL `http://www.nasa.gov/pdf/503466main_space_tech_grand_challenges_12_02_10.pdf`.

[20] Gilmore, F. Equilibrium composition and thermodynamic properties of air to 24,000 ^{o}k. Tech. Rep. RM-1543., U. S. Air Force Research (1955).

[21] Allen, H. J. & Eggers, A. J. *A study of the motion and aerodynamic heating of ballistic missiles entering the earth's atmosphere at high supersonic speeds* (U.S. Government Printing Office, Washington, D.C., 1958).

[22] Anderson, J. D. *Hypersonic and High Temperature Gas Dynamics.* (McGraw - Hill Book Company, 1989).

[23] Anderson, J. D. *Fundamentals of Aerodynamics.* (Tata McGraw - Hill Book Company, 2010).

[24] Suzuki, T., Fujita, K., Ando, K. & Sakai, T. Experimental study of graphite ablation in nitrogen flow. (2008).

[25] Zhang, L., Pejaković, D. A., Marschall, J., Dougherty, M. & Fletcher, D. G. Laboratory investigation of the atomic nitridation of graphite by atomic nitrogen. (2012).

[26] Marschall, J. & MacLean, M. Finite-rate surface chemistry model, i: Formulation and reaction system examples.

[27] Park, C. & Bogdanoff, D. Shock-tube measurement of nitridation coefficient of solid carbon. (2006).

[28] Zinman, W. A study of the interaction between carbon and dissociated gases.

[29] Goldstein, H. W. The reaction of active nitrogen with graphite. (1964).

[30] Goulard, R. On catalytic recombination rates in hypersonic stagnation heat transfer. (1958).

[31] Olander, D. R., Siekhaus, W., Jones, R. & Schwarz., J. A. Reactions of modulated molecular beams with pyrolytic graphite. i. oxidation of the basal plane. (1972).

[32] Olander, D. R., Jones, R. H., Schwarz, J. A. & Siekhaus., W. J. Reactions of modulated molecular beams with pyrolytic graphite. ii. oxidation of the prism plane. (1972).

[33] Keenan, J. A. & Candler, G. V. Simulation of graphite sublimation and oxidation under reentry conditions. (AIAA/ASME Joint Thermophysics and Heat Transfer Conference, Colorado Springs, Colorado, 1994).

[34] Maahs, H. G. Oxidation of carbon at higher temperatures: Reaction-rate control or transport control. Technical Note TN D-6310, NASA (1971).

[35] Metzger, J. W., Engel, M. & Diaconis., N. S. Oxidation and sublimation of graphite in simulated re-entry environments. (1967).

[36] MacLean, M., Marschall, J. & Driver, D. Finite-rate surface chemistry model, ii: Coupling to viscous navier-stokes code. (2011).

[37] Chen, Y. K. & Milos, F. S. Two-dimensional implicit thermal response and ablation program for charring materials. *Journal of Spacecraft and Rockets* **38**, 473–481 (2001). URL `http://dx.doi.org/10.2514/2.3724`.

[38] Gordeev, A. N., Kolesnikov, A. F. & Yakushin, M. Effect of surface catalytic activity on nonequilibrium heat transfer in a subsonic jet of dissociated nitrogen. (1985).

[39] Driver, D. M. & MacLean, M. Improved predictions of pica recession in arc jet shear tests. (49th AIAA Aerospace Sciences Meeting, Orlando, FL, 2011).

[40] Anna, A. & Boyd, I. *Computation of Surface Catalysis for Graphite Exposed to High-Enthalpy Nitrogen Flow* (American Institute of Aeronautics and Astronautics, 2012). URL `http://dx.doi.org/10.2514/6.2012-534`.

[41] Bamford, D., Jusinski, L. & Bischel, W. Absolute two-photon absorption and three-photon ionization cross sections for atomic oxygen. *Phys. Rev. A* **34**, 185–198 (1986). URL `http://link.aps.org/doi/10.1103/PhysRevA.34.185`.

[42] Copeland, R. A., Jeffries, J. B., Hickman, A. P. & Crosley, D. R. Radiative lifetime and quenching of the $3p^4d^o$ state of atomic nitrogen. (1987).

[43] Playez, M. *Titan Atmosphere Plasma Characterization using Spectroscopic Measurement Techniques.* Ph.D. thesis, von Karman Institute for Fluid Dynamics (2006).

[44] Lees, L. Laminar heat transfer over blunt-nosed bodies at hypersonic flight speeds. (1956).

[45] Zoby, E. V. Empirical stagnation-point heat-transfer relation in several gas mixtures at high enthalpy levels. Tech. Rep. TN D-4799, NASA (1968).

[46] Dorodnitsyn, A. A. Laminar boundary layer in compressible fluid. (1942).

[47] Royal Society (London). *Concerning the Effect of Compressibility on Laminar Boundary Layers and Their Separation.*, vol. 200.

[48] Royal Society (London). *Steady Flow in the Laminar Boundary Layer of a Gas.*, vol. 199.

[49] Levy, S. Effect of large temperature changes (including viscous heating) upon laminar boundary layers with variable free-stream velocity. (1954).

[50] Royal Society (London). *Correlated Incompressible and Compressible Boundary Layers.*, vol. 200.

[51] Vancrayenest, B. & Fletcher, D. G. Ablation of carbonaceous heatshields: Spectroscopic emission survey in a subsonic icp flow. (40th Thermophysics Conference, Seattle, Washington, 2008).

[52] Airgas. *Safety Data Sheet - air* (2014).

[53] Uhl, J. *Pyrolysis Investigation in an ICP Torch Facility.* Master's thesis, University of Vermont, Burlington, VT (2012).

[54] Speitel, L. C. Fourier transform infrared analysis of combustion gases. Tech. Rep., Federal Aviation Administration, Washington, D.C. (2001).

[55] Lutz, A. & Danehy, P. Ablative species detection with infrared spectrometry in hymets. (TSGC and NASA EPSCoR Awards Ceremony, Burlington, VT, 2011).

[56] Lofthus, A. & Krupenie, P. H. The spectrum of molecular nitrogen. (1977).

[57] Pillow, M. E. Band intensities in the cn violet system. (2012).

[58] Sneden, C. & Lambert, D. L. The cn red system in the solar spectrum. (1982).

[59] E., S. R. & Osterbrock, D. E. C_2 swan bands in comets. Tech. Rep. X-614-64-232, Goddard Space Flight Center, Greenbelt, MD (1964).

[60] Wiese, W. L., Smith, M. W. & Miles, B. M. Atomic transition probabilities. volume 2. sodium through calcium. Tech. Rep., US Government Printing Office, Washington, D.C. (1969).

[61] URL `http://www.nist.gov/calibrations/upload/sp250-20.pdf`.

[62] Incropera, F. P. & DeWitt, D. P. *Introduction to Heat Transfer* (John Wiley and Sons Inc., 2002).

[63] Owens, W., Meyers, J. M. & Fletcher, D. G. Surface catalysis and oxidation of flexible thermal protection materials in air plasma (44th AIAA Thermophysics Conference, San Diego, CA, 2013).

[64] Meyers, J. M., Owens, W. & Fletcher, D. Surface catalyzed reaction efficiencies in nitrogen and oxygen plasmas from laser induced fluorescence measurements. (44th AIAA Thermophysics Conference, San Diego, CA, 2013).

[65] Laux, C. O. *Specair*. SpectralFit S.A.S., 3.0 edn. (July 15, 2014).

[66] Lutz, A., Owens, W., Meyers, J. & Fletcher, D. Experimental analysis of graphite nitridation and oxidation efficiency with laser-induced fluorescence. (51st AIAA Aerospace Sciences Meeting, Grapevine, TX, 2013).

[67] Laux, C. O., Pierrot, L. & Gessman, R. J. State-to-state modeling of a recombining nitrogen plasma experiment (2012).

[68] Gueron, S. & Deutsch, M. A fast abel inversion algorithm. (1994).

[69] Kalal, M. & Nugent, K. Abel inversion using fast fourier transforms. (1988).

[70] Tatekura, K. Determination of the index profile of optical fibers from transverse interferograms using fourier theory. (1983).

[71] Laux, C. *Optical Diagnostics and Radiative Emission of Air Plasmas.* Ph.D. thesis, Stanford University (1993).

[72] Dunham, J. L. The energy levels of a rotating vibrator. (1932).

[73] Vincenti, W. G. & Kruger, C. H. *Introduction to Physical Gas Dynamics.* (Krieger Publishing Company, 1986).

[74] Eckbreth, A. C. *Laser Diagnostics for Combustion Temperature and Species.* (Abacus Press, 1988).

[75] Hitz, B., Ewing, J. & Hecht, J. *Introduction to Laser Technology* (IEEE Press, 2001).

[76] Griffiths, D. J. *Introduction to Quantum Mechanics.* (Pearson Prentice Hall, 2004).

[77] Gomes, A.-M., Bacri, J., Sarrette, J.-P. . & Salon, J. Measurement of heavy particle temperature in a radiofrequency air discharge at atmospheric pressure from the numerical simulation of the no γ system. (1992).

[78] Maiman, T. Optical and microwave-optical experiments in ruby. *Phys. Rev. Lett.* **4**, 564–566 (1960). URL `http://link.aps.org/doi/10.1103/PhysRevLett.4.564`.

[79] Fletcher, D. G. Personal communication with author (2010).

[80] Pallix, J. B. & Copeland, R. A. Measurement of catalytic recombination coefficients on quartz using laser-induced fluorescence measurement of catalytic recombination coefficients on quartz using laser-induced fluorescence. *Journal of Thermophysics and Heat Transfer.* **10**, 224–233 (1996).

[81] Smith, S. *Investigation of Subsonic and Supersonic Flow Characteristics of an Inductively Coupled Plasma Torch.* Master's thesis, University of Vermont (2013).

[82] Entegris, Inc. *Properties and Characteristics of Graphite: For the Semiconductor Industry.* (2013).

[83] Taylor, R., DeWitt, D. P. & Johnson, P. E. Spectral emissivity at high temperatures. Technical Report AD A085297, Thermophysical Properties Research Laboratory, Purdue University (1980).

[84] White, F. M. *Viscous Fluid Flow* (McGraw - Hill Book Company, 1974).

[85] Fletcher, D. G., Thömel, J., Chazot, O. & Marschall, J. Realization of a gas-surface interaction test case for model validation. (48th AIAA Aerospace Sciences Meeting, Orlando, FL, 2010).

[86] Munson, B. R., Young, D. F. & Okiishi, T. H. *Fundamentals of Fluid Mechanics* (John Wiley and Sons Inc., 2005), 4th edn.

[87] Fletcher, D. G. Arcjet flow properties determined from laser-induced fluorescence of atomic nitrogen. *Applied Optics* **38**, 1850 – 1858 (1999).

[88] Zucker, R. D. & Biblarz, O. *Fundamentals of Gas Dynamics* (John Wiley & Sons Inc., 2002).

[89] Suzuki, T., Fujita, K. & Sakai, T. Numerical analysis of graphite ablation in nitrogen flow. (46th AIAA Aerospace Sciences Meeting, Reno, Nevada, 2008).

[90] Sutton, G. P. & Biblarz, O. *Rocket Propulsion Elements.* (John Wiley & Sons Inc., 2010).

[91] Peck, E. R. & Reeder, K. Dispersion of air (1972).

[92] S., P., Auweter-Kurtz, M., Herdrich, G. & Fertig, M. Recombination coefficients and spectral emissivity of silicon carbide-based thermal protection materials. (2005).

[93] Park, C. & Ahn, H.-K. Stagnation-point heat transfer rates for pioneer-venus probes. (1999).

[94] Herzberg, G. *Atomic Spectra and Atomic Structure.* (Dover Publications, 1944).

[95] Herzberg, G. *Molecular Spectra and Molecular Structure: I. Spectra of Diatomic Molecules.* (D. Van Nostrand Company, Inc., 1950).

[96] Hecht, J. *Optics - Light for a New Age.* (Macmillan Publishing Company, 1987).

[97] Havstad, M. A. & Ferencz, R. M. Comparison of surface chemical kinetic models for ablative reentry of graphite. (2002).

[98] Gülhan, A. Heat flux measurements in high enthalpy flows. (RTO AVT Course, Rhode-Saint-Genése, Belgium, 1999).

[99] Griffiths, D. J. *Introduction to Electrodynamics.* (Pearson Education, Inc., 1999).

[100] Gessman, R. J., Laux, C. O. & Kruger, C. H. Experimental study of kinetic mechanisms of recombining atmospheric pressure air plasmas. (AIAA 28th Plasmadynamics and Lasers Conference, Atlanta, GA, 1997).

[101] Demtröder, W. *Laser Spectroscopy.* (Springer - Verlag, 1982.).

[102] *Lasers in Industry.* (Van Nostrand Reinhold Company, 1972).

[103] Chapman, A. J. *Heat Transfer.* (Macmillan Publishing Co., Inc., 1974).

[104] Çengel, Y. A. & Boles., M. A. *Thermodynamics - An Engineering Approach.* (The McGraw - Hill Companies, 2008).

[105] Castellan, G. W. *Physical Chemistry* (Addison - Wesley Publishing Company, 1983).

[106] Andrews, D. H. & Kokes, R. J. *Fundamental Chemistry* (John Wiley and Sons Inc., 1965).

[107] Anderson, J. D. *Modern Compressible Flow with Historical Perspective.* (McGraw - Hill Book Company, 2004).